OPTICAL AND DEFECT STUDIES OF
WIDE BAND GAP MATERIALS

By

CHARLES RICHARD SHAWLEY

A dissertation submitted in partial fulfillment of
the requirements for the degree of

DOCTOR OF PHILOSOPHY

WASHINGTON STATE UNIVERSITY
School of Mechanical and Materials Engineering

DECEMBER 2008

To the Faculty of Washington State University

The members of the Committee appointed to examine the dissertation of CHARLES RICHARD SHAWLEYfind it satisfactory and recommend that it be accepted.

Kelvin Lynn, Chair

M. Grant Norton

David Field

Matthew McCluskey

ACKNOWLEDGMENT

The author is truly indebted to Dr. Kelvin G. Lynn for his invaluable assistance and guidance and for sponsoring this work. Many thanks are due to all members of the Center for Materials Research at Washington State University. Also, much gratitude is extended to Dr. M.G. Norton, Dr. D.P. Field, and Dr. M.D. McCluskey for their guidance and evaluation. Several of the photographs and plots used in this dissertation were provided by graduate students Denys Solodovnikov and Jalal Nawash as well as by Dr. Marc Weber. Their help is greatly appreciated. Many thanks are extended to Dr. Jim Elliston at the WSU Radiation Center for their help with the neutron activation analysis measurements

The majority of this work was performed under the auspices of the Department of Defense, Joint Electromagnetics Technology Program Office, under the Assistant Secretary of Defense for Command, Control, Communications, and Intelligence (ASD/C^3I), under contract N66001-00-C-6008. This work was supported under a subcontract from VLOC Inc. The author acknowledges and appreciates the discussions with the other YAG and YVO_4 team members at VLOC and at the Advanced Materials Development Center (AMDC) at II-VI Inc.

A portion of the photoluminescence research described in this paper was performed in the Environmental Molecular Sciences Laboratory, a national scientific user facility sponsored by the Department of Energy's Office of Biological and Environmental Research and located at Pacific Northwest National Laboratory. Many thanks are extended to Dr. Zheming Wang for his assistance with the photoluminescence measurements.

OPTICAL AND DEFECT STUDIES OF WIDE BAND GAP MATERIALS

Abstract

by Charles Richard Shawley, Ph.D.
Washington State University
December 2008

Chair: Kelvin G. Lynn

Non-destructive, optical techniques can be used to find and identify defects in solid-state laser materials that can inhibit the material's laser performance. With accurate detection and identification, these defects can be eliminated or their effects minimized through an array of methods. Two materials, YVO_4 and YAG ($Y_3Al_5O_{12}$) are studied, and their most common and problematic defects are optically identified. The presence of grain boundaries in *a*-axis grown YVO_4 and their absence in *c*-axis grown YVO_4 as well as the ability of *c*-axis grown YVO_4 to accommodate a higher concentration level of Nd^{3+} ion suggest that the change of growth-axis direction from *a*-axis to *c*-axis may improve optical quality and laser performance of Nd:YVO_4 laser elements. In Nd:YAG, the improvement in laser performance through aluminum diffusion and oxidizing heat treatment may point to the improvement in stoichiometry by the elimination of both oxygen and aluminum vacancies. Also, the multiple valence state impurity ion, iridium, is identified in YAG through optical measurement techniques and neutron activation analysis, and the minimization of its affect on laser performance through a process of aluminum diffusion and oxidation heat treatment is discussed.

TABLE OF CONTENTS

Page

CHAPTER

APPENDIX

LIST OF TABLES

LIST OF FIGURES

Dedication

This dissertation is dedicated to
my wife, Jessica, and to my family
for all their love and support throughout these many years
and to all my instructors and mentors whose guidance and wisdom
have shaped my passion for scholarship.

CHAPTER ONE

INTRODUCTION AND BACKGROUND

1.1 History of Laser Development

Research and development in the field of solid-state lasers has spanned over the last forty years, but the initial concept of the laser has been around since the late 1950's when C.H. Townes of the United States and the former Soviet Union's N.G. Basov and A.M. Prokhovov both independently conceived the notion of radiation amplification by stimulated emission [1-3]. From this idea sprung forth the maser (Microwave Amplification by Stimulated Emission of Radiation) and the laser (Light Amplification by Stimulated Emission of Radiation), and the research thrust became finding both suitable activator and host media [1,3]. In July of 1960, Theodore Maiman built the world's first working laser, a pulsed, ruby laser, at Hughes Research Laboratories in California [2,3]. Then in 1964, J.E. Geusic, H.M. Marcos, and L.G. Van Uitert of Bell Telephone Laboratories discovered the laser action of neodymium-doped yttrium aluminum garnet (Nd:YAG) [4,5].

The discovery of laser action in various materials led to the formation and commercialization of the laser industry. The first such company was Spectra Physics, the world's first pure laser company. Spectra Physics was founded by Herbert Dwight, Ken Ruddock, Bob Rempel, William Earl Bell, and Arnold Bloom in September of 1961 [2]. Spectra Physics faired well in the fledgling market during its early years which gave rise to competitors. Jim Hobart and Eugene Watson left Spectra Physics in 1966 to form Coherent Radiation [2]. However, even with the competitive market, both Spectra Physics and Coherent Radiation did well throughout the early years of the laser industry, but as laser applications increased, so did the number of laser companies including: Sharplan, Cooperlabs, Rofin Sinar, Amada, Laserplane, Lambda Physik, and several others [2]. Numerous laser patents were issued throughout the 1970's and 1980's, and, predictably, many disagreements resulted between the laser companies. As a result, a unique event occurred in U.S. patent history wherein royalties were paid twice to inventors of the laser [2].

Applications for lasers have come a long way since their invention in 1960. Some of the original applications for lasers were in clothing manufacturing, agricultural irrigation, and alignment applications in construction and in sewer line grading [2]. Applications subsequently expanded resulting in a major breakthrough for laser technology: retail-product scanning and checkout, which came into full swing in 1974. This application was enabled not only by the low-cost, HeNe-based, automated scanners but also by the standardization of product bar-codes [2]. Although laser companies continued to fair well in the rapidly expanding market, it took fifteen years for annual sales of lasers to reach a few hundred million dollars; the major breakthrough coming in the 1980's with the emergence of battery-powered, low-cost, handheld, diode-laser pointers [2]. Laser pointers became the first truly large-volume application for lasers. This breakthrough was eventually only trumped by the sale of lasers for compact disc players. In the 1990's, newly emerging markets for lasers including cosmetic surgery and material processing systems combined with the older, more established markets pushed laser sales across the billion dollar mark, and by the year 2000, the laser printer had become the number one output device for computers with over 100 million sold [2].

With all the type of lasers and their vast applications, solid-state lasers remain one of the most important. Nd^{3+} was the first of the trivalent, rare earth ions to be utilized in a laser material, and Nd:YAG has emerged as one of the most versatile lasers to date [6].

1.2 Laser Operation

To be a good laser on a very simplistic level, the candidate material should be stable in its operational environment. It should have a high stress-fracture limit, high threshold for optical damage, low index of refraction to maximize the stimulated emission cross section, efficient absorption of pump radiation, small quantum defect, high quantum efficiency, and no absorption at the lasing wavelength [1]. For the commercial production of a solid-state laser material, it must also be economical to fabricate and be rugged enough to withstand the fabrication process. Nd:YAG and Nd:YVO_4 meet these requirements, and, in addition, they are hard enough materials to be able to finely polish.

As was stated earlier, the acronym laser denotes Light Amplification by Stimulated Emission of Radiation. Laser operation is accomplished through a complex process. An activator atom absorbs pump light photons, and an activator atom electron is excited from the ground state to an excited state [7,8]. Then a fast decay transition takes place to the upper laser state where the electron stays for relatively a long time (1-1,000μs) and is then available for stimulated emission [9]. During stimulated emission, the electromagnetic field gains energy from the activator atom's electron by having that electron, occupying a specific quantum state in the conduction band, undergo a transition to a lower-energy state spontaneously [10,11]. This transition produces a photon, and the process is known as spontaneous emission [7]. The electron can either then be excited again, remain in its current energy state, or return to the ground state through further decay transitions. These transitions can either involve the emission of other photons or emission of phonons [12]. In order for stimulation to produce a laser, the emitted photons must be able to abscond from the laser material. This is accomplished only if the atom's probability of emitting a photon is higher than the probability of the atom absorbing one [13]. This is a very simplistic explanation of the laser process and was explained in terms of a single activator atom electron. However, in a real laser system, many activator atoms and their electrons are involved.

Most laser systems involve either a 3- or 4-level energy system for operating in the manner described on the previous page. Figure 1.1, shown below, is a simplified energy-level diagram of a 3-level laser system. In the 3-level system, electrons at the ground state, E_0, are excited into the absorption band, denoted as E_2, by pump photons. The electrons then rapidly transition to the E_1 energy-state, which in this diagram is the upper laser-level, and emit phonons and photons in the process. Through spontaneous emission, the electrons transition to the E_0 state emitting photons in the process emitting both phonons and the main lasing photons. Then the pump photons can re-excite the electrons, and the process continues. In comparison, a 4-

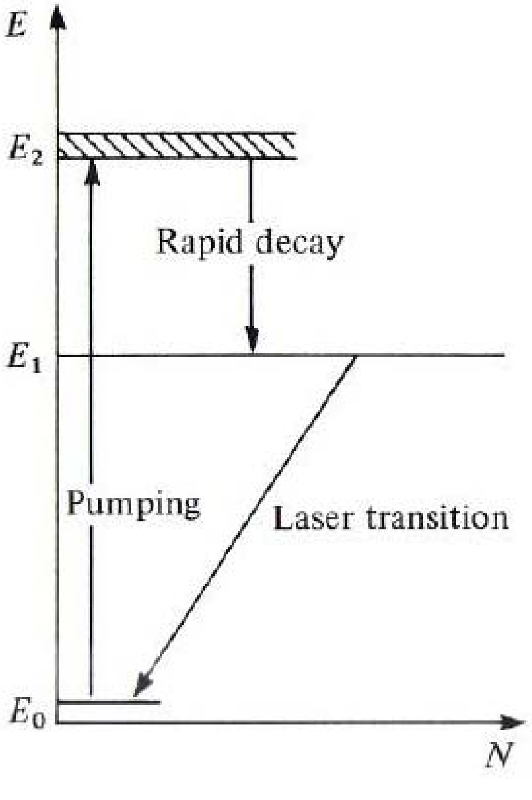

Figure 1.1: Diagram of a 3-level laser system. *Source: http://www.star.le.ac.uk/~rw/courses/lect4313_fig7.jpg accessed 9/26/06.*

level energy system is a 3-level system with one more lower-energy state as can be seen in figure 1.2 below. In this system, as in the 3-level system, pump light excites electrons in the ground state, level 0 in the diagram, to the absorption band marked as level 3 in the diagram. From level 3, the electrons rapidly transition to the upper laser-level, level 2 in the diagram. Again, through spontaneous emission, photons are emitted and the electrons transition to a lower energy-level, level 1 in the diagram. It is this energy-level that is different from a 3-level laser system. Finally, the electrons slowly transition back to the ground state through the emission of photons and phonons where pump light photons can re-excite them, and the process can repeat [14].

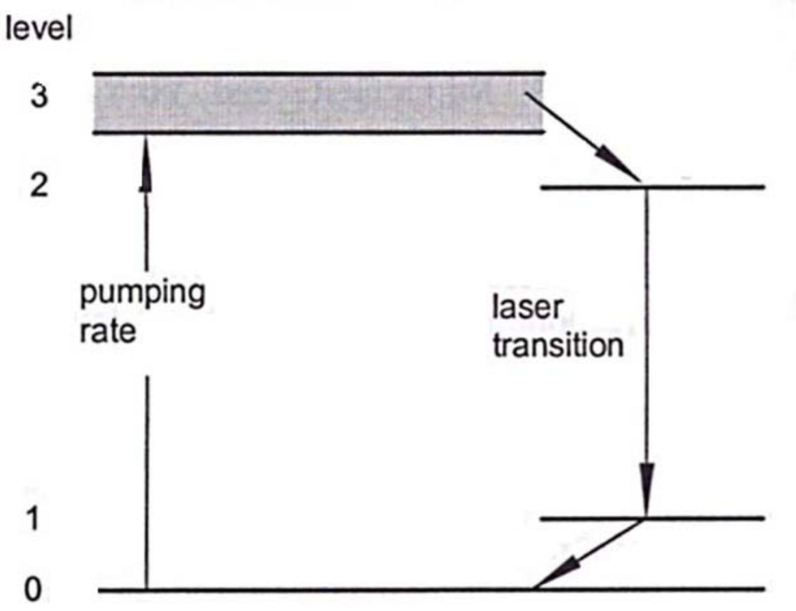

Figure 1.2: Diagram of a 4-level laser system. *Source: R. Iffländer, Solid-State Lasers for Materials Processing: Fundamental Relations and Technical Realizations. Springer-Verlag, Berlin, 2001, p. 4.*

The major distinction between the 3- and 4-level laser systems lies primarily in the fact that the laser transition takes place between the upper-laser level and the ground state for a 3-level system and occurs between the upper-laser level and the terminal-laser level (level 1 in figure 1.2) for a 4-level system. It is this terminal-laser level that makes a 4-level system much more efficient than a 3-level system, making the 4-level system more desirable for solid-state laser applications [6]. For the laser material to qualify as a 4-level system, it must possess a relaxation time between the terminal-laser level and the ground level that is fast in comparison to the fluorescence lifetime which is the average time that the electron spends in the excited state before emitting a photon and returning to the ground state [6]. Also, the terminal-laser level must be higher enough in energy above the ground state that its thermal population is small [6].

In order to produce continuous lasing, a population inversion must be obtained and sustained. A population inversion is a condition that is reached when over fifty percent of the activator atoms are excited into the upper-laser level leaving less than fifty percent of the atoms remaining in the lower-energy state [3]. Mathematically, the population inversion may be represented as:

$$\frac{N_2}{N_1} = \exp\left\{ -\frac{\left(E_2 - E_1\right)}{kT} \right\} \tag{1.1}$$

where N_2 is the population density of the upper-energy state, N_1 is the population density of the lower-energy state, E_2 is the upper-energy state, E_1 is the lower-energy state, k denotes the Boltzmann constant, and T denotes temperature [7]. The process of making $N_2 > N_1$ is called pumping and creates the necessary population inversion needed to achieve lasing. This is accomplished by pumping the activator atoms with specific-energy photons and reflecting emitted photons back into the laser material using reflective output coupling. To obtain initial lasing, the population inversion must compensate for internal losses within the laser material as well as losses due to output coupling, and, in order to maintain laser operation, the amount of round-trip gains experienced by the light wave in the laser cavity must be greater than the round-trip losses [1,9]. The condition whereby the gains and losses are equivalent is known as laser threshold [1]. For emitted photons to further stimulate activator atoms leading to the creation of a population inversion, they must travel back and forth along the length of the laser material many hundreds of times. Only those photons emitted nearly parallel to the laser beam path can make the many required traverses without departing from the side of the laser material which results in the diminutive beam divergence observed in some lasers [14]. Some final distinctions of the emitted photons lie in the fact that the emitted photons are all in-phase, have the same polarization, and propagate in the same direction as the stimulating radiation helping create the population inversion and the coherence necessary for lasing [3].

References

[1] R.C. Powell, Physics of Solid-State Laser Materials. Springer-Verlag, New York, 1998.

[2] J.M. Gill, IEEE J. Selected Topics in Quantum Electron. 6 (2000) 1111-1115.

[3] E. Hecht, Optics. Addison-Wesley, Reading, Massachusetts, 1998.

[4] J.E. Geusic, H.M. Marcos, and L.G. Van Uitert, Appl. Phys. Lett. 4 (1964) 182-184.

[5] A. Ikesue, K. Kamata, and K. Yoshida, J. Am. Ceram. Soc. 79 (1996) 1921-1926.

[6] W. Koechner, Solid State Laser Engineering. Springer-Verlag, Berlin, 1999.

[7] L.V. Azároff and J.J. Brophy, Electronic Processes in Materials. McGraw-Hill Book Company, New York, 1963.

[8] M.T. Bronski, Development of a Process for Characterization of Nd:YAG Crystals. Thesis, Worchester Polytechnic Institute, Worchester, Massachusetts, 2003.

[9] R. Iffländer, Solid-State Lasers for Materials Processing: Fundamental Relations and Technical Realizations. Springer-Verlag, Berlin, 2001.

[10] D.J. Griffiths, Introduction to Quantum Mechanics, Prentice-Hall, Inc., Upper Saddle River, New Jersey, 1995.

[11] A. Javan, Sci. Am. 217 (1967) 238-248.

[12] B. Henderson, Defects in Crystalline Solids. Crane, Russak & Company, Inc., New York, 1972.

[13] J. LeBret, Defect Characterization of Yttrium Orthovanadate. Thesis, Washington State University, Pullman, Washington, 2004.

[14] C.R. Barrett, W.D. Nix, and A.S. Tetelman, The Principles of Engineering Materials. Prentice-Hall, New Jersey, 1973.

CHAPTER TWO

CRYSTAL GROWTH OF SOLID-STATE LASER MATERIALS

2.1 Czochralski Crystal Growth

Crystal growth is an extremely important global industry. In 1999, some 20,000 tons of bulk crystals were grown [1]. Figure 2.1, shown below, is a pie chart showing the distribution by sector for these 20,000 tons of bulk crystals. As is evident from the pie chart, the laser sector accounts for five percent of the total. This broad and growing industry owes its beginning to Auguste Verneuil, the so-called founder of industrial crystal growth [1]. Verneuil invented the flame-fusion growth process and, in 1891, was able to control crystal nucleation creating large, single-crystals of sapphire and ruby [1]. A diagram of Verneuil's process is shown in figure 2.2. In the following years, modifications of Verneuil's principles were adopted. Most notably were those of Tammann (1914), Czochralski (1918), Bridgman (1923), Stöber (1925), Ramsperger and Malvin (1927), and Stockbarger (1936) [1]. Some of these modifications can be seen in figure 2.3.

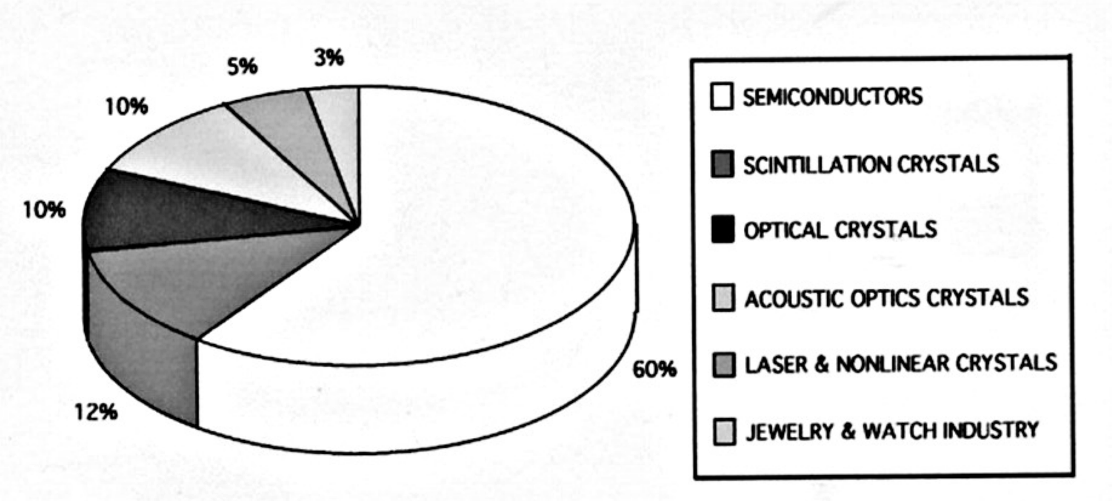

Figure 2.1: Bulk crystal distribution by sector for the year 1999. *Source: H.J. Scheel, J. Cryst. Growth 211 (2000) 3.*

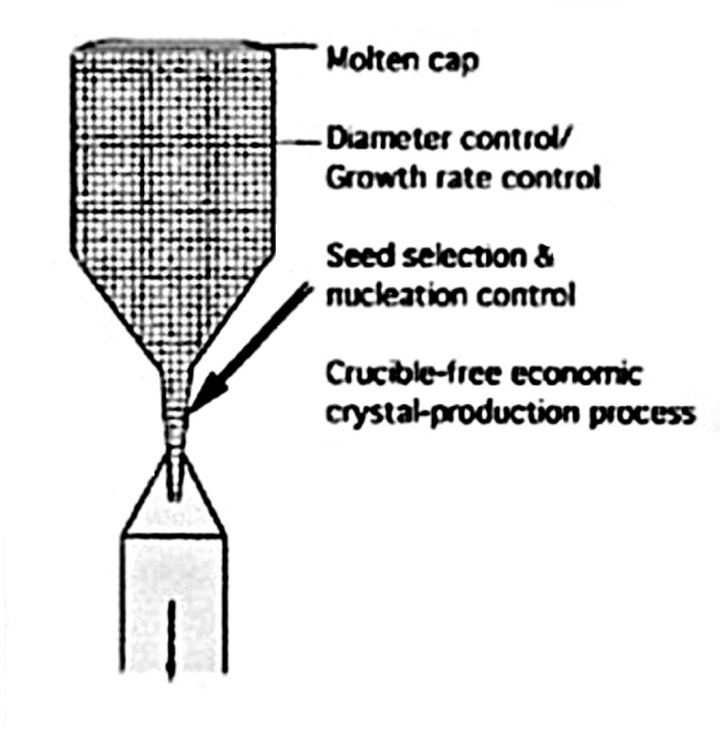

Figure 2.2: The Verneuil process of crystal growth. *Source: H.J. Scheel, J. Cryst. Growth 211 (2000) 3.*

Czochralski's method was discovered by accident in 1916 while he was studying the crystallization of various metals. A crucible containing molten tin was left on a table to cool and re-crystallize while he prepared some notes regarding his research. At some point, Jan dipped his pen into the crucible mistaking it for his inkwell. As Jan withdrew his pen, he saw a thin thread of solidified tin hanging at the tip of the writing nib [2]. Further analysis revealed that this thread was a single crystal of tin. Later, the nib was replaced by a capillary and then eventually by a seed crystal of the material to be grown, and the Czochralski method of crystal growth was born [2]. Czochralski published a paper in 1918 that described the process and stated that for proper crystal growth the rate of crystal withdrawal must be strictly equated to the crystallization velocity, which is a material dependent property [2,3].

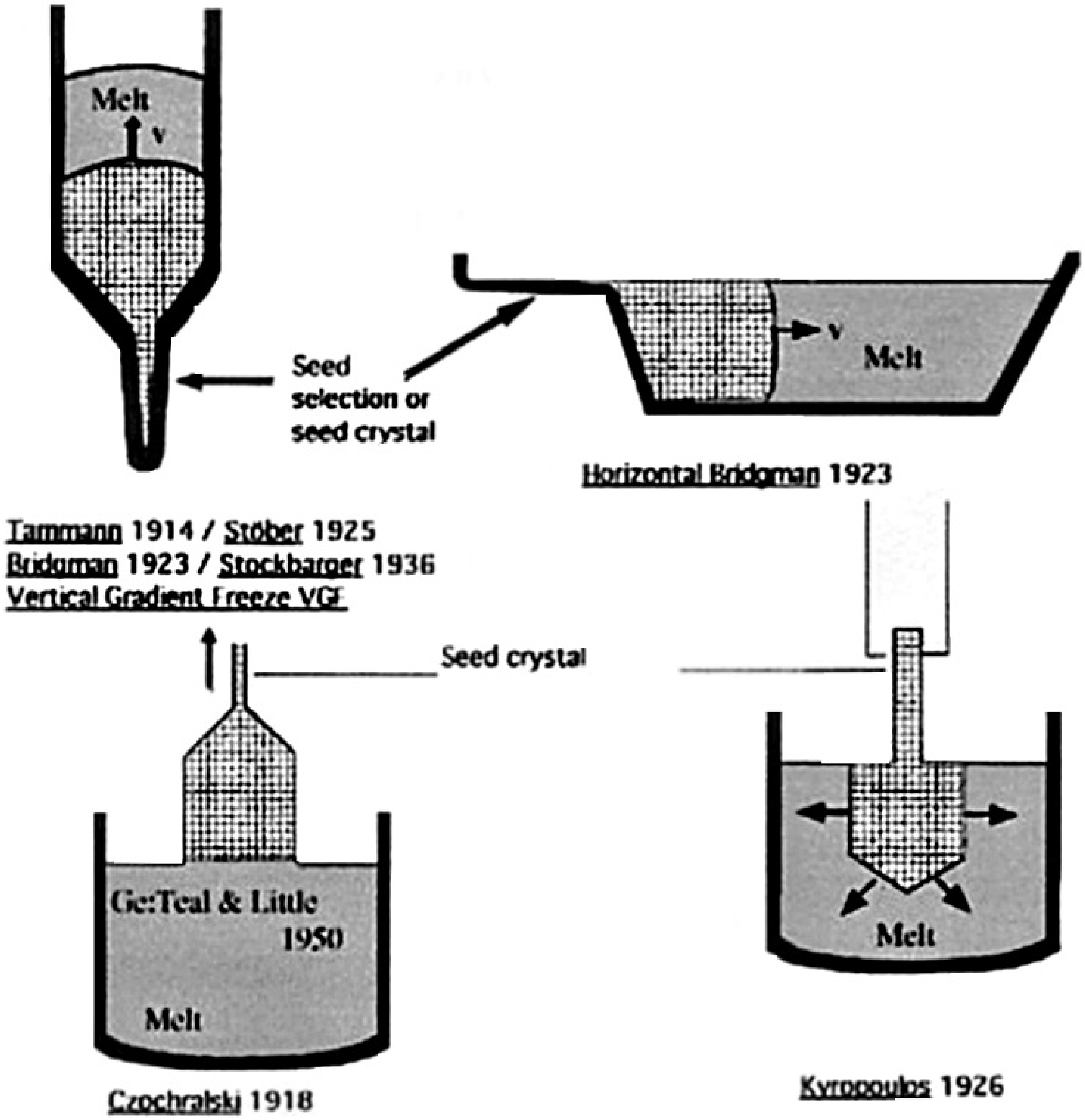

Figure 2.3: Various modifications of the Verneuil process. *Source: H.J. Scheel, J. Cryst. Growth 211 (2000) 3.*

Vast improvements to the original Czochralski design were quickly achieved. Later in 1918, Wartenberg used a seed crystal for the Czochralski growth of single crystals, a first in a list of important improvements to the Czochralski method, [2]. Perhaps the most important adaptation in Czochralski-method history was achieved in 1950 when Gordon Teal transferred the method from metallurgy to semiconductor physics in his growth of single-crystal silicon [2].

Figure 2.4 is a schematic illustration of the growth of single crystal silicon by the Czochralski method.

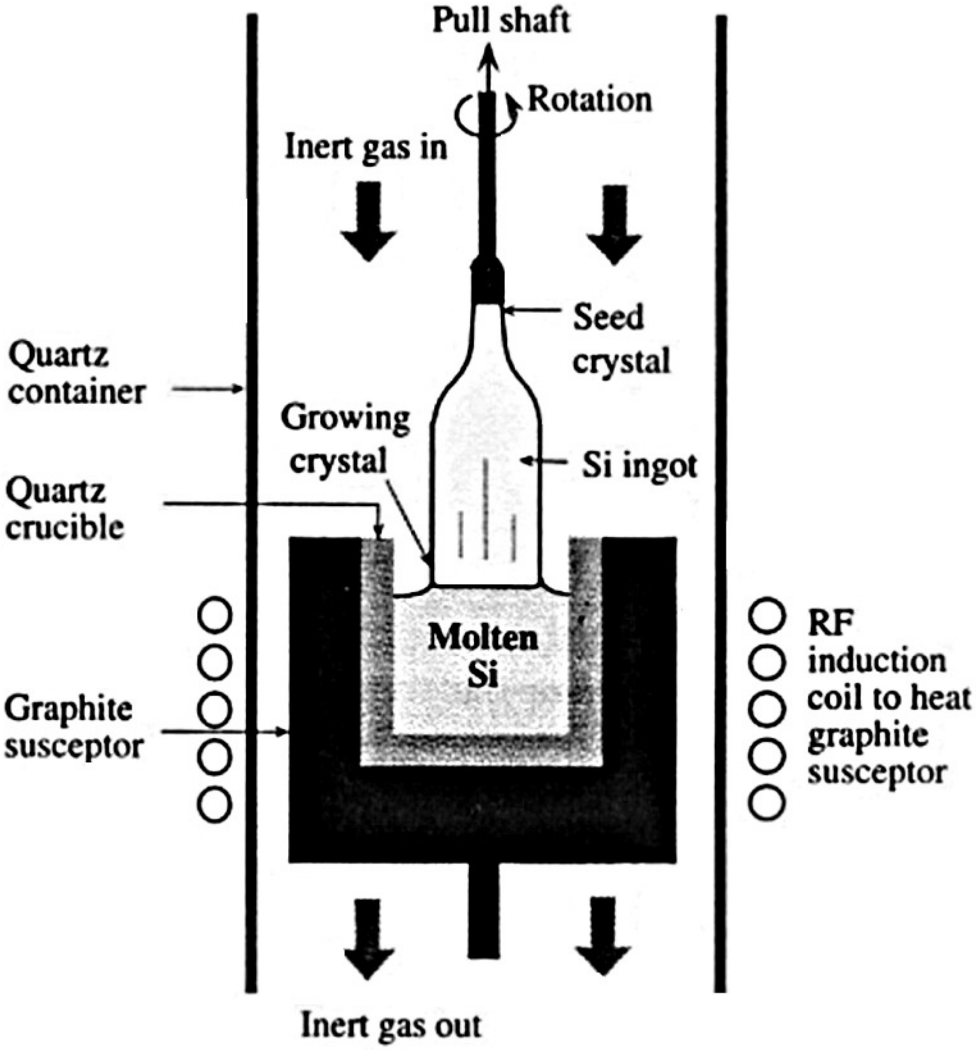

Figure 2.4: Schematic of silicon crystal growth by the Czochralski method. *Source: S.O. Kasap, Principles of Electrical Engineering Materials and Devices. Irwin McGraw-Hill, Boston, 1997, p. 65.*

Czochralski-method crystal growth is a very complex process, and it is constantly being improved for growing different materials. There are many parameters to consider when growing defect-free crystals by this method including, but not limited to, pulling speed, seed-crystal rotation rates, melt temperature, fluid dynamics, and mechanical perturbations. A diagram of a few of the critical parameters and their influence on crystal growth is shown in figure 2.5. The rotation of the seed crystal and the rate of extraction are particularly important parameters as they have a direct influence on crystal dimensions. A slower rotation rate will produce a larger crystal diameter and vice versa [4]. In addition, to avoid core strain and cellular morphology issues, the rotation rate must be increased while the pulling speed is simultaneously decreased [5]. However, the rotating crystal generates a centrifugal force, forced convection, which draws up the melt and accelerates it radially outward so rotation of the seed crystal must be carefully monitored [6]. Also, mechanical perturbations can be the result of irregular rotation of the seed crystal and/or translation of the puller [7]. Czochralski crystal growth furnaces use a rotating

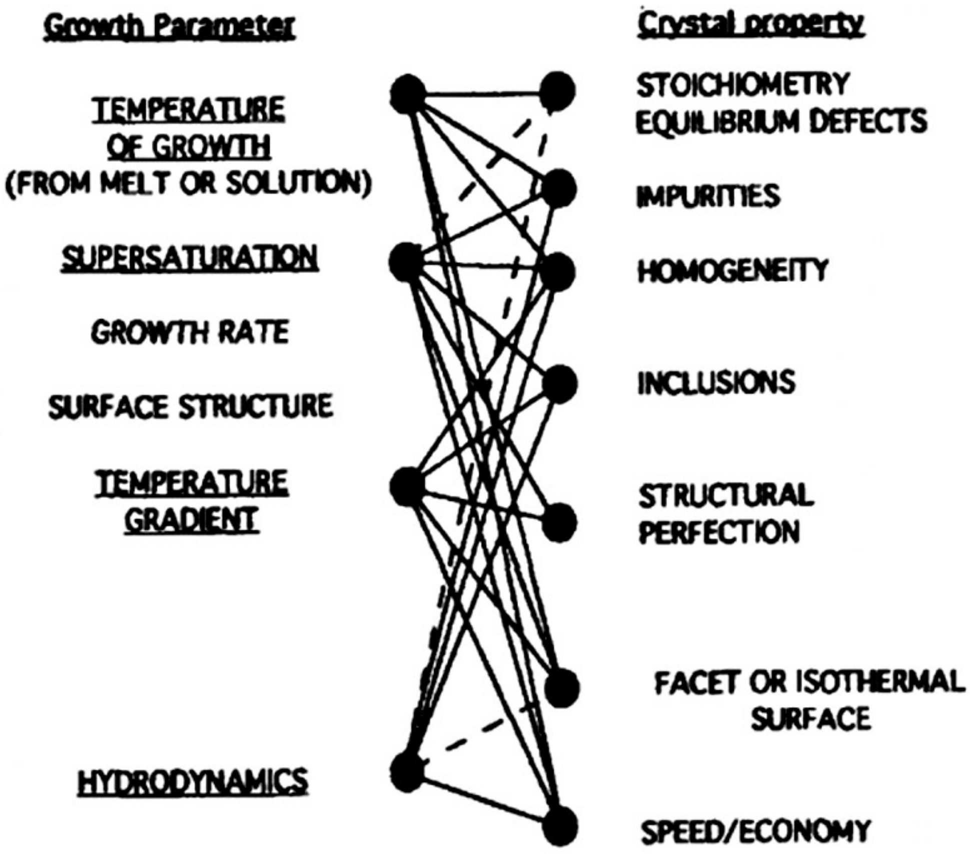

Figure 2.5: Critical parameters involving Czochralski-method crystal growth. *Source: H.J. Scheel, J. Cryst. Growth 211 (2000) 5.*

shaft that holds the seed crystal and controls the growing crystal's diameter by use of an inline load cell which measures the crystal's weight as is it pulled from the melt and compares it to a pre-programmed weight profile [8]. Any deviation from the pre-programmed weight causes a modification of the generator's output power to the crucible thus controlling the diameter of the crystal by generating small changes in heat transfer [8].

Czochralski growth involves two types of generated convections in the melt, natural convection and forced convection. Natural convection is attributed to density differences in the gravity field of the melt and to thermocapillary forces at the melt/gas-atmosphere interface, while forced convection is caused by the rotation of the crystal and/or the crucible [9]. Figure 2.6 is a schematic showing the convection in the melt during growth. These convection flows influence

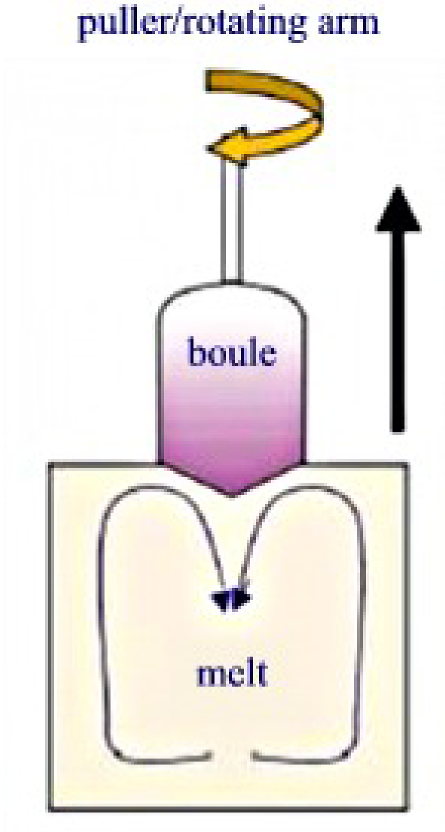

Figure 2.6: Schematic of convection flow in the melt during crystal growth. *Source: E. Kanchanavaleerat, D. Cochet-Muchy, M. Kokta, J. Stone-Sundberg, Ju. Sarkies, and Jo. Sarkies, Opt. Mater. 26 (2004) 339.*

the shape of the melt/crystal interface during growth, which is discussed in greater detail in section 2.2.5. The crystallization of each successive portion of the melt proceeds only on the crystal immersed in it. This only occurs if there is a temperature difference between the crucible wall and the crystal/melt interface causing a free convection flow of the melt [8]. The growing portion is then affected by the hydrostatic and surface tension forces of the melt, the shape of the crystal/melt interface, static heat flow—which determines the temperature difference between the melt and the crystal/melt interface, and dynamic heat flow—which decreases temperature fluctuations in the melt [8]. At crystallization, the melt solidifies at the crystal/melt interface by the removal of the heat of fusion of the melt under controlled conditions matching the rates of heat and mass transfer [8].

To heat the melt, most furnaces use radio frequency (RF) generators which operate in the 10-30kHz range and produce the very high temperatures required for growing some crystals. The lower limit of 10kHz is by far the most preferred frequency as it produces significantly lower voltages on the coupling coils [8]. Additionally, the lower frequencies produce a more uniformly-heated crucible and can simplify the coupling coil designs [8].

Because of the high temperatures involved in growing certain crystals by the Czochralski method, it is often necessary to protect the crucible as well as the melt from environmental influences. This is accomplished by filling the entire system with an inert gas. Frequently, small additions of other gases such as oxygen are mixed with the inert gas in order to control defect formation, melt evaporation, and the oxidation states of dopants [8]. In addition, lower emissivity of the enclosure means higher heat reflectivity resulting in lower heat loss from the crystal and free-melt surfaces [6]. Enclosure emissivity can change during the growth process due to chemical reactions such as the oxidation of the crucible material or evaporation of some of melt constituents from the melt surface [6]. In summary, the growth of defect-free crystals is extremely difficult due to the many growth parameters involved in Czochralski-method crystal growth.

2.2 Growth Issues for YVO_4 and YAG

Many growth issues arise for complex crystals such as solid-state laser materials. Pulling rates, impurities in the crystal, furnace atmosphere, the addition of dopants, the impact of dopant segregation in the crystal, the crystal/melt interface, and heating and cooling are just a few of the many issues that surround defect-free growth of crystals. Some of these issues will be discussed briefly while other issues will be discussed later in greater detail.

Both yttrium aluminum garnet (YAG) and yttrium orthovanadate (YVO_4) are grown by the Czochralski method and are complex crystals to grow. Because a single-crystal seed is required for Czochralski-method crystal growth, the first YVO_4 crystals were grown using an iridium seed crystal [4]. Today, either an *a*-axis or *c*-axis YVO_4 seed crystal is used in this very slow growth process. The following growth parameters affect the quality of the grown crystals for both these materials.

2.2.1 Pulling Rates

The typical pulling rates of Czochralski-grown YVO_4 and YAG are about 0.2 to 0.5mm/hr resulting in total growth times of at least a week for YVO_4 at least 30 days for the larger-sized YAG boules, and typical seed crystal rotation rates are in the 10 to 20rpm range [4,10,11]. These long growth times lead to high manufacturing costs for these crystals [11]. Slower pulling speeds are used to prevent inclusions, bubbles, striations, and other growth inhomogeneities that are caused by fast and inconsistent pulling rates [12]. Unfortunately, defects are unavoidable in these crystals no matter how slow the crystal is pulled from the melt, and growing YAG with faster pulling rates is often very difficult due to YAG's sluggish crystallization from the melt as well as its extreme temperature sensitivity [13].

2.2.2 Crucible Material

To hold the melt during both YVO_4 and YAG crystal growth, iridium crucibles are often used due to their high melting point [10]. However, these crucibles are expensive and iridium contamination of the grown crystal is difficult to avoid [14-16]. This is due to the fact that at high temperatures, oxygen and water vapor can mediate the transport of iridium from hot surfaces such as the crucible walls to colder ones such as the growth capillary thereby reducing the capillary size and contaminating the growing crystal [17]. Iridium inclusions act as scatter centers in the crystal which can inhibit its performance as a laser [18]. Iridium as an impurity in YAG is a possible candidate for one of the main loss mechanisms found in Nd:YAG laser crystals, which is explored in greater detail later.

2.2.3 Growth Atmosphere

Growth atmosphere is also vital in the growth of YVO_4 and YAG. In one study, when YAG crystals were grown in vacuum, iron, chromium and other transition elements were removed from the melt due to their high volatility [19]. However, during high-temperature crystal growth, frequent crusting of the melt surface and frequent bubbling was observed and attributed to oxygen loss from the melt [4]. Therefore, it is important to have a carefully controlled atmosphere throughout crystal growth. Usually, an inert atmosphere containing small concentrations of oxygen is used for growing YVO_4 and YAG. Nitrogen and argon gas containing oxygen concentrations in the 300-1,000ppm range are commonly used [8]. While the inert gas may provide counter-pressure to keep oxygen from leaving the melt and the minute addition of oxygen to the growth atmosphere may absorb into the melt, too much oxygen in the environment may oxidize the iridium crucible reducing the lifetime and structural integrity of the crucible as well as adding deleterious iridium impurities to the resulting crystal [20].

Another interesting aspect of furnace atmosphere is that some oxide liquids, including YVO_4 and YAG show a strong change in melt convection with changing growth atmosphere, going from a condition of turbulent convection under a pure nitrogen atmosphere to a well-structured "spoke" pattern under a small oxygen partial pressure [17]. A photograph of these spoke lines can be seen in figure 2.7. This spoke pattern is observed at low rotation rates, and changes from a circumferential pattern to a vortex-like structure as the rate of rotation is progressively increased suggesting that the morphology of the cellular structure is related to the convective fluid flow within the melt and is radially directed toward the crucible center when the crystal is either stationary or rotating slowly [5]. An explanation for this involves the density differences in the melt which help generate a natural convection causing the melt to rise along the heated crucible walls and turn inward radially at the melt surface (known as Marangoni convection) and then turn downward axially toward the crucible bottom, as can be seen schematically in figure 2.6 [6]. Spoke patterns may shift position during the early stages of crystal growth and the shifting convection flows cause small perturbations that could lead to growth rings, which are commonly found in the earliest-grown part of the boule [12].

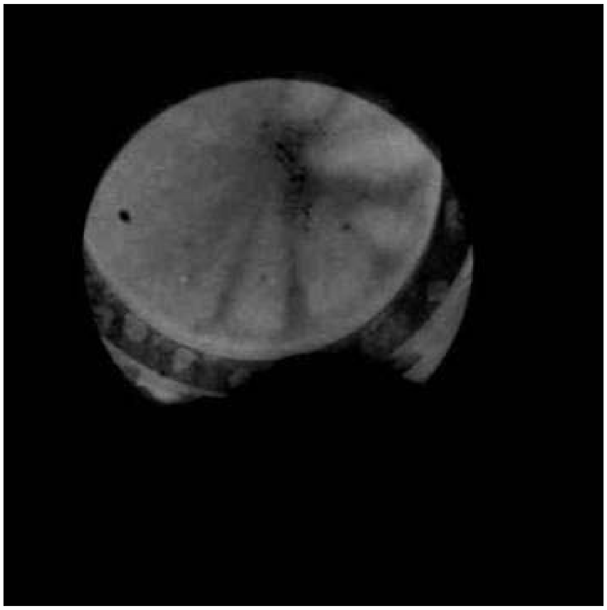

Figure 2.7: Spoke lines seen in the melt during crystal growth of Nd:YAG. *Source: Photo courtesy of Jalal Nawash.*

2.2.4 The Addition of Dopants

To form YAG, a 3:5 ratio of yttria (Y_2O_3) to alumina (Al_2O_3) is used [21]. However, YAG is often grown with excess Y_2O_3 to compensate for the loss of $YAlO_3$ by evaporation when the crystal is grown in a reducing atmosphere [22]. In addition, it has been noted that one can still grow proper YAG with minute Al_2O_3 deficiencies in the melt material [23]. To grow Nd:YVO_4 and Nd:YAG, the larger Nd^{3+} dopant ions are added to the melt. Larger dopant ions are often rejected at the crystal/melt interface, resulting in a lower doping percentage in the crystal than in the melt [16]. To counteract added crystal strain and to allow more larger-sized dopant to be taken into the lattice, Nd:YVO_4 and Nd:YAG are sometimes grown with another, smaller-sized dopant ion that will reduce the crystal strain caused by doping with the larger-sized ion [24]. However, in general, it is easier to obtain better laser crystals from materials grown with the fewest number of chemical constituents [15].

Attached to the problem of doping, is the issue of segregation. The segregation problem causes macroscopic and microscopic inhomogeneities in the crystals [1]. To explain this problem, it is necessary to look at the segregation coefficient of a crystal. The segregation coefficient is the ratio of the concentration of dopant in the crystal to the concentration of dopant in the melt at any given moment. Mathematically, the segregation coefficient is tied to dopant concentration by the following relation:

$$\left(C_s\right)_t = kC_o\left(1-\frac{w_{crystal}}{w_{melt}}\right)^{k-1} \tag{2.1}$$

where $(C_s)_t$ is the concentration of dopant in the crystal grown at time t, C_o is the dopant concentration in the melt at the start of crystal growth, k is the segregation coefficient, $w_{crystal}$ is the weight of the crystal at time, t, and w_{melt} is the original weight of the melt [8,25,26]. Since the segregation coefficient, k, is the ratio of dopant concentration in the crystal to the concentration of dopant concentration in the melt at any given moment, it stands that if $k = 1$, then the dopant concentration in the melt and in the crystal are equivalent, and if $k > 1$, then the melt loses dopant concentration and may need to be replenished as the crystal is grown. However, neither of these situations is observed in either Nd:YVO_4 or Nd:YAG. For the growth of these crystals, $k < 1$ meaning that there will be a doping-concentration gradient in the crystals. The result of this effect is deviation from stoichiometry leading to poor crystal quality and eventual crystal-growth failure [8].

2.2.5 The Crystal/Melt Interface

The common crystal growth axis for YAG is <111> which results in triangular-shaped facets forming on the outside of the grown boule. These facets give YAG boules a hexagonal appearance. Figure 2.8 is a photograph of a boule slice with these facets creating its hexagonal appearance. This faceting may be to some extent controlled by controlling the crystal/melt interface shape by changing the temperature gradient of the melt as well as the rotation rate of the seed crystal [5,6,8]. According to one study, an increase of melt temperature by as little as 45°C decreases the crystal/melt interface deflection by as much as eighteen percent [6]. Higher rotation rates create a strong, forced convection and produce a concave interface, while lower rotation rates produce a highly convex interface [6]. However, small variations of the crystal rotation and fluid motion during growth can lead to the instability of the crystal/melt interface producing growth defects in the crystal [6,9,27]. Moreover, neither a concave nor a convex-shaped crystal/melt interface is desirable. If the growth interface is conical, dislocations will propagate out from the center of the boule and terminate at the boule edges as the crystal grows, and if the growth interface is flat, the dislocations will propagate nearly parallel to the boule axis along the core of the boule [28]. Therefore, a flat interface is the desirable interface shape,

Figure 2.8: Slice of Nd:YAG boule showing hexagonal structure from faceting during growth. The boule slice is 75mm from top to bottom of the photograph.

which may reduce the amount of crystal strain and the number of crystal defects [5,9]. In practice, many YVO_4 and YAG boules are initially grown with a deep interface followed by a transition to a flat interface. This transition is achieved by increasing the rotating rate of the crystal [5]. However, a large number of dislocations can be generated during the transition, so it has become a particularly crucial step in the growth process [28].

2.2.6 Heating and Cooling

The temperature during crystal growth is usually kept between 50-100°C higher than the melting temperature to aid in the elimination of polycrystals that may be present in the melt and to help thoroughly mix the melt constituents [4]. As the crystal is pulled from the melt, a large supercooling of roughly 100°C is required to help solidify the crystallizing material [21]. However, while the crystal/melt interface determines the rate at which heat can be conducted from the melt through the crystal, the pulling rate determines the rate at which latent heat is released from the boule itself [29]. Moreover, any larger amount of supercooling would promote the growth of the energetically-favorable dendritic $YAlO_3$ [21]. In addition to dendrite formation, drastic or inhomogeneous cooling of the boule may result in residual crystal strain which could lead to the possibility of crystal fracture [18].

2.2.7 Non-Stoichiometry and Defects

Many complex oxide crystals grown by the Czochralski method are non-stoichiometric. This includes YVO_4 and YAG. In fact, all YAG crystals prepared from the melt have a somewhat non-stoichiometric composition due to the incorporation of some portion of the Y^{3+} ions into Al^{3+} lattice sites [30]. This is partially the result of alumina loss during crystal growth as well as the fact that many boules are grown with an excess of yttria, as mentioned earlier. Non-stoichiometric crystals also arise as a result of the thermal dissociation of the oxides in the melt [19]. Oxygen loss is prevalent in YVO_4 and YAG and can give rise to anion vacancies as well as excess cations in the grown crystal [19]. This is a major issue for YVO_4 and YAG production, as non-stoichiometric crystals can have significant problems with defect-centers that exhibit photo, chemical, and/or thermal instabilities [15].

Because non-stoichiometry conditions cause defects which may be deleterious to laser performance, it is worthwhile to investigate the types of defects that are most prevalent in these crystals. Non-stoichiometric crystals can contain all four categories of defects: zero-dimensional, one-dimensional, two-dimensional, and three-dimensional. Zero-dimensional defects are known as point defects. These include vacancies, interstitial atoms, common color centers, and their combinations—vacancy pairs, clusters, etc.—and are very prevalent in both YVO_4 and YAG [31]. One-dimensional defects are also known as line defects and include dislocations [31]. Dislocations can be a problem for both YVO_4 and YAG. Two-dimensional defects or surface imperfections include grain boundaries, twin boundaries, stacking faults, and phase boundaries [31]. These defects are prevalent in YVO_4 but are less prevalent in YAG. Finally, three-dimensional defects or volume defects include voids and secondary phases [31]. Again, these defects can be prevalent in YVO_4 but are only commonly found in the worst of YAG boules.

By introducing a point defect such as a vacancy into a perfect lattice, the possible number of atom arrangements increases quite suddenly from one to an massive number on the order of 10^{23} or higher [31]. In other words, the introduction of a point defect significantly increases the configurational entropy of the crystal following the mathematical relation:

$$\Delta S = k \log \frac{N!}{(N-n)!\,n!} \tag{2.2}$$

where N is the number of lattice sites, n is the number of atoms removed, and k is the Boltzmann constant [31]. This increase in configurational entropy is practically enough to compensate for their required energy of formation [31]. In Czochralski-method growth, oxygen ion vacancies are frozen into the crystal because the temperature drop as the crystal is pulled from the melt is large enough to keep them from diffusing out of the crystal [31,32]. Frank showed that the existence of a thermal gradient in the newly-crystallized solid could lead to a variation in thermal-equilibrium vacancy concentration where a high concentration could exist near the crystal/melt interface and a low concentration could exist in a cooler part of the crystal [31].

Non-stoichiometric crystals also contain one-dimensional dislocation defects. The bulk of dislocations in a Czochralski-method grown crystal tend to be screw dislocations as edge dislocations form a step across the whole crystal surface and can be eliminated by subsequent crystal growth [33]. One method of dislocation formation was discussed earlier and involved the crystal/melt interface shape, but there are many other ways to introduce dislocations to a crystal. For example, thermal stresses set up by non-uniform cooling of the crystal can lead to the formation of dislocations during crystal growth [31,34]. Also, in doped crystals, dislocations may arise from the non-uniform distribution of dopant atoms [35]. Further, dislocations can act as collectors of foreign atoms including dopant ions leading to areas of very high dopant concentration [31]. However, dislocations have a small effect on configurational entropy and have large energies of formation in complex oxide crystals [31]. Therefore, dislocation concentration is diminutive in comparison to the number of various point defects in YVO_4 and YAG.

Relatively dislocation-free crystal growth can be achieved through careful selection of a dislocation-free seed crystal as well as by decreasing the dimension of the boule during the beginning of the growth process, often referred to as necking down the boule [35]. Necking down the boule causes dislocations initially present in the crystal to grow out of the boule and stay out when the boule diameter is increased again [35].

An example of a two-dimensional defect that occurs in YVO_4 and YAG is striation. Striations are parallel bands of crystal grains that show up as local refractive index changes, color changes, or birefringence changes [33]. Two types of striations are present in these two crystals. The first type is known as dark contrast-thick striation and is caused by the fluctuation of the heater power of the furnace, and the second type is known as thin and dense striation and can be the result of convection flow in the melt [8,36,37]. Each striation represents a section of a growth surface during crystallization and can also result from the discontinuity of chemical composition in the crystal [33,36]. Striations can reduce the optical gain of a laser material by scattering, distorting the phase, and diverging laser light [15,36].

An example of a three-dimensional defect in these crystals is an inclusion. Inclusions occur in both YVO_4 and YAG and may form local secondary phases within the crystal as well as decorate dislocations or grain boundaries [15]. Two types of scattering centers are created by dislocation decoration. The first type is a line of solid inclusions of different refractive indices than the host crystal [33]. The other is either a veil of small, scattered inclusions or simply a string of inclusions that are caused by migrating dislocations that leave a trail of exsolved impurities [33]. To inhibit inclusions from diffusing into boules, the crystal growth rate must be lowered to a level where the inclusions diffuse back into the melt [5].

These presented topics give the reader a flavor for the types of growth issues that concern crystal growth technicians. The above topics are not exhaustive by any means. Some of the presented topics are expanded in greater detail and a few other issues not specifically mentioned in this section are discussed elsewhere. Issues specific to either YVO_4 or YAG are discussed separately in detail in the chapters corresponding to the material.

References

[1] H.J. Sheel, J. Cryst. Growth 211 (2000) 1-12.

[2] P.E. Tomaszewski, J. Cryst. Growth 236 (2002) 1-4.

[3] H.E. Buckley, Crystal Growth. John Wiley & Sons, Inc., New York, 1958.

[4] J. LeBret, Defect Characterization of Yttrium Orthovanadate. Thesis, Washington State University, Pullman, Washington, 2004.

[5] B. Cockayne, M. Chesswas, and D.B. Gasson, J. Mater. Sci. 4 (1969) 450-456.

[6] Z. Galazka and H. Wilke, Cryst. Res. Technol. 35 (2000) 1263-1278.

[7] E. Kanchanavaleerat, D. Cochet-Muchy, M. Kokta, J. Stone-Sundberg, P. Starkies, Ju. Sarkies, and Jo. Sarkies, Opt. Mater. 26 (2004) 337-341.

[8] M.R. Kokta, Mater. Res. Soc. Symp. Proc. 329 (1994) 33-43.

[9] A. Golubović, S. Nikolić, R. Gajić, S. Đurić, and A. Valčić, J. Serb. Chem. Soc. 67 (2002) 291-300.

[10] M.T. Bronski, Development of a Process for Characterization of Nd:YAG Crystals. Thesis, Worchester Polytechnic Institute, Worchester, Massachusetts, 2003.

[11] W. Koechner, Solid State Laser Engineering. Springer-Verlag, Berlin, 1999.

[12] J.A. L'huillier, G. Bitz, V. Wesemann, P. Von Loewis, R. Wallenstein, A. Borsutzky, L. Ackerman, K. Dupré, D. Rytz, and S. Vernay, Appl. Opt. 41 (2002) 4377-4384.

[13] S. Aasland, P.F. McMillan, Nature 369 (1994) 633-636.

[14] J. Lu, M. Prabhu, J. Song, C. Li, J. Xu, K. Ueda, A.A. Kaminskii, H. Yagi, and T. Yanagitani, Appl. Phys. B 71 (2000) 469-473.

[15] R.C. Powell, Physics of Solid-State Laser Materials. Springer-Verlag, New York, 1998.

[16] J. Wisdom, M. Digonnet, and R.L. Byer, Photonics Spectra. "Ceramic Lasers: Ready for Action," Feb. 2004.

[17] V.J. Fratello and C.D. Brandle, J. Cryst. Growth 128 (1993) 1006-1010.

[18] D.E. Eakins, M. Held, M.G. Norton, and D.F. Bahr, J. Cryst. Growth 267 (2004) 502-509.

[19] N.S. Kovaleva, A.O. Ivanov, and É.P. Dubrovina, Sov. J. Quantum Electron. 11 (1981) 1485-1488.

[20] F. Cornacchia, M. Alshourbagy, A. Toncelli, M. Tonelli, H. Ogino, A. Yoshikawa, and T. Fukuda, J. Cryst. Growth 275 (2005) 534-540.

[21] J. Kumar, M. Thirumavalavan, R. Dhanasekaran, F.D. Gnanam, and P. Ramasamy, J. Phys. D: Appl. Phys. 19 (1986) 1223-1231.

[22] L.B. Pasternak, B.K. Sevastyanov, V.P. Orekhova, Yu.L. Remigailo, Ji. Kvapil, Jos. Kvapil, B. Manek, B. Perner, J. Cryst. Growth 52 (1981) 546-551.

[23] A.Y. Neiman, E. Tkachenko, V. Zhukovskii, Dokl. Akad. Nauk SSSR 240 (1978) 876-879.

[24] P. Wamsley, High-Pressure Optical Studies of Doped Yttrium Aluminum Garnet. Dissertation, University of Michigan, Ann Arbor, Michigan, 1994.

[25] R. Iffländer, Solid-State Lasers for Materials Processing: Fundamental Relations and Technical Realizations. Springer-Verlag, Berlin, 2001.

[26] B. Keszei, J. Paitz, J. Vandlik, and A. Süveges, J. Cryst. Growth 226 (2001) 95-100.

[27] G.J. Zhao, X.H. Zeng, J. Xu, S.M. Zhou, and Y.Z. Zhou, Phys. Status Solidi A 199 (2003) 355-359.

[28] J.A. Caird, M.D. Shinn, T.A. Kirchoff, L.K. Smith, and R.E. Wilder, Appl. Opt. 25 (1986) 4294-4305.

[29] S.O. Kasap, Principles of Electrical Engineering Materials and Devices. Irwin McGraw-Hill, Boston, 1997.

[30] M. Springis, A. Pujats, and J. Valbis, J. Phys.: Condens. Matter 3 (1991) 5457-5461.

[31] H.G. Van Bueren, Imperfections in Crystals. North-Holland Publishing Company, Amsterdam, 1961.

[32] C. Jiang. G. Zhan, J. Hu, P. Den, and F. Gan, J. Cryst. Growth 257 (2003) 301-304.

[33] R.A. Lefever, editor, Preparation and Properties of Solid State Materials, Vol. 1: Aspects of Crystal Growth. Marcel Dekker, Inc., New York, 1971.

[34] J. Weertman and J.R. Weertman, Elementary Dislocation Theory. Oxford University Press, Oxford, 1992.

[35] F.A. Kröger, The Chemistry of Imperfect Crystals. North-Holland Publishing Company, Amsterdam, 1964.

[36] H. Hayakawa, M. Umino, H. Mori, and Y. Fujii, Jpn. J. Appl. Phys. 24 (1985) L614-L616.

[37] Y. Peizhi, D. Peizhen, Y. Zhiwen, and T. Yulian, J. Cryst. Growth 218 (2000) 87-92.

CHAPTER THREE

LITERATURE REVIEW OF YTTRIUM ORTHOVANADATE

3.1 The Growth of YVO_4

YVO_4 was first grown by L.G. Van Uitert and J.J. Rubin in 1962 using a slow cooling technique from a flux [1]. Later, more techniques were used including Czochralski, flux, Verneuil, modified floating zone (MFZ), Bridgman, top-seeded solution growth (TSSG), and laser-heated pedestal growth (LHPG) [1,2]. Some of these growth techniques were discussed earlier; a few are discussed below.

The flux method involves the dissolution at high temperatures of Y_2O_3 in a solvent flux containing vanadium compounds which is then slowly cooled to achieve YVO_4. To separate the flux, the crucible is drawn out from the furnace and quickly inverted, separating the flux from the growing crystals located at the bottom of the crucible [3]. Several fluxes have been successfully used to grow YVO_4 including $Pb_2V_2O_7$, V_2O_5, and Na_2CO_3-V_2O_5 [3]. The choice of flux in each case must be made to accommodate ease of preparation, low vapor pressure at high temperature, optical quality, and compatibility with the crucible [1,3].

In the MFZ method, shown schematically in figure 3.1, a seed crystal is placed at the bottom of the growth materials and a small section of the growth materials is heated turning it into a liquid. The liquid is then slowly moved up the crystal by heating the growth materials above the previously liquefied section. Because impurity atoms have small segregation coefficients, they would prefer to stay in the liquid phase of the growth materials, and as the liquid phase moves higher on the growth materials, the impurities go with it leaving an impurity-free, single crystal behind. At the end of the growth, the impurities have concentrated in the very end of the crystal, leaving almost all of the crystal impurity-free. The benefits of MFZ-method crystal growth include the fact that no crucible is needed, so no crucible impurities can enter the crystal; the atmosphere constituents can be arbitrarily chosen, so oxygen can be used during the growth process; and the volatilization can be decreased due to the shorter times the materials are in the liquid state [4]. Defects such as dislocations can be a problem in MFZ-grown crystals but dislocation density can be lowered by thinning the crystal diameter down to about 3mm [5,6]. Thinning obviously severely limits crystal width, but the MFZ method can produce long crystals in a relatively short time frame with a growth rate of more than 10mm/hr [5,6].

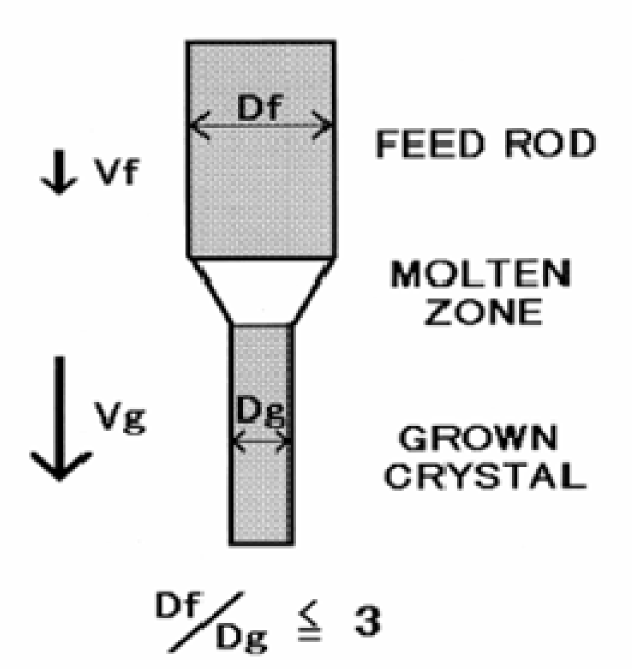

Figure 3.1: Schematic of the MFZ method of crystal growth. *Source: T. Shonai, M. Higuchi, K. Kodaira, Mater. Res. Bull. 35 (2000) 228.*

The LHPG technique is accomplished by creating a melting zone between two powder-sintered ceramic rods containing growth constituents with a CO_2 laser operating at about 200W, producing a temperature close to 3,500°C [1,3,7]. This focused beam creates a very steep temperature gradient in the melt zone [6]. Dopant distribution is not very homogeneous at the beginning of LHPG-method crystal growth but quickly achieves homogeneity as growth progresses [3]. LHPG-grown crystals have better yttrium-vanadium stoichiometry than Czochralski-grown crystals and avoid the problem of oxygen deficiency, a common problem with Czochralski-method growth, but LHPG crystals cannot achieve the diameters produced by Czochralski-method crystal growth [8-10].

Considering all the previously described techniques, the Czochralski method, despite its imperfections, is the most commonly used technique for growing YVO_4 [11]. The Czochralski method is a simple and fast technique to grow large, high-quality crystals, but it has several inherent problems. As mentioned earlier, non-stoichiometry can be a problem with YVO_4 crystal growth, leading to undesirable yttrium-vanadium compositions as well as oxygen vacancies [12]. This can be due to the incongruent vanadium oxide vaporization from the melt as well as material creeping during high-temperature growth, which modifies the melt composition [12,13]. The melt composition continues to change over the entire growth process which could possibly lead to metastable phases and precipitates in the grown boule, especially in rapidly grown boules [8,12]. This is particularly true with material creeping, in which some of the melt creeps along the crucible's inner and outer wall chemically reacting with the crucible and thermal insulation material, usually ZrO_2, to produce precipitates in the boule [13]. Also, YVO_4 grown by the Czochralski method can have a tendency to thermally fracture due to the large thermal stresses in the boule, the result of significant thermal gradients introduced during crystal growth [7].

In order to obtain high-quality YVO_4 by the Czochralski method, the raw materials must be highly pure, usually above 99.99% [14,15]. In addition, a high-quality, defect-free seed crystal must be used, and the seed crystal must be partially immersed in the melt for an hour to melt the seed surface and remove any defects in the seed surface introduced during seed preparation [16]. Usually, a *c*-axis grown seed crystal is used to obtain the most high-quality YVO_4 boule possible as *c*-axis grown crystals can be more uniform in diameter than *a*-axis grown ones [5,14,17]. The seed orientation also helps determine the shape of the resulting boule with *c*-axis grown boules having a rectangular appearance and *a*-axis grown boules having a hexagonal shape, as can be seen in figure 3.2 [16]. While the *a*- and *c*-axis grown boules are most prevalent, YVO_4 has also been grown in the <101> direction, resulting in excellent crystals according to one study [1]. After selection of seed material, the pure powders are placed in a crucible, and the furnace is heated. As stated earlier, YVO_4 is heated to a temperature of 50-100°C above the melting point of YVO_4 for thirty minutes to an hour to avoid the formation of polycrystals during crystal growth [13,18-20]. YVO_4 is typically pulled from the melt at a rate of 1.5-2.5mm/hr and with rotation rates ranging from 5 to 20rpm [14,16,21]. The convection in the growth of $Nd:YVO_4$ is driven by heat loss through radiation from the melt surface, but the

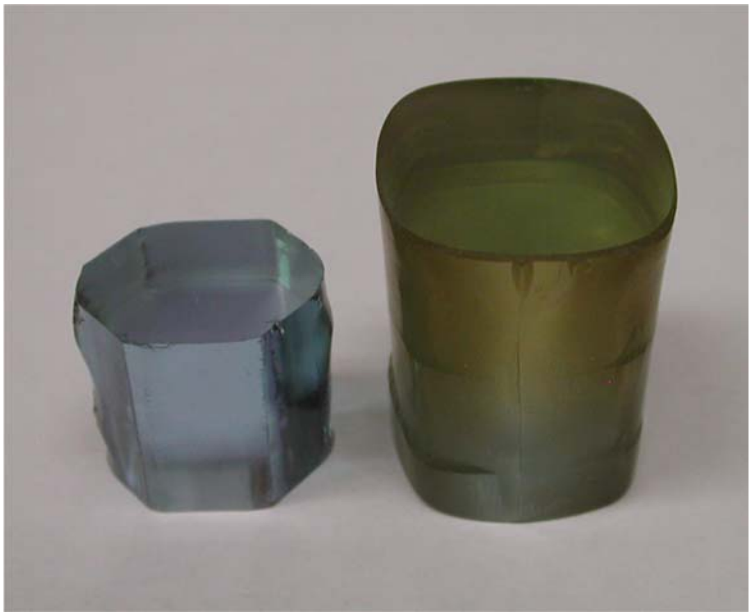

Figure 3.2: Photograph of a hexagonal *a*-axis (left) and a rectangular *c*-axis (right) grown $Nd:YVO_4$ boules.

radiation from the growth interface is sometimes blocked by the non-radiation-transparent region of the crystal referred to as the “grey” crystal region [22]. When this happens, heat transport is carried out through conduction giving rise to very unstable growth conditions [22]. When the growth of the boule is complete, the furnace is cooled to room temperature typically at a rate of 15-20°C/min [16].

YVO_4 crystals are difficult to grow because of their inherent defects including inclusions, precipitates, low-angle grain boundaries, and scatter centers [11,15]. When grown in an iridium crucible, YVO_4 tends to have an affinity for allowing iridium inclusions into the growing crystal. During growth under a partially-oxygenated atmosphere, the iridium crucible is oxidized and can become incorporated into the growing crystal because the iridium floats on top of the melt, much like a layer of oil on water [13,18]. Growth of YVO_4 in pure N_2 atmosphere, however, leads to a large concentration of oxygen vacancies due to oxygen evaporation from the melt. However, growing YVO_4 in a combination of N_2 and CO_2 can eliminate both oxygen vacancies and iridium inclusions, according to one study [23]. This gas mixture has also been utilized for the growth of Nd:YAG which is discussed later.

Another kind of “floating matter” in the melt can occur as the result of water contamination of the furnace [13]. The water vapor can react chemically with the melt surface and form precipitates and other undesirable phase matters with the melt constituents [13]. However, precipitates in YVO_4 are not limited to impurities as incongruent vaporization of vanadium oxide can lead to varying valence states of vanadium in the grown crystal. These changing valence states create phases such as YVO_3 and $Y_8V_2O_{17}$ within the YVO_4 crystal [17,24]. Moreover, V_2O_5 melts before Y_2O_3 and decomposes into lower oxides, V_2O_{5-X}, and O_2 according to the relation [7]:

$$V_2O_5 \rightarrow V_2O_{5\text{-}X} + \frac{x}{2}O_2$$

Oxygen-deficient phases also occur as a result of incongruent vaporization and valence state changes according to the relation:

$$YVO_4 \rightarrow YVO_{4\text{-}X} + \frac{x}{2}\ O_2$$

where V^{5+} ions in the melt become V^{4+} or V^{3+} in a low or oxygen-free atmosphere [7,15].

In addition to precipitates and inclusions, YVO_4 has a tendency of forming low-angle grain boundaries. These grain boundaries start to form early in the crystal growth process and multiply as the crystal continues to grow [25]. These grain boundaries in YVO_4 are the result of the thermodynamic reduction of internal stresses introduced during the growth process [26]. The internal stress is alleviated through the creation of different grains by the activation of slip systems in the crystal [26]. As will be shown later, elimination of these grain boundaries can be achieved through careful selection of the seed crystal, growth axis, and growth conditions—which must be very stable throughout the entire growth process [27].

Unfortunately, it appears that a trade-off exists with the growth of YVO_4. Different phases and undesirable valence states can occur if YVO_4 is grown with little or no oxygen in the growth atmosphere, but iridium oxide inclusions can be introduced into the boule with a high oxygen concentration atmosphere. The solution may include growing the boule with very little oxygen in its growth atmosphere and then performing post-growth annealing in an oxygen environment to reverse any valence changes that occurred during the growth process or by replacing the traditional iridium crucible with a different crucible material such as molybdenum or rhenium.

3.2 Physical Properties of YVO_4

YVO_4, also known as wakefieldite, is a body-centered tetragonal crystal with unit cell parameters: $a = b = 7.118$Å and $c = 6.289$Å and $\alpha = \beta = \gamma = 90°$ [13,16,28,29]. YVO_4 comes in two phases, the zircon-type and the Scheelite type [30]. It belongs to the uniaxial, zircon-type ($ZrSiO_4$) structure family with a space group of $I4_1/amd$ $\left(D_{4h}^{19}\right)$ with Y^{3+} ion site symmetry D_{2d} [2,3,12,15,31-37]. The YVO_4 unit cell can be seen in figure 3.3 and projections of the YVO_4 along the *a*- and *c*-axis can be seen in figure 3.4 and figure 3.5, respectively. The *c*-axis contains four-fold symmetry and the *a*- and *b*-axis are indistinguishable [38]. The YVO_4 crystal structure consists of $(VO_4)^{3-}$ tetragonal units and Y^{3+} ions arranged in an alternating sequence along the *c*-axis direction [39]. Each $(VO_4)^{3-}$ unit consists of a vanadium ion with four equivalent oxygen neighbors that are arranged in a slightly irregular tetrahedron elongated in the *c*-axis direction, while each Y^{3+} ion has eight oxygen neighbors [39-42]. In a unit cell, there are four layer

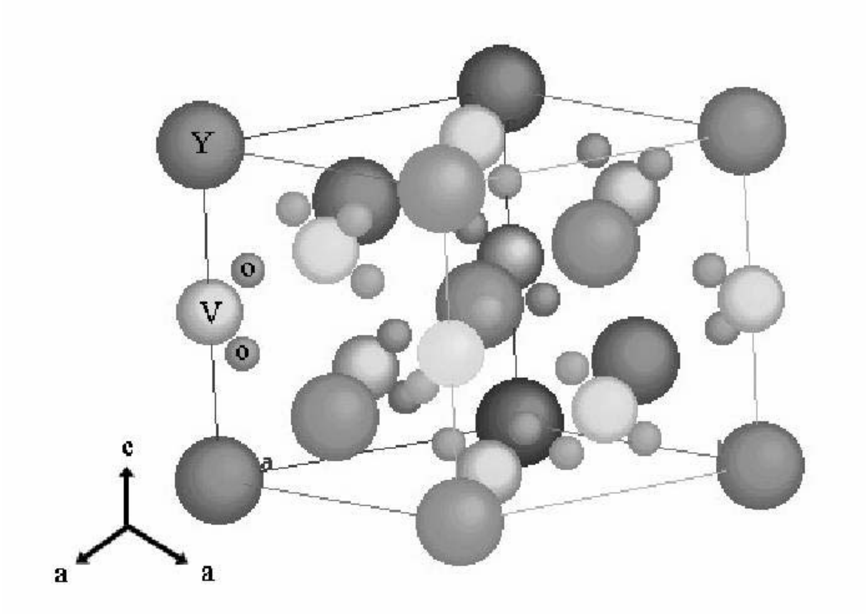

Figure 3.3: The YVO_4 unit cell. The darker atoms are yttrium ions, the light atoms are vanadium ions, and the small atoms are oxygen ions. *Source: J. LeBret, Defect Characterization of Yttrium Orthovanadate. Thesis, Washington State University, Pullman, Washington, 2004, p. 5.*

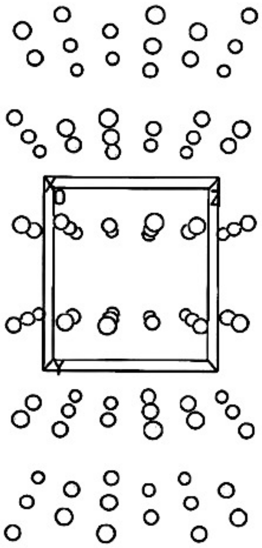

Figure 3.4: The YVO_4 unit cell projected along the *a*-axis. *Source: H.J. Zhang, L. Zhu, X.L. Meng, Z.H. Yang, C.Q. Wang, W.T. Yu, Y.T. Chow, and M.K. Lu, Cryst. Res. Technol. 34 (1999) 1014.*

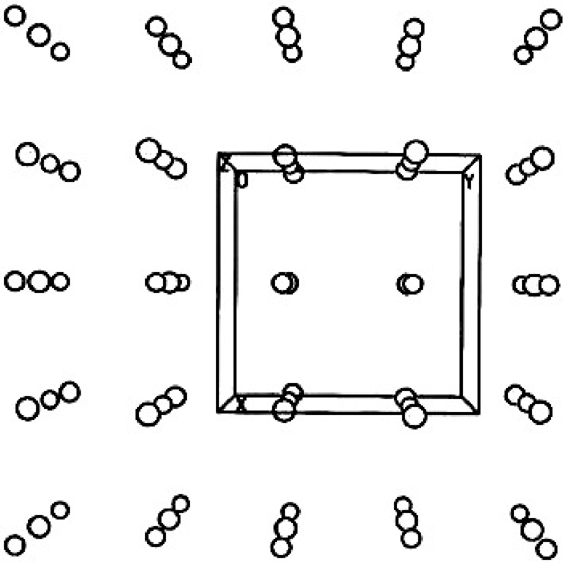

Figure 3.5: The YVO_4 unit cell projected along the *c*-axis. *Source: H.J. Zhang, L. Zhu, X.L. Meng, Z.H. Yang, C.Q. Wang, W.T. Yu, Y.T. Chow, and M.K. Lu, Cryst. Res. Technol. 34 (1999) 1014.*

$(VO_4)^{3-}$ ions in the direction parallel to the *c*-axis, but there are only two layer ions in the direction parallel to the *a*-axis [31]. The lattice parameter along the *a*-axis (3.55Å) is larger than that along the *c*-axis (1.57Å), and, as a result, the ion layers perpendicular to the *c*-axis are denser than those perpendicular to the *a*-axis [31]. Further, the *c*-axis lattice parameter decreases with increasing vanadium content, and the *a*-axis lattice parameter increases with increasing vanadium content [25]. Therefore, the relative expansion in the *c*-axis direction is larger than that in the *a*-axis direction leading to a larger thermal expansion coefficient in the *c*-axis direction than that in the *a*-axis direction. In addition, the segregation coefficients for Nd^{3+} ions are different between the two axes, and more Nd^{3+} ions can be accommodated along the *c*-axis than the *a*-axis leading to slightly higher doping concentrations for *c*-axis grown $Nd:YVO_4$ in comparison to *a*-axis grown $Nd:YVO_4$ under similar melt compositions. This effect has been experimentally verified in literature [26] as well as by research conducted by the author and presented in the next chapter.

Nd^{3+} dopant ions substitute into the Y^{3+} lattice position with D_{2d} symmetry forming a bisdisphenoid shape with the oxygens (NdO_8) [40,43-45]. The eight oxygen ions are grouped into two sets differing by the Y-O bond lengths with four long bonds corresponding to the oxygens shared with the VO_4 tetrahedra and four shorter bonds in connection with the other bisdisphenoids [46,47]. Even at high dopant concentration, 99.9% of Nd^{3+} ions enter the D_{2d} symmetry sites with the other 0.1% located in the orthorhombic D_2 or C_{2V} symmetry sites [36,46]. It is this D_{2d} site symmetry that is responsible for the polarized transitions of the Nd^{3+} ions and the plane-polarized laser output from $Nd:YVO_4$ crystals [48-51].

A $Nd:YVO_4$ crystal is composed of twelve faces belonging to the {100} and {101} families: (100), (010), (011), (101), $(\bar{1}00)$, $(0\bar{1}0)$, $(01\bar{1})$, $(10\bar{1})$, $(0\bar{1}1)$, $(\bar{1}01)$, $(0\bar{1}\bar{1})$, and $(\bar{1}0\bar{1})$ [13]. These faces can be seen in figure 3.6 on the next page. When the crystal is grown in the *a*-axis direction, two faces appear on its shoulder and six faces appear on its cylinder, and when grown in the *c*-axis direction, four faces appear on its shoulder and four faces appear on its

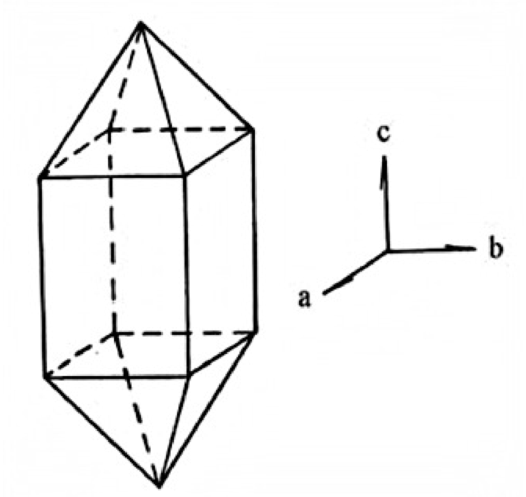

Figure 3.6: The faces of a grown YVO_4 boule. The *a*-axis is [100], the *b*-axis is [010], and the *c*-axis is [001]. *Source: X. Meng, L. Zhu, H. Zhang, C. Wang, Y.T. Chow, and M. Lu, J. Cryst. Growth 200 (1999) 201.*

cylinder [13]. Grown boules of YVO_4 have a tendency to cleave along the {100} faces and sometimes along the {101} faces, but reducing both growth rate and cooling rate can eliminate the cleavage problems [13,21].

YVO_4 is useful for many applications including isolators, circulators, polarizers, and beam displacers [52]. Undoped YVO_4 has been used in optical telecommunications networks operating in the S, C, and L bands extending from 1.48-1.62μm [41]. Most of the uses of YVO_4 rely on its strong birefringence with $n_o \approx 1.958$ and $n_e \approx 2.168$ at 1,064nm [4,14,27]. This is the result of its local differences in atomic packing in specific directions and the resultant difference in scattering along these directions [53].

In tetragonal crystals such as YVO_4, a light ray traveling parallel to the *c*-axis encounters an isotropic structure ($a = b = 7.118$Å for YVO_4), but a light ray in any other direction encounters an anisotropic structure and travels with a different velocity than it does through the isotropic structure [37]. The relative velocities of the two rays are determined by the principal indices of refraction and the difference between these two indices is used to measure the strength of the birefringence of the crystal [37]. A diagram showing the two rays of light proceeding through a birefringent crystal can be seen in figure 3.7. When a light ray traverses parallel to the optic axis, the *c*-axis for YVO_4, the index of refraction is the same regardless of the vibration direction of the electric field, but when a ray traverses the crystal along a direction that is normal to the optic axis, as in the figure, the index of refraction is dependent upon the vibration direction of the electric field [20,37]. When the vibration direction lies between these two directions, then the light ray is split into two components whose electric fields are constrained to vibrate in directions respectively parallel and perpendicular to the optic axis [37]. This results in a birefringent crystal. The index of refraction for the two components of the birefringent YVO_4 crystal can be determined by the Sellmeier equations [48]:

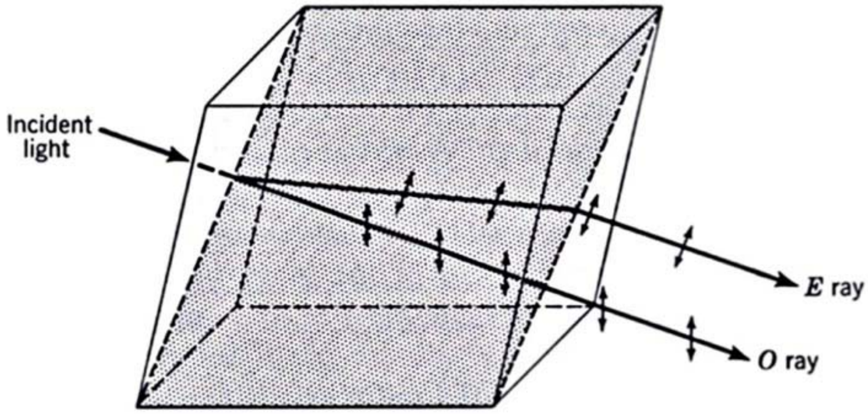

Figure 3.7: Diagram of light passing through a birefringent crystal. *Source: L.V. Azároff and J.J. Brophy, Electronic Processes in Materials. McGraw-Hill Book Company, New York, 1963, p. 436.*

$$n_e^2 = 1 + (3.5930\,\lambda^2)(\lambda^2 - 0.032103\ \mu m^2)^{-1} \tag{3.1}$$

$$n_o^2 = 1 + (2.7665\,\lambda^2)(\lambda^2 - 0.026884\ \mu m^2)^{-1} \tag{3.2}$$

Typical values for the index of refraction using the Sellmeier equations can be seen in table 3.1 for various wavelengths.

Table 3.1: Indices of refraction for YVO_4 at various wavelengths. *Source: J. LeBret, Defect characterization of Yttrium Orthovanadate. WSU Dissertation Services, Pullman, Washington, 2004 p. 6.*

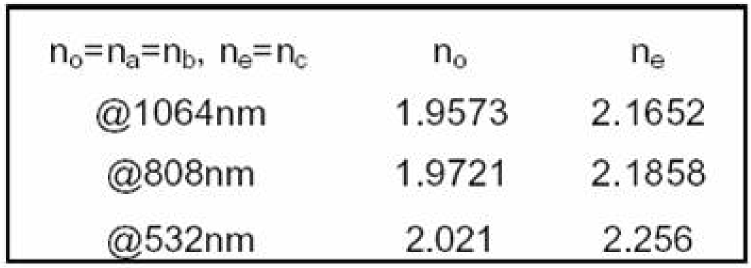

$n_o=n_a=n_b$, $n_e=n_c$	n_o	n_e
@1064nm	1.9573	2.1652
@808nm	1.9721	2.1858
@532nm	2.021	2.256

The measured band gap for YVO_4 is about 3.44eV (~360nm), which is in agreement with calculations based on ligand field theory [35]. A sample absorption spectrum for undoped YVO_4 and Nd:YVO_4 can be seen in figures 3.8 and 3.9, respectively. Because of its wide range of transparency (~400-3,800nm), the band gap can be approximated using the UV fundamental edge. Using the absorption spectra of figures 3.8 and 3.9, the band gap values using the fundamental edge correspond with theory. One interesting note, however, is the fact that only 24 electrons per YVO_4 molecule participate in the observed spectra for YVO_4 [34].

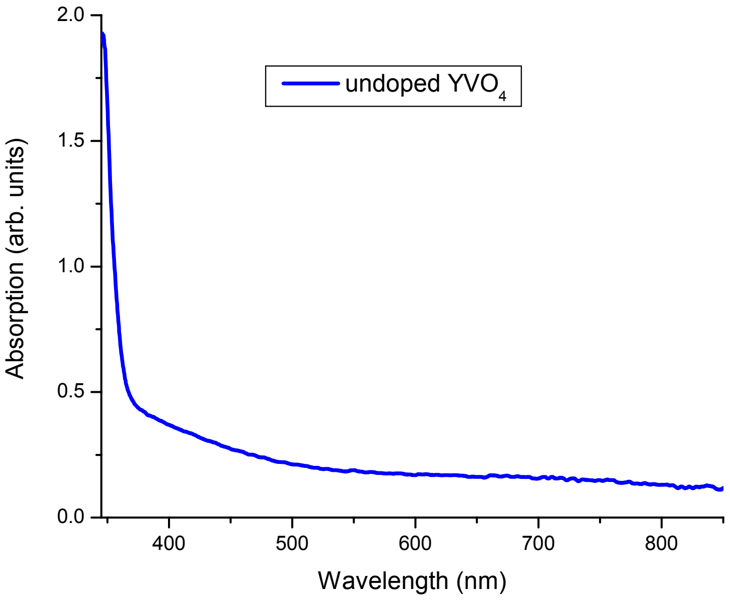

Figure 3.8: Absorption spectrum for undoped YVO_4 boule.

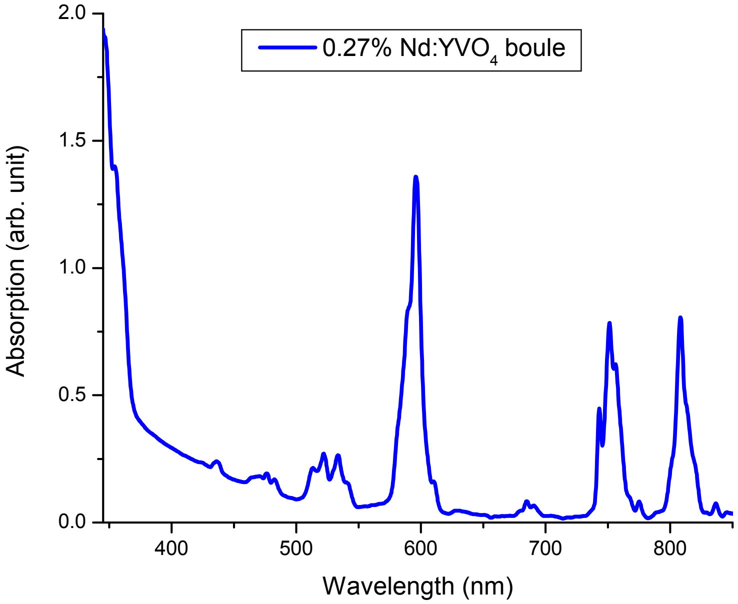

Figure 3.9: Absorption spectrum for 0.27% Nd:YVO_4 boule.

Pure YVO_4 has better physical and mechanical properties than calcite, easier handling and workability than rutile, and a higher birefringence than $LiNbO_3$ [25]. YVO_4 is non-hygroscopic and is resistive to chemicals [52]. Its melting point is 1,810°C, its hardness is 700 Knoop (about 5 on the Mohs scale), and its fracture tensile strength is 53MPa [25,41,52,54,55]. Its Poisson ratio was found to be 0.33, its Young's modulus was measured at 133GPa, and its shear modulus value was determined to be 50GPa [21,25,55]. Thermodynamically, its specific heat is 24.6cal/mol·K, and its thermal conductivity values are 5.23W/mK parallel to the *c*-axis and 5.10W/mK perpendicular to the *c*-axis [31,32,52]. The values for thermal conductivity vary by crystallographic direction due to their difference in density as thermal conductivity is calculated by:

$$\kappa = d\rho C_p \tag{3.3}$$

where d is the thermal diffusivity, ρ is the density and C_p is the specific heat [32]. A few other values are contained in table 3.2.

Table 3.2: Values for several selected physical properties of YVO_4. *Source: H.R. Xia, X.L. Meng, M. Guo, L. Zhu, H.J. Zhang, and J.Y. Wang, J. Appl. Phys. 88 (2000) 5135.*

Property	**Value**
thermal expansion coefficient	*a*-axis: 4.43×10^{-6} K^{-1} *c*-axis: 11.4×10^{-6} K^{-1}
thermal-optical coefficient	$dn_o/dT = 8.5\times10^{-6}$ K^{-1} $dn_e/dT = 3.0\times10^{-6}$ K^{-1}
absorption cross-section	2.7×10^{-19} cm^2
stimulated emission cross-section	12×10^{-19} cm^2
laser diode pumping threshold	~11.8 mW

$Nd:YVO_4$ is an ideal material for end-pumped laser systems due to its large absorption coefficient, low pumping threshold, large emission cross-section, high fracture limit, short absorption depth at the pumping wavelength, and high gain at the lasing wavelength [16,56,57]. In fact, $Nd:YVO_4$ has an emission cross-section five times greater than that in Nd:YAG at its main lasing wavelength (1.064μm) and roughly eighteen times larger at 1.34μm, a secondary lasing wavelength in Nd-doped laser elements [13,25,31,40,50-52,58,59]. Because $Nd:YVO_4$ crystals have a larger absorption cross-section compared to Nd:YAG crystals, it is possible to make thinner samples of $Nd:YVO_4$ absorb the same amount of light as thicker Nd:YAG samples [60]. In addition, YVO_4 allows for a higher Nd-doping concentration than YAG, but highly-doped $Nd:YVO_4$ crystals tend to thermally fracture under intense pumping conditions [13,50,60].

Nd:YVO_4 has a larger absorbance near the peak of the solar spectrum than Nd:YAG which makes it a better candidate for use in an efficient, solar-pumped laser system [48].

However, even with its advantages, YVO_4 has a couple of major drawbacks in comparison to YAG. YVO_4 has poor thermal conductivity in comparison to YAG, less than half the YAG's value, which prevents proper and effective dissipation of heat caused by non-radiative processes in the pumped crystal which can ultimately lead to crystal fracture [61,62]. The second major drawback is YVO_4's low fracture limit of 50MPa compared to YAG's value of 220MPa [56].

3.3 Effects of Increasing Nd^{3+} Ion Concentration

Absorption in Nd:YVO_4 is of particular importance to laser performance. It is important to know which peaks are the result of Nd^{3+} ions in YVO_4, which peaks are inherent to YVO_4, and which peaks are impurity atoms or other defect-related absorptions. Sources of additional absorption peaks found in spectra for Nd:YVO_4 have been regarded as impurity atoms introduced during the growth process, lattice defects inherent to YVO_4, improper Nd^{3+} site selection and spacing, or some combination of these. If a fraction of Nd^{3+} ions were to occupy distorted lattice sites perturbed by neighboring lattice defects such as oxygen vacancies (F-type centers), then an additional absorption peak could arise in the spectrum [43]. Also, an additional absorption peak could arise from a fraction of the Nd^{3+} ions occupying distorted lattice sites perturbed by neighboring Nd^{3+} ions [43]. Ferro- or antiferromagnetically coupled pairs of Nd^{3+} ions in unperturbed sites could give rise to exchange splitting of the optical transitions resulting in anomalous absorption [43]. Finally, some combination of these mechanisms where both exchange splitting and crystal-field shifts occur could result in the appearance of optical satellites in the spectrum [43].

The highest intensity absorption of Nd:YVO$_4$ is observed in the 590nm region. This absorption is the $^4I_{9/2} \rightarrow {}^4G_{5/2}$ band, and it is larger for Nd:YVO$_4$ than for Nd:YAG [1,63]. It is due to this band's overlap with the solar irradiance spectrum which makes Nd:YVO$_4$ a better candidate for solar pumping than Nd:YAG [48]. Another advantage is that unlike Nd:YAG, Nd:YVO$_4$ does not have any closely neighboring transitions which would tend to oscillate at higher pump powers [57]. Also, the bandwidth of Nd:YVO$_4$ is nearly double that of Nd:YAG, making Nd:YVO$_4$ much less sensitive to wavelength drift in pump diodes caused by temperature or aging effects [46,50,51,64]. The intensity of absorption peaks increases monotonically with increasing Nd^{3+} ion concentration [5,63]. However, as Nd^{3+} ion concentration increases, the number of Nd^{3+} ion defect complexes increases. Table 3.3 shows the three types of Nd^{3+} ion environments and their relative percent concentration for different Nd^{3+} ion concentrations in Nd:YVO$_4$. Shallow clusters, as noted in the table, are regions in the crystal containing Nd^{3+} ions whose local concentration is different than the average concentration of the whole crystal [46]. These defects can have a deleterious effect on laser performance as they can absorb laser light.

Table 3.3: Relative concentration of Nd^{3+} ion environments in different Nd:YVO$_4$ crystals. *Source: O. Guillot-Noël, B. Viana, B. Bellamy, D. Gourier, G.B. Zogo-MBoulou, S. Jandl, Opt. Mater. 13 (2000) 435.*

Compounds	Nd^{3+} ions without interaction (%)	Nd^{3+} ions in "shallow clusters" (%)	Nd^{3+} ions in pairs (%)
0.05% Nd:YVO$_4$	80	20	0
0.58% Nd:YVO$_4$	30	55	15

The primary emissions in Nd:YVO$_4$ arrive from three transitions: the $^4F_{3/2} \rightarrow {}^4I_{9/2}$ (914nm), the $^4F_{3/2} \rightarrow {}^4I_{11/2}$ (1,064nm), and the $^4F_{3/2} \rightarrow {}^4I_{13/2}$ (1,342nm) [62,65]. All three transitions occur from the upper laser level which is the $^4F_{3/2}$ level (located around 880nm in the absorption spectra). The strongest of these emissions is the 1,064nm peak as it is the most probable transition of the three and has the quickest transition rate of 326μs compared to 363μs for the $^4F_{3/2} \rightarrow {}^4I_{9/2}$ transition (914nm) and 1,387μs for the $^4F_{3/2} \rightarrow {}^4I_{13/2}$ transition (1,342nm) [48].

To obtain higher laser output power, a higher doping level is used in Nd:YVO_4 crystals. This results in higher and broader absorption peaks near the 808nm pumping level [60]. In addition, the upper-laser-level lifetime decreases but the stimulated emission cross-section increases leaving the same product of the two as the Nd^{3+} ion concentration reaches 2-3at.% [60,66]. Logic would then suggest that one should continue increasing the Nd^{3+} ion concentration in Nd:YVO_4 crystals, but it is very difficult to grow high-quality crystals above 5at.% Nd^{3+} ion concentrations using the Czochralski method [5]. Once again, this is due to the effective distribution coefficient or segregation coefficient as presented earlier in equation 2.1. The value for the segregation coefficient of Nd^{3+} ions in Nd:YVO_4 is 0.63 while that for the rest of the constituents is near unity [13,15,65]. However, non-stoichiometry can lead to changes in these values due to the addition of other phases that appear as a result of non-stoichiometric conditions. For example, in oxygen-deficient conditions, YVO_3 can be present within YVO_4, and its segregation coefficient is greater than unity [9]. Table 3.4 shows the measurements for the segregation coefficient for several Nd:YVO_4 crystals with varying dopant concentrations. From the table, it appears that the segregation coefficient is not dependent upon Nd^{3+}-doping concentration as was confirmed by Meng et al. [13] and Zhang et al [65]. However, the segregation coefficient is dependent upon other growth parameters such as rotation rate and pulling rate [5]. Because the segregation coefficient of Nd^{3+} ions in Nd:YVO_4 is less than unity, the Nd^{3+} ion concentration increases with crystal length. This can lead to variations in the Nd^{3+} ion concentration by about 0.02at.%/cm [27]. This can be seen in figure 3.10. When the doping level is confined, the best length of crystal to use as a laser element is the length at which the crystal just reaches the maximum absorption, as there exists a point where the absorption no longer increases with increasing crystal length due to self-absorption of laser light and scatter caused by defects [60]. These combine to increase the intra-cavity losses resulting in a decrease in slope efficiency. Mathematically, the absorption coefficient, α, can be calculated using the relation:

Table 3.4: Effective segregation coefficient (k_{eff}) of elements in Nd:YVO_4 crystals with different Nd^{3+} ion concentrations. *Source: H. Zhang, X. Meng, L. Zhu, C. Wang, Y.T. Chow, and M. Lu, Opt. Mater. 14 (2000) 27.*

$[Nd^{3+}]$ in melt (at.%)	K_{eff} (Nd)	K_{eff} (Y)	K_{eff} (V)
1	0.641	0.999	0.995
2	0.606	1.020	1.004
3	0.631	1.004	0.991
5	0.626	1.028	0.999

$$\alpha = 20 \cdot \mathrm{Nd}\ (\mathrm{cm}^{-1}) \tag{3.4}$$

where Nd is the Nd^{3+} ion dopant concentration in units of at.% [11,50,67].

Quantum efficiency is related to Nd^{3+} ion concentration in Nd:YVO_4. For a Nd:YVO_4 crystal operating at 1,064nm, the following fitted relation holds true:

$$\eta_Q = \frac{1}{\left(1+\left(\frac{Nd}{Nd_O}\right)^6\right)} \tag{3.5}$$

where η_Q is the quantum efficiency, $Nd_o = 3.5$at.%, and Nd is the Nd concentration of the crystal

[50]. With the value for the quantum efficiency, η_Q, one can find the effective luminescence lifetime using the relation:

$$\tau_f = \tau_{rad}\eta_Q \tag{3.6}$$

where τ_f is the effective luminescence lifetime and τ_{rad} is the radiation lifetime [62]. Therefore, it can be shown that increasing Nd^{3+} ion concentration decreases effective luminescence lifetime.

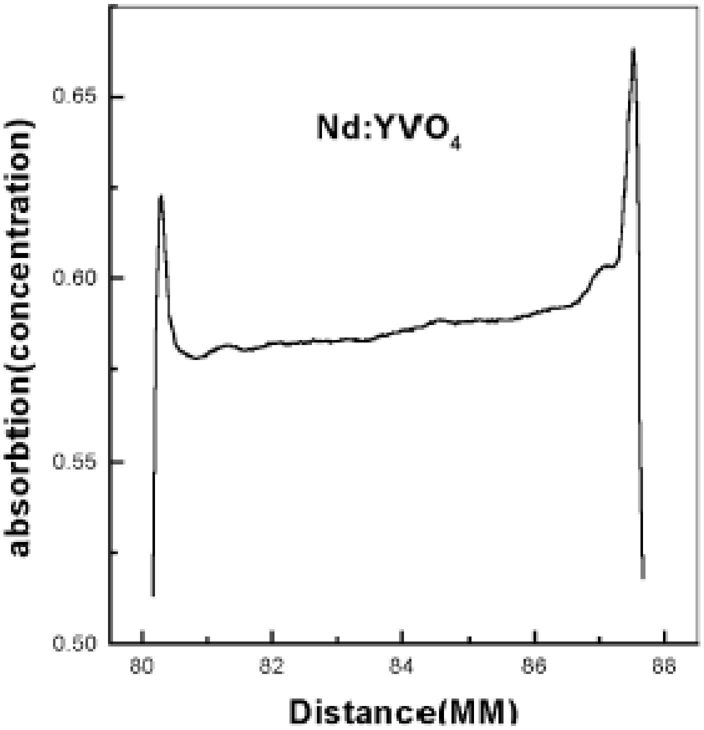

Figure 3.10: Variation in Nd^{3+} ion concentration as a function of growth length. *Source: B.Q. Hu, Y.Z. Zhang, X. Wu, and X.L. Chen, J. Cryst. Growth 226 (2001) 514.*

The quantum defect in Nd:YVO_4 is a function of the pumping scheme and not on Nd^{3+} ion concentration. The quantum defect, q_d, is defined as the ratio of the radiation wavelength used to pump the activator atoms to an excited state with the emitted laser wavelength from the crystal, shown mathematically by the relation:

$$q_d = \frac{\lambda_p}{\lambda_l} \tag{3.7}$$

where λ_p is the pump light wavelength and λ_l is the emitted laser wavelength. For Nd:YAG and Nd:YVO$_4$, 808nm pump light is used to excite the Nd^{3+} ions and the main laser wavelength emitted from the crystals is 1,064nm. This creates a quantum defect value of about 0.76. This means that roughly 24% of the absorbed pump light power is deposited as heat into the crystal [68,69]. The quantum defect in Nd:YAG and Nd:YVO$_4$ could be eliminated by pumping directly into the emitting level, $^4F_{3/2}$ [62]. This would significantly reduce thermal lensing and thermal fracture at lower input powers.

Slope efficiency, η_s, is defined as the rate of change of laser output power with respect to the rate of change for pumping power or:

$$\eta_s = \frac{dP_{out}}{dP_p} \tag{3.8}$$

where P_{out} is the output power of the laser and P_p is the electrical pumping power [65]. For a 1.0at.%-doped crystal, the intrinsic slope efficiency is equal to the ideal value (74%), defined by the quantum defect, but this is never achieved [70]. Laser-crystal quality determines the output power and light-light conversion efficiency and, therefore, slope efficiency [16]. For a high-quality laser system and a high-quality laser rod, the light-light conversion efficiency, which is the fraction of input power into the lamp to the laser output power, can be around 55% and the slope efficiency can reach upwards of 60%.

3.4 Thermal Issues for Nd:YVO_4 Laser Crystals

There are several mechanisms through which the absorbed pump power deposits heat into the Nd:YVO_4 crystal. The quantum defect was previously discussed, and it is the primary source of heat generation. In addition to the quantum defect, cross-relaxation and upconversion, which will be discussed in a later section, non-uniform spatial intensity distribution of the diode, which was already mentioned, and strains and displacements causing inhomogeneous changes in the refractive index of the crystal are several other sources of heat generation in the crystal [70]. This localized change in refractive index is known as thermal lensing [68].

The thermal lensing effect is created when the diode light passes through the sample and the absorbed energy is converted into heat causing expansion of the crystal and effectively changing the optical path length by the relation:

$$s = nL \tag{3.9}$$

where s is the path length, n is the refractive index, and L is the sample length [71]. This uneven expansion in the crystal creates a lens-like shape (bulging) on the end faces of the sample [55]. This lensing will severely degrade the optical quality of the laser beam and will eventually limit laser output power [11]. As the pumping power increases, the thermal lens will cause more and more distortion to scatter laser light [65]. The sign of the thermal lens is dependent upon the sign of the thermal-optical coefficient of the material [68]. Referring back to table 3.2, the thermal-optical coefficient is a positive value, so a positive thermal lens occurs in Nd:YVO_4. For Nd:YVO_4, the contribution of the absorbed pump power to thermal lens formation due to the quantum defect does not depend on doping concentration as the lasing wavelength is not dependent upon doping concentration [70]. However, concentration does play a role in thermal lensing as a higher absorption coefficient creates a larger thermal gradient, and, consequently, a greater amount of stress is produced in the crystal [67].

Besides the thermal lens, the maximum pump power is restricted by the thermal fracture limit of the laser crystal [19,55,67]. Occasionally, the combination of volumetric heating and surface cooling can result in the failure of crystal integrity [11]. The thermal fracture limit of an end-pumped laser crystal is proportional to the inverse absorption coefficient (α^{-1}), and the absorption coefficient linearly increases with increasing dopant concentration [50]. Therefore, the thermal fracture limit of a laser crystal depends on the dopant concentration. It follows that in order to decrease the thermal affects on a crystal, one could simply decrease the Nd^{3+}-doping concentration and/or the length of the crystal [67]. The absorbed pump power at the thermal fracture limit, $P_{abs,lim}$ is given by:

$$P_{abs,\lim} = \frac{1}{\alpha}\left(\frac{4\pi R}{\xi}\right) \tag{3.10}$$

where α is the absorption coefficient at the pump wavelength, ξ is the fractional thermal loading, and R is the thermal shock parameter which is given by:

$$R = \frac{k_c \sigma_{\max}}{\alpha_T E} \tag{3.11}$$

where k_c is the thermal conductivity, E is the Young's modulus, σ_{max} is the maximum stress at which thermal fracture occurs, and α_T is the thermal expansion coefficient [50,55]. The thermal shock parameter for $Nd:YVO_4$ was measured to be 4.8W/cm in one study [55]. Thermal fracture is achieved by a combination of tension and compression of the crystal. The center portion of the crystal is under compression and the outer portions of the crystal are in tension [50]. Even though the center of the crystal is under compressive stresses higher than the maximum tensile stresses occurring on the periphery of the crystal, stress-related fracture is most likely to initiate at the periphery as most materials are stronger in compression than in tension [50]. In addition, periphery defects such as polishing damage and dislocations could also lend themselves to fracture initiation. Thermal fracture can be avoided by reducing the thermal gradient in the crystal. This is accomplished by reducing the crystal's cross-sectional area. Deposited heat can be more effectively removed radially from the crystal by reducing the crystal's cross-sectional area, and, therefore, stress inside the crystal can be relieved [67].

One final thermal consideration mentioned here is the change in band gap with temperature. Such measurements have been made and can be seen in figure 3.11. The fitted line seen in the figure tracks the change of band gap at elevated temperatures mathematically and has the form of:

$$E_g = 358\,nm - 2.3\times 10^{-2}\,nm\left(\frac{T}{°C}\right) + 1.1\times 10^{-4}\,nm\left(\frac{T}{°C}\right)^2 \tag{3.12}$$

where E_g is the approximated band gap in terms of wavelength and T is measured in °C [22]. However, this equation was fitted for a large range of temperatures that could not be achieved in a simple laser cavity. Further, the data from figure 3.11 indicates that the band gap would remain essentially constant over commonly encountered laser operational temperatures.

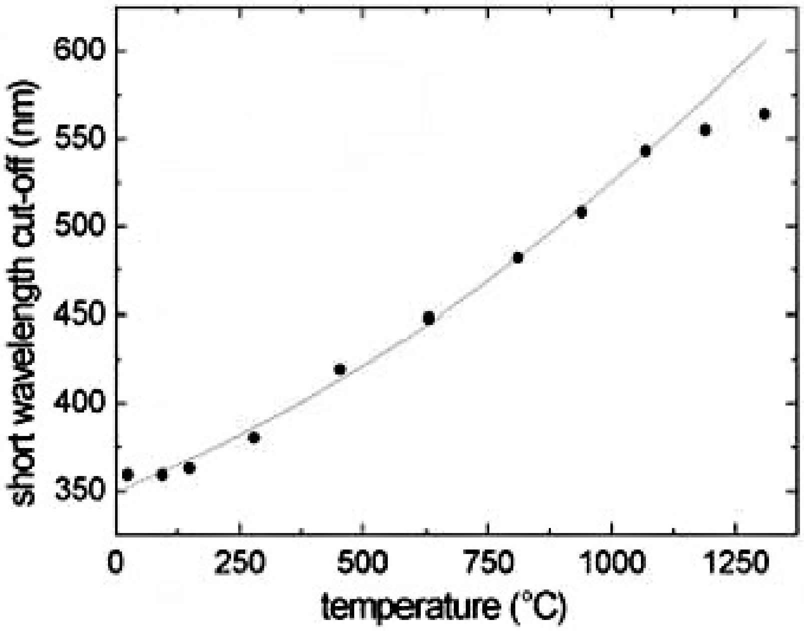

Figure 3.11: The change of band edge with temperature. *Source: A. Polity, D. Schwabe, L. Ackermann, and K. Dupre, Cryst. Res. Technol. 38 (2003) 876.*

3.5 Length, Doping, and Cut Direction Considerations for Nd:YVO_4 Laser Elements

To determine the optimal parameters maximizing laser output power in Nd:YVO_4 crystals, one must look at optimum Nd^{3+} ion concentration and crystal length among other physical parameters. Figures 3.12, 3.13, 3.14, and 3.15 show some of the optimal parameters for Nd:YVO_4 found in literature. From the figures, it was observed that the optimum Nd^{3+}-doping level falls somewhere between 0.2-0.5at.% and the optimum length was between 7-12mm. High Nd^{3+} ion concentrations and long crystal lengths can lead to self-absorption of laser light. However, maximum laser output power is ultimately what is sought, and it can be determined by looking at other parameters. Both output power and threshold power can be calculated using these parameters. Laser output power can be calculated using the following relation:

$$P_{out} = \eta_a \eta_p \eta_m \frac{\lambda_p}{\lambda} \frac{T}{\delta} P_{in} \tag{3.13}$$

where η_a is the absorption efficiency, η_p is the quantum efficiency, η_m is the mode matching efficiency, which is the radius of the output mode waist to the radius of the pumping laser waist, T is the transmission efficiency of the output coupler, δ is the round-trip loss inside the resonator, and P_{in} is the input power [67]. Slope efficiency, η_s, can be calculated using the relation [67]:

$$\eta_s = \eta_a \eta_p \eta_m \frac{T}{\delta} \tag{3.14}$$

and laser threshold, P_{th}, can be determined by [67]:

$$P_{th} = \eta_p \frac{\lambda}{\lambda_p} \frac{T}{\delta} \tag{3.15}$$

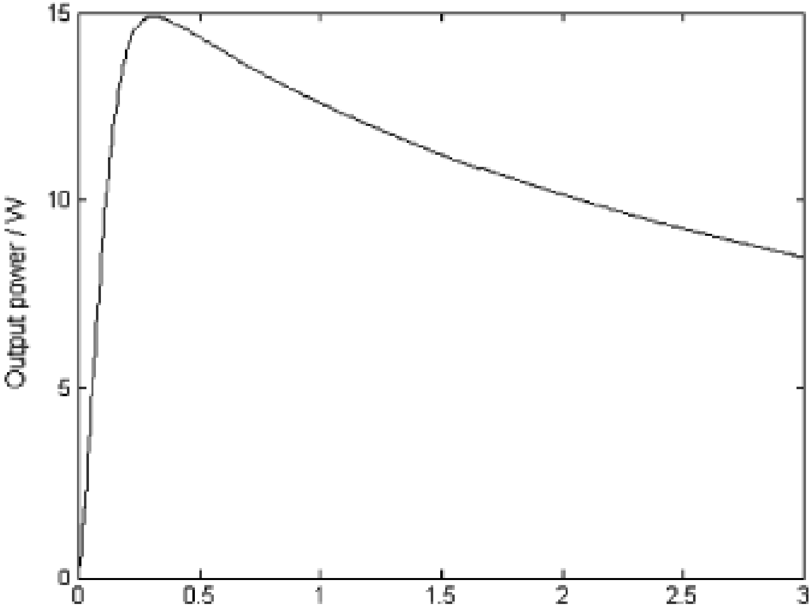

Figure 3.12: Optimum doping concentration leading to maximum laser output power for Nd:YVO$_4$ laser crystals with fixed length. *Source: H. Zhang, M. Chao, M. Gao, L. Zhang, and J. Yao, Opt. Laser Technol. 35 (2003) 447.*

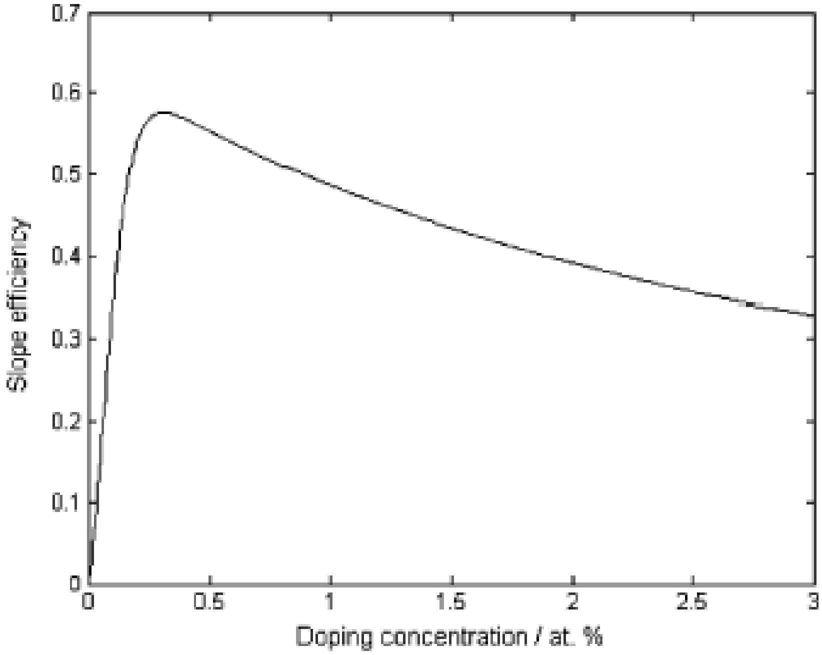

Figure 3.13: Optimum Nd^{3+} ion concentration giving the highest slope efficiency with fixed crystal length. *Source: H. Zhang, M. Chao, M. Gao, L. Zhang, and J. Yao, Opt. Laser Technol. 35 (2003) 447.*

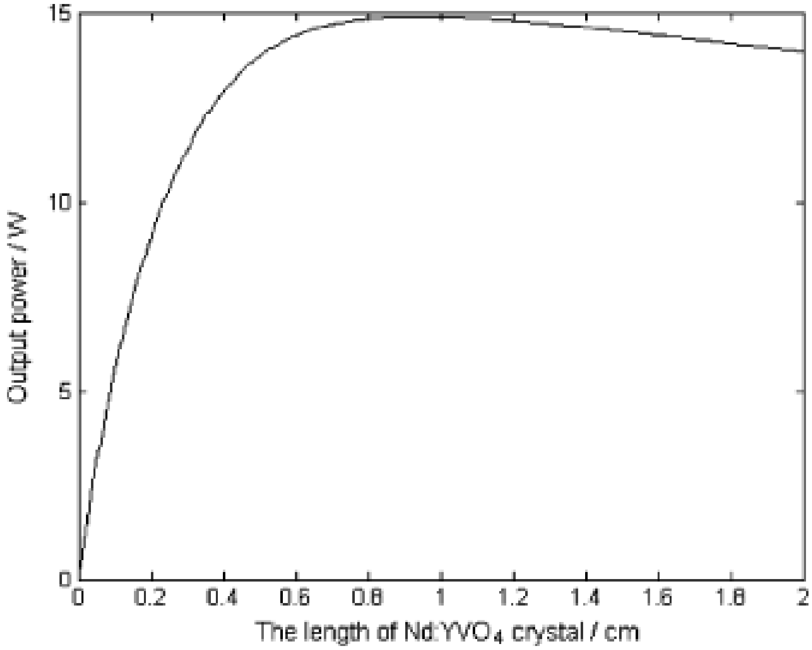

Figure 3.14: Optimum length of Nd:YVO_4 leading to the highest output power with fixed Nd^{3+} ion concentration. *Source: H. Zhang, M. Chao, M. Gao, L. Zhang, and J. Yao, Opt. Laser Technol. 35 (2003) 447.*

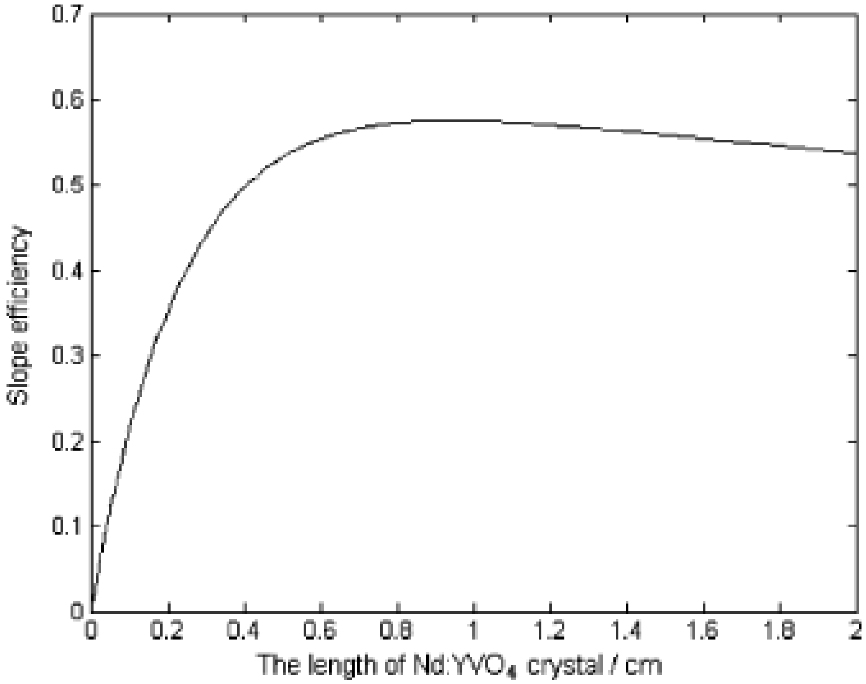

Figure 3.15: Optimum length of Nd:YVO_4 leading to the highest slope efficiency with fixed Nd^{3+} ion concentration. *Source: H. Zhang, M. Chao, M. Gao, L. Zhang, and J. Yao, Opt. Laser Technol. 35 (2003) 447.*

Laser output power is directly related to the gains and losses within the cavity [72]. Laser output power increases linearly with pump power for low input powers. However, at higher input powers, the crystal heats up and losses increase. Figure 3.16 is a plot showing this trend in laser output power. The dip in the TEM_{00} mode power curve seen in figure 3.16 is believed to be caused by the change in stability of the cavity due to the laser power dependence of the thermally-induced lensing in the laser crystal [58,73].

One final power consideration lies in the cutting direction of the laser crystal. As was mentioned earlier, the two axes have different lattice parameters and different properties. Cutting the laser elements in different directions can give rise to different laser output powers due to their different properties. Figure 3.17 shows the difference in laser output power that can be achieved by cutting two otherwise identical crystals in different directions. As is evident from the plot, cutting in the *a*-axis direction gives a slightly higher laser output power than cutting in

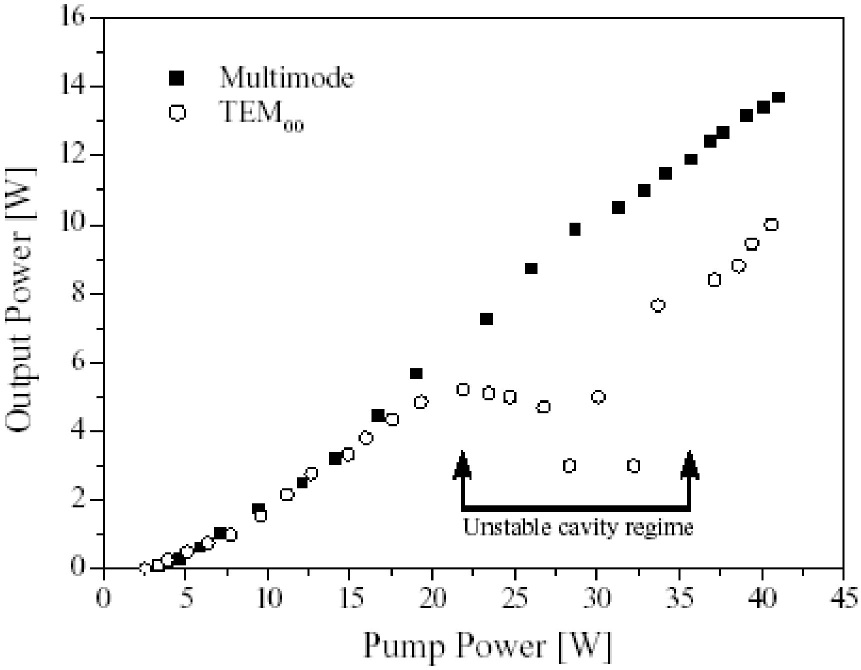

Figure 3.16: Laser output power versus input power for Nd:YVO$_4$ crystal. *Source: A. Minassian and M.J. Damzen, Opt. Commun. 230 (2004) 193.*

the *c*-axis direction. This is due to the difference in Nd^{3+} ion segregation along the two axes. To achieve the highest laser output power, the crystal must be cut in the direction which minimizes the Nd^{3+} ion concentration gradient along the crystal. This is achieved by cutting along the *a*-axis direction. Also, cutting in the *a*-axis direction allows for the utilization of the higher stimulated emission cross-section (25×10^{-19}cm^2 for the direction parallel to the *c*-axis versus 6.5×10^{-19}cm^2 for the direction orthogonal to the *c*-axis) [38].

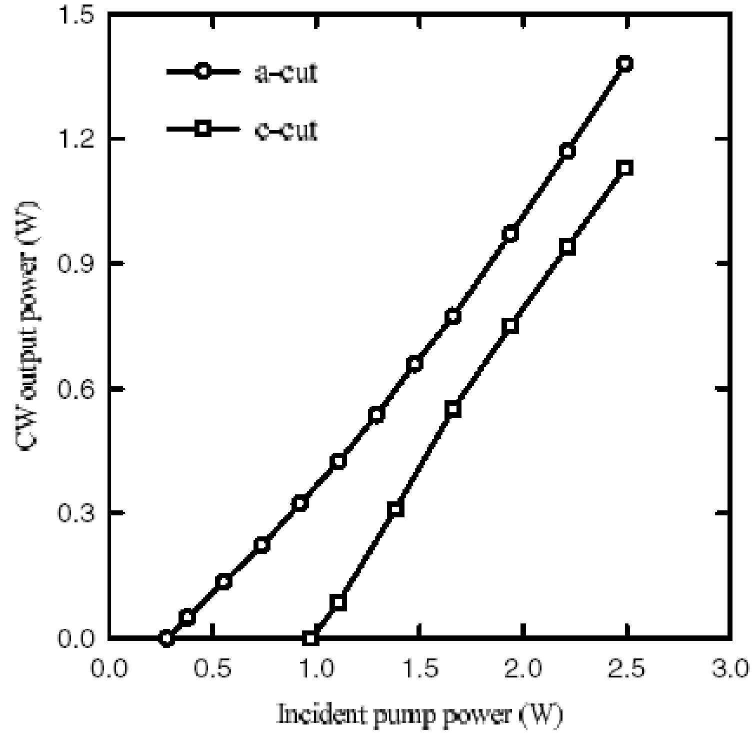

Figure 3.17: Different laser output powers achieved using different cut directions in Nd:YVO_4 crystals. *Source: Y.F. Chen and Y.P. Yan, Appl. Phys. B 74 (2002) 416.*

3.6 Major Defects in Nd:YVO_4

Defects in laser materials are deleterious to laser performance. Eliminating the effects of defects can increase laser power density, but the question of which defects have the great affect on laser performance remains be investigated.

As stated in section 2.2.7, defects in single-crystal YVO_4 can include oxygen vacancies, inclusions, voids, dislocations, and impurity atoms [1]. In YVO_4, voids, dislocations, vacancies, anti-site substitutions, and grain boundaries are several of the common sources of scatter, with the most common sources being voids and grain boundaries. Voids in YVO_4 are quite small and have been measured to be about 10μm in diameter [25]. Photographs taken by the author of voids seen in Nd:YVO_4 boules can be seen in figures 3.18, 3.19, and 3.20. Voids are the result of improper growth parameters and are often associated with rapid growth rates.

Figure 3.18: Photograph of small "growth ring" void clusters in a Nd:YVO_4 boule using UV illumination.

Figure 3.19: Photograph of small void clusters in a Nd:YVO_4 boule using UV illumination.

Figure 3.20: Photograph of small "brain coral" void clusters in a Nd:YVO_4 boule using UV illumination.

While voids are without doubt, deleterious to laser performance, their presence in a grown crystal can be reduced or eliminated through careful selection of growth parameters. Hence, voids are not viable laser performance inhibiting candidates in current production crystals.

3.6.1 Non-Radiative Processes in Nd:YVO_4

As was stated earlier, the absorption coefficient increases with increasing doping concentration. However, laser performance deteriorates at high doping levels. High doping levels can lead to self-quenching, which is caused by interaction between pairs of Nd^{3+} ions [5,70,71]. This interaction produces a significant amount of heat in the crystal due to the loss of pump power through the process of upconversion [69,70,74]. The interaction affects the quantum efficiency and lowers slope efficiency as well as the fluorescence lifetime, which is known as the fluorescence-quenching effect [50,63,66,67,70,71,74]. The process of upconversion involves two nearby ions in the metastable $^4F_{3/2}$ energy state. One ion returns to the $^4I_{9/2}$, $^4I_{11/2}$, $^4I_{13/2}$, or $^4I_{15/2}$ energy state while the other, in turn, goes to a higher energy state

[74]. This process results in the reduction of the inversion density, degrading laser performance [74]. Upconversion becomes significant with increasing output coupler reflectivity [70]. This was observed in one study by the decrease in slope efficiency with output coupler reflectivities above 85% [26].

Upconversion is not the only non-radiative mechanism found in Nd:YVO_4 laser crystals. Another common mechanism is known as cross-relaxation, which occurs when an excited ion transfers part of its energy to a nearby ion in the ground state [71]. Both ions then decay non-radiatively down to the ground state generating heat in the crystal, leading to thermal lensing [70,71]. The process of cross-relaxation occurs primarily in two fashions. The first scheme involves one ion in the $^4F_{3/2}$ energy level decaying down to the $^4I_{15/2}$ energy level with the other ion starting in the $^4I_{9/2}$ energy level and decaying into the $^4I_{15/2}$ energy level, while the other scheme involves the first ion in the $^4F_{3/2}$ energy level decaying down to the $^4I_{13/2}$ energy level with the second ion starting in the $^4I_{9/2}$ energy level and decaying into the $^4I_{15/2}$ energy level, leaving the first ion slightly higher in energy than the second ion [46]. Cross-relaxation, like upconversion, is dependent upon doping concentration [70].

Because of the low doping concentrations used for all the Nd:YVO_4 presented here, the non-radiative processes described in this section were not laser performance inhibiting candidates.

3.6.2 Inclusions and Non-Stoichiometry in Nd:YVO_4

The classical model of compounds, created by Dalton, consisted of equal components of chemicals, but was later modified by thermodynamic considerations that suggested that the composition of every chemical component can vary inside a certain homogeneous region [75].

Albers and Haas emphasized that a given compound AB in a 50at.% A and 50at.% B stoichiometric composition without an extended homogeneity region is stable only at absolute zero [75]. At higher temperatures, the AB compound will have a characteristic solid-solution region whose extent is dependent upon the magnitude of its Gibbs free energy and point defect concentration [75].

Many transition metal-based oxides are non-stoichiometric, and non-stoichiometry in YVO_4 has been observed since the 1960's [10,76]. Non-stoichiometry in YVO_4 is important because of its influence on the optical properties and laser performance of Nd:YVO_4 [77]. The non-stoichiometry of YVO_4 has been shown to be 50.7% ± 0.2% Y_2O_3 to 49.3% ± 0.2% V_2O_5, giving rise to a crystal of $YV_{0.97}O_{3.93}$ [1,76]. The origin of non-stoichiometry in YVO_4 develops through three mechanisms. The first mechanism, though not very common to YVO_4, is known as the substitution model where Y^{3+} ions partially fill the V^{5+} lattice sites creating yttrium antisites, Y_V [77]. This requires an oxygen vacancy in order to retain charge neutrality. The substitution model is unlikely to occur because the ionic radius of Y^{3+} ions (r = 1.16Å) is much larger than that of V^{5+} ions (r = 0.68Å) [9,77]. The second mechanism is known as the vacancy model in which the V_2O_5 concentration in the melt is decreased due to incongruent evaporation causing the generation of vanadium vacancies, V_V [77]. This model also requires an oxygen vacancy for charge neutrality. The third mechanism is known as the yttrium interstitial model through which the yttrium ion is located in an interstitial space near its normal lattice site [77]. This model requires a vanadium vacancy for charge compensation.

During crystal growth and cooling, the near-congruent YVO_4/YVO_{4-x} single crystals will become metastable [76]. As a result, two unwanted effects will arise simultaneously. The first effect is that the Y-V-O stoichiometry in the melt is continuously changing due to the incongruent vaporization causing the Y-V ratio to shift toward yttrium excess while slowly creating more and more oxygen defects and causing non-pentavalent vanadium ions to enter the lattice [76]. The second effect is that the actual congruent composition is also gradually changing, thus changing the relevant phase transitions [76]. This is a result of the Czochralski-method growth of YVO_4 boules [76]. Figure 3.21 is a schematic view of the phase relations and precipitation effects of YVO_{4-x}. From the figure, it can be seen that a complex solid-solution system exists where oxygen-deficient YVO_3 can create the solid-solution with oxygen-deficient-free yttrium or vanadium-excess precipitates [79]. YVO_3, a perovskite-structured crystal, is formed close to the melting point of YVO_4 where loss of oxygen occurs which may result in YVO_4 turning a black color [3,24,27]. This oxygen deficiency causes distortion of the $(VO_4)^{3-}$ tetrahedron [81].

Although oxygen defects in YVO_4 crystals can have deleterious effects in laser performance, it is even more crucial for proper Y-V congruence [9]. At high temperatures, there exists incongruent vaporization of vanadium oxide, leading to changes in Y-V-O stoichiometry, as was stated earlier. This change in stoichiometry allows for various defect structures to exist in the grown crystal such as yttrium-excess precipitates, vanadium-excess precipitates, oxygen-deficient regions, and vanadium valence changes [1,8,10,78,79]. Figure 3.22 is a schematic of the Y_2O_3-V_2O_5-V_2O_3 ternary system. V_2O_3 is the only congruently vaporizing phase of vanadium oxide, and V_2O_5 and other intermediate V-O phases vaporize incongruently by the mechanism:

$$V_2O_{(5-y)} \rightarrow V_2O_{(5-y)-2x} + xO_2$$

in a stepwise manner, ultimately yielding V_2O_3 [24]. This is further backed by the observation of V_2O_5-V_2O_3 inclusions seen in both Nd:YVO_4 and Nd:$GdVO_4$ [18]. Another common inclusion in YVO_4 crystals is the yttrium-rich $Y_8V_2O_{17}$, a secondary phase of YVO_4 [2,3,24,54]. The existence of this phase indicates inclusions; yttria-rich inclusions of $4Y_2O_3$-V_2O_5 with a zirconia-type crystal structure are seen in boules grown with improper amounts of V_2O_5 [3,5,6]. $Y_8V_2O_{17}$ can be formed by the following reaction:

$$8YVO_4 \rightarrow Y_8V_2O_{17} + 3V_2O_5$$

and can possibly be formed during growth or by annealing a grown crystal at 1,550°C for long periods of time [3].

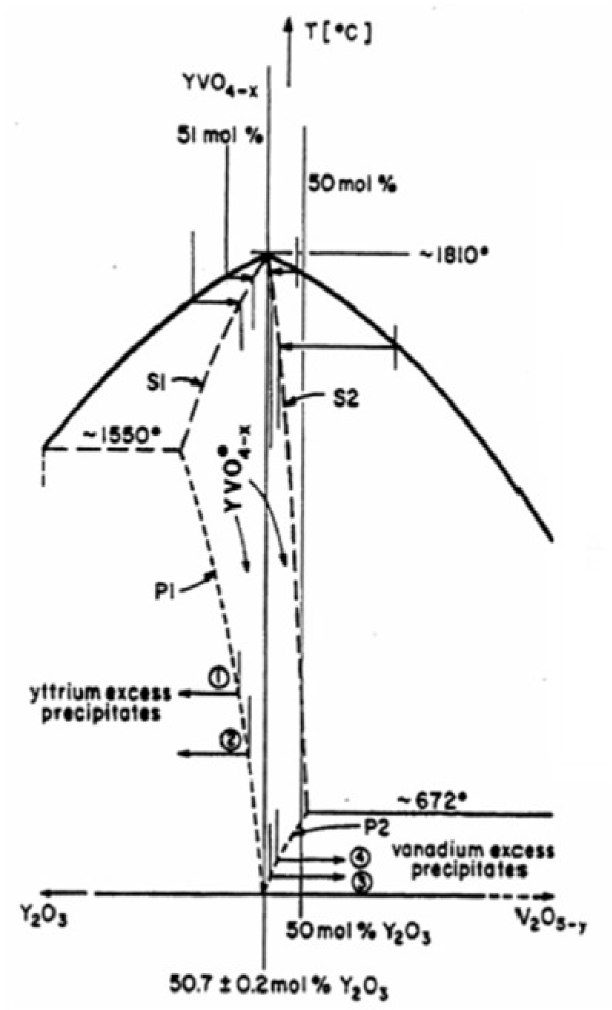

Figure 3.21: A schematic of the phase relations and precipitate effects of YVO_4. *Source: S. Erdei, B.M. Jin, F.W. Ainger, B. Keszei, J. Vandlik, and A. Süveges, J. Cryst. Growth 172 (1997) 467.*

To improve stoichiometry, annealing in an oxygen atmosphere has been suggested [9]. During annealing, the heavily oxygen-deficient regions of the crystal change their non-pentavalent vanadium ions to pentavalent ions [9]. Since the smaller pentavalent ions cannot be substituted by Y^{3+} ions, the originally oxygen-deficient YVO_4 crystals have unstable Y^{3+} ion substitutions giving rise to yttrium-rich phases resulting in a more congruent stoichiometric composition for the whole crystal, but not in those local areas of component-rich precipitations [9].

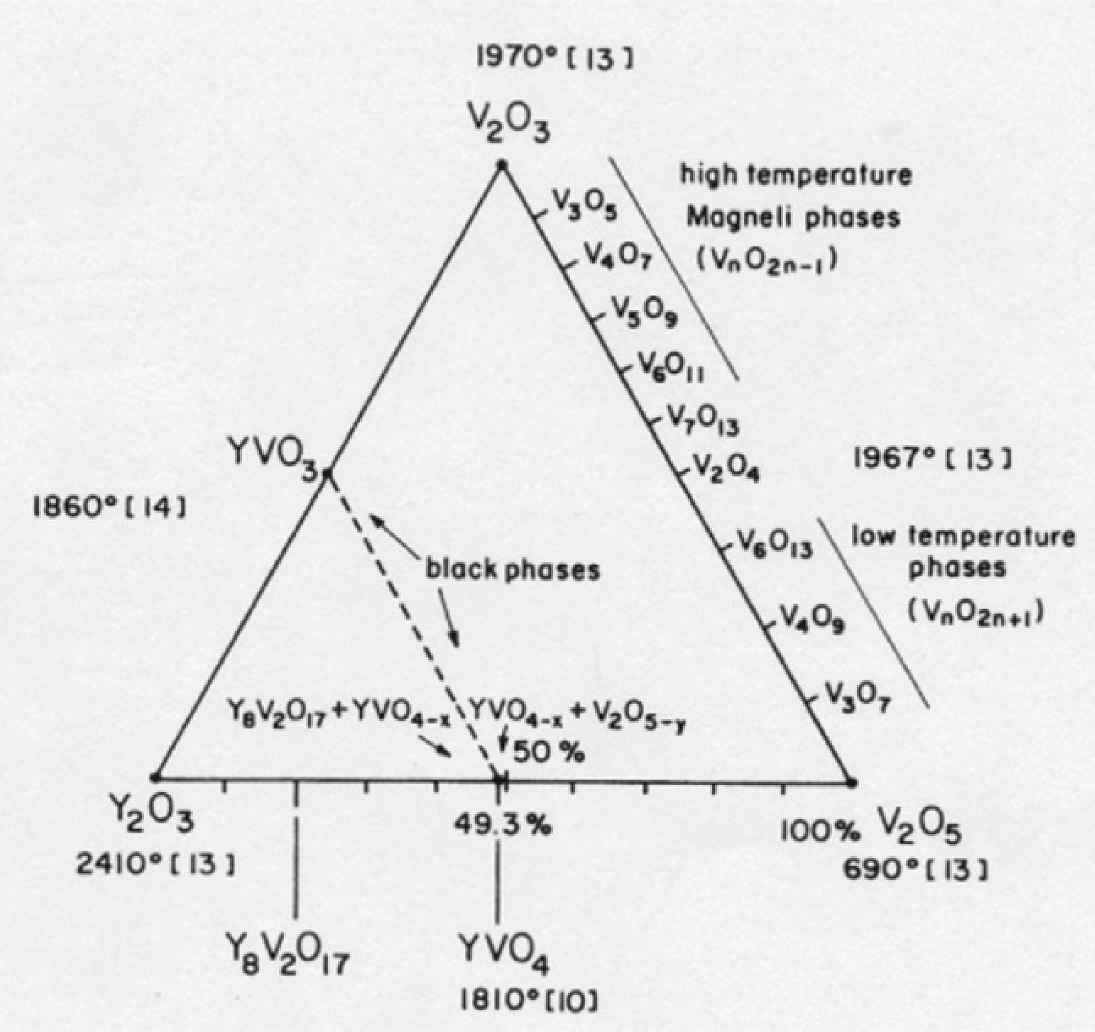

Figure 3.22: The Y_2O_3-V_2O_5-V_2O_3 ternary system. *Source: S. Erdei and F.W. Ainger, Mater. Res. Soc. Symp. Proc. 329 (1994) 247.*

One final inclusion of note comes from the crucible itself as was described in section 2.2.2. IrO_2 crystallizes into a tetragonal crystal system and becomes a contaminant in the crystal [18,79]. IrO_2 inclusions can possibly be avoided by growing the crystal in a reducing atmosphere, but doing so results in the YVO_3 formation described earlier. Therefore, it is necessary to carefully balance the composition of the growth atmosphere to minimize the oxidation of the crucible walls as well as limit formation of the oxygen-deficient YVO_3. This may include the combination of an 80% N_2 and 20% CO_2 gas mixture for the growth atmosphere, as was previously mentioned [23]. While these stoichiometry effects are important for growing YVO_4, their role was not the main focus of the research presented here as careful measurement of raw materials and correct growth parameters can minimize their affect on laser output power.

3.6.3 Silicon Impurities in Nd:YVO_4

Besides hydroxyl-ion impurities, silicon and zirconium are probably the most common impurities found in YVO_4 crystals and both act similarly in the lattice even though Si^{4+} ions substitute for V^{5+} ions and Zr^{4+} ions substitute for Y^{3+} ions [80]. Silicon and vanadium ions have similar ionic radii (0.26Å for Si^{4+} ions versus 0.36Å for V^{5+} ions) and like V^{5+} ions, Si^{4+} ions prefer to participate in tetrahedral bonding with oxygen [41]. When a Si^{4+} ion enters the lattice and substitutes for a V^{5+} ion, a charge imbalance is created. In order to maintain charge neutrality, a hole, h^+, is trapped near the Si^{4+} ion by an adjacent oxygen ion [80]. This highly-stable defect is known as the Si^{4+}-h^+ center [41]. Figure 3.23 is a schematic of this defect center. From the schematic, it can be inferred that the oxygen ion containing the hole has a $2p^5$

configuration ($2p_x^2$, $2p_y^2$, $2p_z$) with the $2p_z$ orbital containing the hole making the oxygen ion O^- instead of O^{2-} [41].

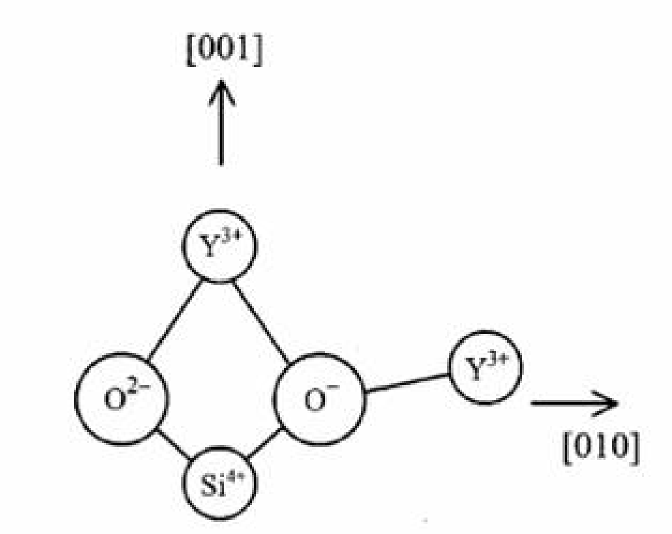

Figure 3.23: A schematic of the Si^{4+}-h^+ center in YVO_4. *Source: N.Y. Garces, L.E. Halliburton, K.T. Stevens, M. Shone, and G.K. Foundos, J. Appl. Phys. 91 (2002) 1358.*

Although the Si^{4+}-h^+ centers themselves may not significantly contribute to the coloration of YVO_4 crystals, they may introduce other charge-compensating defects such as oxygen vacancies or cation antisites that do produce coloration of these crystals [41]. If a V^{4+} ion replaces a Y^{3+} ion, then the extra hole needed for the charge neutrality of a Si^{4+} ion substituting for a V^{5+} ion would be obtained, and the Si^{4+}-h^+ center would not be created [41,80]. In addition, if two Si^{4+} ions enter the lattice, the creation of a doubly-ionized oxygen vacancy would meet the requirements for retaining charge neutrality [41]. Today, however, with the highly-pure raw materials used for the growth of YVO_4, the concentration of silicon in YVO_4 is rather small and its influence on laser output power is even smaller.

References

[1] F.S. Ermeneux, C. Goutaudier, R. Moncorge, M.T. Cohen-Adad, M. Bettinelli, and E. Cavalli, Opt. Mater. 13 (1999) 193-204.

[2] D. Reyes Ardila, A.S.S. de Camargo, J.P. Andreeta, and L.A.O. Nunes, J. Cryst. Growth 233 (2001) 253-258.

[3] C. Goutaudier, F.S. Ermaneux, M.T. Cohen-Adad, R. Moncorgé, M. Bettinelli, and E. Cavalli, Mater. Res. Bull. 33 (1998) 1457-1465.

[4] Z. Hong, Y. Huaguang, Z. Yunzhi, Z. Jianfei, X. Hongchang, W. Xing, and J. Yandao, J. Cryst. Growth 160 (1996) 136-140.

[5] T. Shonai, M. Higuchi, and K. Kodaira, J. Cryst. Growth 233 (2001) 477-482.

[6] T. Shonai, M. Higuchi, and K. Kodaira, Mater. Res. Bull. 35 (2000) 225-232.

[7] C.H. Huang and J.C. Chen, J. Cryst. Growth 229 (2001) 184-187.

[8] S. Erdei, B.M. Jin, and F.W. Ainger, J. Cryst. Growth 174 (1997) 328-330.

[9] S. Erdei, B. Jin, F.W. Ainger, A.S. Bhalla, B. Kersei, J. Vandlik, and A. Süveges, J. Appl. Phys. 79 (1996) 2834-2838.

[10] S. Erdei, L. Kovács, Á. Pető, J. Vandlik, P.D. Townsend, and F.W. Ainger, J. Appl. Phys. 82 (1997) 2567-2571.

[11] H. Zhang, J. Liu, J. Wang, C. Wang, L. Zhu, Z. Shao, X. Meng, X. Hu, Y.T. Chow, and M. Jiang, Opt. Lasers in Engin. 38 (2002) 527-536.

[12] B. Jin, S. Erdei, A.S. Bhalla, and F.W. Ainger, Mater. Lett. 22 (1995) 281-284.

[13] X. Meng, L. Zhu, H. Zhang, C. Wang, Y.T. Chow, and M. Lu, J. Cryst. Growth 200 (1999) 199-203.

[14] S. Wu, G. Wang, J. Xie, X. Wu, and G. Li, J. Cryst. Growth 249 (2003) 176-178.

[15] H. Zhang, J. Wang, C. Wang, L. Zhu, X. Hu, X. Meng, M. Jiang, and Y. Chow, Opt. Mater. 23 (2003) 449-454.

[16] S. Wu, G. Wang, and J. Xiea, J. Cryst. Growth 226 (2004) 496-499.

[17] V.V. Kochurikhin, M.A. Ivanov, W.S. Yang, S.J. Suh, and D.H. Yoon, J. Cryst. Growth 229 (2001) 179-183.

[18] L. Qin, X. Meng, J. Zhang, L. Zhu, H. Zhang, B. Hu, and H. Jiang, J. Cryst. Growth 242 (2002) 183-188.

[19] H. Zhang, X. Meng, L. Zhu, and Z. Yang, Mater. Res. Bull. 34 (1999) 1589-1593.

[20] J.B. LeBret, M.G. Norton, D.F. Bahr, D.P. Field, and K.G. Lynn, J. Mater. Sci. 40 (2005) 3347-3353.

[21] D.E. Eakins, J.B. LeBret, M.G. Norton, and D.F. Bahr, J. Cryst. Growth 266 (2004) 411-414.

[22] A. Polity, D. Schwabe, L. Ackermann, and K. Dupre, Cryst. Res. Technol. 38 (2003) 874-880.

[23] J. Chen, F. Guo, N. Zhuang, J. Lan, X. Hu, S. Gao, J. Cryst. Growth 243 (2002) 450-455.

[24] S. Erdei, F.W. Ainger, Mater. Res. Soc. Symp. Proc. 329 (1994) 245-251.

[25] J. LeBret, Defect Characterization of Yttrium Orthovanadate. Thesis, Washington State University, Pullman, Washington, 2004.

[26] C.R. Shawley, C.L. Wang, and K.G. Lynn, J. Appl. Phys. 99 (2006) 123109.

[27] B.Q. Hu, Y.Z. Zhang, X. Wu, and X.L. Chen, J. Cryst, Growth 226 (2001) 511-516.

[28] M.J. Weber, Handbook of Optical Materials. CRC Press, Boca Raton, 2002.

[29] R. Jablonski, S.M. Kaczmarek, M. Swirkowicz, and T. Lukasiewicz, J. Alloys Comp. 300-301 (2000) 310-315.

[30] T. Oshiro and K.W. Hipps, unpublished internal report (2001).

[31] H.J. Zhang, L. Zhu, X.L. Meng, Z.H. Yang, C.Q. Wang, W.T. Yu, Y.T. Chow, and M.K. Lu, Cryst. Res. Technol. 34 (1999) 1011-1016.

[32] H.R. Xia, G.W. Lu, P. Zhao, S.Q. Sun, X.L. Meng, X.F. Cheng, L.J. Qin, L. Zhu, and Z.H. Yang, J. Mater. Res. 20 (2005) 30-35.

[33] L. Kovács, S. Erdei, and R. Capelletti, Solid State Commun. 11 (1999) 95-99.

[34] J.D. Kinsley and G.W. Ludwig, J.Appl. Phys. 41 (1970) 370-375.

[35] H.R. Xia, X.L. Meng, M. Guo, L. Zhu, H.J. Zhang, and J.Y. Wang, J. Appl. Phys. 88 (2000) 5134-5137.

[36] S. Jandl, O. Guillot-Noël, and D. Gourier, Opt. Mater. 19 (2002) 449-454.

[37] L.V. Azároff and J.J. Brophy, Electronic Processes in Materials. McGraw-Hill Book Company, New York, 1963.

[38] Y.F. Chen and Y.P. Lan, Appl. Phys. B 74 (2002) 415-418.

[39] N.Y. Garces, K.T. Stevens, G.K. Foundos, and L.E. Halliburton, J. Phys.: Condens. Matter 16 (2004) 7095-7106.

[40] P.P. Yaney and L.G. DeShazer, J. Opt. Soc. Am. 66 (1976) 1405-1414.

[41] N.Y. Garces, L.E. Halliburton, K.T. Stevens, M. Shone, and G.K. Foundos, J. Appl. Phys. 91 (2002) 1354-1358.

[42] W. Barendswaard, R.T. Weber, and J.H. van der Waals, J. Chem. Phys. 87 (1987) 3731-3738.

[43] O. Guillot-Noël, V. Mehta, B. Viana, and D. Gourier, Phys. Rev. B 61 (2000) 338-346.

[44] N. Karayianis, C.A. Morrison, and D.E. Wortman, J. Chem. Phys. 62 (1975) 4125-4129.

[45] O. Guillot-Noël, Ph. Goldner, P. Higel, and D. Gourier, J. Phys.: Condens. Matter 16 (2004) R1-R24.

[46] O. Guillot-Noël, B. Viana, B. Bellamy, D. Gourier, G.B. Zogo-Mboulou, and S. Jandl, Opt. Mater. 13 (2000) 427-437.

[47] F.W. Kutzler, D.E. Ellis, D.J. Lam, B.W. Veal, A.P. Paulikas, A.T. Aldred, and V.A. Gubanov, Phys. Rev. B 29 (1984) 1008-1021.

[48] T.S. Lomheim and L.G. DeShazer, J. Appl. Phys. 49 (1978) 5517-5522.

[49] L. Zundu and H. Yidong, J. Phys.: Condens. Matter 6 (1994) 3737-3748.

[50] Y.F. Chen, IEEE J. Quantum Electron. 35 (1999) 234-239.

[51] W. Koechner, Solid State Laser Engineering. Springer-Verlag, Berlin, 1999.

[52] W. Ryba-Romanowski, Cryst. Res. Technol. 38 (2003) 225-236.

[53] C.R. Barrett, W.D. Nix, and A.S. Tetelman, The Principles of Engineering Materials. Prentice-Hall, New Jersey, 1973.

[54] F.S. Ermeneux, C. Goutaudier, R. Moncorgé, M.T. Cohen-Adad, M. Bettinelli, and E. Cavalli, Opt. Mater. 8 (1997) 83-90.

[55] X. Peng, A. Asundi, Y. Chen, and Z. Xiong, Appl. Opt. 40 (2001) 1396-1403.

[56] J.A. L'huillier, G. Bitz, V. Wesemann, P. von Loewis, R. Wallenstein, A. Borsutzky, L. Ackermann, K. Dupré, D. Rytz, and S. Vernay, Appl. Opt. 41 (2002) 4377-4384.

[57] G.J. Friel, A.J. Kemp, T.K. Lake, B.D. Sinclair, Appl. Opt. 39 (2000) 4333-4337.

[58] K. Waichman, L. Kravchik, J. Kaga, C. Labbe, and Y. Kalisky, Opt. Mater. 16 (2001) 163-172.

[59] R.C. Powell, Physics of Solid-State Laser Materials. Springer-Verlag, New York, 1998.

[60] Z. Wang, L. Sun, S. Zhang, X. Meng, R. Cheng, and Z. Shao, Opt. Laser Technol. 33 (2001) 47-51.

[61] J. Wisdom, M. Digonnet, and R.L. Byer, Photonics Spectra. "Ceramic Lasers: Ready for Action," Feb. 2004, pp. 50-56.

[62] Y. Sato, T. Tiara, N. Pavel, and V. Lupei, Appl. Phys. Lett. 82 (2003) 844-846.

[63] M.G. Hur, W.S. Yang, S.J. Suh, M.A. Ivanov, V.V. Kochurikhin, and D.H. Yoon, J. Cryst. Growth 237-239 (2002) 745-748.

[64] R.A. Fields, M. Birnbaum, and C.L. Fincher, Appl. Phys. Lett. 51 (1987) 1885-1886.

[65] H. Zhang, X. Meng, L. Zhu, C. Wang, Y.T. Chow, and M. Lu, Opt. Mater. 14 (2000) 25-30.

[66] J.G. Sliney, Jr., K.M. Leung, M. Birnbaum, and A.W. Tucker, J. Appl. Phys. 50 (1979) 3778-3779.

[67] H. Zhang, M. Chao, M. Gao, L. Zhang, and J. Yao, Opt. Laser Technol. 35 (2003) 445-449.

[68] A.J. Kemp, R. S. Conroy, G.J. Friel, and B.D. Sinclair, IEEE J. Quantum Electron. 35 (1999) 675-681.

[69] A. Agnesi and P. Uggetti, Opt. Commun. 212 (2002) 371-376.

[70] P.K. Mukhopadhyay, K. Ranganathan, J. George, S.K. Sharma, and T.P.S. Nathan, Pramana J. Phys. 59 (2002) 75-89.

[71] A.A. Andrade, T. Catunda, R. Lebullenger, A.C. Hernandes, and M.L. Baesso, J. Non-Cryst. Solids 284 (2001) 255-260.

[72] F. Song, C. Zhang, X. Ding, J. Xu, G. Zhang, M.Leigh, and N. Peyghambarian, Appl. Phys. Lett. 81 (2002) 2145-2147.

[73] J.H. García-López, V. Aboites, A.V. Kir’yanov, M.J. Damzen, and A. Minassian, Opt. Commun. 218 (2003) 155-160.

[74] Y.F. Chen, Y.P. Lan, S.C. Wang, IEEE J. Quantum Electron. 36 (2000) 615-619.

[75] S. Erdei and F.W. Ainger, J. Cryst. Growth 174 (1997) 293-300.

[76] S. Erdei, B.M. Jin, F.W. Ainger, B. Kerzei, J. Vandlik, and A. Süveges, J. Cryst. Growth 172 (1997) 466-472.

[77] T. Katsumata, H. Takashima, T. Michino, and Y. Nobe, Mater. Res. Bull. 29 (1994) 1247-1254.

[78] B.M. Jin, S. Erdei, A.S. Bhalla, and F.W. Ainger, Mater. Res. Bull. 30 (1995) 1293-1300.

[79] S. Erdei, M. Klimkiewicz, F.W. Ainger, B. Keszei, J. Vandlik, and A. Süveges, Mater. Lett. 24 (1995) 301-306.

[80] N.Y. Garces, K.T. Stevens, G.K. Foundos, L.E. Halliburton, J. Phys.: Condens. Matter 16 (2004) 7095-7106.

CHAPTER FOUR

DEFECT STUDIES OF YTTRIUM ORTHOVANADATE

4.1 Experimental Motivation

The improvement of Nd:YVO_4 as a laser crystal is important to industry. Increasing laser power density, the amount of laser power that can be generated per unit volume of crystal, gives crystal growers higher profit margins and allows for the design of smaller laser devices. Scaling down size without loss of power is significant to both military and civilian markets, especially in the use of long-range laser range finders and target acquisition devices.

However, improving laser power density in Nd:YVO_4 laser crystals has proven difficult. The addition of more Nd^{3+} ions into the YVO_4 matrix presents a challenge as the ionic size difference between Y^{3+} and Nd^{3+} introduces stress into the lattice. Growing highly-doped Nd:YVO_4 is difficult, and industry has considered alterative host lattices including $GdVO_4$, which is discussed in Appendix A.

The focus of this research centered around the goal of increasing power density of Nd:YVO_4 by identifying power-limiting defects within grown crystal. By limiting the affect of these defects, an increase in laser power density was achieved to industry benchmark levels.

Each section of this chapter focuses on an issue that pertains to laser power in Nd:YVO_4. In addition, several power-limiting candidates pointed out by literature are identified and discussed. Each literature-prescribed candidate is evaluated by the author. The influence of that candidate on laser performance is assessed. The candidates found to greatly impact laser performance are separately addressed, and steps to limit the influence of such candidates are presented.

4.2 Dependence of Segregation Coefficient on Growth Axis

In addition to growth length, growth axis can influence the amount of Nd^{3+} ion concentration in grown boules. To measure the differences in Nd^{3+} ion concentration along the two axes in Nd:YVO_4, four *c*-axis grown and four *a*-axis grown Nd:YVO_4 crystals were obtained. All eight crystals were grown under congruent conditions with the same Nd^{3+} ion concentration. The resulting crystal Nd^{3+} ion concentration was then measured by x-ray fluorescence (XRF). In these XRF measurements, incident x-rays caused the removal of electrons from the inner L shell of the Nd^{3+} ion within the Nd:YVO_4 crystal and M shell electrons replaced the removed L-shell electrons. The energy difference resulting from the electron replacement is emitted in the form of a photon and is collected by a detector. The wavelength of the emitted photon is characteristic of the element from which it was emitted, and for neodymium that photon wavelength is 0.2370nm. The results of the XRF measurements can be seen in table 4.1.

As is evident from the table, the segregation coefficient for Nd^{3+} ions is different between the two axes, and more Nd^{3+} ions can be accommodated along the *c*-axis than the *a*-axis leading to slightly higher doping concentrations for *c*-axis grown Nd:YVO_4 in comparison to *a*-axis grown Nd:YVO_4 under similar melt compositions. This is due to the density difference between the two axes of the crystal. This also makes *c*-axis grown Nd:YVO_4 a potentially better laser material than *a*-axis grown Nd:YVO_4 [1]. In this study, the *c*-axis grown Nd:YVO_4 samples had, on average, roughly 25% higher Nd^{3+} ion concentration than the *a*-axis grown samples. This is an important finding as less dopant material is needed to reach a set dopant concentration if the crystal is grown along its denser axis direction.

Table 4.1: Nd^{3+} ion concentration difference between *a*-axis grown $Nd:YVO_4$ and *c*-axis grown $Nd:YVO_4$.

Sample ID	Growth Axis	Nd^{3+} Concentration (% at.)
Sample 1-C	*c*	0.31 ± 0.01
Sample 2-C	*c*	0.32 ± 0.01
Sample 3-C	*c*	0.30 ± 0.01
Sample 4-C	*c*	0.30 ± 0.01
Sample 1-A	*a*	0.23 ± 0.01
Sample 2-A	*a*	0.24 ± 0.01
Sample 3-A	*a*	0.26 ± 0.01
Sample 4-A	*a*	0.26 ± 0.01

4.3 The Laser Cavity and Cooling Unit for Laser Power Measurements

The laser cavity used to take all the power curves for $Nd:YVO_4$ laser bricks presented here was a Spectra Physics z-configuration laser cavity model Z-106C-08. A simplified schematic of the z-configuration cavity can be seen in figure 4.1. The $Nd:YVO_4$ crystal is held in place by a copper clamp system with indium foil between the crystal and the copper to aid in heat removal from the crystal. Some pertinent thermodynamic properties of the crystal, copper, and indium foil can be seen in table 4.2. The heat transfer coefficient is an important parameter when considering heat removal. For indium in contact with $Nd:YVO_4$ and indium in contact with copper, the heat transfer coefficient is 1.5×10^{-2}W/k·mm^2, and for the two air-cooled end faces, the heat transfer coefficient is 6.5×10^{-6}W/k·mm^2 [2]. Temperature control is vital for laser operation as $Nd:YVO_4$ has a tendency to thermally fracture if not adequately cooled. The cooling unit used in these studies was the Neslab Merlin Series M25 refrigeration unit. Temperature control is more crucial for lower doping levels and shorter $Nd:YVO_4$ crystals due to their lower-intensity and narrower-band absorption near the pumping wavelength [3]. As is

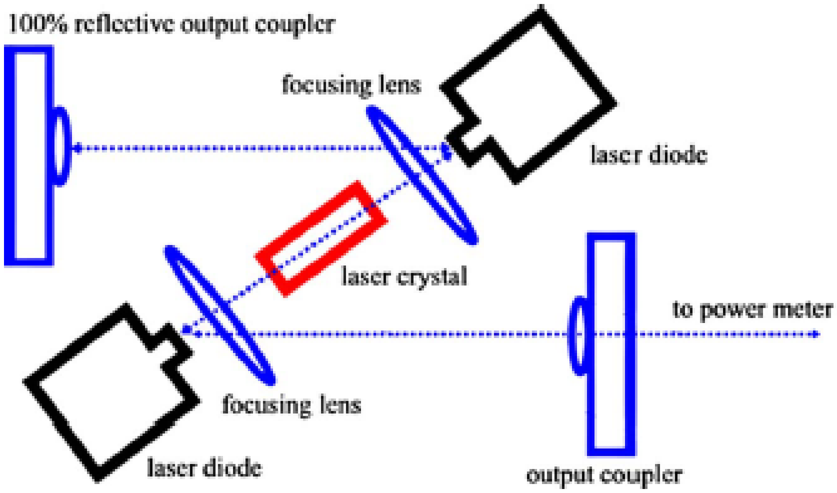

Figure 4.1: Schematic of a z-configuration laser cavity. *Source: C.R. Shawley, C.L. Wang, and K.G. Lynn, J. Appl. Phys. 99 (2006) 123109-2.*

evident from figure 4.1, the z-configuration laser cavity allows for end-pumping of the Nd:YVO_4 crystal. End-pumping has the potential to yield highly-efficient, high-beam-quality laser emissions provided that the diode-laser-emitting area can be properly matched to the intracavity mode size and the emission of the diode properly matches the desired pumping level of the crystal [4]. However, Nd:YVO_4 is more tolerant to diode wavelength variations than many materials, and diodes with wavelengths in the region of 801-821nm can pump a Nd:YVO_4 laser at no less than 50% its peak operating capacity with optimum performance occurring around 808nm [5,6]. GaAlAs is by far the most common diode pump source used for Nd:YVO_4, and it was utilized in the Spectra Physics laser cavity for all power measurements reported here [7]. Diode wavelength emission can be controlled by diode cooling, and the optimum operating temperature can be determined for each power measurement. The variation of wavelength and temperature can be determined for each power measurement. The variation of wavelength and emission intensity for the diodes used in the Spectra Physics laser cavity was measured using an Ocean Optics spectrometer and can be seen in figure 4.2. As is evident from the figure, as the

Table 4.2: Thermodynamic properties of z-configuration laser cavity components. *Source: X. Peng, A. Asundi, Y. Chen, and Z. Xiong, Appl. Opt. 40 (2001) 1400.*

Parameter	**Nd:YVO$_4$**	**Copper**	**Indium foil**
Thermal conductivity ($W \cdot m^{-1} \cdot K^{-1}$)	5.23 ($\parallel$c) 5.10 ($\perp$c)	111	5.1
Thermal expansion coefficient (1×10^{-6} K^{-1})	11.37 ($\parallel$c) 4.43 ($\perp$c)	-	3.412
Heat capacity ($kJ \cdot kg^{-1} \cdot K^{-1}$)	0.8	0.38	0.2
Density (1×10^{-3} kg/cm^3)	4.24	8.6	1.1

diode-operating temperature increases, so does the emission wavelength. There exists an optimum diode-operating temperature that provides the highest intensity possible for pumping the Nd:YVO$_4$ crystal. This optimum temperature was measured for each crystal that was measured regardless of growth axis or Nd^{3+}-ion doping concentration. The GaAlAs diodes and their controlling device used for all power measurements presented for Nd:YVO$_4$ in this chapter were the Spectra Physics model T40-8SS-08.

Diode pumping efficiency can be determined by the following relation:

$$\eta_{laser}^{ideal} = \frac{P_{stim} + P_{om}}{P_{abs} - P_{abs}^{thr}} \approx \frac{P_{fluo}}{P_{abs}} = 1 - \xi = 0.6 \tag{4.1}$$

where η_{laser}^{ideal} is the diode pumping efficiency of an ideal laser, P_{stim} is the stimulated emission that is partly lost in the resonator, P_{om} is the radiative power above threshold outside the laser mode volume, P_{abs} is the absorbed pump power, P_{abs}^{thr} is the absorbed pump power at the measured threshold, P_{fluo} is the spontaneous and stimulated emission, and ξ is the heat generated relative to the absorbed power and is known as fractional thermal loading [8,9]. Equation 4.1 indicates that roughly 40% of the absorbed power is transferred into heating the crystal, so although diode end-pumped lasers can produce excellent beam quality, they are limited in power scalability due to thermally-induced lensing and thermal fracture [10].

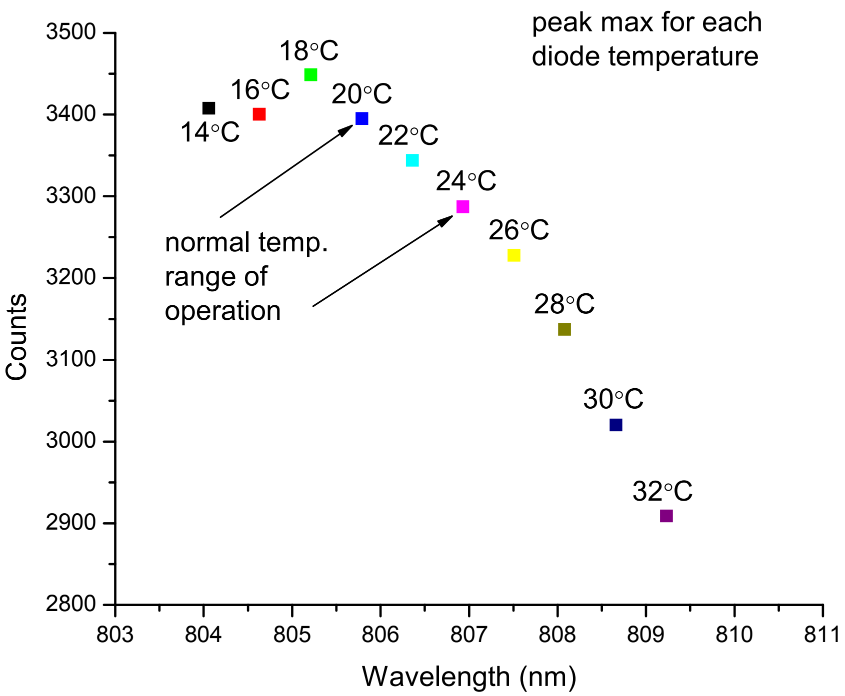

Figure 4.2: Variation of emission wavelength and intensity with varying diode operating temperature.

4.4 Oxygen Vacancy Studies of Nd:YVO_4

Color centers in a transparent oxide crystal add electronic states to its band structure and can give rise to the actual coloration of the crystal. For YVO_4, color centers, being the addition of a dopant ion and/or the small deficiency of oxygen resulting in oxygen vacancies, provide the vast array of coloration seen in many boules [11]. Oxygen-deficiency-related defects are easily incorporated in oxide crystals by modifying the homogeneity within a region of the crystal [12]. Oxygen vacancies can cause a distortion of the oxygen tetrahedra and can necessitate the valence change of the vanadium ions which both result in color center introduction to the crystal [13-15]. As-grown YVO_4 boules can often appear yellow in color which literature attributes to the presence of V^{4+} ions and oxygen vacancies within the crystal [16-18]. Heavily oxygen-deficient crystals can appear dark brown or black in color [19].

4.4.1 Solarization Measurements of Undoped YVO_4

Both *a*- and *c*-axis grown YVO_4 crystals were obtained and partially solarized using an ultraviolet dental light from Electro-Lite (model ELC-410). The crystals were solarized for ten minutes. Photographs of the crystal were taken both before and after solarization. Figure 4.3 contains photographs of as-received and solarized undoped YVO_4 displaying the solarization-induced black coloration, and figure 4.4 is a photograph of an undoped YVO_4 boule that contains the yellow coloration which could be due to such defects. Another example of vanadium valence change and oxygen vacancies is V^{3+} ion defects which are formed when an oxygen atom leaves the crystal during growth or when a doubly-ionized oxygen vacancy traps two electrons [20]. To compensate for the resulting charge imbalance, a V^{5+} ion spatially close to the oxygen vacancy changes into a V^{3+} ion [21]. In addition, V^{4+} ions are present in YVO_4 crystals, and their presence is also connected with oxygen vacancies [14,22]. The presence of V^{4+} ions in YVO_4 may suggest two formation mechanisms. The first mechanism is the presence of the V^{4+} ion next to an oxygen vacancy, known as the $[V^{4+}]_A$ center, which is an important defect in YVO_4 because of its concentration correlation with the unwanted optical absorption occurring near the band edge [21].

To test this, an undoped YVO_4 boule slice was obtained. It was pumped using an ultraviolet dental light (Electro-Lite ELC-410) for thirty minutes. Figure 4.3 shows both before and after photographs of this UV-induced coloration. The crystal was then heated at 200°C for ten minutes to eliminate this coloration.

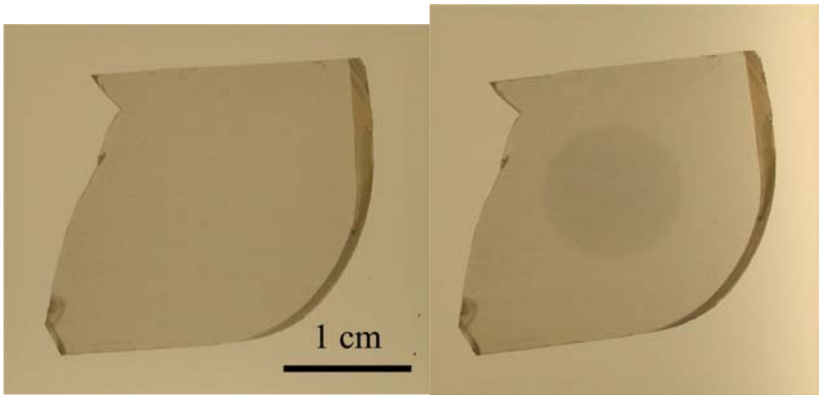

Figure 4.3: An undoped YVO_4 boule slice before (left) and after (right) UV solarization.

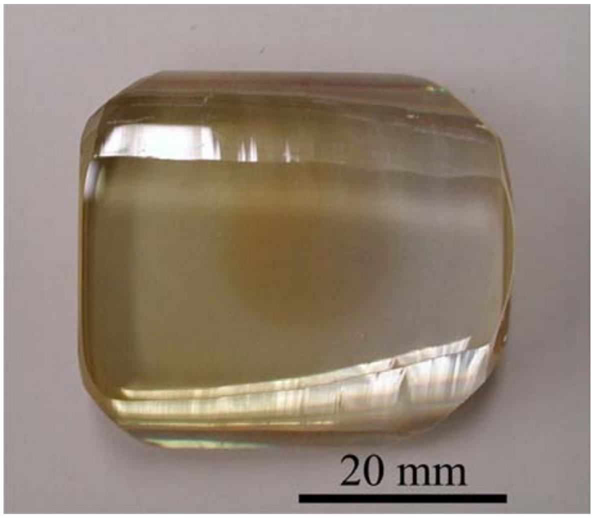

Figure 4.4: Photograph of a yellow, undoped YVO_4 boule slice with a circular region of UV-induced $[V^{4+}]_A$ centers in the middle of the crystal.

4.4.2 Fluorescence and Absorption Studies of Undoped YVO_4

Oxygen deficiency is not simply a color center problem; it also generates inhomogeneities in the Y-V stoichiometry and can cause precipitates [17]. These defects, all the result of oxygen vacancies, can scatter light and seriously alter the lasing performance of a crystal [23]. Therefore, their identification and elimination is very important for obtaining maximum power from a laser crystal.

Thermoluminescence and photoluminescence measurement techniques have shown that the 450nm wavelength emission observed in YVO_4 may be due to oxygen vacancies [12]. To test for this, fluorescence studies were performed. An undoped YVO_4 crystal was pumped with a Spectroline (model 11SC-1) mercury vapor pen lamp filtered with an Edmund Optics U-330 bandpass filter and the corresponding fluorescence was measured with an Ocean Optics spectrometer. The emission referenced in the literature was seen in undoped YVO_4 samples and can be seen in figure 4.5. Other techniques seen in literature such as pumping YVO_4 crystals with an ultraviolet laser beam having a wavelength band of 351nm-364nm and subsequently measuring the resulting electron paramagnetic resonance (EPR) signals have also indicated that oxygen vacancies are inherent to the Czochralski-method crystal growth of YVO_4 [16].

Also, measuring absorption changes by solarizing the crystal with ultraviolet light to change the vanadium valence and oxygen vacancy concentration has been done. An undoped YVO_4 crystal was measured for absorption. The crystal was then solarized for 30 minutes. Absorption measurements were then taken again. These oxygen vacancy/vanadium-valence complexes generate increasing visible-region absorption with increasing ultraviolet solarization, which was consistent with literature [1]. Figure 4.6 is a plot showing YVO_4 absorption and how it changes with the ultraviolet solarization of the crystal. From the plot, it can be seen that solarization affects the absorption of YVO_4, with the most significant change occurring in the 375-600nm wavelength range. To eliminate the extra absorption, it is often necessary to anneal the crystal in an oxygen-rich environment for long periods of time, allowing the oxygen vacancies to be filled and the vanadium valence to return to its proper value [11,18]. Figure 4.7 is a plot containing absorption spectra for an undoped YVO_4 crystal—as-grown, after ultraviolet solarization, and after subsequent air anneal. As is evident from the plot, annealing at a high temperature for a long period of time in an oxygen-rich environment can reduce the additional absorption created by the solarization process, and the annealing process can even reduce the absorption below the as-grown level in the 400-500nm wavelength range.

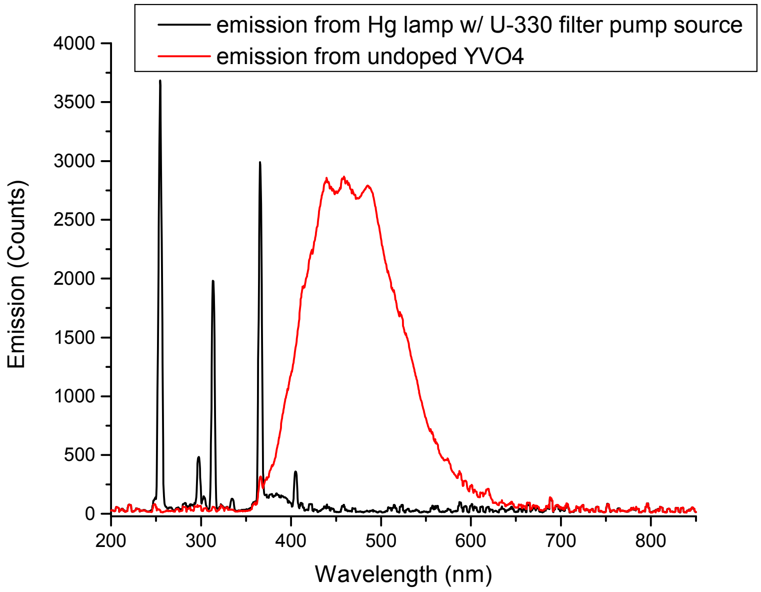

Figure 4.5: Fluorescence emission from an undoped YVO_4 boule being pumped by ultraviolet light from a filtered Hg lamp.

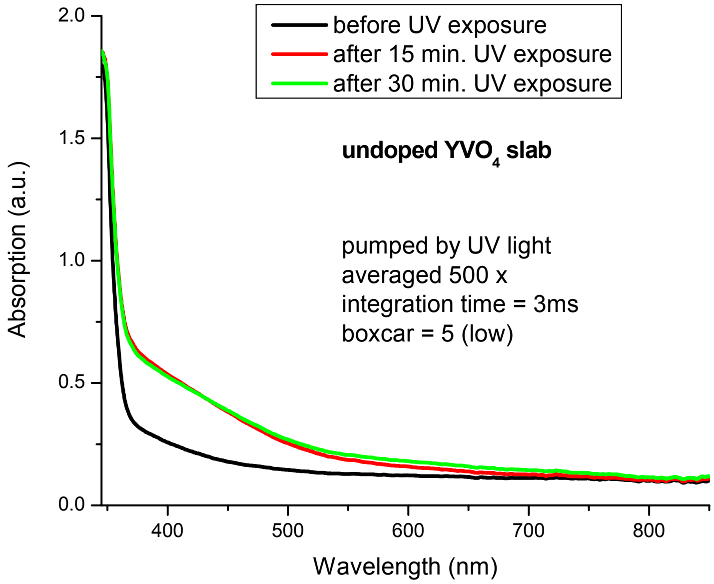

Figure 4.6: Absorption of YVO_4 before and after ultraviolet solarization.

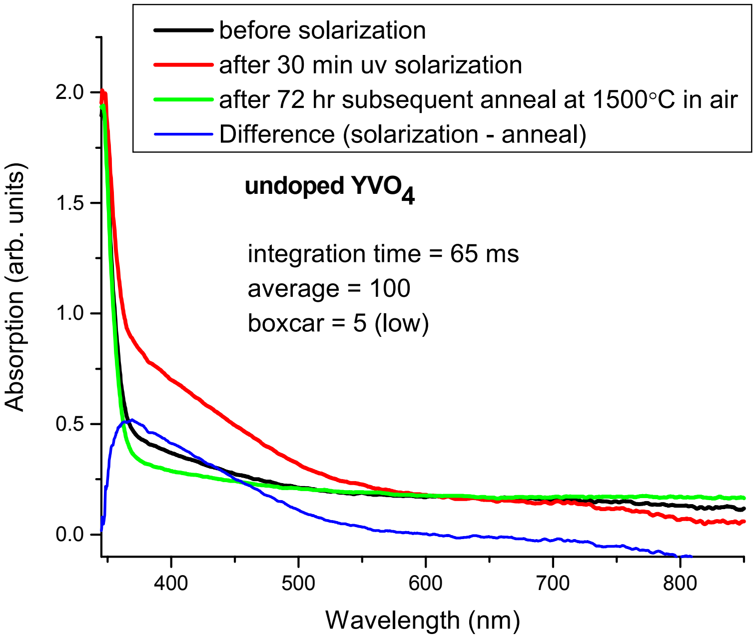

Figure 4.7: Absorption spectrum of undoped YVO_4 as-grown, after solarization, and after subsequent annealing in air.

4.5 Dislocations, Grain Boundaries, and Polygonization in Nd:YVO_4

The presence of grain boundaries in laser materials can be deleterious on laser performance due to their tendency to scatter light and create local changes to the refractive index of the crystal [25]. Therefore, their reduction or elimination is crucial for maximizing laser output power, even possibly more than the other defects listed in this chapter.

Low-angle grain boundaries in Nd:YVO_4 form due to the migration of dislocations introduced during the crystal growth process and subsequent post-growth cooling [26]. They are found nearly parallel to the *a*-face and have been noted in crystals grown in the *a*-axis direction [26]. Low-angle boundaries can be produced in a number of ways during crystal growth including during creep deformation and during phase transformations [27]. Also, dislocations can be introduced into the crystal as a result of defects in the seed material [22,26,28]. It was also shown in several studies that the density of dislocations in Nd:YVO_4 increases with increasing Nd^{3+} ion concentration [20,26]. However, in YVO_4 and $Nd:YVO_4$, dislocations have the opportunity to align and partially annihilate in order to relieve internal stresses that have been created as a result of the growth process [29,30]. This rearrangement is known as polygonization. Polygonization occurs as a result of the introduction of an excess number of dislocations of the same sign. When the crystal is heated, thermal stresses from anisotropy in the thermal expansion coefficients are created [20,26]. As the crystal cools, radial hoop stresses remaining in the material activate slip systems allowing dislocation glide [20,25,26]. The dislocations group themselves into the lowest-energy configuration possible through both glide and climb mechanisms resulting in a low-angle grain boundary [11,20,25,27,31,32]. The result is a polygon-like network of these grain boundaries. A schematic diagram of the process of polygonization can be seen in figure 4.8. It is energetically favorable for dislocations to form low-angle grain boundaries as the formation energy of such boundaries is between $1\text{-}2 J \cdot m^{-2}$, and low-angle grain boundaries have only a few minutes of arc or, at most, a few degrees difference in orientation from one another [11,20,26,27]. The average misorientation angle in one study of low-angle grain boundaries in $Nd:YVO_4$ was determined to be 0.14° [20,26]. The Burgers vector for the dislocations responsible for low-angle grain boundary formation in YVO_4 is $\frac{1}{2}[\bar{1}11]$, and is obtained through a complicated process [20]. The [021] direction links the

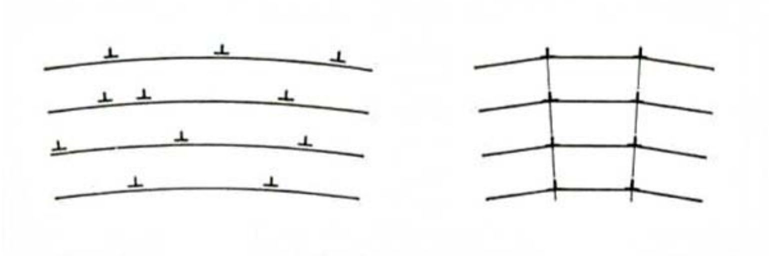

Figure 4.8: A schematic of the polygonization process in a crystal. The diagram on the left is a number of random, same-sign dislocations and through polygonization, they group together to form the diagram on the right. *Source: G.E. Dieter,* <u>Mechanical Metallurgy</u>*. McGraw-Hill, Boston, 1986, p. 196.*

nearest neighbor like-atoms, but the Burgers vector is not ¼[021] because further glide would require a yttrium atom to move into a vanadium lattice site and the dislocation would become sessile [28]. Furthermore, the positions of the oxygen atoms must be preserved with respect to the surrounding yttrium and vanadium atoms [28]. Therefore, the Burgers vector is obtained through the following relation [28]:

$$\tfrac{1}{4}[021] + \tfrac{1}{4}[\bar{2}01] = \tfrac{1}{2}[\bar{1}11]$$

4.5.1 Cross-Polarization Studies of YVO_4

Low-angle grain boundaries can be easily seen using a light table and a cross-polarization technique, the setup for which can be seen in figure 4.9. Many undoped and Nd^{3+}-doped YVO_4 crystals were studied for the presence of low-angle grain boundaries using this technique. Low-angle grain boundaries were only found in *a*-axis grown YVO_4 boules. To date, none have been found in *c*-axis grown boules. This observation is also backed by the preferential etching along the *a*-axis faces as well as by the increased etch pit concentrations on samples grown along the *a*-axis direction [20,26]. Photographs of several *a*-axis and *c*-axis grown boules can be seen in figure 4.10 and figure 4.11, respectively. As can be seen in the figures, low-angle grain boundaries are only seen in *a*-axis grown boules, and their presence and concentration do not seem to be related to Nd^{3+}-dopant concentration. Since low-angle grain boundaries scatter light and have a deleterious effect on laser output power, one must be careful in the selection of rod-coring locations. Cutting the laser element from an area where low-angle grain boundaries are located could limit the laser output power of the crystal. Photographs of laser elements grown in both directions can be seen in figure 4.12. The presence of grain boundaries in the *a*-axis grown laser element in figure 4.12 could reduce its laser output power, while the output power for the *c*-

axis grown laser element seen in the figure should not be limited and maximum laser output power could be higher for the *c*-axis grown laser element.

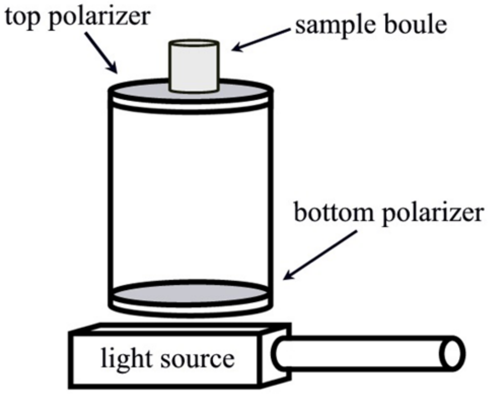

Figure 4.9: Cross-polarization arrangement for viewing low-angle grain boundaries in YVO_4.
Source: C.R. Shawley, C.L. Wang, and K.G. Lynn, J. Appl. Phys. 99 (2006) 123109-2.

Because low-angle grain boundaries are not as likely to form in *c*-axis grown crystals due to the higher stress required for dislocation motion, internal stresses produced during crystal growth and subsequent cooling have no method for liberation which leads to the frequent cracking observed in *c*-axis grown boules [20,26]. A photograph of the cracking often associated with *c*-axis grown boules can be seen in figure 4.13. To avoid this cracking, proper care must be taken during growth and especially during post-growth cooling.

Therefore, only properly grown *c*-axis growth crystals, containing no low-angle grain boundaries, may be more suited for higher output power applications than *a*-axis grown crystals which contain these grain boundaries [1]. However, to avoid the cracking problem associated with *c*-axis grown boules, making a smaller diameter *a*-axis grown boule lowers the dislocation density which may help prevent the formation of low-angle grain boundaries [33].

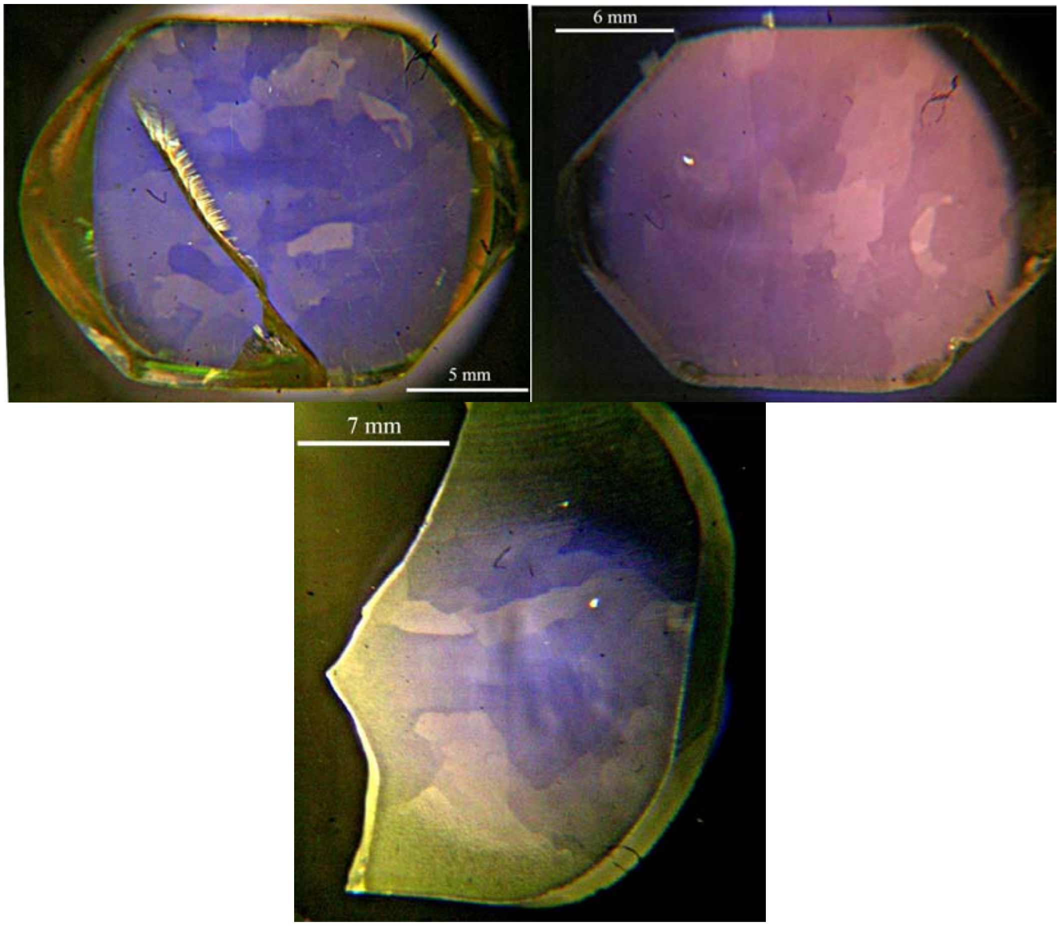

Figure 4.10: Cross-polarization photographs of several YVO_4 and Nd:YVO_4 boules grown in the *a*-axis direction. The photograph in the upper left is of a 0.27% Nd:YVO_4 boule. The photograph in the upper right is of a 1.0% Nd:YVO_4 boule, and the photograph on the bottom is of a piece of an undoped YVO_4 boule.

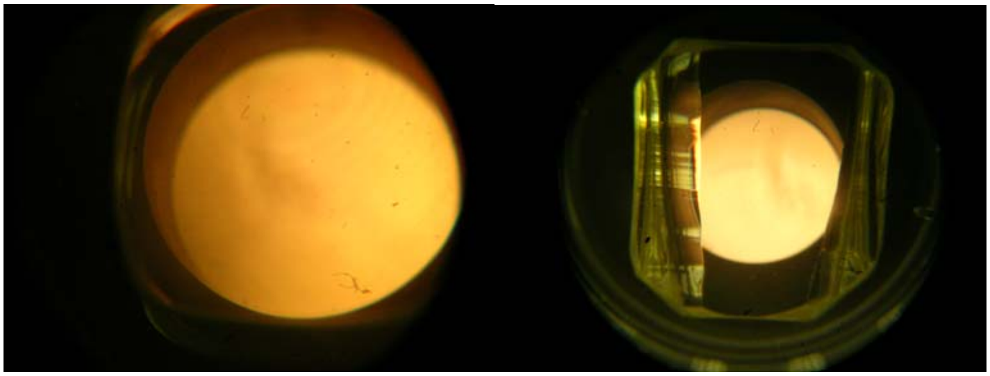

Figure 4.11: Cross-polarization photographs of several YVO_4 and Nd:YVO_4 boules grown in the *c*-axis direction. The photograph on the left is of a 0.27% Nd:YVO_4 boule, and the photograph on the right is of an undoped YVO_4 boule. The illuminated part of the crystal in each photograph is approximately 30mm in diameter.

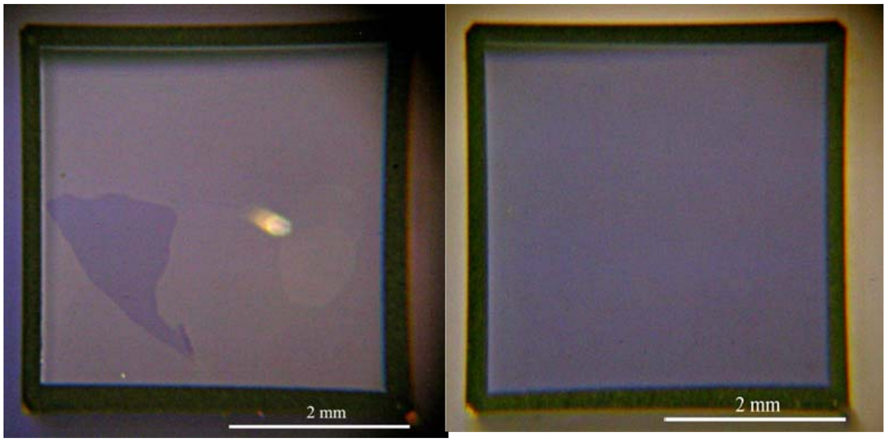

Figure 4.12: Cross-polarization photographs of two Nd:YVO$_4$ laser elements. The laser element on the left was grown in the *a*-axis direction and contains two low-angle grain boundaries, while the element on the right was grown in the *c*-axis direction and does not contain any low-angle grain boundaries. *Source: C.R. Shawley, C.L. Wang, and K.G. Lynn, J. Appl. Phys. 99 (2006) 123109-3.*

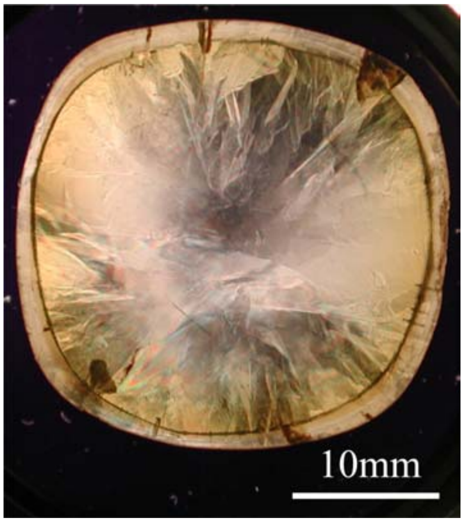

Figure 4.13: Cross-polarization photograph of the cracking problem associated with *c*-axis grown Nd:YVO$_4$ boules.

4.5.2 Laser Power Studies of *a*- and *c*-axis Grown Nd:YVO$_4$

Four a-axis grown Nd:YVO$_4$ and four c-axis grown Nd:YVO$_4$ laser elements were obtained. Laser power was measured in a z-configuration laser cavity, a schematic of which can be seen in figure 4.1, for each laser element using several different output coupler reflectivities. The laser power results for each growth axis were averaged for each output coupler reflectivity and the results can be seen in figure 4.14. As can be seen from the figure, the average maximum laser output power using the optimum output coupler reflectivity was higher for the *c*-axis grown samples than for the *a*-axis grown ones. Laser output powers for highly reflective output couplers (R ≥ 90%) were higher for *a*-axis grown samples, but this expected as concentration quenching becomes an issue when considering these highly-reflective output couplers, and *a*-axis grown crystals may show less concentration quenching due to their increased light scattering, a direct result of possessing low-angle grain boundaries [1].

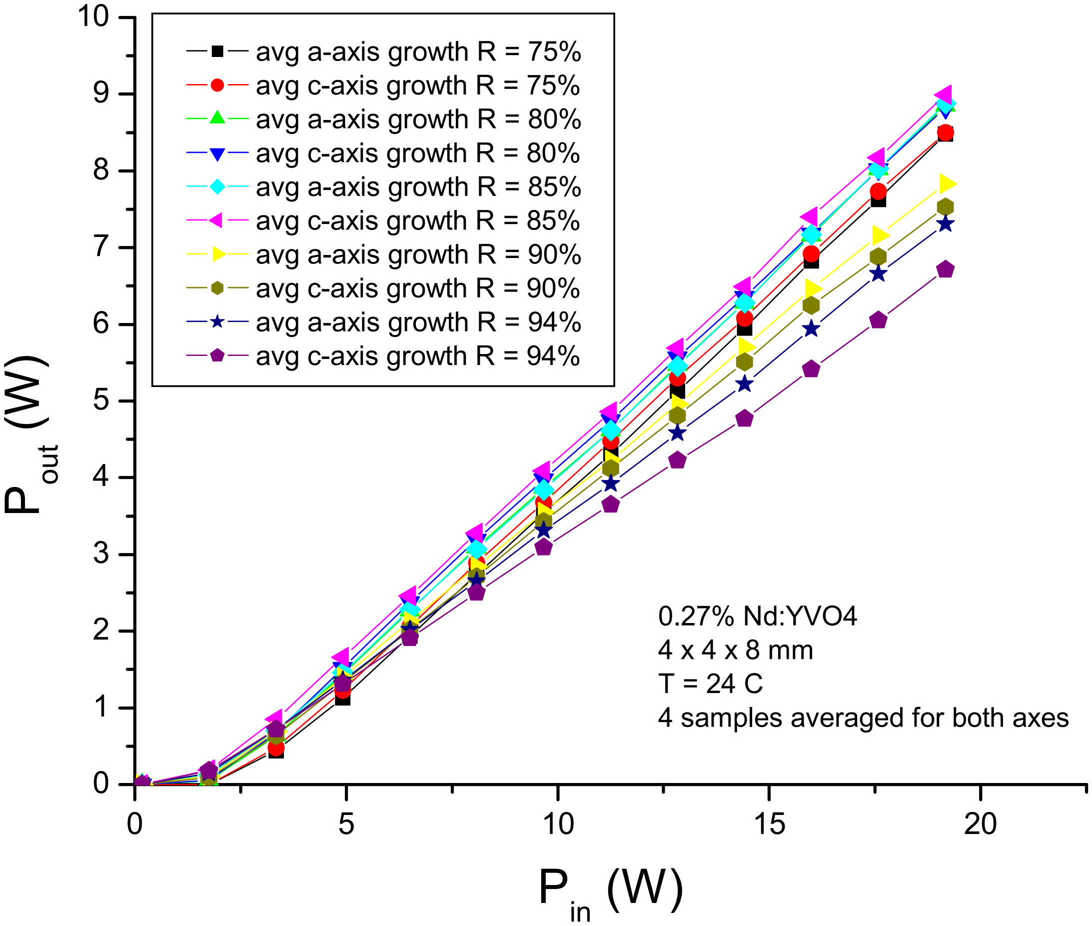

Figure 4.14: Laser output power measurements for several *a*-axis and *c*-axis grown laser elements using various output coupler reflectivities. *Source: C.R. Shawley, C.L. Wang, and K.G. Lynn, J. Appl. Phys. 99 (2006) 123109-2.*

4.6 Measurements of Hydroxyl Impurities in Nd:YVO_4

OH^- ions substitute for O^{2-} ions in YVO_4 and play a charge-compensating role for other point defects in the lattice [34]. In fact, the hydroxyl ion may help compensate for the Y^{3+}-V^{5+} non-stoichiometry caused by the incongruent vaporization of vanadium oxide during crystal growth [34]. However, hydroxyl impurities may inhibit laser performance as the ^4I ground-term energy-levels for Nd^{3+} ions lie in the infrared region where the vibrational frequency of hydroxyl ions occur [34]. Introduction of OH^- ions is the result of water in the growth atmosphere and/or from melt constituents that have not been properly calcified [34,35]. Hydroxyl-ion defects are prominent in air-grown YVO_4 boules but are less prominent when grown in an atmosphere of dry nitrogen and oxygen [34]. In the lattice, the OH^- ion dipole lays in the plane parallel to the *c*-axis along the O-O bond of the $(VO_4)^{3-}$ tetrahedron [34]. Its characteristic stretching vibration at 3,307cm^{-1} (~3μm) can be found using IR spectroscopy and is the tell-tale sign of hydroxyl presence in YVO_4 [34].

Both *a*-axis grown and *c*-axis grown Nd:YVO_4 boules were obtained and measured using IR spectroscopy in the 3μm wavelength range. Figure 4.15 shows this stretching vibration indicative of the presence of hydroxyl impurities in Nd:YVO_4. Of some interest is the lack of a hydroxyl stretching band in *c*-axis growth Nd:YVO_4. However, this is due to the previously mentioned fact that the OH^- dipole lies in the (001) plane and its stretching band is therefore not observed in *c*-axis grown Nd:YVO_4 [34]. This apparent lack of hydroxyl impurity absorption may also be another reason for choosing *c*-axis grown Nd:YVO_4 over *a*-axis grown Nd:YVO_4.

To eliminate hydroxyl ions entering the lattice, careful monitoring of growth atmosphere, high-temperature calcinations of melt constituents for long periods of time, and longer crystal growth times should be done [35]. However, even with all these precautions, keeping water vapor out of the furnace and thus out of the crystal may still be difficult if not nearly impossible. In addition to the presence of hydroxyl impurities in the crystal being deleterious to laser power, the presence of water vapor in the growth chamber also allows for other impurities to be added to melt.

Iridium crucible material oxidizes in the presence of water vapor and can be absorbed into the melt and subsequently the growing crystal [36]. Therefore, the elimination of water vapor from the growth atmosphere is doubly important to the resulting laser efficiency. However, hydroxyl presence in presently-grown crystals is miniscule, and, therefore, its ability to reduce laser output power is rather diminutive compared to other defects such as low-angle grain boundaries. However, because the dipole lies parallel to the *c*-axis, *c*-axis grown Nd:YVO_4 is preferable over *a*-axis grown Nd:YVO_4.

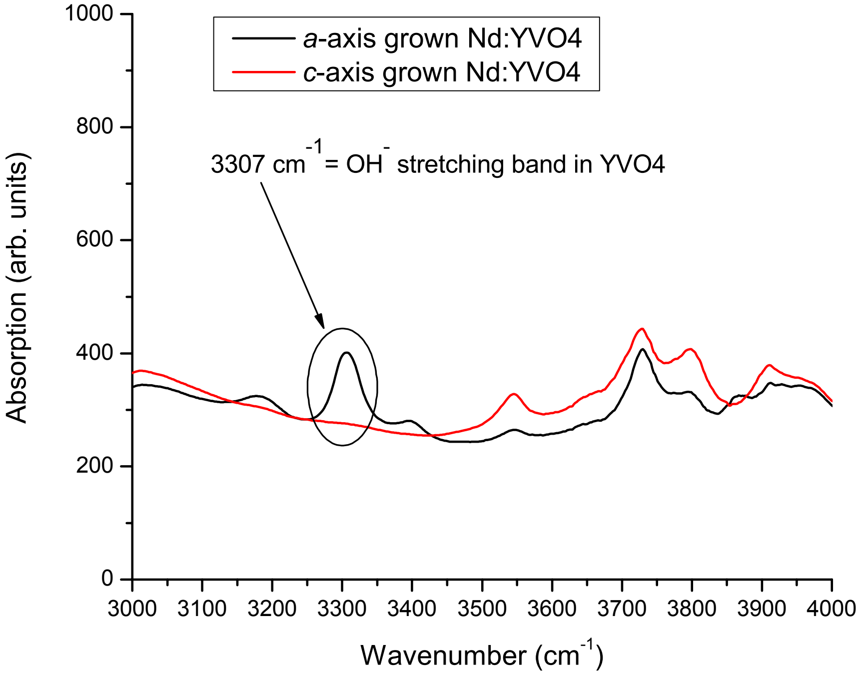

Figure 4.15: OH^{-} stretching band in Nd:YVO_4. The OH^{-} dipoles lay in the plane perpendicular to the tetragonal axis; the dipoles lay in the (001) plane. *Source: Measurements courtesy of Slade Jokela.*

4.7 Annealing Considerations in Nd:YVO_4

In an effort to eliminate defects and restore stoichiometry in some crystals, thermal treatments such as annealing are often done. Many anneals of YVO_4 are done in an oxygen atmosphere at temperatures of 1,000 -1,500°C in an attempt to fill oxygen vacancies created during crystal growth by the incongruent vanadium oxide vaporization [18,37,38]. These anneals can often eliminate the yellow coloration of these oxygen-deficient YVO_4 crystals and lower the intensity of some of the absorption peaks found in YVO_4 by forcing oxygen back into the lattice [20,18]. Figure 4.16 is a plot of varying annealing temperatures and their affect on absorption intensity for Nd:YVO_4.

However, the act of filling these oxygen vacancies increases the unit cell size and can add stress to the crystal [12,39-42]. The difference in unit cell volume of an oxygen-deficient YVO_4 crystal after oxygen annealing was found in one study to be 0.2271$Å^3$ [41]. In addition to oxygen-vacancy filling, vanadium ions may also change valence as a result of oxygen annealing, oxidizing V^{3+} ions and V^{4+} ions into V^{5+} ions [18,20,40]. However, annealing at these temperatures cannot change the size and location of low-angle grain boundaries as these defects are very energetically stable [20,26].

Annealing temperature and temperature ramping rates are very important to treating YVO_4. Annealing above 1,350°C in one study resulted in scattering from the generation of inclusions and additional phases at such a high temperature [43]. In addition, dendrite-like growth on the crystal has been observed.

This was experimentally verified by obtaining an undoped YVO_4 crystal and annealing it in air for 72 hours at a temperature of 1,500°C. Dendritic growth was observed. Figure 4.17 is a photograph of undoped YVO_4 both before and after being air annealed at 1,500°C for 72 hours.

It can be seen from the photograph that the yellow coloration of the crystal reduced as a result of the annealing, but dendrite-like growth formed on the surface of the crystal reducing surface quality of the crystal. Other studies have also reported precipitate formation and micro-cracking as a result of annealing [37,40]. Cracking is also a major problem with annealing YVO_4. YVO_4 is most likely to crack along the *c*-axis face due to its larger thermal expansion coefficient in comparison to that of the *a*-axis (see table 3.2) [44,45]. Therefore, the temperature ramping rates must be slow enough to ensure that the crystal does not thermally fracture.

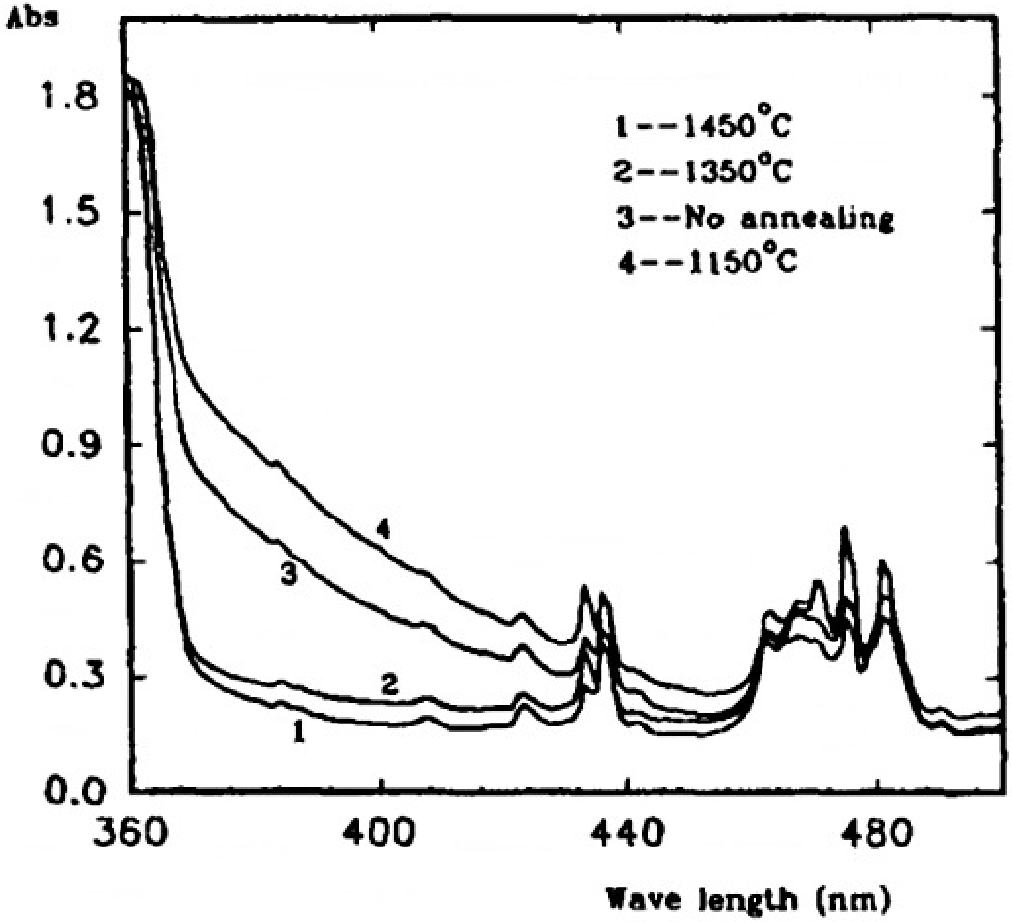

Figure 4.16: Absorption spectra for Nd:YVO_4 with different annealing temperatures. *Source: Z. Hong, Y. Huaguang, Z. Yunzhi, Z. Jianfei, X. Hongchang, W. Xing, and J. Yandao, J. Cryst. Growth 160 (1996) 139.*

According to one study, annealing appears to have no influence on the pumping threshold for Nd:YVO_4, but it can influence the overall output power, slope efficiency and light-light conversion efficiency [38]. Therefore, annealing can be a great tool for improving laser performance if the proper annealing environment, correct temperature, and sufficiently slow temperature ramping rates are applied. With the dendrite formation observed on the surface, subsequent crystal processing including polishing may be required to obtain the suggested improvement in laser performance.

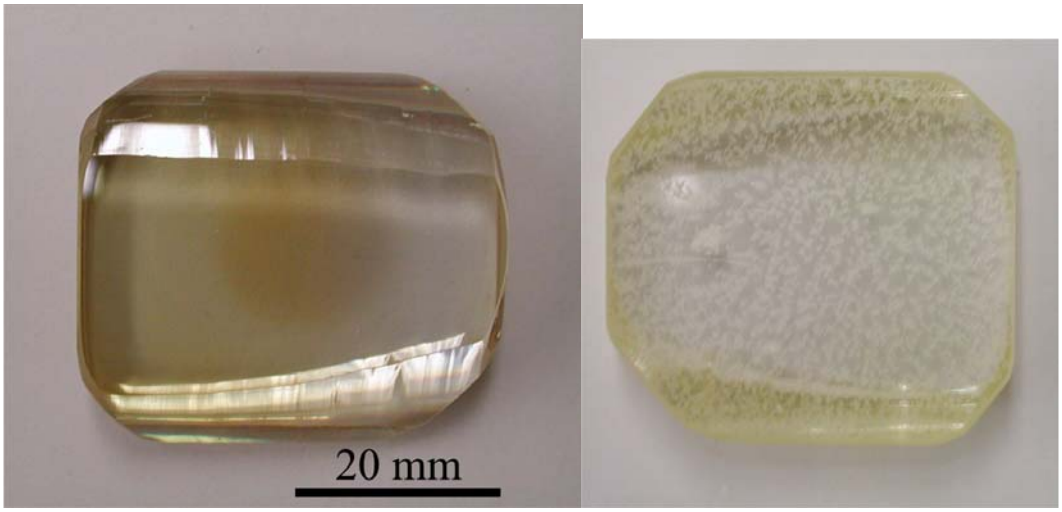

Figure 4.17: Photograph of an undoped YVO_4 crystal before (left) and after (right) being annealed in air for 72 hours at 1,500°C.

4.8 Summary for Improving Laser Performance of Nd:YVO_4

While Nd:YVO_4 has many issues surrounding its growth and processing, it is possible to improve its laser performance through a combination of choosing the correct growth parameters—of which, the case for choosing *c*-axis grown Nd:YVO_4 has been presented, switching to a different crucible material such as molybdenum or rhenium or by using an iridium crucible and growing the crystal in an 80% N_2 and 20% CO_2 atmosphere as well as superheating the melt and cooling slowly, and by proper post-growth processing through oxidation heat treatment.

However, it is much more important in terms of laser performance to select the correct growth and cut axis. Using *a*-cut laser elements taken from *c*-axis grown Nd:YVO_4 have been shown to be competitive with the *a*-axis grown Nd:YVO_4 elements that were considered benchmarks for laser output power for this laser material. The *c*-axis grown elements can accommodate a higher Nd^{3+} ion concentration, do not exhibit parasitic absorption from hydroxyl impurities, and do not contain low-angle grain boundaries. All these aspects may help increase the lasing efficiency of *c*-axis grown Nd:YVO_4 laser elements, allowing for the average laser crystal to have a laser output profile that matches or outperforms the benchmark samples grown in the *a*-axis direction.

4.9 Suggestions for Future Work

Because of the advantageous properties of *c*-axis grown Nd:YVO_4, laser growth technicians should focus on its growth over that of the *a*-axis grown crystal. One major commercial producer of Nd:YVO_4 has done just that. Adjusting the growth parameters to limit thermal fracture and reduce internal stress would be a good starting point. Optimizing Nd^{3+} ion concentration to maximize laser output power is also necessary. Characterization could focus on measuring internal stress from grown crystal and adjusting laser cavity properties such as diode temperature, optimal output coupler reflectivity, and crystal orientation.

References

[1] C.R. Shawley, C.L. Wang, and K.G. Lynn, J. Appl. Phys. 99 (2006) 123109.

[2] X. Peng, A. Asundi, Y. Chen, and Z. Xiong, Appl. Opt. 40 (2001) 1396-1403.

[3] Z. Wang, L. Sun, S. Zhang, X. Meng, R. Cheng, and Z. Shao, Opt. Laser Technol. 33 (2001) 47-51.

[4] J.A. L'huillier, G. Bitz, V. Wesemann, P. von Loewis, R. Wallenstein, A. Borsutzky, L. Ackermann, K. Dupré, D. Rytz, and S. Vernay, Appl. Opt. 41 (2002) 4377-4384.

[5] K. Waichman, L. Kravchik, J. Kaga, C. Labbe, and Y. Kalisky, Opt. Mater. 16 (2001) 163-172.

[6] R.A. Fields, M. Birnbaum, and C.L. Fincher, Appl. Phys. Lett. 51 (1987) 1885-1886.

[7] W. Koechner, Solid State Laser Engineering. Springer-Verlag, Berlin, 1999.

[8] U. Brauch and M. Schubert, Opt. Commun. 117 (1995) 116-122.

[9] A. Sennaroglu, Appl. Opt. 38 (1999) 3253-3257.

[10] A. Minassian and M.J. Damzen, Opt. Commun. 230 (2004) 191-195.

[11] B.Q. Hu, Y.Z. Zhang, X. Wu, and X.L. Chen, J. Cryst, Growth 226 (2001) 511-516.

[12] S. Erdei and F.W. Ainger, J. Cryst. Growth 174 (1997) 293-300.

[13] B. Jin, S. Erdei, A.S. Bhalla, and F.W. Ainger, Mater. Lett. 22 (1995) 281-284.

[14] R. Jablonski, S.M. Kaczmarek, M. Swirkowicz, and T. Lukasiewicz, J. Alloys Comp. 300-301 (2000) 310-315.

[15] T. Katsumata, H. Takashima, T. Michino, and Y. Nobe, Mater. Res. Bull. 29 (1994) 1247-1254.

[16] N.Y. Garces, L.E. Halliburton, K.T. Stevens, M. Shone, and G.K. Foundos, J. Appl. Phys. 91 (2002) 1354-1358.

[17] S. Erdei, B.M. Jin, F.W. Ainger, B. Kerzei, J. Vandlik, and A. Süveges, J. Cryst. Growth 172 (1997) 466-472.

[18] Y. Nobe, H. Takashima, and T. Katasumata, Opt. Lett. 19 (1994) 1216-1218.

[19] W. Ryba-Romanowski, Cryst. Res. Technol. 38 (2003) 225-236.

[20] J. LeBret, Defect Characterization of Yttrium Orthovanadate. Thesis, Washington State University, Pullman, Washington, 2004.

[21] N.Y. Garces, K.T. Stevens, G.K. Foundos, and L.E. Halliburton, J. Phys.: Condens. Matter 16 (2004) 7095-7106.

[22] L. Qin, X. Meng, J. Zhang, L. Zhu, H. Zhang, B. Hu, and H. Jiang, J. Cryst. Growth 242 (2002) 183-188.

[23] C. Goutaudier, F.S. Ermaneux, M.T. Cohen-Adad, R. Moncorgé, M. Bettinelli, and E. Cavalli, Mater. Res. Bull. 33 (1998) 1457-1465.

[24] F.S. Ermeneux, C. Goutaudier, R. Moncorge, M.T. Cohen-Adad, M. Bettinelli, and E. Cavalli, Opt. Mater. 13 (1999) 193-204.

[25] B. Cockayne, B. Lent, J.S. Abell, and P.M. Marquis, J. Mater. Sci. 10 (1975) 1874-1878.

[26] J.B. LeBret, M.G. Norton, D.F. Bahr, D.P. Field, and K.G. Lynn, J. Mater. Sci. 40 (2005) 3347-3353.

[27] G.E. Dieter, Mechanical Metallurgy. McGraw-Hill, Boston, 1986.

[28] D.E. Eakins, J.B. LeBret, M.G. Norton, and D.F. Bahr, J. Cryst. Growth 266 (2004) 411-414.

[29] B. Henderson, Defects in Crystalline Solids. Crane, Russak & Company, Inc., New York, 1972.

[30] H.G. Van Bueren, Imperfections in Crystals. North-Holland Publishing Company, Amsterdam, 1961.

[31] T. Shonai, M. Higuchi, and K. Kodaira, Mater. Res. Bull. 35 (2000) 225-232.

[32] D. Hull and D.J. Bacon, Introduction to Dislocations. Butterworth Heinemann, Oxford, 2001.

[33] T. Shonai, M. Higuchi, and K. Kodaira, J. Cryst. Growth 233 (2001) 477-482.

[34] L. Kovács, S. Erdei, and R. Capelletti, Solid State Commun. 11 (1999) 95-99.

[35] J. Chen, F. Guo, N. Zhuang, J. Lan, X. Hu, S. Gao, J. Cryst. Growth 243 (2002) 450-455.

[36] S.E. Stokowski, M.H. Randles, and R.C. Morris, IEEE J. Quantum Electron. 24 (1988) 934-948.

[37] S. Erdei, L. Kovács, Á. Pető, J. Vandlik, P.D. Townsend, and F.W. Ainger, J. Appl. Phys. 82 (1997) 2567-2571.

[38] H. Zhang, X. Meng, L. Zhu, C. Wang, Y.T. Chow, and M. Lu, Opt. Mater. 14 (2000) 25-30.

[39] D. Reyes Ardila, A.S.S. de Camargo, J.P. Andreeta, and L.A.O. Nunes, J. Cryst. Growth 233 (2001) 253-258.

[40] S. Erdei, B. Jin, F.W. Ainger, A.S. Bhalla, B. Kersei, J. Vandlik, and A. Süveges, J. Appl. Phys. 79 (1996) 2834-2838.

[41] S. Erdei, F.W. Ainger, Mater. Res. Soc. Symp. Proc. 329 (1994) 245-251.

[42] B.M. Jin, S. Erdei, A.S. Bhalla, and F.W. Ainger, Mater. Res. Bull. 30 (1995) 1293-1300.

[43] Z. Hong, Y. Huaguang, Z. Yunzhi, Z. Jianfei, X. Hongchang, W. Xing, and J. Yandao, J. Cryst. Growth 160 (1996) 136-140.

[44] S. Wu, G. Wang, J. Xie, X. Wu, and G. Li, J. Cryst. Growth 249 (2003) 176-178.

[45] S. Wu, G. Wang, and J. Xiea, J. Cryst. Growth 226 (2004) 496-499.

CHAPTER FIVE

LITERATURE REVIEW OF YTTRIUM ALUMINUM GARNET

5.1 The Growth of YAG

YAG ($Y_3Al_5O_{12}$), lovingly referred to as “nature’s trashcan” was first grown by the Czochralski crystal growth method in the mid-1960’s for the purpose of being a synthetic diamond [1]. Its growth is very similar to that of YVO_4 and many of the same crystal growth techniques that have been utilized for YVO_4 have also been employed in the growth of YAG. The color of YAG has been controlled by the addition of impurity ions such as manganese coloring YAG red, titanium coloring YAG yellow, chromium coloring YAG green, cobalt to color YAG blue, and, of course, neodymium coloring it purple [2]. YAG is usually grown in the (111) direction, and grown boules exhibit a hexagonal cross-section [3].

Like Nd:YVO_4, high-quality Nd:YAG growth is governed by the growth temperature gradient, growth velocity, slope of the liquidus, solute concentration, segregation of solute, and diffusion coefficient of the solute into the melt [4]. These parameters, mathematically, govern growth by the following relation:

$$\frac{G}{V} = \frac{mC_0(1-k)k}{D} \tag{5.1}$$

where *G* is the temperature gradient, *V* is the growth velocity, *m* is the slope of the liquidus, C_0 is the solute concentration, *k* is the segregation coefficient, and *D* is the diffusion coefficient of the solute into the melt [4]. Also, like Nd:YVO_4, the segregation coefficient is based on Burton, Prim, and Slichter (BPS) theory:

$$k = \frac{1}{1 + \left(\frac{1}{k_0} - 1 \right) e^{-f\sigma / D}} \tag{5.2}$$

where k is the segregation coefficient, k_0 is the equilibrium distribution coefficient, f is the pull rate, and σ/D is a constant [5].

The issues that are important for the growth of YVO_4 are also vital for YAG growth. However, several issues are more vital to the growth of YAG than YVO_4 as YAG boules can be grown to much larger sizes than YVO_4 boules. One particular growth issue is the rate of growth and cone angle of the boule top, which are especially important to YAG growth. Too high of a pulling rate will increase the cone angle, and too large of a cone angle will result in significant temperature gradients near the corner of the shoulder region of the boule which often leads to boule cracking from the resulting thermal stresses [6]. Most YAG boules are grown with a cone angle of 35° [6].

In addition to growth parameters, growth materials are also important to the growth of Nd:YAG. However, there is some leniency in the growth of Nd:YAG, and, in general, it is easier for YAG to accommodate extra Y^{3+} ions in the lattice than Al^{3+} ions, and often more yttria is used in the melt than alumina [7].

5.2 Physical Properties of YAG

$Y_3Al_5O_{12}$, is an optically isotropic, body-centered cubic crystal with a lattice constant of 12.01Å [8-10]. Its primitive unit cell is complicated and consists of four formula units or sixty atoms, and its system space group is Ia3d [7,8,11-13]. The garnet structure family, of which YAG is a member, consists of a group of compounds of the type $A_3B_2C_3O_{12}$ where the A sites are dodecahedral sites with eight nearest neighbors, the B sites are tetrahedral sites with four nearest neighbors, and the C sites are octahedral sites with six nearest neighbors [2,8,14]. In YAG, the A sites are filled by Y^{3+} ions or Nd^{3+} ions if that ion is being used as a dopant, and the B and C sites are filled by Al^{3+} ions with approximately 60% of the Al^{3+} ions in the octahedral B sites and 40% of the Al^{3+} ions in the tetrahedral C sites [2,10,15-18]. The oxygen bond length for the Y-O bond is 2.40Å, the Al-O octahedral bond length is 1.93Å, and the bond length is 1.76Å for the Al-O tetrahedral bond [9,19]. The complicated crystal structure of YAG can be seen in figure 5.1 and figure 5.2. YAG is difficult to grow due to the fact that the Al^{3+} ions prefer the octahedral C site, and the rate of decrease of Al^{3+} ions in the melt controls the rate of growth of the crystal [20].

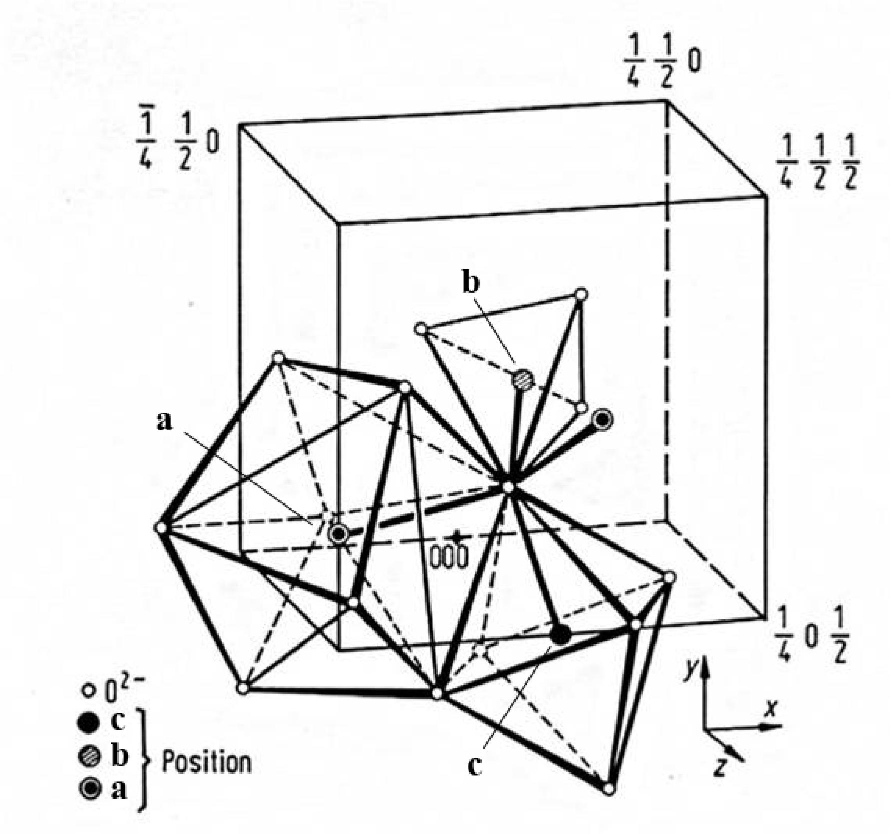

Figure 5.1: The structure of YAG. *Source: A.A. Kaminskii, Laser Crystals. Springer-Verlag, Boston, 1990, p. 402.*

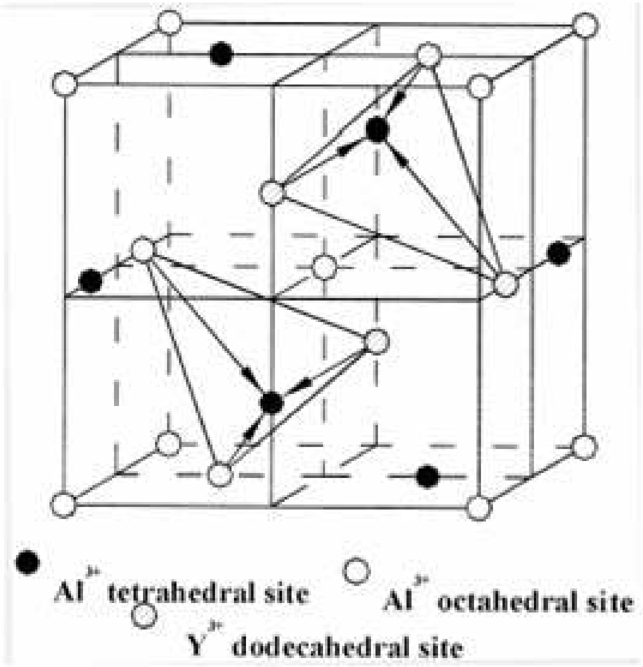

Figure 5.2: The unit cell of YAG. *Source: J. Dong, P. Deng, J. Xu, Opt. Commun. 170 (1999) 258.*

The melting point of YAG is 1,980°C [2]. Its thermal diffusion is 0.46-0.50cm^2/s, its heat capacity is 0.59J/g·K, and its thermal expansion coefficient is 6.9×10^{-6}/°C [21-23]. YAG has a hardness of 8.5 on the Mohs scale, a Poisson ratio of 0.3, a Young's modulus of 315GPa, a bulk modulus of 180GPa, a fracture toughness of 1.4MPa·m$^{1/2}$, a Debye temperature of 754K, and a breaking strain of 1.75-2.10kg/cm^2 [12,22-24]. Some other physical properties of YAG can be seen in table 5.1.

YAG has many optical properties that are advantageous to laser action. The refractive index of YAG is 1.81633 at 1.06μm [12,22]. The refractive index of YAG can be calculated using the following equation:

$$n^2 - 1 = \frac{2.2831\lambda^2}{\left(\lambda^2 - 0.012604\right)} \qquad (5.3)$$

where n is the refractive index and λ is the wavelength measured in micrometers [25]. The linear

Table 5.1: Some of the physical properties of YAG. *Source: P. Wamsley,* High-Pressure Optical Studies of Doped Yttrium Aluminum Garnet*. Dissertation, University of Michigan, Ann Arbor, Michigan, 1994, p. 132.*

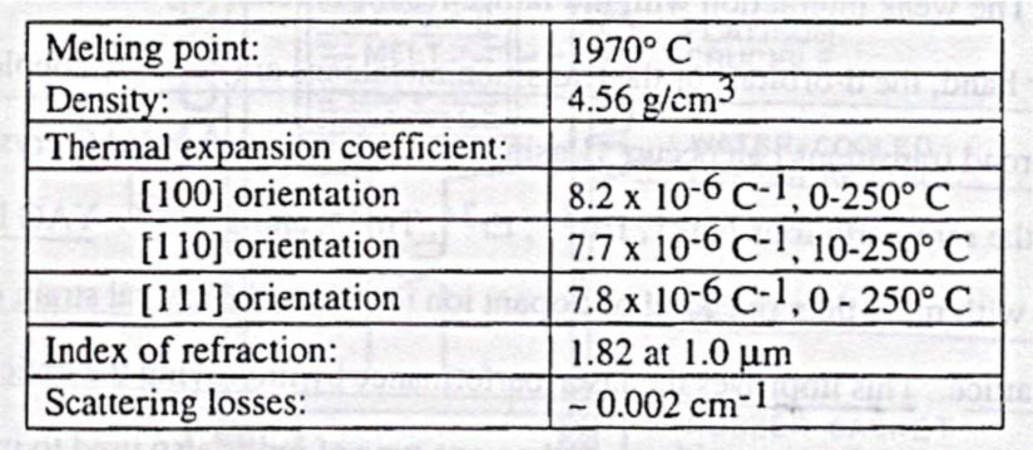

Melting point:	1970° C
Density:	4.56 g/cm^3
Thermal expansion coefficient:	
[100] orientation	8.2 x 10^{-6} C^{-1}, 0-250° C
[110] orientation	7.7 x 10^{-6} C^{-1}, 10-250° C
[111] orientation	7.8 x 10^{-6} C^{-1}, 0 - 250° C
Index of refraction:	1.82 at 1.0 μm
Scattering losses:	~ 0.002 cm^{-1}

dispersion for YAG is 9.86×10^{-6}/K [22]. YAG is a wide band gap material with a band gap of roughly 7eV with a Fermi level of 1.9eV, and the band gap decreases with increasing temperature [17,26-29]. YAG's intrinsic band edge is at 186nm [30]. Its band structure is formed with oxygen orbitals acting as the valence band and aluminum acting as the conduction band, and because aluminum lies in both the octahedral and tetrahedral positions, the conduction band can be divided into overlapping sub-bands [17].

The absorption and fluorescence spectra for Nd:YAG are quite complicated. For the Nd^{3+} ion in YAG, there exist 241 configurations of states of electrons with 5,393 allowed energy transitions [31]. The great complexity of the rare-earth spectrum arises from the large number of states that have nearly identical energies [31]. However, because Nd^{3+} ions substitute for Y^{3+} ions in low-symmetry lattice sites, most of the degeneracy of the field is lifted leading to a relatively large separation of energy-state lines [32]. Also, due to its tight atomic packing in the lattice, YAG is the garnet with the strongest crystal field [32]. Thus, absorption spectroscopy is an effective tool for studying Nd:YAG. The absorption spectrum for Nd:YAG can be seen in figure 5.3.

Doping concentration in Nd:YAG is vital for obtaining maximum laser output power. Determination of the optimal doping concentration in Nd:YAG is subject to a couple of conditions. The first condition is that the optimum concentration should be high enough to absorb the pumping light completely [33]. The second condition is that since the lifetime of the upper laser-energy level is reduced with increasing concentration, the concentration must be low enough to avoid concentration quenching of the pumping light [33]. Figure 5.4 is a plot of luminescence intensity of the 1.064μm laser line versus Nd^{3+} ion concentration. As can be seen from the plot, the maximum luminescence intensity of the $^4F_{3/2} \rightarrow {}^4I_{11/2}$ transition falls at 1.1at.% dopant concentration [21,22]. Increasing the dopant concentration results in a higher absorption coefficient, fluorescence lifetime, and greater overall laser efficiency, as mentioned earlier, but raising the Nd^{3+} ion concentration also increases the occurrence of cracking during growth due to the large ionic radius mismatch between Nd^{3+} ions and Y^{3+} ions (1.12Å for Nd^{3+} ions compared to 1.01Å for Y^{3+} ions) resulting in significant lattice stress [4,34,35]. Also, by increasing the doping concentration, it becomes possible to pump Nd^{3+} ion absorption bands that are not normally pumped at lower concentrations [36]. This is the case with the 885nm absorption band. By pumping at the 885nm absorption band instead of the traditional 808nm, it is possible to reduce the quantum defect by roughly 30% thereby reducing heat generation in the crystal leading to the reduction of thermal lensing and the increase of laser output power and cavity stability [36-39]. However, growing highly-doped Nd:YAG is extremely difficult. Dopant levels above 1.0at.% are hard to achieve due to boule cracking [35,40,41].

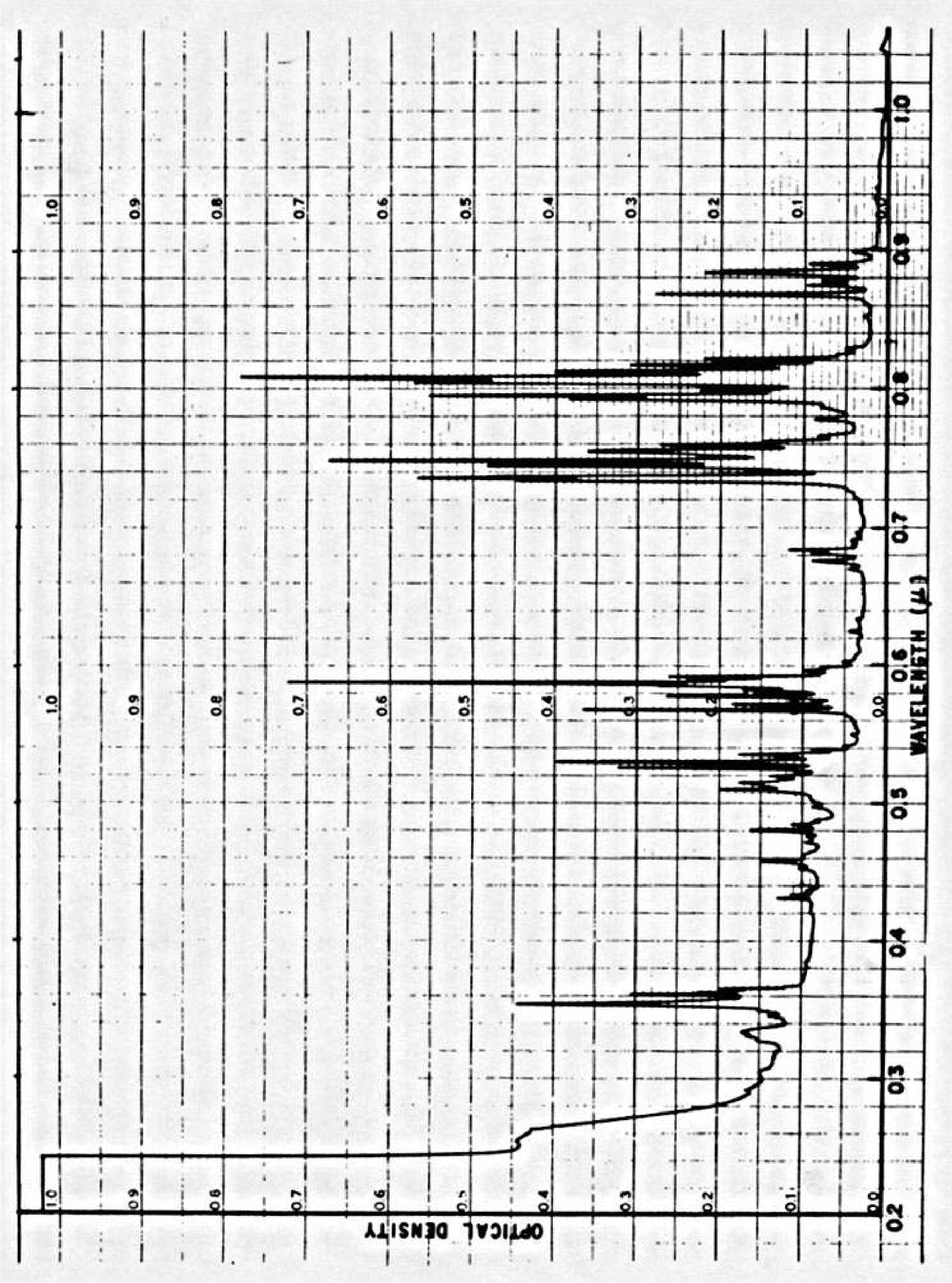

Figure 5.3: The absorption spectrum of Nd:YAG from 0.2-1.0μm. *Source: M.J. Weber, editor, <u>CRC Handbook of Laser Science and Technology</u>. CRC Press, Cleveland, 1990, p. 37.*

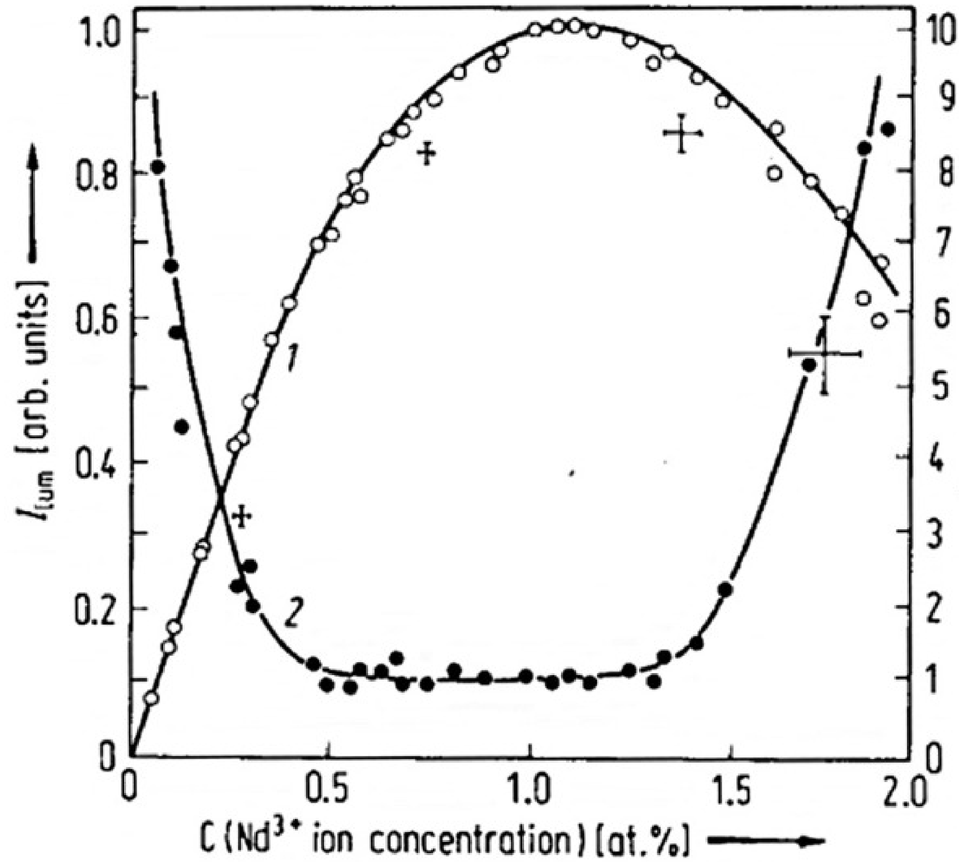

Figure 5.4: Luminescence intensity of the 1.064μm laser line versus Nd^{3+}-doping concentration. *Source: A.A. Kaminskii, Laser Crystals. Springer-Verlag, Berlin, 1990, p. 330.*

Another reason that highly-doped Nd:YAG crystals are difficult to grow is because of the segregation coefficient of Nd^{3+} ions in the YAG lattice. Segregation is a function of ionic size differences, surface energy, and heat of mixing, and, in oxide crystals, there exist additional electrostatic forces that influence segregation [10]. The segregation coefficient for Nd^{3+} ions in YAG is 0.18 [5,22,42-45]. Because the segregation coefficient is less than unity, the last material to crystallize during Nd:YAG growth has a slightly higher Nd^{3+} ion concentration than the first material to crystallize [46].

5.3 Laser Performance of Nd:YAG

The methods used to calculate power-related equations for Nd:YVO_4 can be adapted with minor variation for use with Nd:YAG. Near the threshold, the measured output power is not linear due to inhomogeneous pump-light distribution which can cause the laser to oscillate [33]. This oscillation can continue until the pump light is increased above threshold where the laser output power becomes linear [33]. It is from this linear section of the power profile that the intrinsic slope efficiency is measured. This slope efficiency can be calculated by the following relation:

$$\eta_{slope} = \eta_{excit}\left(\frac{\ln R}{\ln R - L}\right) \tag{5.4}$$

where η_{excit} is the excitation efficiency of a perfect system with no intrinsic loss, R is the output coupler reflectivity, and L is the loss term defined as $2\delta l$, where d is the loss, l is the length of the crystal, and the factor of 2 indicates that it is a round-trip loss [21,33,46,47]. The threshold power can also be used to calculate the insertion loss coefficient by the relation:

$$P_{th}(R) = \frac{(L - \ln R)}{2\eta_{excit}} \tag{5.5}$$

where R is the output coupler reflectivity, L is the loss term, and η_{excit} is the pumping efficiency coefficient all defined in equation 5.4 [21,48]. The average intrinsic slope efficiency for arc-lamp-pumped Nd:YAG lasers is about 2-3.5%, and a typical insertion loss coefficient is around 0.002cm^{-1} [21,46].

The linear section of the laser output power profile can be described mathematically without any other effects taken into consideration by the relation:

$$P_{out} = \eta_{slope}\left(P_{in} - P_{th}\right) \tag{5.6}$$

with η_{slope} and P_{th} both described in equations 5.4 and 5.5, respectively, and P_{in} being the input power supplied to the lamp [21,33]. However, the laser output power is not linear over the entire profile. Figure 5.5 is a plot of the laser output power profile for a Nd:YAG laser rod measured in a Control 512 laser cavity by the author. From the plot, it can be seen that at lower input powers (1,000-4,000W), the laser output power is linear, but above 4,000W of input power, the laser output power deviates from linearity. This may be due to the fact that high input powers often lead to strong thermally-induced optical distortions such as thermal lensing, thermal birefringence, and concentration quenching which can make the laser beam unstable and/or reduce the beam's intensity [23]. Figure 5.6 is a plot of laser output power and cavity stability versus input power to the lamp. From the plot, it can be seen that the crystal absorbs pump light and laser power increases in a linear fashion until the beam becomes unstable, at which point the laser output power decreases dramatically [49]. For Nd:YAG, the maximum absorbed pump power per unit length is roughly 115W/cm [49].

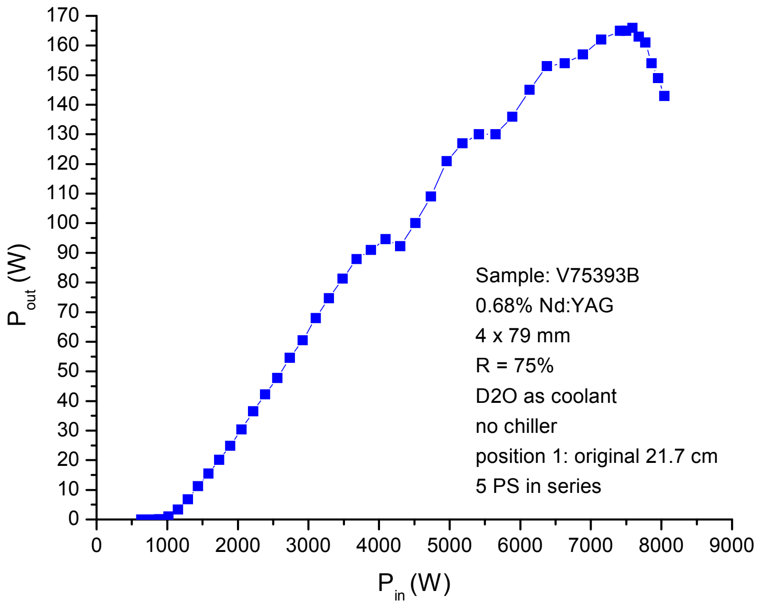

Figure 5.5: Laser output power curve for a Nd:YAG laser rod in a Control 512 laser cavity.

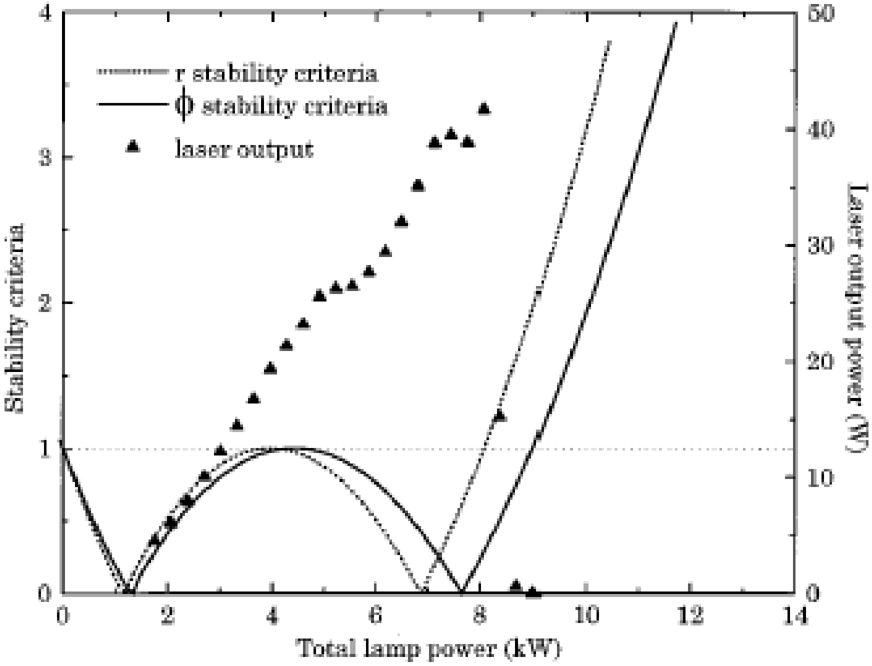

Figure 5.6: Nd:YAG laser output power versus beam stability. *Source: M.P. Murdough and C.A. Denman, Appl. Opt. 35 (1996) 5930.*

5.4 Temperature Effects in Nd:YAG

The temperature of the laser rod heavily influences laser performance. The temperature gradient present in the crystal as a result of heating from the pump radiation and cooling from water creates thermal stress, thermal birefringence, thermal lensing, and possibly crystal fracture. In addition, the temperature of the laser crystal can change the lifetimes of the upper- and lower-laser levels as well as the cross-sections [33]. The temperature also affects laser output power even without any other thermally-related effects taken into consideration by a relation similar to equation 5.6:

$$P_{out} = \eta_{slope}\left(P_{in} - P_{th} - P_T\right) \tag{5.7}$$

where P_T is a thermal power term that takes into account the thermal population of the upper-laser level and the emission cross-section [33]. As the Nd:YAG crystal temperature fluctuates, the laser lines shift creating a tunability effect of up to 5Å per 100°C temperature variation [50,51]. Figure 5.7 is a plot of peak fluorescence wavelength as a function of temperature.

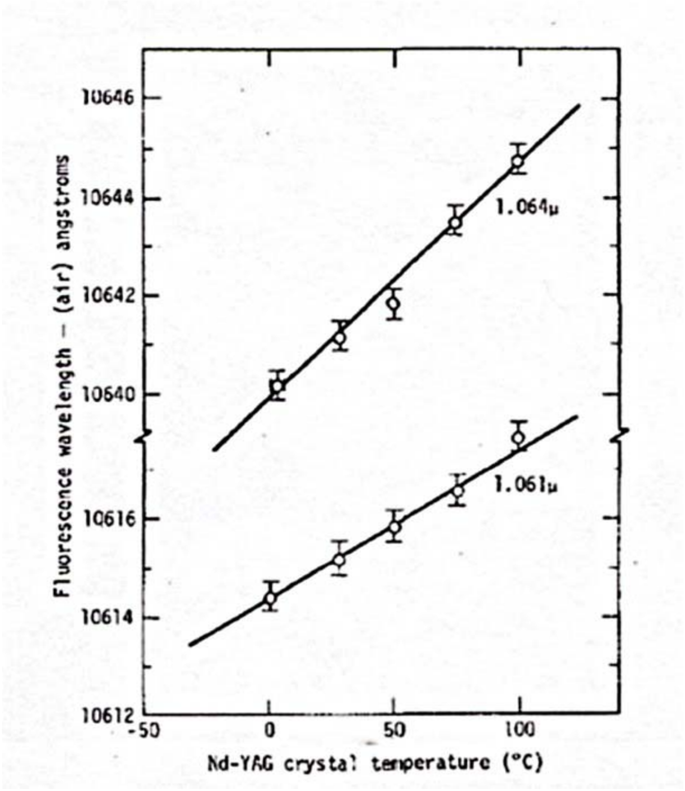

Figure 5.7: Wavelength of laser lines as a function of temperature for Nd:YAG. *Source: J. Marling, IEEE J. Quantum Electron. 14 (1978) 58.*

The main heating mechanisms in arc-lamp-pumped Nd:YAG are due to the quantum defect, color center or impurity absorption, and non-radiative transitions from the upper-laser level [33,52]. These mechanisms account for about 35-40% of the total pump power [53]. However, the crystal does not heat homogeneously. The heat produced by the quantum defect can be expressed by:

$$E_{h,f} = hc\left(\frac{1}{\lambda_p} - \frac{1}{\lambda_l}\right) \tag{5.8}$$

where h is Planck's constant, c is the speed of light, λ_p is the pump wavelength, and λ_l is the lasing wavelength [38]. The heat generated per unit volume can be expressed as:

$$Q = \frac{P_a}{\pi r_O^2 L} \tag{5.9}$$

where P_a is the pump power absorbed by the crystal, r_O is the outer radius of the crystal, and L is the length of the crystal [52,54]. The temperature of the center of the crystal is considerably higher than that of the surface, and the maximum allowable temperature difference is given by:

$$\left(T_M - T_O\right) \leq \frac{\left(1-\upsilon\right)}{5} \frac{\sigma_{\max}}{F\alpha E} \tag{5.10}$$

where T_M is the temperature of the middle of the rod, T_O is the temperature of the outside surface of the rod, ν is the Poisson ratio, F is a geometrical factor and for a cylindrical rod is equal to 0.5, α is the expansion coefficient, E is the elastic modulus, and σ_{max} is the maximum allowable stress before fracture [33].

To avoid thermal fracture of both the crystal and the lamp, a cooling fluid is pumped across the laser cavity to remove heat. Since the cooling fluid only travels on the surface of the crystal, a temperature gradient is created between the center of the rod and the surface of the rod as was mentioned earlier. The temperature difference between the surface of the crystal and the center of the crystal is a function of the velocity and the thermodynamic properties of the flowing liquid [47]. High fluid-flow velocities are most desirable as the flow becomes turbulent leading to a more efficient heat transfer process [47]. However, the turbulent flow of water around the crystal creates changes in the heat transfer between the crystal and water causing temperature variations within the rod which can ultimately lead to optical distortions through the dependence of the index of refraction on temperature [47,54,55]. Figure 5.8 is a qualitative plot showing temperature versus radial position of the rod. As can be seen from the rod, the temperature of the crystal is highest in the center of the rod, and the temperature of the surface of the crystal is roughly equivalent to the temperature of the cooling fluid. The better the thermodynamic properties, such as heat capacity of the cooling fluid, the better the fluid can remove heat from the crystal, and this can result in higher laser output power.

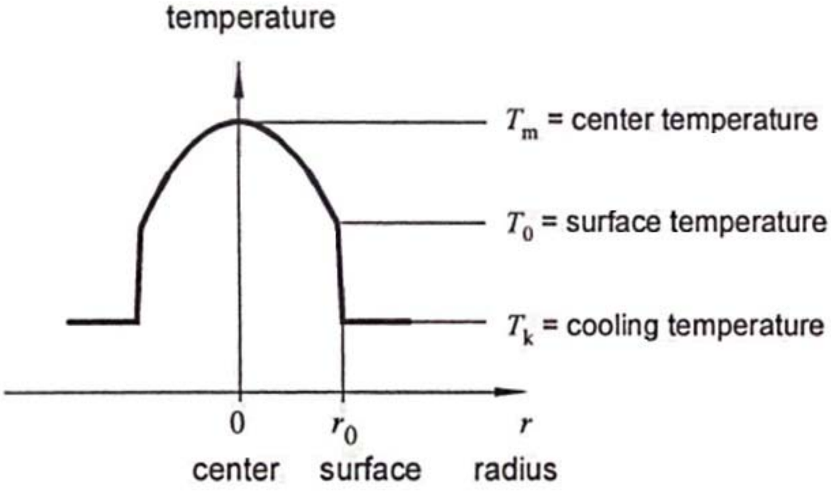

Figure 5.8: Temperature versus radius position in a cooled crystal. *Source: R. Iffländer, Solid-State Lasers for Materials Processing: Fundamental Relations and Technical Realizations. Springer-Verlag, Berlin, 2001, p. 102.*

5.5 Thermal Lensing and Thermal Fracture

Thermal lensing is related to birefringence. Thermal lensing is the result of the faster expansion of the hotter center portion of the crystal in comparison to the cooler outer region of the crystal creating a convex lens shape on the end of the rod [33,56]. The extent of the thermal lens end-effect is about one rod radius as any further rod expansion would be the same for the whole rod cross-section [53]. The radius of curvature, of the thermal lens can be calculated by the following expression:

$$\frac{1}{R} = \frac{\alpha r_0 P_H}{4\kappa V} \tag{5.11}$$

where R is the radius of curvature of the thermal lens, α is the thermal expansion coefficient, r_0 is the radius of the rod, P_H is the amount of heat absorbed in the crystal, V is the rod's total volume, and κ is the thermal conductivity [33]. Thermal lensing, like thermally-induced birefringence, is caused by stresses in the crystal and can lead to laser beam distortion and reduced laser output power [52]. In arc-lamp-pumped Nd:YAG lasers, the variation of the index of refraction due to temperature accounts for roughly 74% of the thermally-induced focusing behavior observed in the rod, according to one study [57]. For a homogeneously-pumped rod, the fraction of the thermal lens contributed by the end effect, $\Gamma_{homogeneous}$, is given by:

$$\Gamma_{\mathrm{hom}\,ogeneous} \approx \frac{1}{1 + \left(\frac{dn}{dT}\right)\left(\frac{L}{2\alpha(n-1)r_0}\right)} \tag{5.12}$$

where dn/dT is the thermal-optical coefficient, L is the length of the rod, α is the thermal expansion coefficient, n is the refractive index, and r_0 is the radius of the rod [56].

To eliminate the thermal lensing of the crystal, several methods have been suggested. One method has been to filter out all pumping light under 700nm in wavelength, as these shorter wavelengths contribute significantly to heat production in the crystal [33]. A second suggestion involves grinding a negative lens on the ends of the rod making a concave lens system [49,51]. When the rod heats up the center expands faster than the surface and because the rod was already concave, the resulting end-face shape becomes flat effectively eliminating the thermal lens effect. However, this suggestion is extremely difficult to carry out in the commercial production of laser rods as most polishing is done by hand, and because polishing is done by hand, variations in the quality of the concave lens would be ever-present. This variation would lead to changes in the focal length of the lens. The final suggestion listed here would be to reduce the cooling fluid temperature to help remove more heat from the rod [58]. This does work with the substitution of heavy water for regular water, effectively removing more heat from the rod, but this can only be extended so far as crystal or lamp fracture could result.

Thermally-induced tensile stresses in the laser rod can easily exceed the fracture strength of the rod leading to rod fracture, so in order to avoid fracture, the tensile stress should be kept smaller than the fracture limit, σ_{max}, by a factor of at least 5 or mathematically:

$$\sigma \leq \frac{\sigma_{\max}}{5} \tag{5.13}$$

where σ is the maximum operating tensile stress allowable to avoid fracture [33,59]. In addition to the condition in equation 5.13, the thermal shock parameter, R_T, can be used to determine the amount of stress a laser material can withstand using the relation:

$$R_T = \frac{\sigma_{\max}\kappa(1-\upsilon)}{\alpha E} \tag{5.14}$$

where σ_{max} is the maximum tensile stress before fracture, κ is the thermal conductivity, ν is the Poisson ratio, α is the thermal expansion coefficient, and E is the elastic modulus [33,47,60]. The thermal shock parameter for Nd:YAG is 7.9W/cm [47].

5.6 Major Defects in Nd:YAG

As with most solid-state laser crystals, defects are the main cause of pump-light loss. Loss can occur through various mechanisms including absorption and/or scattering by impurities, voids, inclusions, striations, dislocations, core strain, concentration quenching, non-radiative transitions from the upper-laser level, and intrinsic absorption from the lower-laser level [33,46,61]. These losses can contribute to heat generation in the crystal further reducing laser quality and performance [40]. The next few subsections describe a few of the different loss mechanisms observed in Nd:YAG crystals.

5.6.1 Concentration Quenching and Non-Radiative Relaxations

There are three main mechanisms for quenching in Nd:YAG. In the first mechanism, known as energy migration, the excitation energy of one ion is transferred to the next ion and so on until it reaches a lattice imperfection that traps and dissipates the energy [62]. The second mechanism, known as cross-relaxation, involves the partial transference of excitation energy from one ion to an unexcited ion, and each ion dissipates its share of the energy [62]. The third and final mechanism, known as Auger recombination, involves the excitation of two ions which are then both partially relaxed through energy dissipation [62]. A schematic for these processes can be seen in figure 5.9. Cross-relaxation is perhaps the most commonly observed quenching mechanism in Nd:YAG. In this process, one ion is initially in a metastable state and another ion is in the ground state, and, after excitation, the first ion relaxes by the $^4F_{3/2} \rightarrow {}^4I_{15/2}$ transition while the other ion goes through the $^4I_{9/2} \rightarrow {}^4I_{15/2}$ transition [21,22,39,63]. The exact transitions and their intensities, however, are dependent upon the phonon density capable of compensating for the energy difference between the excitation energy and the cross-relaxation process [22]. These processes help contribute to thermal loading [64].

The effect of concentration quenching increases as dopant-ion concentration increases. This is due to the fact that as dopant concentration increases, the individual ions begin to interact with one another through dipole-dipole interactions [21,65,66]. These pairs decrease the lasing

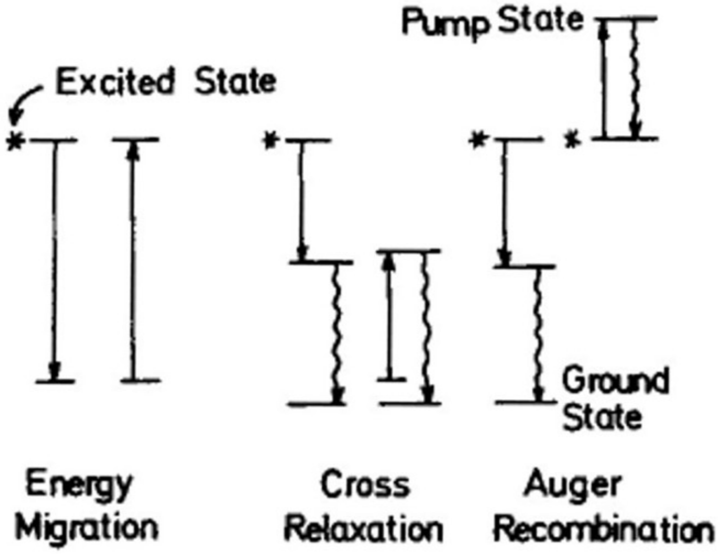

Figure 5.9: Schematic of the three mechanisms for concentration quenching. *Source: H.G. Danielmeyer, M. Blätte, and P. Balmer, Appl. Phys. 1 (1973) 272.*

potential of the individual, isolated ions [21]. On average there are about ten Nd^{3+} ion nearest-neighbors for each Nd^{3+} ion for 1at.% Nd^{3+} ion doping making the potential for pairing quite high [62]. This is also evidenced by the observation that the fluorescence lifetime decreases dramatically when the Nd^{3+} ion concentration exceeds 1.0at.% [35,45,62]. However, concentration quenching can be observed at doping levels less than 1.0at.%, but it has not been observed at levels of less than 0.3at.% [22,67].

Non-radiative transitions can be a significant problem in Nd:YAG laser crystals. Because YAG is a hard crystal, high-energy phonons help cascade energy non-radiatively with almost perfect efficiency so that no radiative leakage can be seen—as long as the excitation is below the high-energy metastable states such as the $^2P_{3/2}$ and $^2P_{1/2}$ states [21]. Nd:YAG non-radiative processes occur across energy gaps of about $10^3 cm^{-1}$ that separate pump levels above the $^4F_{3/2}$ metastable level [68]. As mentioned before, these non-radiative relaxations contribute to heat generation within the crystal. The contribution to heat generation from these relaxations can be measured by tuning a laser to an absorption line in Nd:YAG and noting that the heating is detectable by the sum of the thermal expansion effects and thermal-optic coefficient [68]. Also, the fraction of nonradiative sites can be derived from the fractional thermal loading, η_h, by the relation:

$$\eta_h = 1 - \eta_p \left[(1 - \eta_l) \eta_r \left({}^{\lambda_p}\!\!\diagup_{\lambda_f} \right) + \eta_l \left({}^{\lambda_p}\!\!\diagup_{\lambda_l} \right) \right] \tag{5.15}$$

where η_p is the pumping quantum efficiency, η_r is the radiative (upper-level) quantum efficiency, η_l is the fraction of ions excited to the upper metastable-level that are extracted by stimulated emission, λ_p is the pumping wavelength, λ_f is the average fluorescence wavelength, and λ_l is the stimulated emission wavelength [64]. In addition to knowing the amount of non-radiative sites, it is of value to calculate the generated heat power, P_h, inside the crystal due to non-radiative sites which can be accomplished through the relation:

$$P_h = \frac{(1 - \eta_h) n_2 V h \upsilon f T}{\tau} \tag{5.16}$$

where n_2 is the population density of the upper-laser level, V is the irradiated volume of the rod, $h\nu$ is the average energy of the emitted photons, f is the repetition rate of the pumping, T is the pulse duration of the laser, τ is the lifetime of the excited Nd^{3+} ions, and η_h is the fractional thermal loading term [57].

Non-radiative processes can be both intrinsic and extrinsic to the crystal. Figure 5.10 is a schematic showing a few of the intrinsic and extrinsic processes in Nd:YAG crystals. As can be seen from the figure, extrinsic processes involve some sort of impurity extrinsic to the Nd:YAG crystal which can be eliminated with proper and careful growth conditions while intrinsic processes can be present even in properly-grown crystal. Some of the extrinsic processes are discussed in greater detail further in this section. There are several other non-radiative processes that can occur in solid-state laser crystals and are shown in figure 5.11. One example is known as radiative reabsorption in which an ion is excited by photon absorption and another photon is emitted through radiative decay which, in turn, is then absorbed by another ion [21]. In addition, if the photon incident on an ion in the crystal is energetic enough, photoconductivity and subsequent exciton migration can occur even in wide band gap materials. Most of these processes occur very quickly in the crystal [21]. Upconversion can also occur in Nd:YAG, and at higher pump intensities, more upconversion processes are activated which can involve the $^4G_{5/2}$, $^4G_{7/2}$, and $^4G_{9/2}$ energy levels [63].

Another important process in Nd:YAG is two-photon absorption and its variant, excited-state absorption (ESA), both of which can be seen schematically in figure 5.12. In two-photon absorption, a virtual, intermediate state, seen on the left-side diagram in figure 5.12, is used instead of a real intermediate state for completing the transition, as seen in the middle diagram in the figure [21]. With a two-photon excitation below 400nm, a direct excitation from the valence band to the conduction band is possible [57]. In this case, the released electrons can relax either to the regular lattice, to impurity ions, and/or to other traps [57]. However, due to the ultraviolet-radiation filtering of the flow tube, this transition is extremely unlikely to occur during laser operation. In ESA, excitation occurs to a metastable state where the electron partially relaxes and then is excited again to a higher energy state. In ESA, the pump absorption transitions take place from the lasing metastable state or from any excited level where relaxation to the metastable state normally occurs [21]. It is this ESA phenomenon that prevents Ce:YAG from being a good laser material [65]. ESA generates heat in the crystal, which results in the decrease of pumping efficiency [21,69].

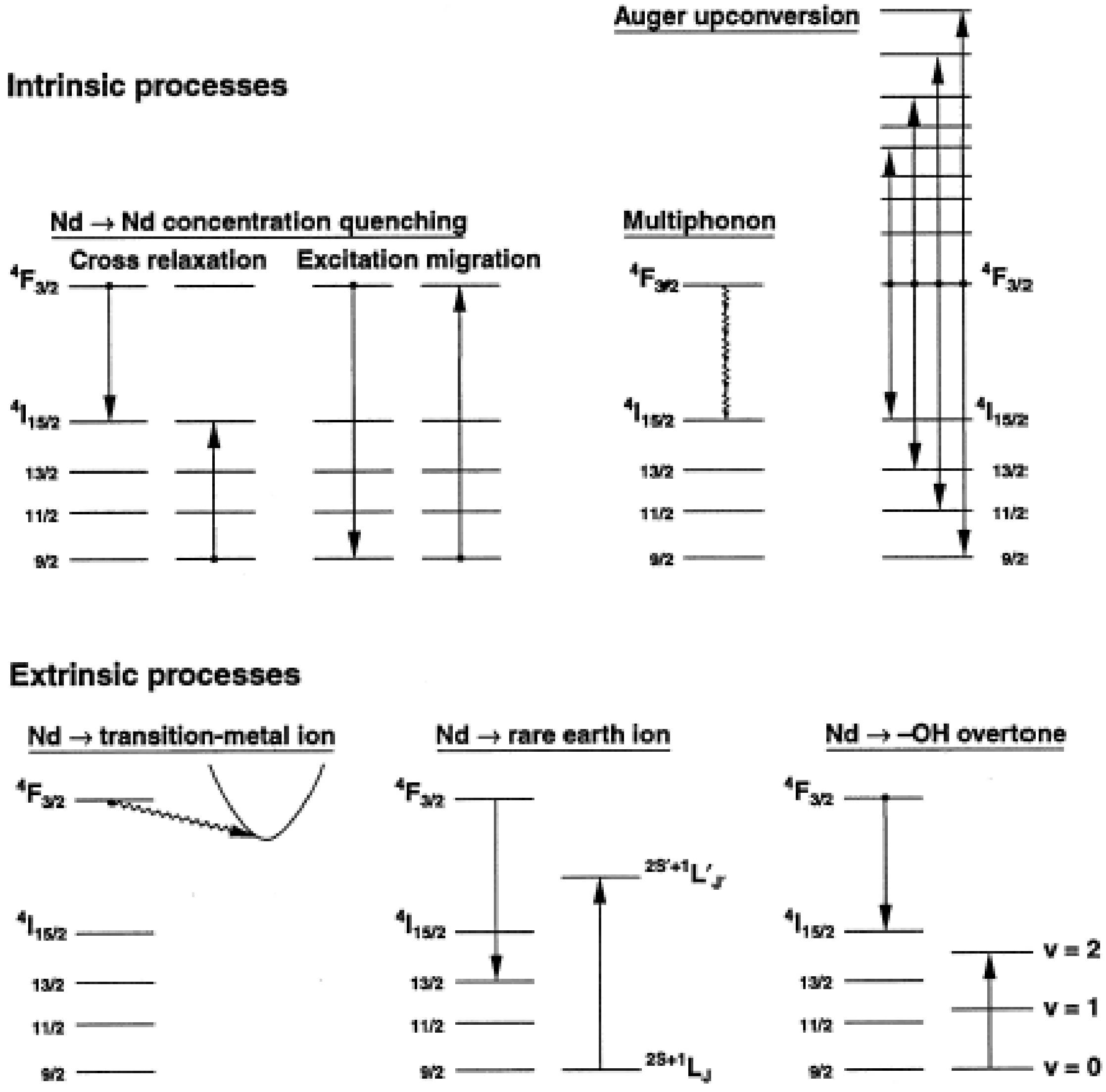

Figure 5.10: Some of the non-radiative processes found in Nd:YAG crystals. *Source: J.H. Campbell and T.I. Suratwala, J. Non-Cryst. Solids 263-264 (2000) 326.*

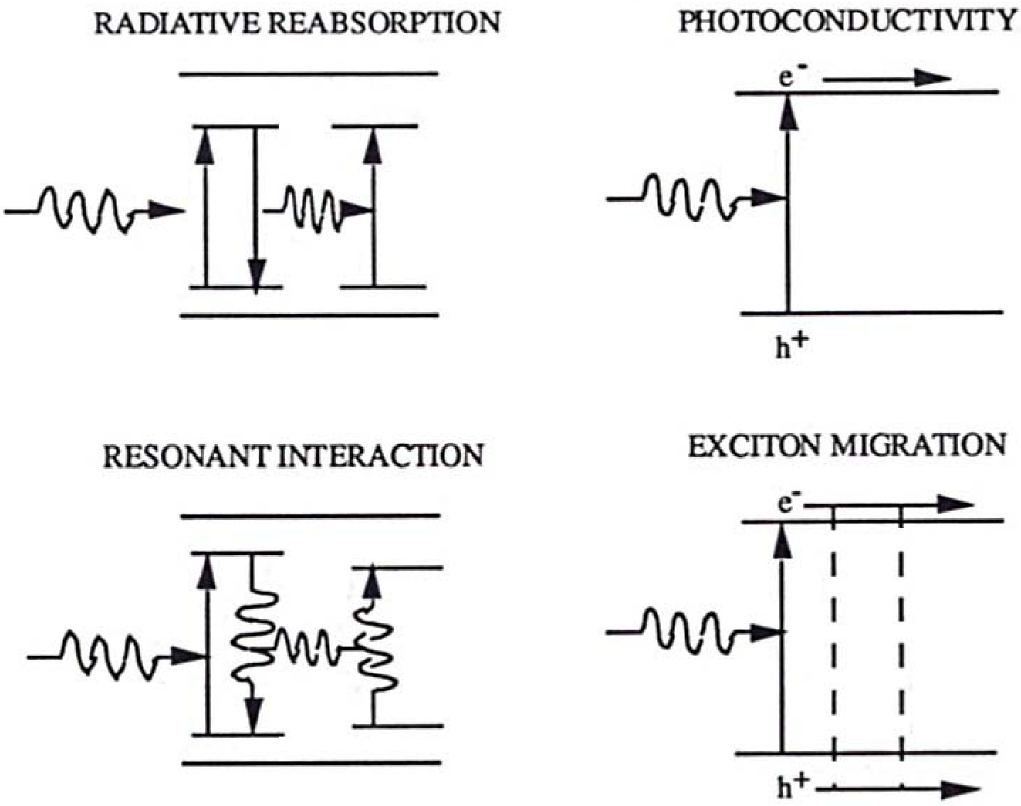

Figure 5.11: Several non-radiative processes that can occur in solid-state laser media. *Source: R.C. Powell, Physics of Solid-State Laser Materials. Springer-Verlag, New York, 1998, p. 176.*

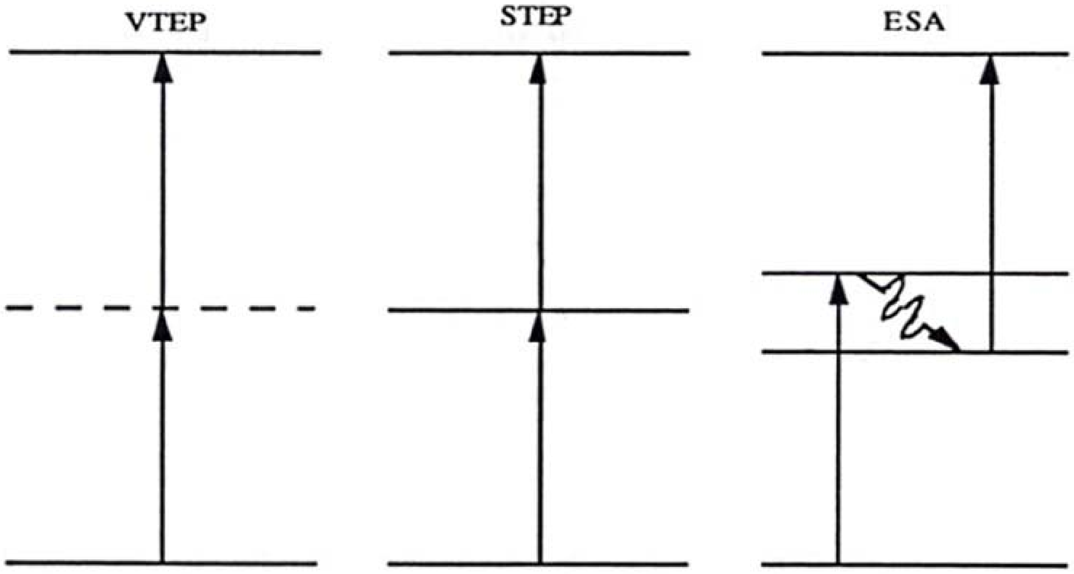

Figure 5.12: Diagram of excited-state absorption (ESA). *Source: R.C. Powell, Physics of Solid-State Laser Materials. Springer-Verlag, New York, 1998, p. 111.*

Most of the non-radiative processes that have been described rely on phonon generation which compensates for energy differences that occur during these processes [63,65]. Phonons result from local crystal-field modulation by ligand vibration which causes an energy-level broadening and a spread of the electron transition frequencies [66]. Phonon emission results in both a reduction in the lifetime and luminescence quantum yield [66]. Because of the high energy of phonons in YAG (up to energies of about 850cm^{-1}), effective electron-phonon interaction takes place between closely-spaced energy levels which can result in a significant amount of heat generated in the crystal [63,68].

While most of these non-radiative effects can be deleterious to laser performance, their role is seen diminutively as careful growth and choice of laser-operating conditions limit its affect on laser output power. However, extrinsic processes such as Nd^{3+}-transition-metal ion energy exchange are very relevant to limiting laser power loss in grown crystal. This will be discussed further in another section.

5.6.2 Stress and Strain Issues in Nd:YAG

There are two major categories of stress/strain in Nd:YAG—intrinsic stress from the growth process and extrinsic stress from laser operation. The first part of this subsection discusses intrinsic stresses that arise as a result of the growth process, while the second part of this subsection discusses stresses that are the result of thermal gradients generated during laser operation.

The most common imperfections in the YAG structure include inclusions, dislocations, striations, and facet strain which create localized stresses and optical anisotropy through the stress-optic effect [46]. These imperfections are due to the fact that during the growth of the crystal, it is inevitable that impurity atoms will be introduced into the lattice creating elastic strains within the crystal because of their differing ionic radius size [70]. To relieve the impurity-related stresses in YAG, dislocations are created [70]. In fact, dislocations can be generated at any point in the crystal where a large amount of strain is present [46]. Normally, dislocations tend to propagate normal to the crystal/melt interface; hence their effect depends to some extent on the shape of that interface [46]. Because dislocations travel along the lowest energy path through the crystal, they can become trapped at inclusions, grain boundaries, and/or other defects in the crystal [71]. Many impurities and defects tend to congregate in the grain-boundary region in a crystal due to the fact that fewer bonds are broken because of the presence of voids as well as the fact that bonds that are present in these regions are strained and thus easily broken [72]. This is evidenced by the observation that dislocations in transparent solids may be revealed by precipitation decoration on the dislocation line [73].

Striations also occur from strain in the boule caused by the segregation of gaseous impurities absorbed into the crystal during growth [74]. These striations allow impurities to congregate along them forming rather large inclusions that are roughly 0.5-1.0mm in diameter, according to one study [74]. Striations can represent the history of the crystal's growth and can give information about the change in the shape of the crystal/melt interface during the growth process [74]. Figure 5.13 and figure 5.14 are photographs of Nd:YAG boules under cross-polarization showing gaseous striations coming from their boule cores. Striations in a boule can be minimized through the use of a congruently-melting crystal stoichiometry [46].

A significant source of stress/strain in the boule is from the introduction of a dopant to the lattice. The difference in size between a dopant atom and the solvent atom produces a center of elastic distortion in the lattice, as was mentioned earlier [73]. This strain can degrade the optical quality of the crystal [8]. For Nd:YAG, Nd^{3+} ions have a larger ionic radius by 0.008Å in comparison to Y^{3+} ions [16]. The mechanical strain-energy associated with this difference, ΔG_{strain}, can be calculated by the relation:

$$\Delta G_{strain} = 4\pi E N_A \left[\frac{r_0}{2}(r_i - r_0)^2 + \frac{1}{3}(r_i - r_0)^3 \right] \tag{5.17}$$

where E is the elastic modulus, N_A is Avogadro's number, r_0 is the ionic radius of Y^{3+} ion, and r_0 is the ionic radius of the Nd^{3+} ion [16]. Moreover, Nd^{3+} ions do not substitute homogeneously throughout the lattice. In some areas of the boule, mainly in the central part known as the core, the dopant concentration can be as much as twice that of the outer portions of the boule, and Nd^{3+} ion inclusions can be found [34,40,47]. It may be this inhomogeneity in the substitution that makes Nd:YAG difficult to dope over 1.0at.% [34].

While intrinsic stress/strain is a major issue concerning the performance of laser crystals, extrinsic stress/strain can also lead to the reduction of laser output power. Thermal stresses during laser operation and cooling can provide a significant amount of stress within the laser rod. As was mentioned earlier, the center of the rod is under compression, and the surface of the rod is in tension, and the maximum allowable stress can be calculated [53,54]. To reduce the influence of thermal stress on the rod, the volume of the laser rod must be minimized by reducing the diameter of the rod [75]. This allows for more effective heat transmission from the center of the crystal to the cooling fluid surrounding the crystal.

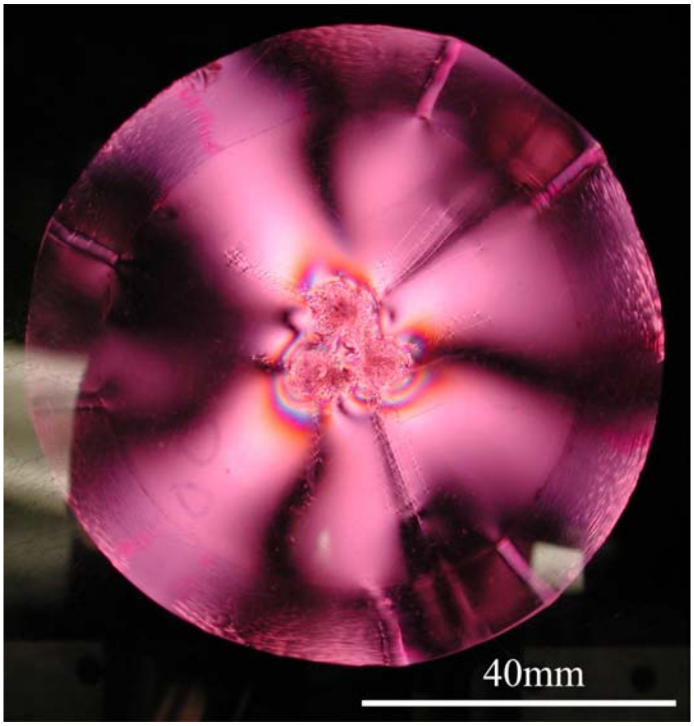

Figure 5.13: Cross-polarization photograph of a few striations observed in a Nd:YAG boule.

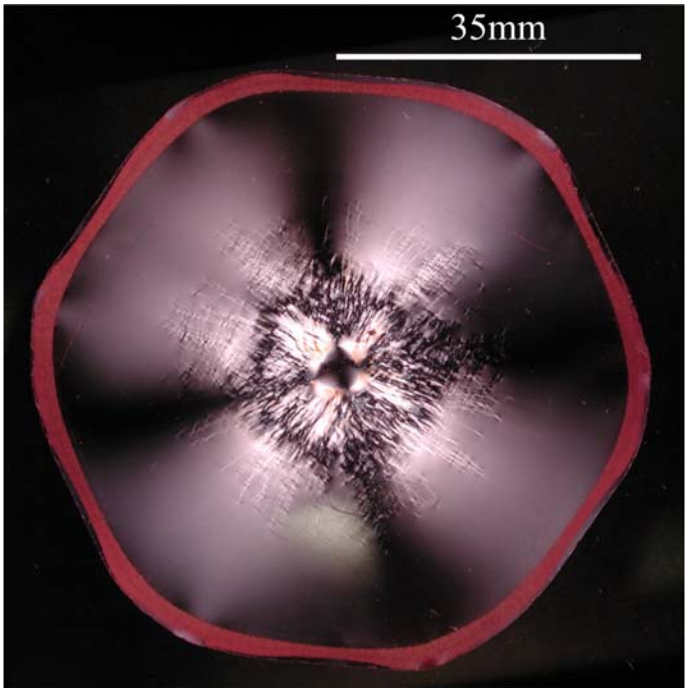

Figure 5.14: Cross-polarization photograph of many striations observed in a Nd:YAG boule.

5.6.3 Color Centers in Nd:YAG

The term color center is an ambiguous term used to describe defects in transparent crystals. Its meaning covers a wide spectrum of defects from vacancies, impurities, and other simple point defects to intricate complexes of point defects. Some color centers arise during the growth of the crystal, and some may be introduced to the crystal by irradiation or heating [76]. Color centers are generally divided into two categories, stable color centers and transient color centers [77]. Stable color centers can have a lifetime of a few seconds to many years, while transient color centers usually carry a lifetime of less than one second [77]. Even with varying lifetimes, the presence of color centers in a crystal is thermodynamically desirable since the free energy of the crystal, G, may be reduced by their presence which is given by the relation:

$$G = U - TS \tag{5.18}$$

where U is the internal energy of the crystal, T is the temperature of the crystal, and S is the entropy of the crystal [73].

Most insulators are transparent to visible light because of their wide band gap. However, impurity atoms and intrinsic lattice defects with localized energy levels that fall within the band gap may cause selective absorption in the visible region of the spectrum giving these defects the name color centers, as they appear to color the otherwise transparent crystal [73,78,79]. The intensity of this coloration is dependent upon color center concentration [79]. In non-stoichiometric crystals, color centers are rather prevalent, and many non-stoichiometric crystals such as YAG contain a built-in excess of color centers so that their color cannot be permanently removed without chemically altering them [78,80]. Color centers affect almost all structure-sensitive properties of solids including electrical resistivity, heat conductivity, diffusivity, elastic modulus, and magnetic and optical properties [81]. Color centers tend to add broad absorption bands with long tails on the longer wavelengths of the spectrum [77,78].

Impurity-ion color centers are usually associated with positively-charged ions such as Ca, Fe, Na, and Si and normally have concentrations below 10ppm [81]. Impurity-ion color centers can be substitutional or interstitial in the lattice, with the latter resulting in a large increase in both internal energy and configurational entropy [73]. These impurity ions influence the concentration of electrons in the crystal which affects the Fermi level; the donor ions promote a higher Fermi level and acceptor ions promote a lower Fermi level [82]. Because the charge transfer between the host and the impurity ion depends on the spatial overlap between the initial and final electronic states, intense metal-to-ligand charge transfer bands may appear in an ion's excited-state absorption spectrum even when no corresponding feature is observed in the ground-state absorption spectrum [83].

In addition to impurity-ion color centers, vacancy color centers are also prevalent in oxide laser crystals. In these color centers, an anion is removed and replaced by one or more free electrons [80,84]. Vacancies can act as donors if the number of unpaired electrons near the vacancy is smaller than half the number of valence electrons present near the same site in the perfect crystal, as the number of electrons that can be accepted is equal to the number needed to make the "shell" of the vacancy either completely full or completely empty [82]. In YAG, there can exist three types of cation vacancies and one type of anion vacancy which include the octahedral aluminum vacancy, the tetrahedral aluminum vacancy, the yttrium vacancy and the oxygen vacancy, and only the aluminum and oxygen vacancies and will cause a widening of the fundamental absorption edge [1,77]. However, with all these possible color-center combinations in YAG crystals, cation Frenkel defects are very unlikely to occur in any significant concentration, according to one study [1]. Also, cation vacancies may arise as charge compensating defects for impurities, although this has not been previously thought of as a significantly-prevalent defect in YAG crystals [1]. This topic will be discussed later in this chapter.

As mentioned earlier, color centers can be generated during crystal formation or by some sort of energetic process such as heating, irradiation, or plastic deformation [80]. Irradiation of laser crystals is of great importance as the process of pumping crystals such as Nd:YAG with arc lamps for long periods of time may lead to the formation of color centers. One such irradiation mechanism may be the recharging of as-grown defects leading to parasitic absorption of the pumping light [77]. Irradiation with ultraviolet light, known as solarization, often can diminish the crystal's optical and lasing properties since it creates stable and/or transient color centers that can lead to additional absorption bands in both the ultraviolet and visible spectral regions [33,85-87]. In YAG, solarizing with wavelengths of 200-500nm can produce color centers with absorptions having wavelengths larger than 360nm, effectively creating short-lived color centers [33,49,57,88,89]. The color centers produced by ultraviolet solarization can often absorb light at wavelengths greater than 500nm bringing about absorption loss at pumping centers resulting in the reduction of lasing efficiency [21,88,90]. However, these color centers can also create or enhance absorption peaks in the ultraviolet region as well. Xenon gas lamps have been shown to be capable of creating these ultraviolet-light-induced color centers [57,91]. These increased absorption peaks from solarization can lead to an increase of thermal loading on the crystal during laser operation [49,57].

In addition to ultraviolet-light solarization, other forms of high-energy irradiation can also produce color centers and have the same deleterious effect on laser performance [92]. Both neutron and gamma-ray irradiation are commonly performed on YAG. Neutron irradiation can color undoped YAG crystals from colorless to a pale yellow and can increase its absorption spectrum in the 200-700nm range, according to one study [93]. Further, gamma-ray irradiation can give rise to wide, complex additional absorption bands in the 200-900nm range which can reduce the lasing performance of Nd:YAG laser rods [68,94,95].

Figure 5.15 is a model of the band structure of YAG and the placement of color centers within the band gap. The energy location of the stable color centers in the band structure determines their characteristic absorption wavelengths and their ability to inhibit laser performance in the Nd:YAG laser rod.

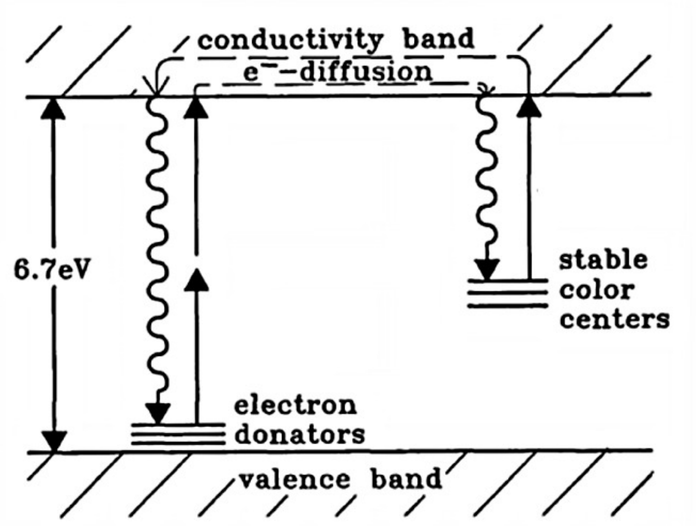

Figure 5.15: Model of color centers in YAG. *Source: G. Phillipps, and J. Vater, Appl. Opt. 32 (1993) 3214.*

5.6.3.1 The F-centers in Nd:YAG

Oxygen vacancies can be formed during crystal growth, especially in low oxygen-atmosphere pressures [96,97]. Increasing the concentration of oxygen vacancies increasingly changes YAG from p-type to n-type [96]. The generation of oxygen vacancies by this reducing atmosphere can be accomplished by the relation [98,99]:

$$O_O \longrightarrow V_O^{\bullet\bullet} + 2e' + \frac{1}{2}O_2$$

The anion vacancy is one of the most energetically-favorable defects in garnets since lattice disorder is most preferable in the oxygen sublattice positions [7,10]. Moreover, oxygen vacancies are the most mobile ionic defect in YAG [100]. The number of oxygen vacancies in YAG is dependent upon the number of divalent impurity ions as well as location, as the core region of the boule contains considerably more oxygen vacancies than elsewhere [98,99]. Oxygen vacancies come in several forms depending on their environment in the crystal, and the most important vacancies in regards to laser performance may be those that contain trapped electrons [30].

When a free electron encounters a vacancy, it becomes attracted to it because of the vacancy's positive charge. In fact, in order to obtain local charge neutrality, it may be necessary for electrons to be drawn to the positively-charged oxygen vacancies [73,78]. When this special defect, analogous to an inside out hydrogen atom, occurs, the defect is referred to as an F-center [17,73,80]. The "F" in F-center stands for Farbe, the German word for color [78,101]. The F-centers lie very near the bottom of the conduction band, and it is possible for trapped electrons in F-centers to be thermally excited to the conduction band [78]. The optical absorption of an F-center arises from an electric dipole transition to a bound excited state of the center [101]. The location of the absorption peaks corresponding to F-centers is largely dependent upon the type of F-center and, therefore, the number of trapped electrons by the vacancy [78]. The absorption bands from F-centers are most often found in the 200-500nm range [17,77,102]. In addition to absorption spectroscopy, F-centers, in one study, have been identified by electron paramagnetic resonance (EPR) techniques [78].

The various types of F-centers can be seen pictorially in figure 5.16. The first type of F-center is known as the F^+-center, which is a single electron in an anion vacancy absorption spectrum [103]. The F^+-center is semi-unstable at room temperature [77,86]. However, according to several studies performed at low temperature, the F^+-center absorbs at 258nm and at 353nm and has a luminescence peak at 400nm [90,104,105]. However, the validity of this claim is still unknown. This 400nm luminescence peak observed in these studies is thought to be more intense for crystals grown in reducing atmospheres and with melts consisting of excess yttria [104]. A second type of F-center is the F'-center, which is an anion vacancy with two trapped electrons, as can be seen in figure 5.16 [73,78,80,106]. Like the F^+-center, the F'-center is unstable at room temperature [73]. A low-temperature study indicates that the F'-center has a luminescence peak of 521nm [106]. A third type of F-center is known as the F^--center, which is an anion vacancy with three trapped electrons [105]. The F^--center is extremely unstable at room temperature but low-temperature measurement has shown that it may have absorption peaks at 360nm, 480nm, and 830nm [105]. Several other types of F-centers involve combinations of various F-center species. For example, the F_2-center is the combination of two nearest-neighbor F^+-centers, as can be seen in figure 5.16 [73]. The F_3-center is the combination of three nearest-neighbor F^+-centers, and so on [73]. The final modification of the F-center presented here is the F_A-center which results when a neighboring cation differs from the expected cation in the lattice as can also be observed in figure 5.16 [73]. While oxygen vacancies play an important role in laser output power, their direct affect on laser output power is thought to be only in conjunction with another type of defect which is explored in greater detail later. However, the role of oxygen vacancies in laser performance was studied.

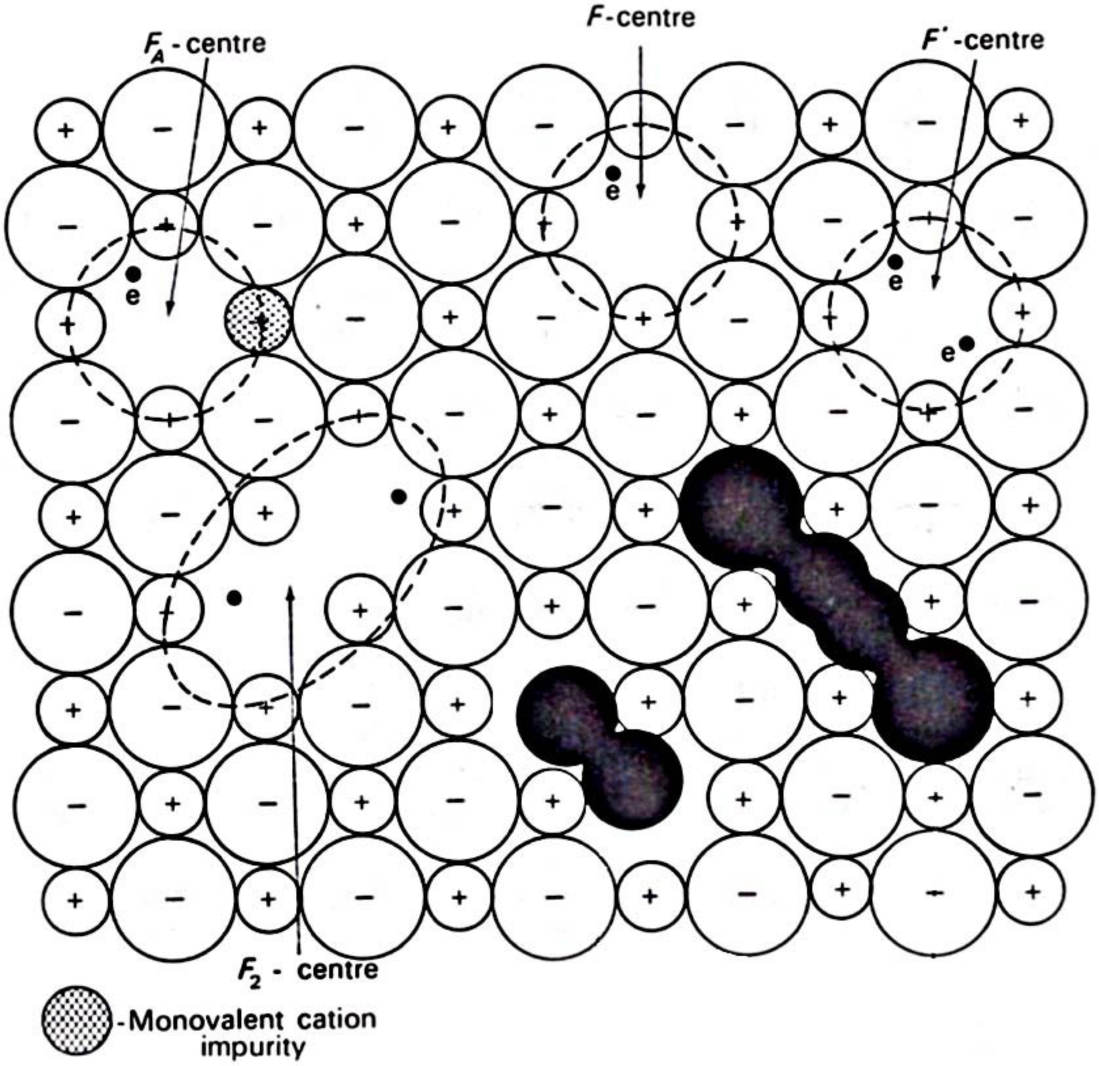

Figure 5.16: Common F-centers found in alkali halides. *Source: B. Henderson, Defects in Crystalline Solids. Crane, Russak & Company, Inc., New York, 1972, p. 71.*

5.6.3.2 The O_h^{--}-center in Nd:YAG

The O_h^{-}-center consists of a self-trapped hole located between two O^{2-} ions or near defects in the cation sublattice [78,80,95,107,108]. The O_h^{-}-center can be created using high-energy ultraviolet photons, solarization, which causes electron photo-ionization from the valence band to the conduction band [17,103,109]. A schematic for the model of the band-structure formation of the O_h^--center can be seen in figure 5.17. The O_h^--center is not completely stable at room temperature, and the defect can be removed by heating the crystal, according to several studies, to ~700K [17,77]. Absorption peaks arising from the O_h^--center in YAG are thought to be located in the region of 300-400nm [77,110,111]. Luminescence from the O_h^--center is thought to be found in the 400-500nm region [110].

The O_h^--center is an important defect, but its role in diminishing laser output power has been lessened with proper growth and post-growth heat treatment. Therefore, it is not a primary candidate for the main-loss mechanism observed in Nd:YAG.

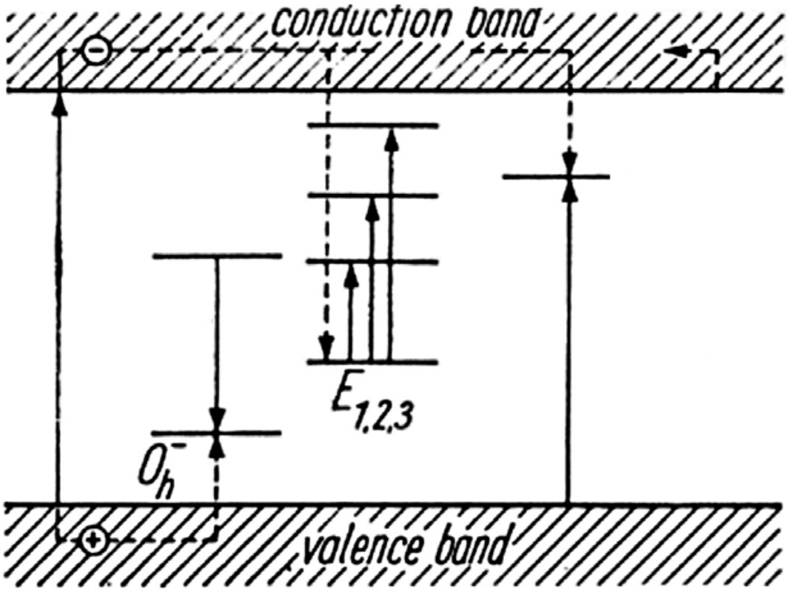

Figure 5.17: Model for the band structure formation of the O_h^--center. *Source: K. Mori, Phys. Status Solidi A 42 (1977) 383.*

5.6.3.3 Exciton Defects in Nd:YAG

Another defect in Nd:YAG is the presence of excitons which can rob pump light and degrade laser performance. An exciton is an electron-hole pair that mutually interact very strongly near the location where the pair were formed [21,73,78,80]. Excitons are created by energetic photons, and they can migrate a distance of roughly one micrometer through the YAG crystal before recombination occurs [78,112]. In Nd:YAG, free electrons can become bound excitons at defects such as the O_h^--center, and these excitons can transfer energy to or receive energy from a nearby Nd^{3+} ion [112]. Very weak exciton absorption peaks can be found in YAG near the fundamental absorption edge at roughly 180nm [73,78,113]. The exciton is not currently considered a major loss mechanism in Nd:YAG.

5.6.3.4 Hydroxyl Defects in Nd:YAG

Hydroxyl defects are a major issue in the growth of Nd:YAG boules. Their concentration in YAG is usually of the order of 10^{20} per cubic centimeter of crystal [68]. Hydroxyl peaks in YAG can be formed by the incorporation of hydrogen in the form of H^+ or $(OH)^-$ into the lattice as a charge compensator to maintain charge neutrality in the crystal [114]. The hydroxyl peak may also be formed by utilizing a coordinated, reducible cation impurity, Me, through the following reaction:

$$Me^{n}{}_{(c)} + H^{+}{}_{(i)} + e^{-}{}_{(i)} + O^{2-}{}_{(c)} \rightarrow Me^{n-1}{}_{(c)} + OH^{-}{}_{(c)}$$

where the subscript (c) indicates that the constituent is coordinated in the lattice [68,114]. Another hydroxyl complex, $(OHO)^{3-}$, can be formed as well in YAG through the reaction [114]:

$$H^{+}{}_{(i)} + 2O^{2-} \rightarrow (OHO)^{3-}{}_{(c)}$$

Hydroxyl peaks have a tendency to be found in areas of cation non-stoichiometry as they aid in charge compensation [114]. Hydrogen-bonding is also prevalent in perturbed lattice sites in the Al^{3+}-octahedral and Y^{3+}-dodecahedral positions [68,114]. Hydrogen-bonding to the dodecahedral sites is very important as hydroxyl ions can couple to Nd^{3+} ions, which may result in the lowering of lasing efficiency [68]. Hydroxyl groups of water molecules that are in the Nd:YAG lattice can contribute considerably to the non-radiative de-excitation of the Nd^{3+} ions and can promote luminescence quenching even in lowly-doped Nd:YAG crystals [66]. In addition, the hydroxyl vibration frequency of 3,000cm^{-1} is relatively high in comparison to those of the ligands in the YAG lattice, indicating that hydroxyl defects in Nd:YAG may inhibit the lasing process [66]. In addition to the presence of the hydroxyl itself contributing to lasing loss, hydroxyl impurities can also lead to oxidation of the crucible metal resulting in heightened crucible-material impurity concentration within the grown crystal. Figure 5.18 is a plot of the absorption of hydroxyl impurities in a Nd:YAG boule slice. As can be seen from the figure, the signal due to hydroxyl impurities within the grown boule is rather low in intensity which could indicate low concentration of hydroxyl impurities within the crystal possibly eliminating hydroxyl impurities as the main-loss mechanism candidate observed in some Nd:YAG laser rods.

Elimination of the hydroxyl group may be possible through internal oxidation via a surface reaction resulting in the outgassing of water vapor from the crystal by the reaction:

$$2(OH)^{-}_{(c)} \rightarrow O^{2-}_{(c)} + \square_{(c)} + H_2O_{(g)}$$

where $\square$ indicates an anion vacancy [114]. However, sufficient care should be been taken to eliminate water from the raw materials before beginning crystal growth, which should help eliminate the problem of hydroxyl impurities within the grown crystal. In addition, the high furnace temperature helps eliminate any water vapor from the furnace chamber as well as from the melt materials. If possible, the powders should be hot-loaded into the crucible which should also be heated to avoid water from re-absorbing back into the powders as they are loaded into the crucible.

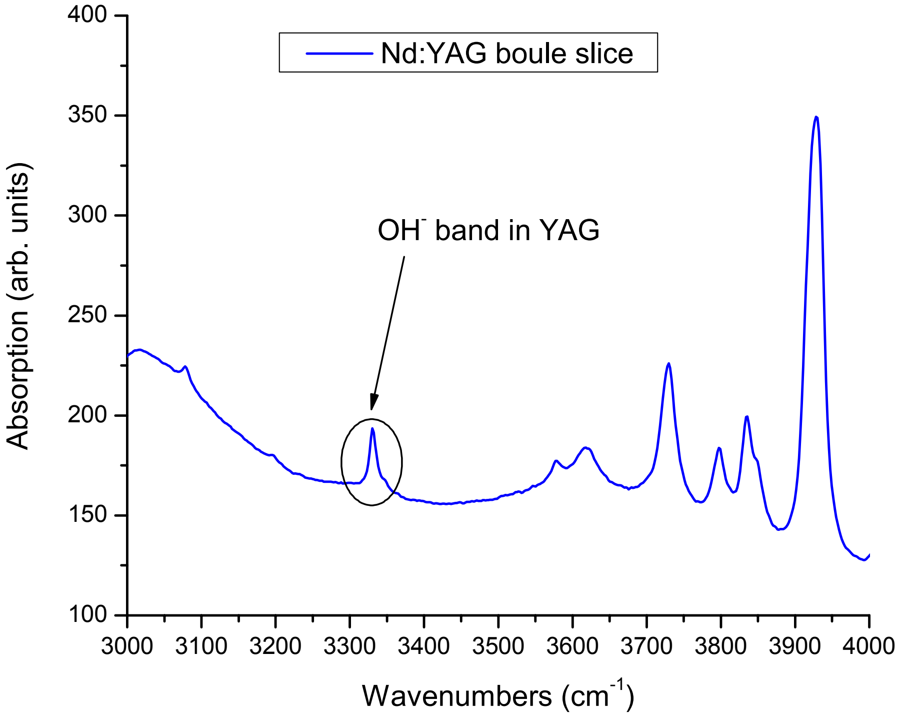

Figure 5.18: The OH^- band in Nd:YAG. *Source: Data for plot courtesy of Slade Jokela.*

5.6.3.5 Chromium Impurities in Nd:YAG

Chromium impurities are also very common in YAG, and, in fact, chromium is often added as an optical sensitizer for Nd:YAG to make the laser up to twice more efficient [8,14,21]. However, there is still an intrinsic energy waste due to this energy transfer because of the difference in energy between the Cr^{3+}-ion absorption bands and the laser emission energy level of Nd:YAG [51].

Chromium ions can enter the YAG lattice in a variety of valence states, from Cr^{2+} to Cr^{4+}, but the most commonly observed valence state is Cr^{3+} [115]. Cr^{3+} ions prefer the octahedral aluminum site which give the chromium ions their largest field stabilization energy among all the possible lattice sites [7,15,115-118]. However, Cr^{3+} ions can also go into the tetrahedral sites as well. According to several studies, Cr^{3+} ions in YAG have absorption bands of 285nm, 310nm, 335nm, 421nm, 446nm, 590nm, and 625nm which give the doped crystal a brownish coloration [14,15,76,115,118,119]. Cr^{4+} ions can also be found in YAG resulting in broad absorption peaks centered at 290nm, 480nm, 640nm, 960nm, and 1,100nm [14,15,115,120]. Although less commonly found in YAG, Cr^{2+} ions have an absorption band around 310nm [76]. The luminescence of chromium in YAG also depends on the valence state with Cr^{3+} ions fluorescing in the 650-850nm wavelength range and Cr^{4+} ions fluorescing in the 1.2-1.6μm wavelength range [14,121-123]. Since Cr^{3+} ions do not require charge compensation, it is the preferable chromium species in YAG. Annealing in a reducing environment such as argon can help reduce Cr^{4+} ions to Cr^{3+} ions.

Because chromium is often used as a co-dopant for Nd:YAG, it is not considered to be a candidate for the source of the loss observed in Nd:YAG.

5.6.3.6 Cerium Impurities in Nd:YAG

Cerium-doped YAG has been used as a solid-state scintillator material with some success over the past few years. For some time it was thought that co-doping Nd:YAG with cerium would make the crystals less sensitive to irradiation and would help with Nd^{3+} ion energy transfer similar to that observed in chromium co-doped Nd:YAG [92]. However, co-doping is often difficult due to the added stress of incorporating the relatively large cerium ions (ionic radius of 1.18Å compared to 1.12 Å for Nd^{3+} ions) as well as the very small segregation coefficient of 0.082 [74,124]. However, new studies are being carried out by industry in an attempt to revitalize (Nd,Ce):YAG.

Cerium can also be a very common impurity ion found in YAG as many times the same crucible used to grow Ce:YAG is mistakenly used for the growth of Nd:YAG. Cerium is an n-type dopant in YAG as the cerium 4f donor-state lies about 1.5eV above the valence band and the empty cerium 5d state is about 2.5eV higher [28,30]. However, in an oxidized crystal, cerium may appear in its 4+ valence state making the Fermi energy fall below the cerium band creating a p-type environment in the crystal [30]. Figure 5.19 is a simplistic schematic showing the energy levels of cerium in YAG. Absorption peaks for cerium in YAG are due to the $4f^1 \rightarrow 5d^1$ transitions and are located at 340nm and 455nm, as can be seen in figure 5.20 [125,126]. Luminescence of cerium in YAG, achieved by pumping with blue light, gives rise to the 550nm peak which can be seen in figure 5.21 [30,125]. As can be seen in figure 5.21, the luminescence peak is not symmetric. This is due to self-absorption of the emission on the shorter wavelength side of the spectrum by the 455nm absorption peak [126]. The appearance of Ce^{4+} ions in YAG increases the ultraviolet absorption below the 350nm wavelength region [92,127]. The appearance of Ce^{4+} ions in YAG is usually associated with thermal processing. During high-temperature annealing in an oxidizing atmosphere, Ce^{3+} ions can become Ce^{4+} ions [92,127].

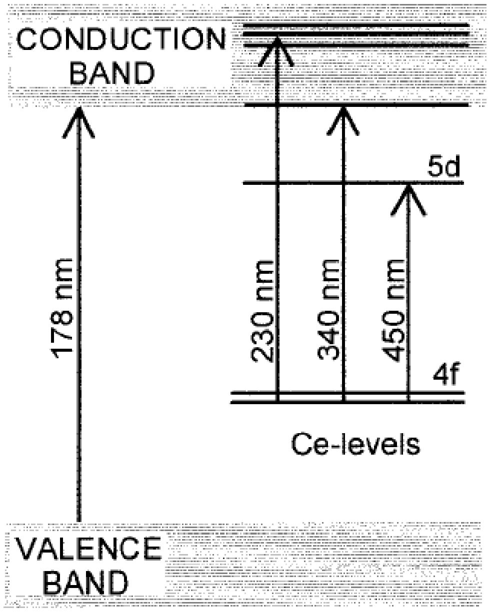

Figure 5.19: Simple band structure for Ce:YAG. *Source: D.S. Hamilton, S.K. Gayen, G.J. Pogatshnik, R.D. Ghen, and W.J. Miniscalco, Phys. Rev. B 39 (1989) 8813.*

This can change the absorption spectrum as is evident in figure 5.22. As Ce^{3+} ions oxidize to Ce^{4+} ions, the intensity of the 550nm peak, resulting from Ce^{3+} ions, decreases. Figure 5.23 shows the reduction of luminescence intensity of a Ce:YAG sample where part of the crystal has been annealed in an oxidizing environment.

Ce^{4+} ions are not a desirable impurity in YAG as they require charge compensation to maintain charge neutrality. Ce^{4+} ions can act as a hole traps and have a role in the production of the O_h^--center [128,129]. In addition, exciton complexes can arise as a result of Ce^{4+} ion impurities coupling with oxygen vacancies [130].

Because cerium is not found naturally in YAG, its unintentional incorporation into grown Nd:YAG boules is most likely the result of cerium ions left over in the crucible after a Ce:YAG growth. Simply using an unused crucible for each growth may prevent this contamination. However, it is thought that cerium can be used as a co-dopant for Nd:YAG, so the presence of cerium-impurity ions can be considered beneficial to the laser performance of Nd:YAG laser rods.

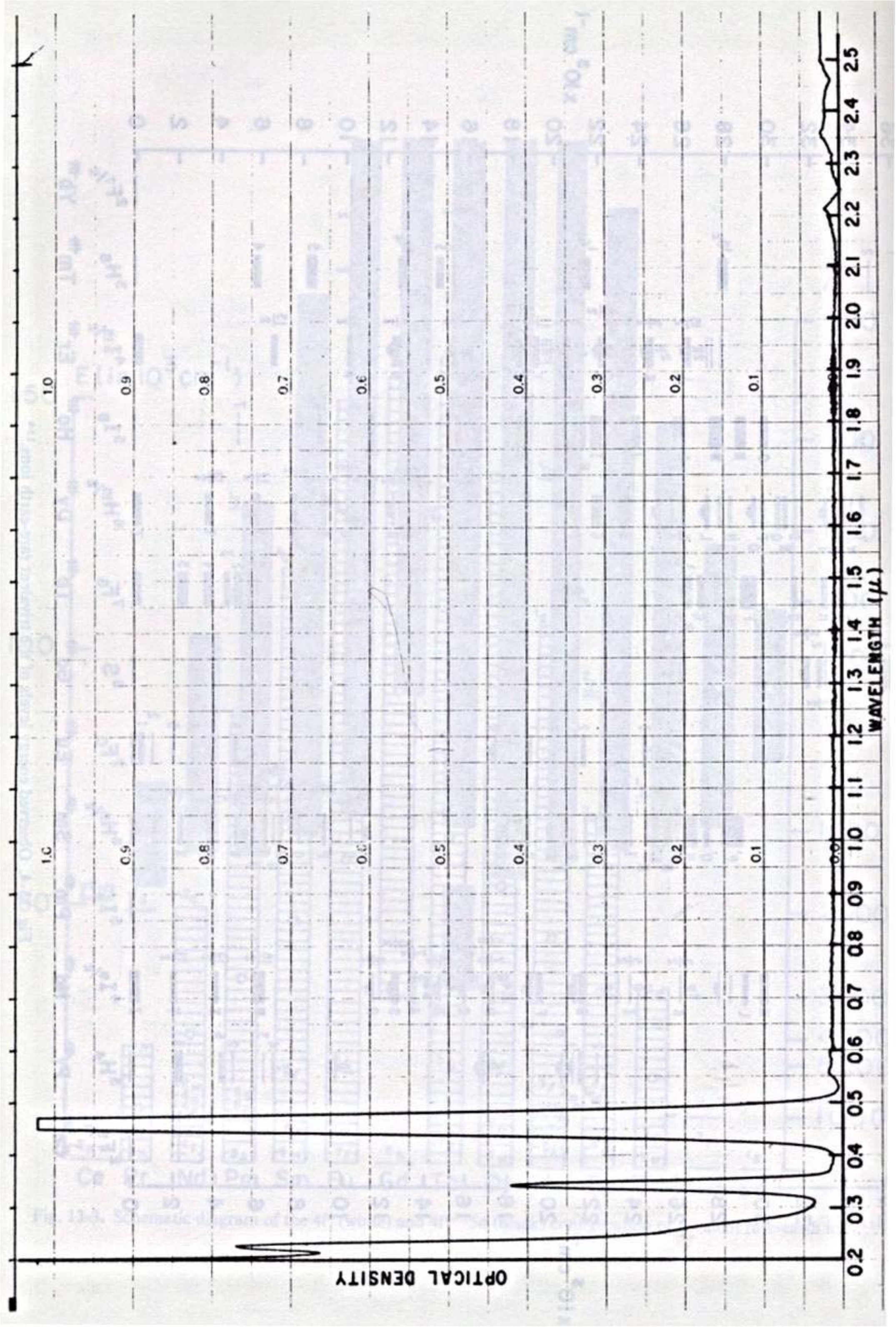

Figure 5.20: Absorption plot of Ce:YAG. *Source: R.J. Pressley, editor, CRC Handbook of Laser Technology. CRC Press, Cleveland, 1971, p. 398.*

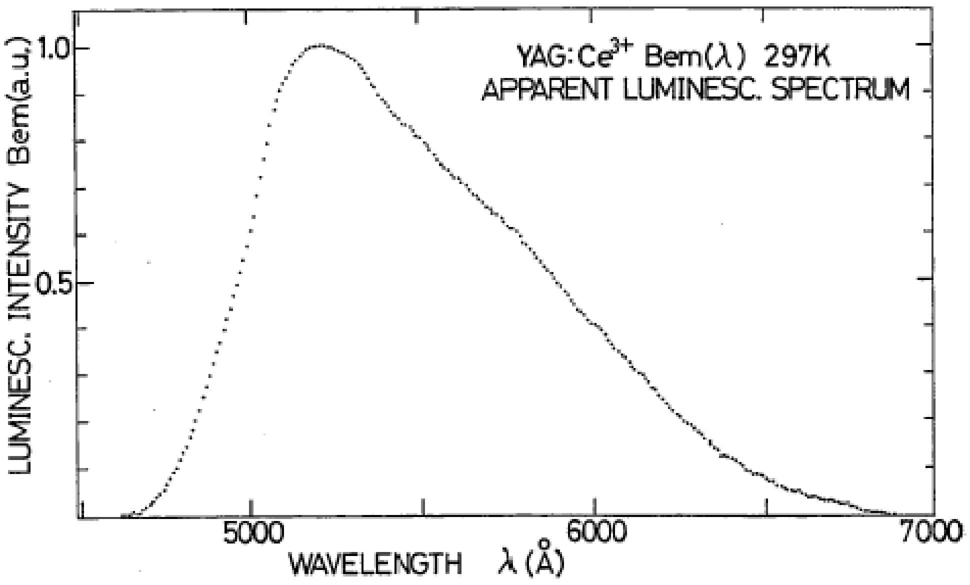

Figure 5.21: Luminescence spectrum of Ce:YAG showing 550nm emission peak. *Source: T. Tomiki, H. Akamine, M. Gushiken, Y. Kinjoh, M. Miyazato, T. Miyazato, N. Toyohawa, M. Hiraoka, N. Hirata, Y. Ganaha, and T. Futemma, J. Phys. Soc. Jpn. 60 (1991) 2441.*

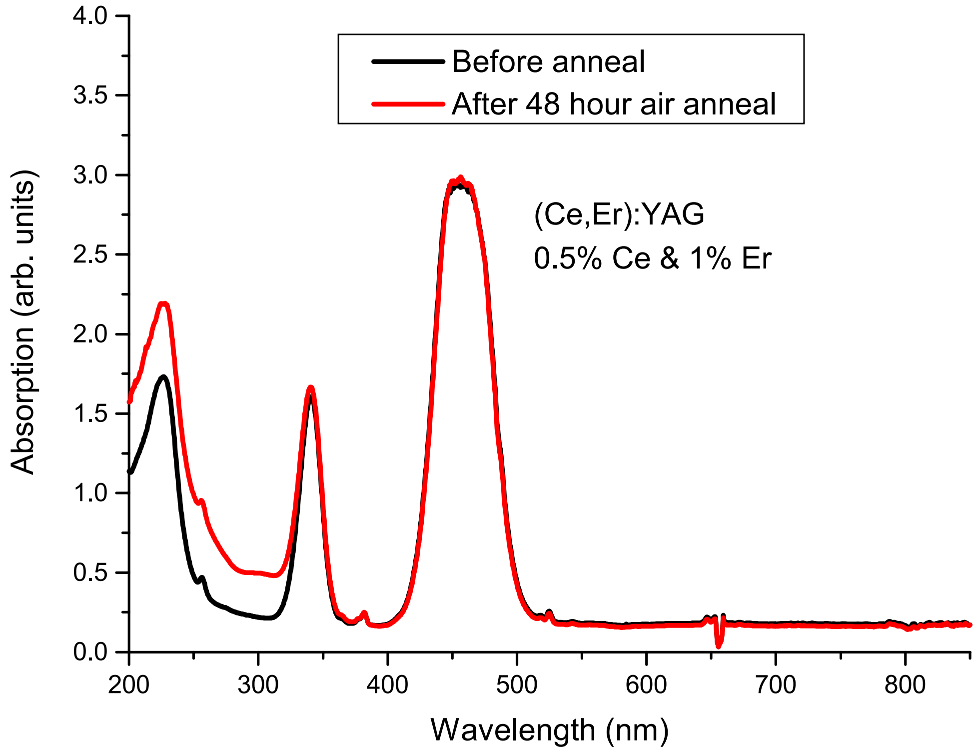

Figure 5.22: Absorption plot of a (Ce,Er):YAG sample before and after air anneal. *Source: Graph courtesy of Denys Solodovnikov.*

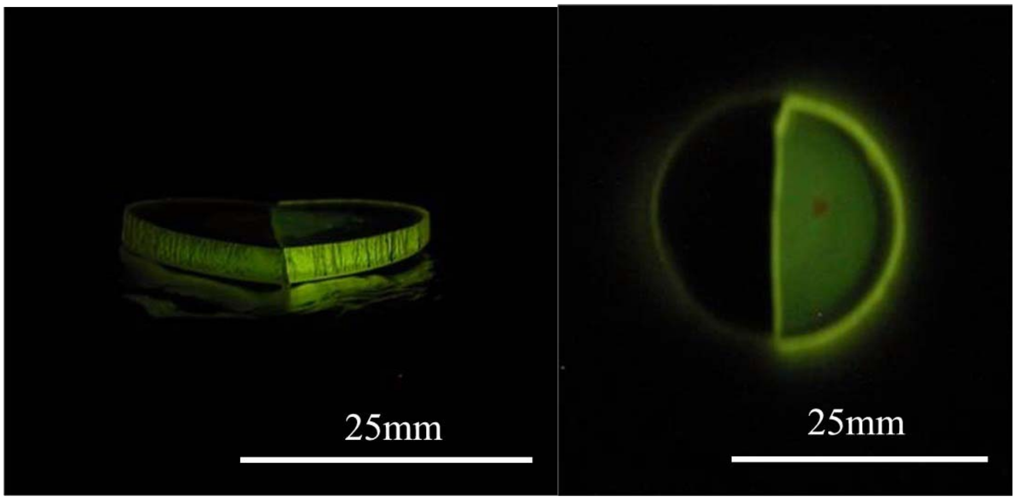

Figure 5.23: Reduction in Ce:YAG luminescence intensity as a result of oxidation anneal.

5.6.3.7 Erbium Impurities in Nd:YAG

Erbium is another dopant that has been added to Nd:YAG in part to help with charge transfer as well as to help reduce stress in the boule, the result of the previously-mentioned ionic radius size difference between Y^{3+} ions and the larger Nd^{3+} dopant ions. Er^{3+} ions have an ionic radius of 1.004Å which is smaller than that of the Y^{3+} ions, which can help reduce the stress caused by the incorporation of Nd^{3+} ions into the YAG lattice [131]. Because of this reduction in stress, it is thought that co-doping Nd:YAG with erbium would allow for higher Nd^{3+}-ion doping levels, but this has not yet proven to be the case. It has also been suspected that co-doping with erbium may reduce the size of the core-faceting structure in grown boules, although this has yet to be substantiated.

Er:YAG has a complicated absorption spectrum as can be seen in figure 5.24. Some of its absorption peaks overlap those of Nd^{3+} ions. Er^{3+} ions provide several absorption peaks in the ultraviolet region of Nd:YAG's absorption spectrum, so care must be taken when assigning the source of absorptions seen in this region. Also, Er^{3+} ions can fluoresce near the 550nm wavelength region, leading to possible misidentification of erbium impurities with cerium impurities. However, the distinction lies in the excitation wavelength. Erbium requires ultraviolet-energy excitation to give rise to the 550nm fluorescence while cerium's 550nm fluorescence can be excited using ordinary blue light.

Erbium is often used as a co-dopant for Nd:YAG, and its incorporation into YAG is usually purposely done. Erbium, therefore, is not considered a candidate for the source of the loss mechanism observed in Nd:YAG.

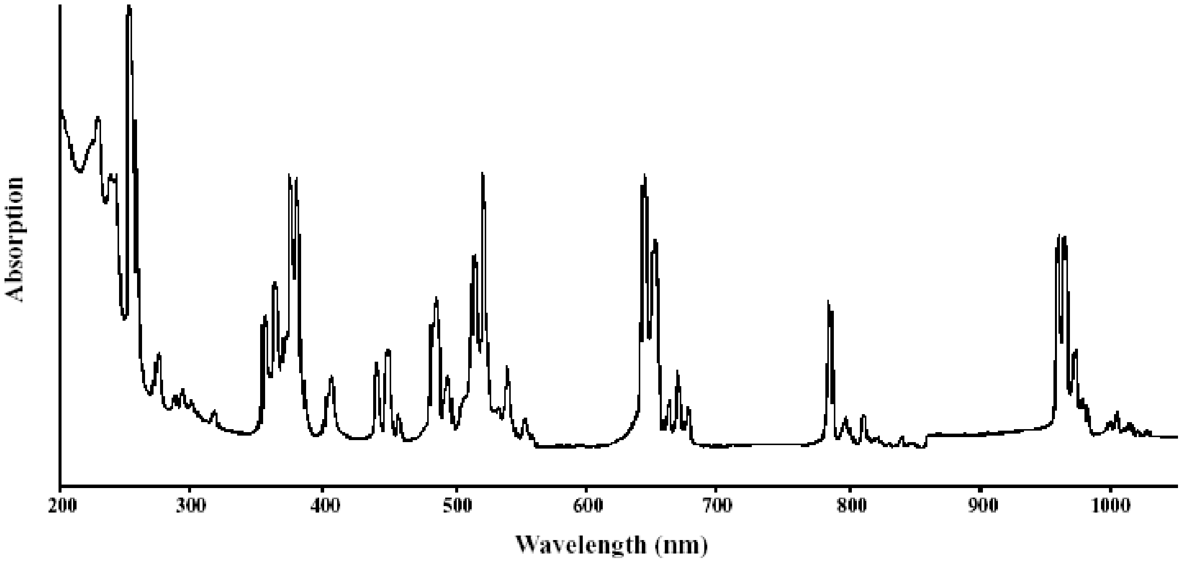

Figure 5.24: Absorption spectrum of Er:YAG. *Source: H. Xu, Z. Dai, and Z. Jiang, Eur. Phys. J. D 17 (2001) 80.*

5.6.3.8 The Antisite Defect in Nd:YAG

There are several disorders possible in YAG, both Schottky-like and Frenkel-like. Some of the Schottky-like disorders include the reactions noted in table 5.2. Some of the Frenkel-like disorders include the reactions noted in table 5.3. The antisite disorders in YAG can be seen in table 5.4. Schottky-like disorders such as those found in table 5.2 are more energetically favorable than Frenkel-like disorders such as those found in table 5.3 [100]. However, the antisite disorders found in table 5.4 are much more energetically favorable than both the Schottky-like and Frenkel-like disorders possibly indicating that, in YAG, substitutional defects form much more readily than incorporation-associated defects [1,10,100]. The antisite substitution of $Y_{Al(oct)}$ is the most favorable of all the possible mechanisms for accommodating extra Y^{3+} ions in the YAG structure [1,7]. Moreover, the formation of antisite defects, when YAG is grown with excess yttria or alumina, are the most probable way of accommodating the deviation from stoichiometry [7]. This is evidenced by the defect formation energies for various disorders in YAG found in table 5.5. Y_{Al} antisites are likely the most common disorder in YAG

Table 5.2: Schottky-like disorders in YAG and their corresponding reaction enthalpies. *Source: M.M. Kuklja, J. Phys.: Condens. Matter 12 (2000) 2957.*

Reaction	Enthalpy (eV)
$O \leftrightarrow 3V_Y^{\prime\prime\prime} + 5V_{Al}^{\prime\prime\prime} + 12V_O^{\cdot\cdot}$	4.26
$3O_O + 2Al_{Al} \leftrightarrow Al_2O_3 + 2V_{Al}^{\prime\prime\prime} + 3V_O^{\cdot\cdot}$	4.70
$3O_O + 2Y_Y \leftrightarrow Y_2O_3 + 2V_Y^{\prime\prime\prime} + 3V_O^{\cdot\cdot}$	3.88
$3O_O + Y_Y + Al_{Al} \leftrightarrow YAlO_3 + V_Y^{\prime\prime\prime} + V_{Al}^{\prime\prime\prime} + 3V_O^{\cdot\cdot}$	4.21

Table 5.3: Frenkel-like disorders in YAG and their corresponding reaction enthalpies. *Source: M.M. Kuklja, J. Phys.: Condens. Matter 12 (2000) 2957.*

Reaction	Enthalpy (eV)
$Al_{Al} \leftrightarrow V_{Al}^{\prime\prime\prime} + Al_i^{\cdot\cdot\cdot}$	6.36
$Y_Y \leftrightarrow V_Y^{\prime\prime\prime} + Y_i^{\cdot\cdot\cdot}$	6.28
$O_O \leftrightarrow V_O^{\cdot\cdot} + O_i^{\prime\prime}$	4.88

Table 5.4: Antisite disorders in YAG and their corresponding reaction enthalpies. *Source: M.M. Kuklja, J. Phys.: Condens. Matter 12 (2000) 2957.*

Reaction	Enthalpy (eV)
$Y_Y + Al_{Al(oct)} \leftrightarrow Y_{Al(a)} + Al_Y$	0.9
$Y_Y + Al_{Al(tet)} \leftrightarrow Y_{Al(d)} + Al_Y$	1.8

as aluminum oxide shows preferential evaporation during crystal growth, leaving excess yttrium in the melt that is then available for incorporation into aluminum lattice sites in the lattice [1,110,132]. Excess yttrium in the melt is a common occurrence, and the phase diagram for YAG growth can be seen in figure 5.25. The presence of antisites in YAG is further evidenced by measurements of Y_{Al} antisites in YAG boules that were grown with increasing amounts of yttria in the melt [132]. Concentrations of antisite defects in YAG can reach $10^{20}cm^{-3}$, according to several studies [104,133,134].

Table 5.5: Defect formation energies for various disorders in YAG. *Source: M.M. Kuklja, J. Phys.: Condens. Matter 12 (2000) 2965.*

Cation Vacancies	**Defect Formation Energy (eV)**
V_{Al}	53.76 (Al_{oct}); 53.44 (Al_{tet})
V_Y	49.42
V_O	21.54
Interstitials	**--**
Al_i	-40.72
Y_i	-36.85
O_i	-11.38
Antisites	**--**
Y_{Al}	2.38 ($Y_{Al(oct)}$); 4.16 ($Y_{Al(tet)}$)
Al_Y	-0.69

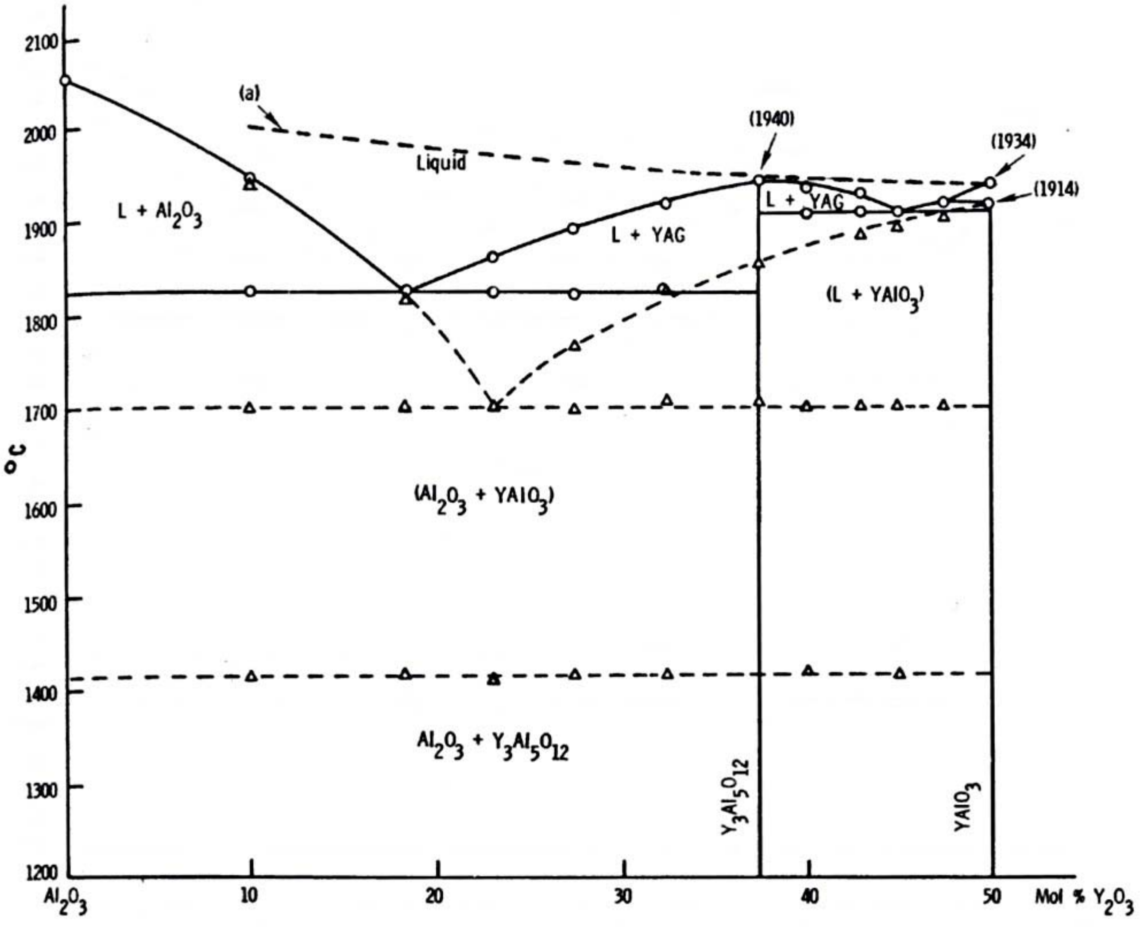

Figure 5.25: Phase diagram of the alumina-rich portion of the Al_2O_3-Y_2O_3 system. *Source: J.L. Caslavsky and D.J. Viechnicki, J. Mater. Sci. 15 (1980) 1715.*

5.6.3.9 Other Minor Impurities in Nd:YAG

Many ions can be introduced into YAG during crystal growth. Some ions enter the lattice with only one valence state and others have multiple valence state options that depend on the lattice site in which the impurity substitutes. Some are more readily accepted into the lattice than others due to their ionic radius. This subsection discusses a few of these minor impurities in YAG and their corresponding valence states.

Divalent impurities are common in YAG. They represent a point defect with a negative charge with respect to the surrounding crystal lattice, and they require charge compensation [7]. Their substitution mechanisms can be written as:

$$MO + N_N \rightarrow M_N' + \tfrac{1}{2}V_O^{\cdot\cdot} + \tfrac{1}{2}N_2O_3 \quad \text{(vacancy mechanism)}$$

or

$$MO + N_N \rightarrow M_N' + {}^{1}\!/_{3}N_i^{\cdot\cdot\cdot} + {}^{1}\!/_{3}N_2O_3 \quad \text{(interstitial mechanism)}$$

where M is the divalent impurity ion, N is the host ion, and M_N' is the singly-charged defect in the cation site [7]. The divalent impurities tend to form precipitates in the garnet structure, which should be located near oxygen vacancies for charge compensation [7].

Trivalent impurities represent a neutral defect with respect to the surrounding lattice, and, as a result, they do not require charge compensation [7]. Trivalent impurities can enter the lattice through the following mechanism:

$$M_2O_3 + 2N_N \rightarrow 2M_N + N_2O_3$$

where M is the trivalent impurity and N represents the possible host cations [7]. Trivalent impurities have low solution-enthalpies indicating that they have high solubility in YAG [7]. The cation size enthalpies for several trivalent impurities are listed in table 5.6.

Table 5.6: Cation size enthalpies for several trivalent impurities. *Source: M.M. Kuklja, J. Phys.: Condens. Matter 12 (2000) 2963.*

Impurity	**Al_{oct}**	**Al_{tet}**	**Y_{dod}**
Fe^{3+}	0.07eV	1.39eV	2.71eV
Cr^{3+}	0.09eV	2.41eV	3.07eV
Nd^{3+}	5.29eV	8.83eV	0.89eV

Tetravalent impurities act as positively-charged defects in YAG. The most common tetravalent defect in YAG, according to one study, is silicon, which prefers the tetragonal aluminum lattice site [7]. SiO_2 enters the YAG lattice through the following mechanism:

$$SiO_2 + {}^{5}/_{6}Al_{Al} + {}^{1}/_{2}Y_Y \leftrightarrow Si_{Al}' + {}^{1}/_{3}V_Y''' + {}^{1}/_{6}Y_3Al_5O_{12}$$

which suggests that aluminum inclusions will be formed when SiO_2 enters the YAG lattice [7,77]. Because alumina inclusions are not very soluble in YAG, they may segregate on the surface or along grain boundaries and/or dislocations [7]. Transitional metal cations such as vanadium, nickel, manganese, iridium, and many others have been found to occupy both tetrahedral and octahedral sites, adopting a 3+ valence in the former and a 4+ valence in the latter [10].

Calcium is a divalent impurity that can be found in YAG. It is often used as a charge compensator for the production of Cr^{4+}:YAG Q-switching crystals [15,121]. Ca^{2+} ions prefer to substitute for Y^{3+} ions in the dodecahedral lattice site [10]. They are usually charge compensated by oxygen vacancies [10]. However, their solubility in YAG is rather low at only 400ppm, and calcium impurity concentrations above this level tend to precipitate in YAG [10,100]. Ca^{2+} ions in relatively high concentrations can exhibit a red fluorescence in the 600-700nm range in YAG [135].

Manganese ions can have a valence of 2+, 3+, or 4+ in YAG. Mn^{4+} ions prefer the octahedral aluminum lattice sites and have a 350nm absorption band, while Mn^{2+} ions prefer the tetrahedral aluminum sites and absorb at 400nm [107,114]. Mn^{3+} ions have three main absorption bands located at 317nm, 368nm, and 452nm [136]. However, manganese ions are not one of the more common impurities found in YAG boules.

Nickel ion impurities in YAG come in two valence states, 2+ and 3+, and prefer the octahedral aluminum sites [98]. Ni^{2+} ions absorb at 620nm and are located about 1.6eV below the conduction band-edge in YAG [98,137]. Ni^{3+} ions absorb at 420nm and exhibit a broad absorption band [136,137]. Ni^{3+}-ion energy levels sit about 3.2eV above the valence band in YAG [137].

Vanadium is another impurity that can substitute in YAG as V^{2+}, V^{3+}, or V^{4+}. V^{2+} ions substitute in the larger Y^{3+} ion dodecahedral sites, while V^{3+} ions prefer the octahedral aluminum sites and have absorption bands at 350nm, 425nm, and 615nm [14,135]. V^{4+} ions have absorption features at 700nm and 800nm [135]. Vanadium impurities in YAG show luminescence at 1,024nm, but vanadium ion to neodymium ion energy transfer is undesirable as vanadium competes with some of the strong neodymium absorption bands, resulting in vanadium acting as a luminescence quencher in Nd:YAG [135].

Defect formation energies can be a good indicator of their relative likelihood of being present in YAG boules. Table 5.7 contains information regarding a few of the impurities' defect formation energies in the various lattice sites in YAG. As can be seen from the table, Cr^{3+} ions and Fe^{3+} ions are easily incorporated in the YAG lattice, which makes the probability of finding these impurities in YAG boules quite high.

Table 5.7: Defect formation energies in YAG. *Source: M.M. Kuklja, J. Phys.: Condens. Matter 12 (2000) 2965.*

Impurity	**Al_{oct}**	**Al_{tet}**	**Y_{dod}**
Ca^{2+}	31.16eV	31.96eV	27.40eV
Mg^{2+}	25.72eV	25.89eV	23.59eV
Cr^{3+}	-2.93eV	-1.77eV	-3.59eV
Fe^{3+}	-0.99eV	-0.33eV	-1.82eV
Si^{4+}	-43.48eV	-44.46eV	-41.44eV

5.6.3.10 Iron and Iridium Impurities in Nd:YAG

While many prospective sources of the main loss mechanism observed in Nd:YAG have been briefly presented here, none of them have yet proven to be the best candidates responsible for the loss. Two possible main candidates for the main loss mechanism observed in Nd:YAG could include iron and iridium.

Iron is the most common, natural impurity found in garnets. In Czochralski-grown YAG, it can be a quite common impurity, and crystal-growth technicians strive to eliminate this impurity. Iron impurities can act as quenching sites for Nd^{3+} ion luminescence as they have a broad absorption band centered at 1.1μm [88,138].

Fe^{3+} ions prefer the $Al_{(a)}$ sites but because $Al_{(d)}$ site-enthalpy is low enough, Fe^{3+} ions may substitute there as well [7]. Whenever iron is on both aluminum sites in approximately equal concentrations, the tetrahedral luminescence will be much stronger due to its lack of inversion symmetry [119]. Also, the Fe—O tetrahedral bond is less covalent than the Fe—O octahedral bond [139]. Because of its similar charge, Fe^{3+} ions can also substitute for Y^{3+} ions as well [136].

Iron impurities are most likely situated near oxygen vacancies [90]. This claim is substantiated by the observation of Fe^{2+} ions in YAG that require oxygen vacancies for charge compensation [17]. Further, under solarizing conditions, electrons released by divalent iron impurities have been found to trap at oxygen vacancies [77,90,109]. These oxygen vacancies also facilitate the charge exchange between divalent and trivalent iron when the impurities are illuminated using ultraviolet light [17,109,140]. This exchange, achieved with ultraviolet solarization, follows the reaction [17,96]:

$$O^{2-} + Fe^{3+} \leftrightarrow O^{-} + Fe^{2+}$$

According to literature, this electron transfer from oxygen ligands to the empty orbitals of Fe^{3+}-ion impurities has a characteristic absorption band at 256nm (4.89eV) in Nd:YAG [90,95,109,119,138,141]. The corresponding Fe^{2+} ion absorption band can be found at 310nm [17,93,109]. The Fe^{3+}-ion energy level was found to be roughly 4.8eV above the conduction band, placing it above the midpoint of the band gap [99]. This information, plus additional band-structure information, can be put into a diagram, thus mapping out the iron-oxygen complex energy levels in YAG as can be seen in figure 5.26. In addition to these absorption bands, iron impurities have many luminescence bands in YAG including several important peaks: 407nm, 455nm, and, 490nm [93,136,142].

While the presence of iron in a Nd:YAG crystal would be deleterious to its laser output power as literature points out, the actual presence of iron in YAG is disputed by the author. A critical look at the literature may reveal that the 256nm absorption peak is not due to an iron-oxygen charge transfer band as many studies have observed. While careful measurements of the 256nm absorption band have been made, the interpretation of these results is disputed here due to the fact that the source of the 256nm peak is often cited by literature using claims made by another journal article, which in turn cited another journal article's research as to the identification of the 256nm absorption peak. For example, in one study, C. Jiang grew YAG using both the Czochralski method (Cz) and the temperature gradient technique (TGT) and found a 256nm absorption peak in the Cz-grown YAG but no 256nm peak in the TGT-grown crystal [93]. With these results, C. Jiang cited C.Y. Chen et al. [138] for the identification of the source of the 256nm peak, which was said to be an iron-oxygen charge transfer band. Chen et al. performed electron paramagnetic resonance measurements in an Fe:YAG rod and compared those results with those from a Cz-grown Nd:YAG rod that they grew. However, the Fe:YAG rod was also grown by the Cz-method and no mention was made of crucible material, possibly indicating that the crucible material used for both growths was the commonly-used and seldomly-mentioned iridium. However, Chen et al. cited D.E. Lacklison et al. [143] for their determination of the source of the 256nm absorption peak that they found in their measurements, and in turn Lacklison et al. cited H.H. Tippins [144] for the source of the 256nm absorption peak they found. However, Tippins grew his crystal using the Czochralski-growth method and did not specify the crucible material used, again possibly indicating the use of iridium as the crucible material [144].

This same analysis and tracking of citations can be done with almost all papers that focus on the 256nm absorption peak. From the literature, it can therefore be argued that the 256nm absorption peak is not from iron impurities, but could be in fact from iridium, the most commonly-used crucible material in the Czochralski-method growth of YAG. However, the literature is useful for the measurements that were done on the 256nm peak. While the reasoning behind the identification of the peak may be flawed, the measurements themselves are of value as they are direct measurements of the peak.

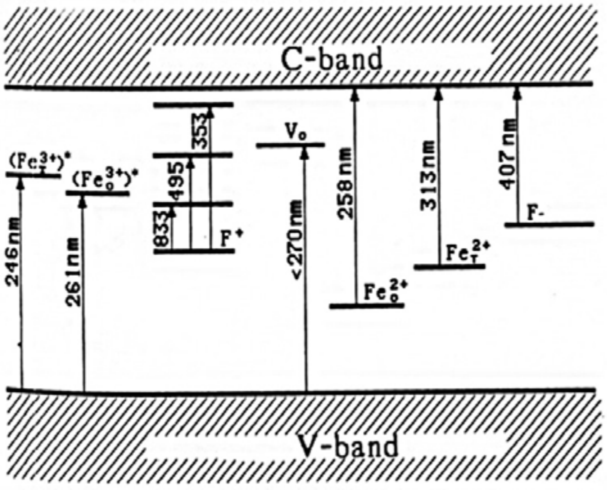

Figure 5.26: Band structure of iron impurities in YAG. *Source: I.Sh. Akhmadullin, S.A. Migachev, and S.P. Mironov, Nucl. Instrum. Methods B 65 (1992) 273.*

5.6.3.11 Properties of the 256nm Absorption Peak

S.M. Kaczmarek observed that irradiating YAG with gamma-rays reduced the 256nm absorption-peak intensity while an oxidizing-atmosphere heat treatment restored the absorption intensity of the 256nm absorption peak [95]. C. Jiang noted similar results with the 256nm absorption peak reducing its intensity upon gamma-ray irradiation as well as a new absorption band centered at 370nm emerging as a result of the irradiation [140]. I.I. Kuratev et al. found that the lowest lasing efficiency was observed and the highest induced laser losses were found for crystals having the highest 370nm-centered absorption peak [88].

Further, Kuratev et al. found that filtering the 256nm absorption peak from lamp excitation did not make a difference in laser output power, but filtering the 370nm absorption band vastly improved the laser performance of the laser crystal [88]. Also, Kuratev et al. found that high-temperature oxidation treatment increased the 256nm absorption peak and resulted in reducing laser losses and improved laser-energy characteristics [88].

Taken alone, these results do not specifically prove that iron is not responsible for the 256nm absorption peak. However, these articles as well as others may help show that the origin of the 256nm absorption peak is not due to iron at all. For example, in the work done by X. Xu et al., two growth methods were used to grow YAG, one growth used the Czochralski method with an iridium crucible while the other growth used the TGT method with a molybdenum crucible. The same high-quality raw materials were used for each growth. Subsequent analysis showed that the 256nm absorption peak was found in the Cz-method grown crystals while no 256nm peak was found in the TGT-method grown crystal [145]. C. Jiang also performed the same experiment finding the same results [93]. C. Jiang et al. confirmed this finding as well [140]. In addition to experiments done on single-crystal YAG, experiments have also been done on ceramic YAG. A. Ikesue et al. grew ceramic YAG and did not find any 256nm absorption peak in the measured rods [35]. Further, S.R. Rotman et al. grew Fe:YAG by the floating-zone method in which no crucible was used and found no 256nm absorption peak [119]. P.A. Arsen'ev et al. grew YAG using the zone-refining method and even purposely added iron to the melt during growth and did not find the 256nm absorption peak—even with the purposeful contamination of the crystal with iron [136]. Arsen'ev et al., however, did find several characteristic absorptions of iron including the 405nm absorption peak and the 440nm absorption peak [136]. This all indicates that the incorporation of iron in YAG does not result in the presence of the 256nm absorption peak. Even changing materials does not seem to help. G.J. Pogatshnik et al. grew GGG by the Czochralski method with an iridium crucible and found the 256nm absorption peak [86]. Since GGG uses different raw materials, the question is then raised regarding how Pogatshnik et al. presume that iron was incorporated into their crystal, and why the source of the 256nm absorption peak could not be iridium, the material used as a crucible for the growth.

I.Sh. Akhmadullin et al. grew YAG by the Cz-method using an iridium crucible and performed EPR measurements which showed that the crystal contained iron and no iridium [17]. This would seem to indicate that iron and not iridium is responsible for the 256nm absorption peak. While the EPR measurements found that iron was present and iridium was not, this result can be explained by the fact that Ir^{3+} ions are not paramagnetic and could therefore not be found using EPR measurements [146]. As a consequence to their findings, the EPR measurements may indeed show the presence of iron, but they cannot show the lack of iridium in the crystal, indicating that iridium could still be responsible for the presence of the 256nm absorption peak observed in their samples. Another method must be used to determine whether or not iridium is contained in their crystal. This same argument can be used for the EPR measurements carried out by K. Mori [109]. Even the paramagnetic Ir^{4+} ions are hard to detect using EPR as it has a $5d^5$ configuration with only one unpaired electron and is a low spin and high-field species [146,147]. Throughout literature, the only time the 256nm absorption peak has been detected was when an iridium crucible was used in the growth of the YAG crystal.

5.7 Improving Nd:YAG by Post-Growth Etching

When the Nd:YAG laser rod is cored out of the boule, its surface is grit-blasted to remove some material from the rod's surface and to remove surface defects introduced by the coring process. The end-faces of the barrel are then polished with decreasing grit sizes until these faces have a glass-like smoothness. However, there still may be tiny flaws and scratches as a result of this processing [59]. The processing can leave subsurface damage that may extend as far as 50μm into the bulk of the rod [59,60]. This damage can severely limit the fracture strength of the rod as flaws lead to stress concentration, and crack initiation can occur at the flaws [148].

Tensile fracture strength can be improved by reducing the flaw size in the material [60]. Grit-blasted Nd:YAG rods have a fracture strength of about 134MPa while polished rods have a fracture strength of about 175Mpa [59,60]. However, when the rod is etched, its fracture strength can increase significantly reaching values of up to 2,360MPa with maximum strength being obtained by the removal of 60-80μm of material from the barrel surface [60].

Barrel surface impurities such as microscopic cracks, dislocations, and imbedded polishing compound can strongly absorb pump light from the krypton arc-lamp [47,91]. This absorption on the surface leads to heat generation, which can lead to thermal lensing and increased thermal stress in the rod [48].

Elimination of these subsurface flaws can be accomplished by etching. Many methods of etching can be used including chemical, ion beam, and plasma etching, but chemical etching is fast, simple, and cheap [59]. Heated H_3PO_4 is the most commonly-used etchant for etching Nd:YAG [59]. However, heated H_3PO_4 tends to dehydrate during heating following the reactions:

$$2H_3PO_4 \rightarrow H_2O + H_4P_2O_7$$

and

$$3H_3PO_4 \rightarrow 2H_2O + H_5P_3O_{10}$$

so it must be refreshed after prolonged heating or etching [59]. Etching Nd:YAG has been shown to improve the fracture strength and, in some cases, the laser output power of the rod—the result of the elimination of the subsurface flaws on the barrel surface [59]. Etching, however, can be detrimental for some rods. Etching has a tendency to preferentially remove material around the point where a dislocation emerges at the surface of the rod, and because of YAG's large unit cell and, as a result, its large Burgers vector ($||\mathbf{b}|| = 10.4$Å; $\mathbf{b} = \frac{1}{2}[111]$), etching around dislocations may actually lead to stress concentration around them which can help promote thermal fracture of the rod [148,149]. Etching can improve laser performance of diode-pumped Nd:YAG by eliminating surface defects, but etching does not seem to help every Nd:YAG rod, and it does not address the issue of iridium in the rod as well as the presence of aluminum vacancies that act as charge compensators for the iridium impurities. Thus, another method for improving rods may be necessary.

5.8 Post-Growth Heat Treatment to Improve Laser Performance

Oxidation annealing and diffusion processing may help Nd:YAG crystals increase their laser output power and efficiency. This could be the result of the reduction of defects in the crystal. It has been shown that color-center formation in annealed crystals depends on annealing atmosphere with an oxidizing atmosphere reducing the concentration of color centers in the crystal and a reducing atmosphere increasing the concentration of color centers within the crystal [28,68,88,150]. This can be measured by sensing the value of the charge of the charge carriers in the crystal with oxidized crystals being more p-type and reduced crystals being more n-type [28]. Moreover, the amount of oxygen in the atmosphere also influences color center removal with more color centers removed with increased oxygen partial pressure in the annealing atmosphere [90,150].

During high-temperature oxygen anneal, oxygen vacancies diffuse to the surface of the crystal as well as to grain boundaries and dislocations within the crystal [81]. They can then be eliminated from the lattice and replaced by oxygen ions. It is important to have oxygen available to replace the oxygen vacancies as annealing in vacuum can create thermally-generated vacancies adding to the concentration of as-grown oxygen vacancies in the crystal [111]. The oxygen diffusion coefficient, *D*, is strongly influenced by the annealing atmosphere as well as by the temperature, *T*, during the annealing and is given by:

$$D = \left(2.34 \times 10^{-8}\right)\exp\left(\frac{-315KJ/mol}{RT}\right)\left[m^2/s\right] \tag{5.19}$$

in an air atmosphere at 1,400°C, where $R = 8.314$J/mol·K [150]. Effective anneals in an oxidizing atmosphere must be carried out at a significantly high temperature around 1,400-1,500°C to eliminate oxygen vacancies and their related color centers [76]. However, even at these high temperatures, annealing does not seem to eliminate the core faceting structure or its corresponding stress that it produces in the crystal despite the finding that oxygen diffusion coefficients in the faceted region are a few times larger than the coefficients outside the core-faceted region [115,150]. Since oxygen diffusion is related to oxygen vacancy concentration, this is further evidence that the core region of the grown boule contains higher oxygen vacancy concentration [150]. Also, one study has found that some stress caused by the core-faceting can be relieved through annealing in oxygen at high temperatures ($T \geq 1{,}400°C$) for long periods of time of 50 hours or more [115].

Impurities with variable charge states can increase or decrease their valence under varying annealing atmospheres [90]. In an oxidizing atmosphere, Ir^{3+} ions are proposed to become Ir^{4+} ions in YAG, and vice versa for reducing atmospheres. This is substantiated by the increase in intensity of the 256nm absorption peak attributed to the Ir^{3+}-ion impurity complex in YAG as well as the reduction of the ~330nm absorption peak that has been attributed to the Ir^{4+} ion. This oxidation reaction can be written as:

$$2Me^{n-1}{}_{(c)} + \tfrac{1}{2}O_{2(g)} \rightarrow 2Me^{n}{}_{(c)} + O^{2-}{}_{(c)}$$

where Me represents an variable-charge-state impurity ion and the subscript (c) indicates that the ion is in a coordinated, condensed phase [114].

References

[1] C.R. Stanek, K.J. McClellan, M.R. Levy, C. Milanese, and R.W. Grimes, submitted to Nucl. Instrum. Methods A (2006).

[2] K. Nassau, J. Nassau, E. Schönherr, D.E. Ovsienko, G.A. Alfintsev, and A.H. Morrish, Crystals: Growth, Properties, and Applications. Springer-Verlag, Berlin, 1980.

[3] F. Cornacchia, M. Alshourbagy, A. Toncelli, H. Ogino, A. Yoshikawa, and T. Fukuda, J. Cryst. Growth 275 (2005) 534-540.

[4] E. Kanchanavaleerat, D. Cochet-Muchy, M. Kokta, J. Stone-Sundberg, P. Sarkies, Ju. Sarkies, and Jo. Sarkies, Opt. Mater. 26 (2004) 337-341.

[5] R.R. Monchamp, J. Cryst. Growth 11 (1971) 310-312.

[6] A. Golubović, S. Nikolić, R. Gajić, S. Đurić, and A. Valčić, J. Serb. Chem. Soc. 67 (2002) 291-300.

[7] M.M. Kuklja, J. Phys.: Condens. Matter 12 (2000) 2953-2967.

[8] P. Wamsley, High-Pressure Optical Studies of Doped Yttrium Aluminum Garnet. Dissertation, University of Michigan, Ann Arbor, Michigan, 1994.

[9] G.A. Slack, D.W. Oliver, R.M. Chrenko, and S. Roberts, Phys. Rev. 177 (1969) 1308-1314.

[10] K.R. Brown and D.A. Bonnell, Surf. Sci. 414 (1998) 341-352.

[11] Y.N. Xu and W.Y. Ching, Phys. Rev. B 59 (1999) 10530-10535.

[12] M.J. Weber, Handbook of Optical Materials. CRC Press, Boca Raton, 2002.

[13] M.R. Kokta, Mater. Res. Soc. Symp. Proc. 329 (1994) 33-43.

[14] R. Feldman, Y. Shimony, and Z. Burshtein, Opt. Mater. 24 (2003) 333-344.

[15] B.M. Tissue, W. Jia, L. Lu, and W.M. Yen, J. Appl. Phys. 70 (1991) 3775-3777.

[16] D.J. Cheriak, Phys. Chem. Minerals 26 (1998) 156-163.

[17] I.Sh. Akhmadullin, S.A. Migachev, and S.P. Mironov, Nucl. Instrum. Methods B 65 (1992) 270-274.

[18] T. Tomiki, Y. Isa, Y. Kadekawa, Y. Ganaha, N. Toyokawa, T. Miyazato, M. Miyazato, T. Kohatsu, H. Shimabukuro, and J. Tamashiro, J. Phys. Soc. Jpn. 65 (1996) 1106-1113.

[19] M.A. Gülgün, W.Y. Ching, Y.N. Xu, and M. Rühle, Philo. Mag. B 79 (1999) 921-940.

[20] J.L. Caslavsky and D.J. Viechnicki, J. Mater. Sci. 15 (1980) 1709-1718.

[21] R.C. Powell, Physics of Solid-State Laser Materials. Springer-Verlag, New York, 1998.

[22] A.A. Kaminskii, Laser Crystals. Springer-Verlag, Berlin, 1990.

[23] M. Schmid, Th. Graf, and H.P. Weber, J. Opt. Soc. Am. B 17 (2000) 1398-1404.

[24] X. Peng, A. Asundi, Y. Chen, and Z. Xiong, Appl. Opt. 40 (2001) 1396.

[25] T. Tomiki, J. Tamashiro, M. Hiraoka, N. Hirata, and T. Futemma, J. Phys. Soc. Jpn. 57 (1988) 4429-4433.

[26] C.W. Thiel. H. Cruguel, Y. Sun, G.J. Lapeyre, R.M. Macfarlane, R.W. Equall, and R.L. Cone, J. Lumin. 94-95 (2001) 1-6.

[27] N.Yu. Konstantinov, L.G. Karaseva, V.V. Gromov, and A.V. Yakovlev, Phys. Status Solidi A 83 (1984) K153-K157.

[28] W.M. Mullins and B.L. Averbach, Surf. Sci. 206 (1988) 29-40.

[29] W. Van Gool, Principles of Defect Chemistry of Crystalline Solids. Academic Press, New York and London, 1966.

[30] S.R. Rotman, H.L. Tuller, and C. Warde, J. Appl. Phys. 71 (1992) 1209-1214.

[31] B.A. Lengyel, Introduction to Laser Physics. John Wiley & Sons, Inc., New York, 1966.

[32] R.K. Watts, Point Defects in Crystals. John Wiley & Sons, Inc., New York, 1977.

[33] R. Iffländer, Solid-State Lasers for Materials Processing: Fundamental Relations and Technical Realizations. Springer-Verlag, Berlin, 2001.

[34] D.E. Eakins, M. Held, M.G. Norton, and D.F. Bahr, J. Cryst. Growth 267 (2004) 502-509.

[35] A. Ikesue, K. Kamata, and K. Yoshida, J. Am. Ceram. Soc. 79 (1996) 1921-1926.

[36] J. Wisdom, M. Digonnet, and R.L. Byer, Photonics Spectra. “Ceramic Lasers: Ready for Action,” Feb. 2004.

[37] V. Lupei, N. Pavel, and T. Taira, IEEE J. Quantum Electron. 38 (2002) 240-245.

[38] S. Goldring, R. Lavi, A. Tal, E. Lebiush, Y. Tzuk, and S. Jackal, IEEE J. Quantum Electron. 40 (2004) 384-389.

[39] V. Lupei, N. Pavel, and T. Taira, Opt. Lett. 26 (2001) 1678-1680.

[40] J.A. L'huillier, G. Bitz, V. Wesemann, P. von Loewis, R. Wallenstein, A. Borsutzky, L. Ackermann, K. Dupré, D. Rytz, and S. Vernay, Appl. Opt. 41 (2002) 4377-4384.

[41] A. Ikesue, Opt. Mater. 19 (2002) 183-187.

[42] V. Lupei, A. Lupei, N. Pavel, T. Taira, and A. Ikesue, Appl. Phys. B 73 (2001) 757-762.

[43] J. Dong, P. Deng, F. Gan, Y. Urata, R. Hua, S. Wada, and H. Tashiro, Opt. Commun. 197 (2001) 413-418.

[44] J. Lu, M. Prabhu, J. Xu, K. Ueda, H. Yagi, T. Yanagitani, and A.A. Kaminskii, Appl. Phys. Lett. 77 (2000) 3707-3709.

[45] J. Lu, M. Prabhu, J. Song, C. Li, J. Xu, K. Ueda, A.A. Kaminskii, H. Yagi, and T. Yanagitani, Appl. Phys. B 71 (2000) 469-473.

[46] J.A. Caird, M.D. Shinn, T.A. Kirchoff, L.K. Smith, and R.E. Wilder, Appl. Opt. 25 (1986) 4294-4305.

[47] T.S. Rose, M.S. Hopkins, and R.A. Fields, IEEE J. Quantum Electron. 31 (1995) 1593-1602.

[48] C.L. Wang, K.G. Lynn, S. Tebaldi, M.H. Weber, K. Shafer, R. Tjossem, T.T. Williams, and J.D. Dougherty, Proc. SPIE Solid State Lasers XII 4968 (2003) 143-150.

[49] M.P. Murdough and C.A. Denman, Appl. Opt. 35 (1996) 5925-5936.

[50] T. Kushida, Phys. Rev. 185 (1969) 500-508.

[51] J. Marling, IEEE J. Quantum Electron. 14 (1978) 56-62.

[52] R. Lavi, S. Jackel, A. Tal, E. Lebiush, Y. Tzuk, and S. Goldring, Opt. Commun. 195 (2001) 427-430.

[53] R. Weber, B. Neuenschwander, and H.P. Weber, Opt. Mater. 11 (1999) 245-254.

[54] W. Koechner, Appl. Opt. 9 (1970) 1429-1434.

[55] I. Moshe and S. Jackel, Opt. Commun. 214 (2002) 315-325.

[56] M.P. MacDonald, Th. Graf, J.E. Balmer, and H.P. Weber, Opt. Commun. 178 (2000) 383-393.

[57] W. Xie, S.C. Tam, L. Yee-Loy, J. Liu, H. Yang, J. Gu, W. Tan, and F. Zhou, Opt. Laser Technol. 32 (2000) 199-203.

[58] R. Wynne, J.L. Daneu, and T.Y. Fan, Appl. Opt. 38 (1999) 3282-3284.

[59] M. Gerber and Th. Graf, Opt. Laser Technol. 33 (2001) 449-453.

[60] J. Marion, Appl. Phys. Lett. 47 (1985) 694-696.

[61] D.J. Keast and B.E. Storey, Brit. J. Appl. Phys. 1 (1968) 524-527.

[62] H.G. Danielmeyer, M. Blätte, and P. Balmer, Appl. Phys. 1 (1973) 269-274.

[63] V. Lupei, Opt. Mater. 16 (2001) 137-152.

[64] T.Y. Fan, IEEE J. Quantum Electron. 29 (1993) 1457-1459.

[65] B. Di Bartolo, Spectroscopy of Solid-State Laser-Type Materials. Plenum Press, New York, 1987.

[66] M. Ajroud, M. Haouari, H. Ben Ouada, H. Maaref, A. Brenier, and C. Garapon, J. Phys.: Condens. Matter 12 (2000) 3181-3193.

[67] S.R. Rotman, Appl. Phys. Lett. 54 (1989) 2053-2055.

[68] D.P. Devor, L.G. DeShazer, and R.C. Pastor, IEEE J. Quantum Electron. 25 (1989) 1863-1873.

[69] U.J. Greiner and H.H. Klingenberg, Opt. Lett. 19 (1994) 1207-1209.

[70] J. Weertman and J.R. Weertman, Elementary Dislocation Theory. Oxford University Press, Oxford, 1992.

[71] Y. Peizhi, D. Peizhen, Y. Zhiwen, and T. Yulian, J. Cryst. Growth 218 (2000) 87-92.

[72] S.O. Kasap, Principles of Electrical Engineering Materials and Devices. Irwin McGraw-Hill, Boston, 1997.

[73] B. Henderson, Defects in Crystalline Solids. Crane, Russak & Company, Inc., New York, 1972.

[74] G. Zhao, X. Zeng, J. Xu, and Y. Zhou, J. Cryst. Growth 253 (2003) 290-296.

[75] M. Lando, J. Kagan, B. Linyekin, and V. Dobrusin, Opt. Commun. 222 (2003) 371-381.

[76] L.B. Pasternak, B.K. Sevastyanov, V.P. Orekhova, Yu.L. Remigailo, Ji. Kvapil, Jos. Kvapil, B. Manek, and B. Perner, J. Cryst. Growth 52 (1981) 546-551.

[77] A. Matkovskii, P. Potera, D. Sugak, L. Grigorjeva, D. Millers, V. Pankratov, and A. Suchocki, Cryst. Res. Technol. 39 (2004) 788-795.

[78] L.V. Azároff and J.J. Brophy, Electronic Processes in Materials. McGraw-Hill Book Company, New York, 1963.

[79] C.R. Barrett, W.D. Nix, A.S. Tetelman, The Principles of Engineering Materials. Prentice-Hall, New Jersey, 1973.

[80] H.G. Van Bueren, Imperfections in Crystals. North-Holland Publishing Company, Amsterdam, 1961.

[81] B. Gruber, editor, Theory of Crystal Defects. Academic Press, New York and London, 1966.

[82] F.A. Kröger, The Chemistry of Imperfect Crystals. North-Holland Publishing Company, Amsterdam, 1964.

[83] C.W. Thiel, H. Cruguel, H. Wu, Y. Sun, G.J. Lapeyre, R.L. Cone, R.W. Equall, and R.M. Macfarlane, Phys. Rev. B 64 (2001) 1-13.

[84] A. Javan, Sci. Am. 217 (1967) 238-248.

[85] A. Matkovskii, D. Sugak, S. Melnyk, P. Potera, A. Suchocki, and Z. Frukacz, J. Alloys Comp. 300-301 (2000) 395-397.

[86] G.J. Pogatshnik, L.S. Cain, Y. Chen, and B.D. Evans, Phys. Rev. B 43 (1991) 1787-1794.

[87] H. Jiang, J. Myers, D. Rhonehouse, M. Myers, and J. Ballato, Am. Ceram. Soc. 102 (2000) 1-7.

[88] I.I. Kuratev, S.P. Nasel'skiĭ, V.K. Novikov, A.I. Ryabov, G.N. Toropkin, and V.G. Yanchuk, Sov. J. Quantum Electron. 15 (1985) 861-862.

[89] G. Zeidler, IEEE J. Quantum Electron. 4 (1968) 1016-1017.

[90] T. Masumoto and Y. Kuwano, Jpn. J. Appl. Phys. 24 (1985) 546-551.

[91] G. Mann and G. Phillipps, Opt. Mater. 4 (1995) 811-814.

[92] S.M. Kaczmarek, D.J. Sugak, A.O. Matkovskii, A. Moroz, M. Kwaśny, and A.N. Durygin, Nucl. Instrum. Methods B 132 (1997) 647-652.

[93] C. Jiang, Physica B 373 (2006) 42-45.

[94] S.M. Kaczmarek, R. Jablonski, Z. Moroz, I. Pracka, and T. Lukasiewicz, Cryst. Res. Technol. 34 (1999) 719-728.

[95] S.M. Kaczmarek, Cryst. Res. Technol. 34 (1999) 1183-1190.

[96] A.Y. Neiman, E. Tkachenko, and V. Zhukovskii, Dokl. Akad. Nauk SSSR 240 (1978) 876-879.

[97] V.V. Gromov, L.G. Karaseva, and E.I. Saunin, J. Radioanalytical Chem. 30 (1976) 441-450.

[98] S.R. Rotman and H.L. Tuller, J. Appl. Phys. 62 (1987) 1305-1312.

[99] S.R. Rotman and H.L. Tuller, J. Electroceramics 2 (1998) 95-104.

[100] L. Schuh, R. Metselaar, and G. de With, J. Appl. Phys. 66 (1989) 2627-2632.

[101] C. Kittel, Introduction to Solid State Physics. John Wiley & Sons, Inc., New Jersey, 1996.

[102] S.M. Kaczmarek, J. Wojtkowska, Z. Moroz, and I. Pracka, J. Alloys Comp. 286 (1999) 167-173.

[103] E.A. Kotomin and A.I. Popov, Nucl. Instrum. Methods B 141 (1998) 1-15.

[104] M. Springis, A. Pujats, and J. Valbis, J. Phys.: Condens. Matter 3 (1991) 5457-5461.

[105] A. Pujats and M. Springis, Radiat. Eff. Def. Solids 155 (2001) 65-69.

[106] M.Kh. Ashurov, A.F. Rakov, and R.A. Erzin, Solid State Commun. 120 (2001) 491-494.

[107] H.J. Bernhardt, Phys. Status Solidi B 87 (1978) 213-219.

[108] W. Hayes, M. Yamaga, D.J. Robbins, and B. Cockayne, J. Phys. C: Solid State Phys. 13 (1980) L1085-L1089.

[109] K. Mori, Phys. Status Solidi A 42 (1977) 375-384.

[110] N.S. Kovaleva, A.O. Ivanov, and É.P. Dubrovian, Sov. J. Quantum Electron. 11 (1981) 1485-1488.

[111] J. Kvapil, Jo. Kvapil, and B. Perner, Kristall. und Technik. 10 (1975) 161-165.

[112] G.E. Venikouas, G.J. Quarles, J.P. King, and R.C. Powell, Phys. Rev. B 30 (1984) 2401-2409.

[113] Y.N. Xu, Y. Chen, S.D. Mo, and W.Y. Ching, Phys. Rev. B 65 (2002) 235104-1-235104-4.

[114] D.P. Devor, R.C. Pastor, L.G. DeShazer, J. Chem. Phys. 81 (1984) 4104-4117.

[115] D. Jun, D. Peizhen, and X. Jun, J. Cryst. Growth 203 (1999) 163-167.

[116] S. Ishibashi, K. Naganuma, and I. Yokohama, J. Cryst. Growth 183 (1998) 614-621.

[117] J. Dong, P. Deng, and J. Xu, Opt. Commun. 170 (1999) 255-258.

[118] D.L. Wood, J. Ferguson, K. Knox, and J.F. Dillion, Jr., J. Chem. Phys. 39 (1963) 890-898.

[119] S.R. Rotman, C. Warde, and H.L. Tuller, J. Appl. Phys. 66 (1989) 3207-3210.

[120] S. Kück, K. Petermann, U. Pohlmann, and G. Huber, J. Luminesc. 68 (1996) 1-14.

[121] J.C. Chen, C.Y. Lo, K.Y. Huang, F.J. Kao, S.Y. Tu, and S.L. Huang, J. Cryst. Growth 274 (2005) 522-529.

[122] M. Khanlary, D.E. Hole, and P.D. Townsend, Nucl. Instrum. Methods B 227 (2005) 379-384.

[123] M.A. Kramer and R.W. Boyd, Phys. Rev. B 23 (1981) 986-991.

[124] G.J. Zhao, X.H. Zeng, J. Xu, S.M. Zhou, and Y.Z. Zhou, Phys. Status Solidi A 199 (2003) 355-359.

[125] H.J. Reyher, N. Hausfeld, M. Pape, J. Baur, and J. Schneider, Solid State Commun. 110 (1999) 345-349.

[126] T. Tomiki, H. Akamine, M. Gushiken, Y. Kinjoh, M. Miyazato, T. Miyazato, N. Toyohawa, M. Hiraoka, H. Hirata, Y. Ganaha, and T. Futemma, J. Phys. Soc. Jpn. 60 (1991) 2437-2445.

[127] S.M. Kaczmarek, G. Domianiak-Dzik, W. Ryba-Romanowski, J. Kisielewski, and J. Wojtkowska, Cryst. Res. Technol. 34 (1999) 1031-1036.

[128] J.F. Owen, P.B. Dorain, and T. Kobayasi, J. Appl. Phys. 52 (1981) 1216-1222.

[129] L.A. Kappers, R.H. Bartram, D.S. Hamilton, A. Lempicki, and J. Glodo, J. Luminesc. 102-103 (2003) 162-165.

[130] C.H. Lu, H.C. Hong, and R. Jagannathan, J. Mater. Chem. 12 (2002) 2525-2530.

[131] Ł. Dobrzycki, E. Bulska, D.A. Pawlak, Z. Frukacz, and K. Woźniak, Inorg. Chem. 43 (2004) 7656-7664.

[132] M.Kh. Ashurov, Yu.K. Voronko, V.V. Osiko, A.A. Sobol, and M.I. Timoshechkin, Phys. Status Solidi A 42 (1977) 101-110.

[133] V. Babin, K. Blazek, A. Krasnikov, K. Nejezchleb, M. Nikl, T. Savikhina, and S. Zazubovich, Phys. Status Solidi C 2 (2005) 97-100.

[134] Y. Zorenko, A. Voloshinovskii, I. Konstankevych, V. Kolobanov, V. Mikhailin, and D. Spassky, Radiat. Measurements 38 (2004) 677-680.

[135] M.J. Weber and L.A. Riseberg, J. Chem. Phys. 55 (1971) 2032-2038.

[136] P.A. Arsen'ev and D.T. Sviridov, Sov. Phys. Crystallogr. 14 (1970) 578-580.

[137] S.R. Rotman, C. Warde, and H.L. Tuller, J. Appl. Phys. 66 (1989) 1366-1369.

[138] C.Y. Chen, G.J. Pogatshnik, Y. Chen, and M.R. Kokta, Phys. Rev. B: Condens. Matter 38 (1988) 8555-8561.

[139] P. Köhler and G. Amthauer, J. Sol. State Chem. 28 (1979) 329-343.

[140] C. Jiang, G. Zhou, J. Xu, P. Den, and F. Gan, J. Cryst. Growth 257 (2003) 301-304.

[141] M.L. Meil'man, M.V. Korzhik, V.V. Kuz'min, M.G. Livshits, Kh.S. Bagdasarov, and A.M. Kevorkov, Sov. Phys. Dokl. 29 (1984) 61-63.

[142] Y.A. Voitukevich, M.V. Korzhik, V.V. Kuzmin, M.G. Livshits, and M.L. Meilman, Opt. Spectrosc. (USSR) 63 (1987) 480-484.

[143] D.E. Lacklison, G.B. Scott, and J.L. Page, Solid State Commun. 14 (1974) 861-863.

[144] H.H. Tippins, Phys. Rev. B 1 (1970) 126-135.

[145] X. Xu, Z. Zhao, G. Zhao, P.X. Song, J. Xu, and P. Deng, J. Cryst. Growth 257 (2003) 297-300.

[146] L. Pidol, O. Guillot-Noël, M. Jourdier, A. Kahn-Harari, B. Ferrand, P. Dorenbos, and D. Gourier, J. Phys.: Condens. Matter 15 (2003) 7815-7821.

[147] J. Owens, Platinum Metals Rev. 3 (1959) 137-139.

[148] K.E. Shafer, D.E. Eakins, D.F. Bahr, M.G. Norton, and K.G. Lynn, J. Mater. Res. 18 (2003) 2537-2539.

[149] M.I. Peters and I.E. Reimanis, J. Am. Ceram. Soc. 86 (2003) 870-872.

[150] H. Haneda, Y. Miyazawa, and S. Shirasaki, J. Cryst. Growth 68 (1984) 581-588.

CHAPTER SIX

DEFECT STUDIES OF YTTRIUM ALUMINUM GARNET

6.1 Experimental Motivation

Since its discovery, the laser output power potential of Nd-doped yttrium aluminum garnet (Nd:YAG) has never been fully realized. Many impurities have been looked at to provide an explanation for the losses observed in laser rods, but to date few studies have proved fruitful. The identification of parasitic impurities and defects remains an important area of research in Nd:YAG. While most of the focus has remained on impurity ions found in the melt constituents, little progress has been made correlating these impurities to laser performance. This chapter identifies and explores the impurities and defects that been researched in the past and attempts to determine their relative affect on laser performance. In addition, proposed methods of improving laser performance through post-growth processing are explored. A possible candidate is identified that has been ignored or overlooked in the past which could help steer future research in a different direction and possibly aid in the quest to obtain maximum laser performance of Nd:YAG. The effect of this impurity is characterized, and the minimization of its deleterious effect on laser performance is presented through several post-growth studies such as oxidation annealing and diffusion.

6.2 Properties of the Control 512 Laser Cavity

Although many laser cavities exist for the various Nd:YAG laser rod shapes and sizes, the Control 512 laser was the only laser cavity used for Nd:YAG laser power measurements reported here. The Control 512 laser cavity is a single lamp head, krypton arc lamp, elliptical cavity in which the Nd:YAG laser rod is mounted parallel to the lamp. A photograph of the Control 512 laser cavity can be seen in figure 6.1. The laser cavity is traditionally cooled by distilled water that is pumped from an external heat exchanger. The schematic of this standard cooling cycle can be seen in figure 6.2. The cooling system cycles 2.5 gallons of water at a pressure of up to 35psi with a flow rate of three to five gallons per minute. The cycled cooling water is cooled by a heat exchanger that is regulated by an external water supply. The elliptic optical cavity is heavily electroplated with 24-karat gold which acts as a light reflector. The power system for the krypton arc lamp consists of a dc power supply that operates the lamp at 10-20amps. In addition, the power system supplies a lamp ignition pulse in the form of a positive-going spike of 26kV dc for a 1μs duration. Various adaptations to this standard design have been made. The cooling system has been modified by the addition of a Neslab Instruments chiller model #450001 that uses R-416A refrigerant. A schematic of the cooling system with the adaptation can be seen in figure 6.3. Another major alteration to the cooling system was the

Figure 6.1: Photograph of inside of Control 512 laser cavity. The rod on the top is the Nd:YAG rod and is 79mm in length, and the rod on the bottom is the krypton-arc lamp.

replacement of deionized water with ultra-clean heavy water. This was done in response to a patent filed by Ian Peter Mercer (patent #20040247003) in 2004 that suggested that laser output power could be increased by using heavy water instead of deionized regular water due to the fact that it can remove heat from the laser cavity more efficiently than regular water. Also, heavy water can be used to decrease ultraviolet light absorption by the rod as heavy water absorbs more ultraviolet light than regular water along with absorbing the 970nm light that Nd:YAG absorbs [1]. The absorption of ultraviolet light for both heavy water and regular water was measured by filling a cuvette with each water type and measuring with an Ocean Optics spectrometer, the details of which are located in Appendix C. The results of this absorption measurement can be seen in figure 6.4. Other suggestions have been made to increase ultraviolet light absorption by the cooling fluid. For example, adding sodium nitrate, potassium chromate, or potassium dichromate to the cooling fluid has been suggested [2-4].

In addition to the changes in the cooling system, changes in the power system were also made. To extend the amount of power that could be supplied to the lamp, three Optima car batteries part #SC34U were added in series to the original power supply. Each Optima battery was capable of 1,000 cranking amps and 800 cold-cranking amps, and each provided an extra 12V to the lamp. A schematic of the adapted power system can be seen in figure 6.5. As can be seen from the figure, a voltmeter was added to the system to help accurately measure the voltage being supplied to the lamp. In addition to that voltmeter, another voltmeter was added to the shunt (variable resistor) to help measure the potentiometer changes made by the laser operator to increase the voltage to the lamp. Finally, an ammeter was added to the system to measure the amperage supplied by the power supply. Input powers supplied to the lamp were then calculated using Ohm's law.

The laser cavity utilizes two light-filtering tubes that filter out light from the lamp that is not suitably utilized by the Nd:YAG laser rod. These light-filtering tubes, also known as flow tubes, consist of Sm-doped glass for the Control 512 laser cavity used for these measurements. Figure 6.6 contains a plot of the Sm-doped flow tube absorption versus wavelength. The use of the flow tubes reduces the thermal load on the crystal. This is because absorption in the Nd:YAG rod increases as the wavelength drops from 500nm, whereas the fluorescence at the lasing line remains nearly constant [5]. Therefore, the short-wavelength radiation contributes to rod heating which affects the polarized laser output due to thermally-induced birefringence [5].

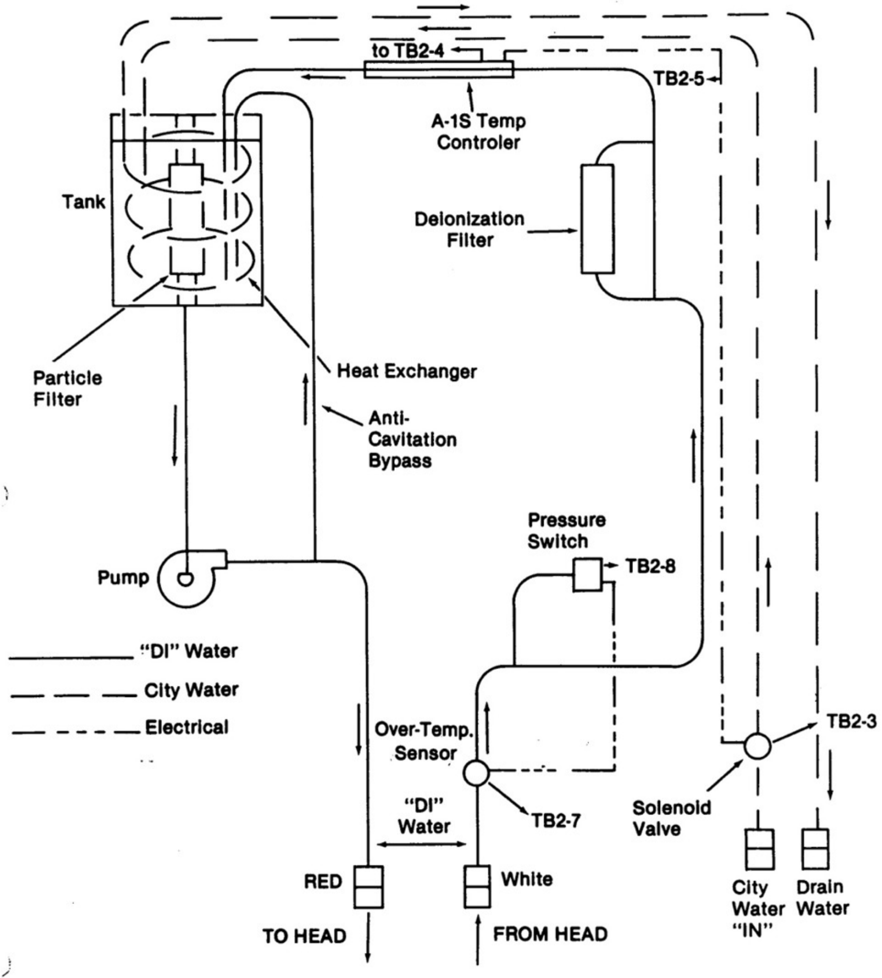

Figure 6.2: The standard cooling system for the Control 512 laser. *Source: Control 512 laser manual p. 7-3.*

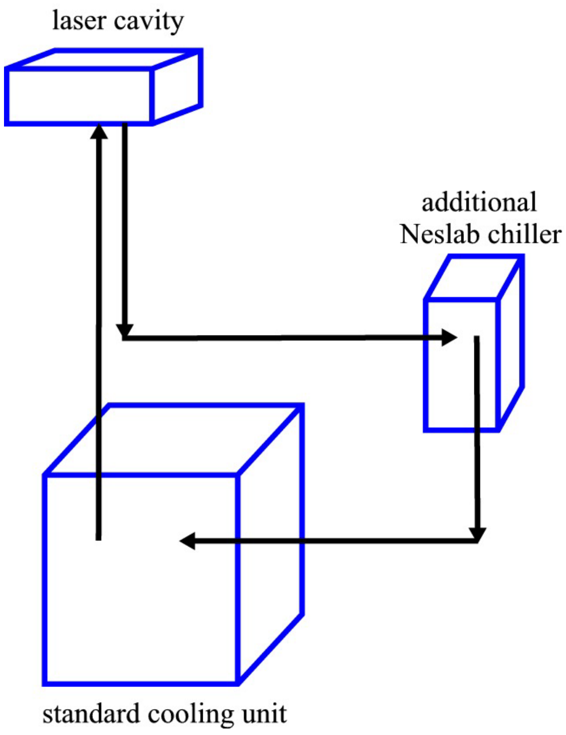

Figure 6.3: Schematic of improved cooling system for Nd:YAG laser.

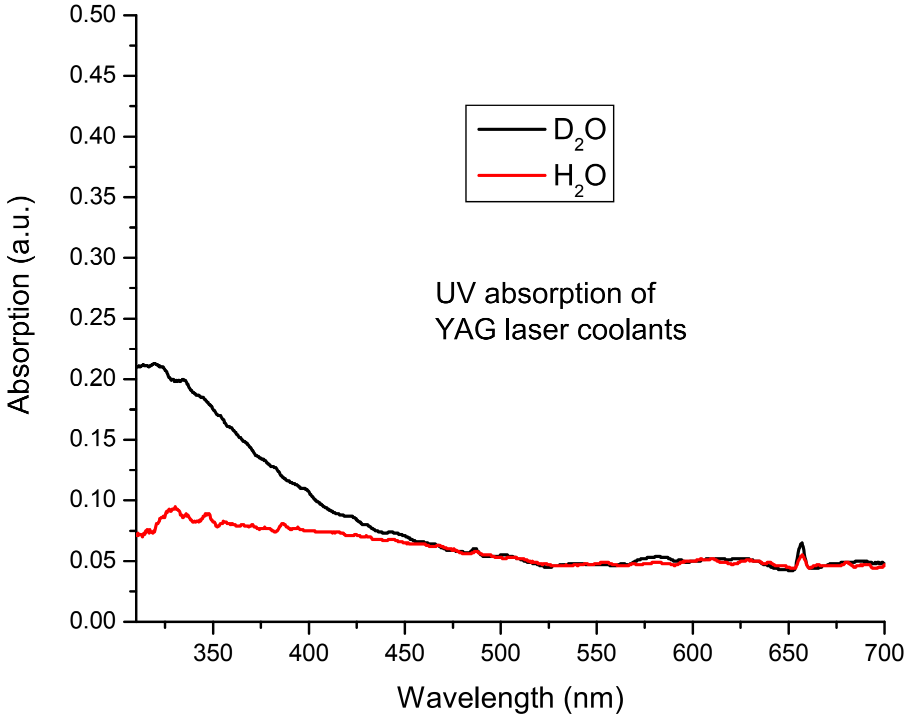

Figure 6.4: Ultraviolet absorption versus wavelength for the cooling fluids used to cool the laser cavity.

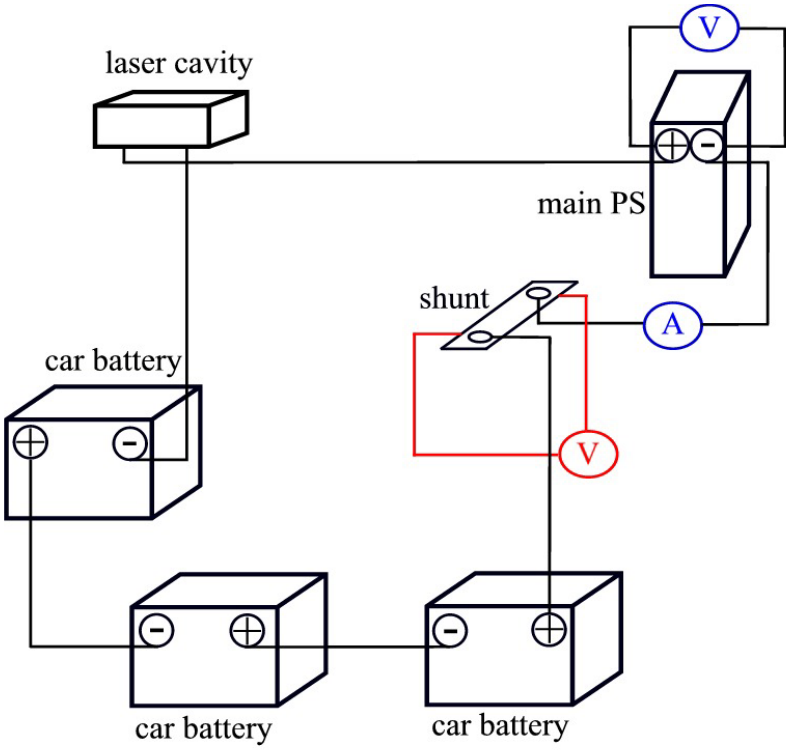

Figure 6.5: Schematic of improved power system for Nd:YAG laser.

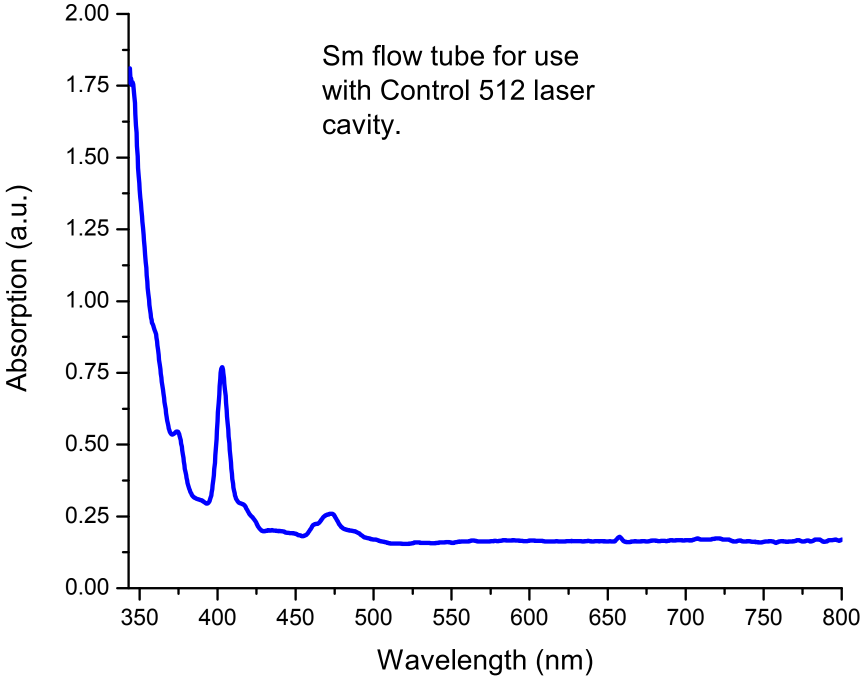

Figure 6.6: Absorption versus wavelength for a Sm-doped flow tube.

The inside of the laser cavity, as was mentioned earlier, is electroplated with 24-karat gold. Gold is often used as a reflector due to its resistance to corrosion even though it is roughly 25% less efficient than silver [6]. The less-efficient reflectivity is the result of the fact that the reflectivity of gold falls drastically at wavelengths shorter than 500nm while that of silver remains high down to 350nm [6]. This is not a problem for Nd:YAG lasers because most of the pumping of the crystal occurs between 700nm and 900nm [2]. Figure 6.7 is a plot of reflectivity versus wavelength for metals commonly used as reflectors in the laser cavity.

Output coupler reflectivity must be matched to each crystal to obtain optimum laser output power. The optimal output coupler reflectivity can be matched to the crystal either empirically or by derivation. The optimal reflection coefficient decreases with increasing pumping power and should, therefore, be optimized for the maximum output power [7]. Mathematically, the optimal output coupler reflectivity, R_{opt}, is given by:

$$-\ln\sqrt{R_{opt}} = \sqrt{\alpha l \frac{P_P}{P_S}} - \alpha l \tag{6.1}$$

where $-\alpha l$ is the loss factor, P_p is the pump power, and P_s is a system constant that depends on the pump lamp and laser cavity and has units of power [7].

The laser rods themselves have anti-reflective coatings on the ends of the barrel that help prevent unnecessary heating of the crystal. The reflectivity of the anti-reflective coatings on the crystal can be determined by:

$$R = \left(\frac{n_S - n_1^2}{n_S + n_1^2} \right)^2 \tag{6.2}$$

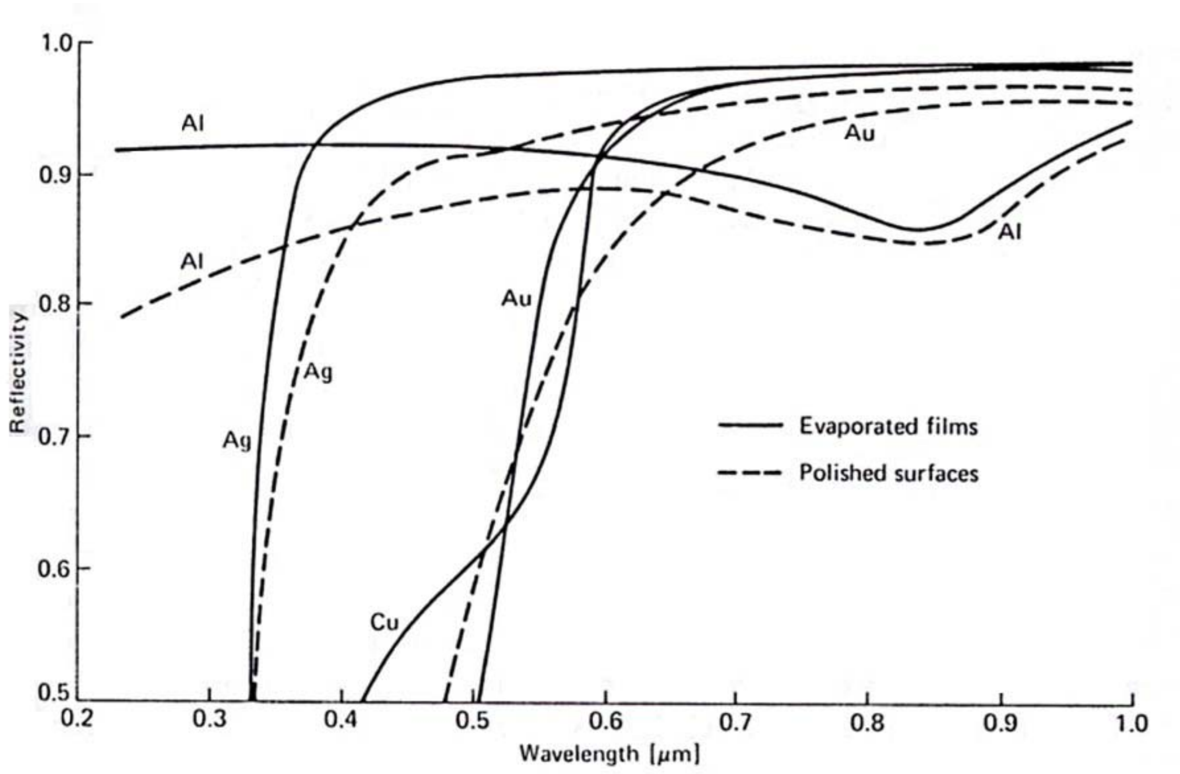

Figure 6.7: Reflectivity versus wavelength for reflectors used in laser cavities. *Source: W. Koechner, Solid State Laser Engineering. Springer-Verlag, Berlin, 1999, p. 395.*

where n_1 is the refractive index of the anti-reflective coating and n_S is the refractive index of the substrate [2]. In the case of Nd:YAG, most anti-reflective coatings are composed of MgF_2 which has a refractive index of 1.38 [2]. MgF_2 is the most common material used because the refractive index of Nd:YAG is very close to 1.90 which mathematically would create a near perfect reflection [2].

In addition to the need for anti-reflective coatings, the laser rods have tight tolerances tuned for each laser cavity. For the Control 512 laser cavity, each laser rod must have a barrel-end flatness of $\lambda/10$ with a parallelism of the end faces being ± 4arcsec [8]. The physical length of the laser rod must be within ± 0.5mm, and the diameter of the crystal must be within ± 0.025mm to achieve a proper fit in the laser cavity [8].

Doping concentration is also very important for optimal lasing operation. As a general guideline, a low doping concentration of roughly 0.6-0.8at.% is used for continuous-wave lasing, and a high doping concentration of approximately 1.2at.% is most desirable for Q-switching operation due to its high energy storage [2]. Q-switching operation occurs when the light path is interrupted in the resonator for a specific time to allow for a maximal inversion to be achieved [7]. Then the buildup is released through stimulated emission.

6.3 Properties of Kr and Xe Arc Lamps

Of all the parameters mentioned in this section, perhaps the most important aspect of Nd:YAG laser operation is the arc lamp used to pump the crystal. A typical arc lamp design can be seen in figure 6.8. Desirable characteristics of an optical pumping source include high conversion efficiency, good overlap of the emission spectrum to the absorption spectrum of the crystal, a sufficiently intense irradiance, and the ability to be operated at high powers [9]. There are three stages to lamp operation: ionization, expansion of the plasma, and operation current [7]. During ionization, a voltage is applied, and current flows through the lamp connections [7]. After ionization, the lamp is kept in operation with a low current in the milliamps to a few amps range [7]. The arc expands and heats up until the arc nearly fills the inner diameter of the tube [7,10]. The plasma arc is then stabilized by the inner tube wall [7].

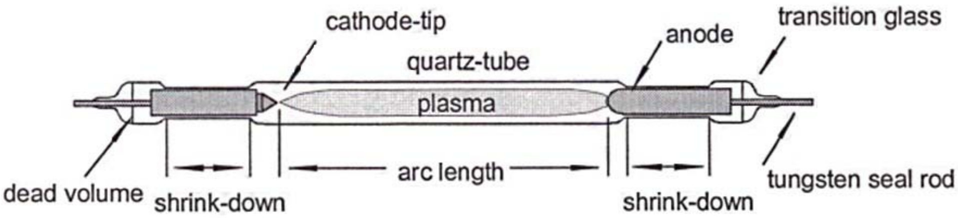

Figure 6.8: A typical design of an arc lamp. *Source: R. Iffländer, Solid-State Lasers for Materials Processing: Fundamental Relations and Technical Realizations. Springer-Verlag, Berlin, 2001, p. 149.*

The luminescence of the lamp then increases with increasing input power to the lamp. However, at considerably high powers, the effect of plasma self-absorption becomes significant and the emitted radiation comes from a thin sheath around the perimeter of the plasma [11]. This problem is solved by lowering the fill pressure of the gas inside the lamp, but the intrinsic emission capabilities of the lamp are sacrificed as a result [11]. In addition to gas pressure inside the lamp, the lamp bore diameter also plays a vital role in light emission. Too large of a lamp bore gives rise to insufficient excitation of the plasma, and too small of a lamp bore results in high wall losses [11]. As the input power to the lamp is increased, the emission spectrum of the lamp suffers. The background radiation increases at a rate nominally 20% greater than the rate of increase of power in the line spectra [11]. At very high lamp input powers, the radiation profile looks similar to that of an ideal blackbody, effectively masking the characteristic line emission from the gas [11]. This effect is more pronounced in gases of light atomic weight [11]. Also, because of Wein's law, the ratio of the ultraviolet output to the electrical pump energy increases with increasing pump energy, effectively producing more heat in the crystal as well as in the lamp itself [12].

It is important to be able to measure the properties of the arc lamps used in pumping Nd:YAG crystals. The instantaneous lamp voltage can be measured using the following relation:

$$V_i = 1.28\left(\frac{L}{d}\right)i^{0.5} \tag{6.3}$$

where *L* is the tube length, *d* is the tube diameter, and *i* is the measured current [54,55]. In addition, the resistance of the lamp in Ohms can be calculated by:

$$R = 0.58\frac{L}{d}\frac{\sqrt[3]{P}}{\sqrt{W}} \tag{6.4}$$

where *L* and *d* are the same parameters as in equation 6.3, *P* is the fill pressure of the gas in the lamp, and *W* is the input power to the lamp [10,13].

Two gases, xenon and krypton, are primarily used to pump Nd:YAG. Krypton lamps have emerged as the most suitable for pumping Nd:YAG, but xenon is still in wide use. Xenon has the higher overall conversion efficiency between the two, but the infrared line spectra of xenon misses all of the Nd:YAG pump bands while the line spectra of krypton proximate well to the Nd:YAG absorption bands [2,9,11,14]. This makes the absorption efficiency for krypton about twice that of xenon [2,15]. In fact, about 60% of the emission of Kr lamps is in the pumping range of Nd:YAG [6]. The emission spectra for both these gases can be seen in figure 6.9.

Laser output power was measured for a Nd:YAG rod using both Kr and Xe arc lamps. The laser output power curves using both gases to pump the Nd:YAG rod can be seen in figure 6.10. As is evident from the figure, Kr arc lamps result in higher laser output power as the spectral output of the Kr lamp matches the Nd^{3+} ion 808nm absorption band much more efficiently than that for Xe.

The lifetime of an arc lamp is dependent upon use. Many ignitions and high current densities limit the lifetime of the lamp through thermal stress and wall darkening. Generally, 10-20% of the electrical input power is dissipated as heat through the electrodes and 30-50% is dissipated through the quartz envelope [2]. At both electrodes, heat is generated by the bombardment of electrons, conduction of heat from the plasma, and absorption of radiation [2,13]. The kinetic energy of electrons incident on the anode is very high as compared to ions impinging on the cathode, and, as a result, the anode heats up much more than the cathode [2]. In addition, the anode conducts more heat from the plasma as its area in contact with the plasma

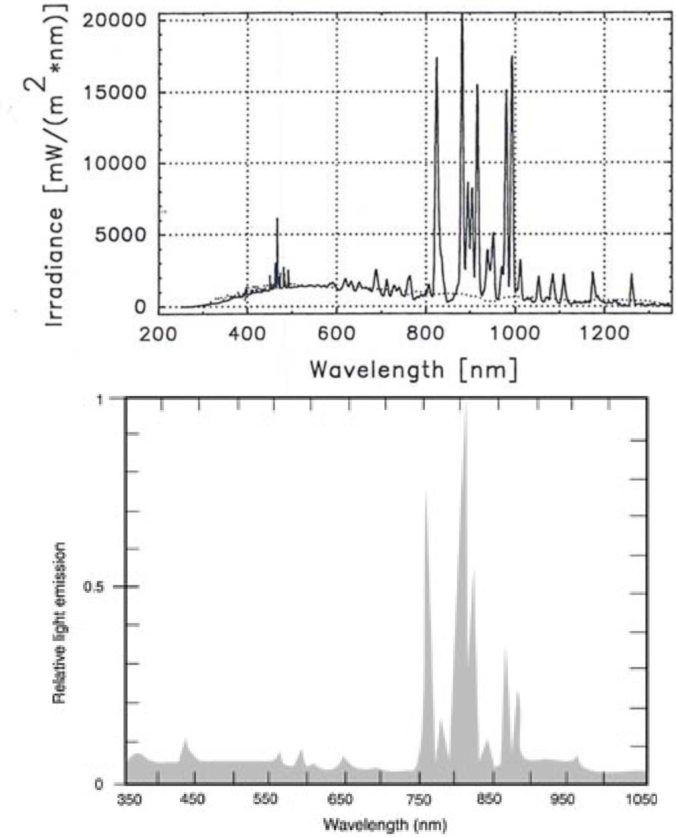

Figure 6.9: Emission spectra of xenon (top) and krypton (bottom). *Sources: (top) http://ncr101.montana.edu/Light1994Conf/5_9_Kofferlein/Fig%20Pay%201.jpg accessed 11-6-08; (bottom) http://www.newport.com/images/webclickthru-EN/images/727.gif accessed 11-6-08.*

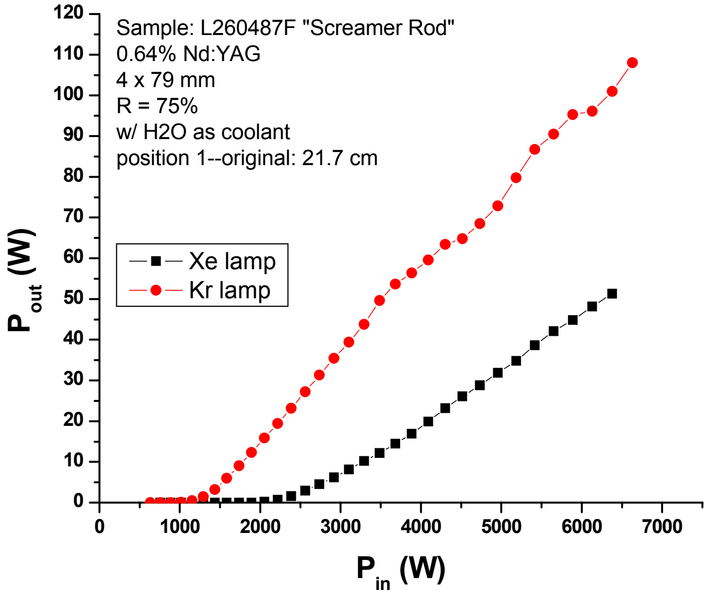

Figure 6.10: Laser output power curve comparison using Xe and Kr lamps.

is larger than that of the more pointed cathode [2]. Moreover, in the course of time, particles sputtered from the cathode of the lamp are deposited at the wall near the cathode leading to a darkening of the inner wall of the quartz [7,13]. This sputtered material absorbs some of the arc radiation and increases thermal loading [2,16]. Eventually, cracks arise starting from the cathode region until the lamp shatters into fragments [7]. A photograph of several used lamps showing this wall darkening can be seen in figure 6.11.

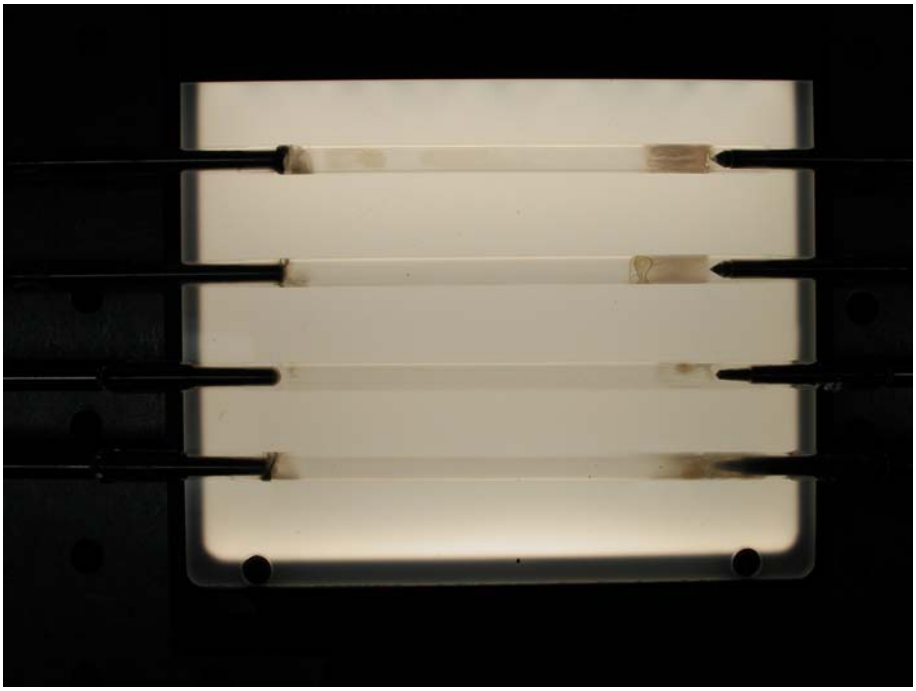

Figure 6.11: Wall darkening in krypton-filled arc lamps seen after several uses.

The maximum input power of a continuous-wave-pumped arc lamp is determined by the permissible thermal stresses in the quartz envelope [2]. The thermal gradient in the quartz envelope can be determined by:

$$\Delta T = \frac{P_W D}{k} \tag{6.5}$$

where P_W is the thermal wall loading per unit area, D is the wall thickness, and k is the thermal conductivity for quartz which has a value of 0.017W/°C [13].

During operation, the inner wall of the quartz envelope is under compression whereas the outer wall experiences tension [2]. Therefore, the total stress is largest on the outside of the quartz envelope, and failure eventually occurs from excessive thermal stress built up in the quartz, which has a rupture stress of 500kg/cm^2 [2].

The laser operation process for arc-lamp-pumped Nd:YAG is quite complicated with many different actions that decrease the output power of the crystal. Some of these actions are from the power system or the cooling system and some are from the properties of the crystal and the arc lamp. Figure 6.12 is a flow chart of the different actions and their corresponding efficiencies. From the figure, it can be seen that only about 2% of the original power becomes laser power.

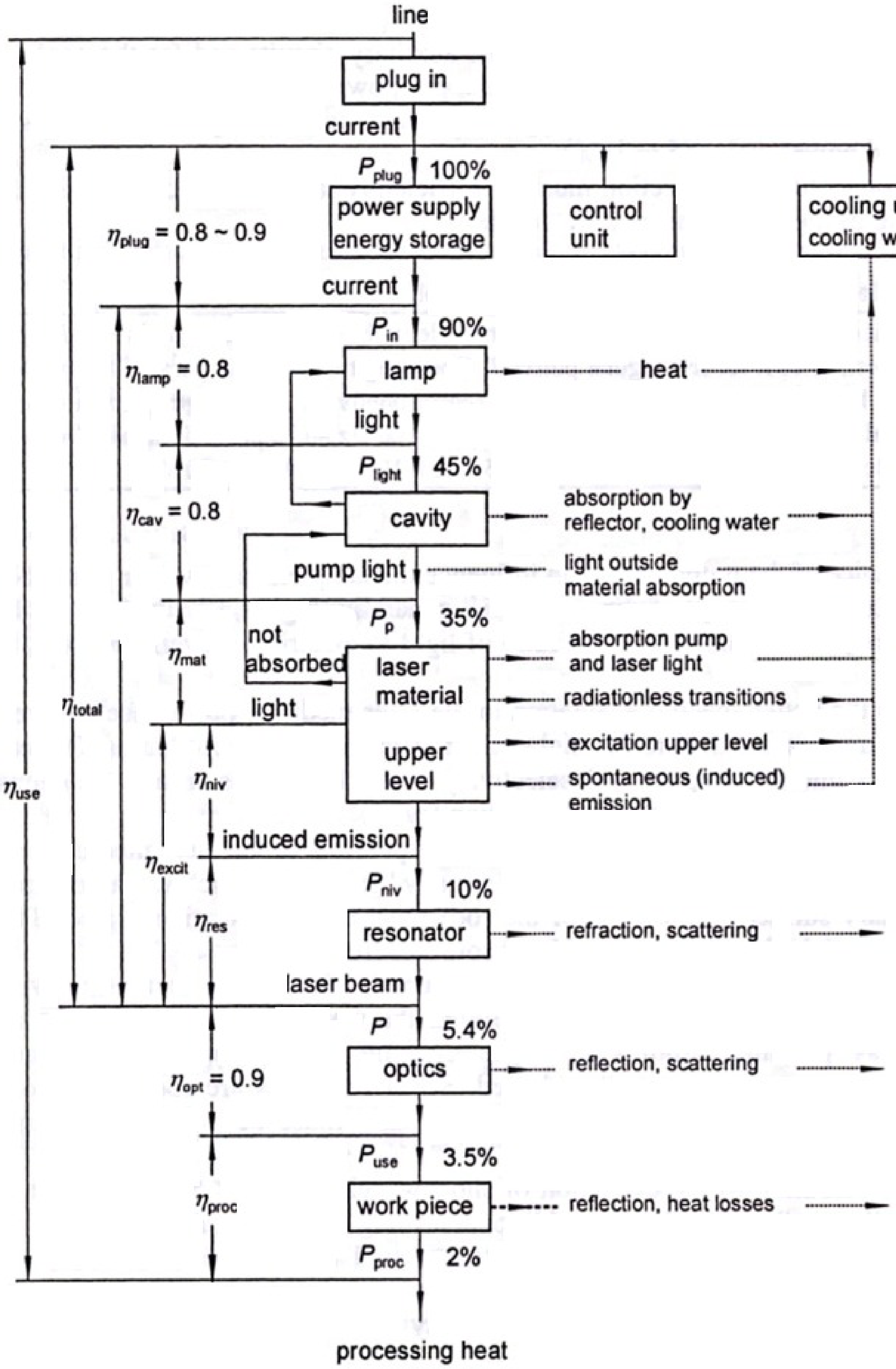

Figure 6.12: Numerical values of efficiencies for Nd:YAG laser operation. *Source: R. Iffländer, Solid-State Lasers for Materials Processing: Fundamental Relations and Technical Realizations. Springer-Verlag, Berlin, 2001, p. 44.*

6.4 D_2O vs. H_2O as a Cooling Fluid and Thermal-Induced Birefringence

Because the heat capacity is higher for heavy water than regular water (20.16cal/°C/mol compared to 17.99cal/°C/mol according to NIST data), heavy water can remove more heat from the crystal and lamp thus cooling the crystal and lamp more efficiently. This can result in higher laser output power as well as higher slope efficiency when heavy water is used as a cooling fluid. To determine the veracity of this claim, the laser performance of a Nd:YAG laser rod was measured using deionized water as a cooling fluid. The deionized water was then replaced with deionized heavy water and laser performance was measured once again. This was done for several Nd:YAG laser rods. Results were typical to the plot seen in figure 6.13. Laser output power and slope efficiency were improved. Table 6.1 gives values for the various rods. The use of heavy water as a coolant increases maximum laser output power and slope efficiency.

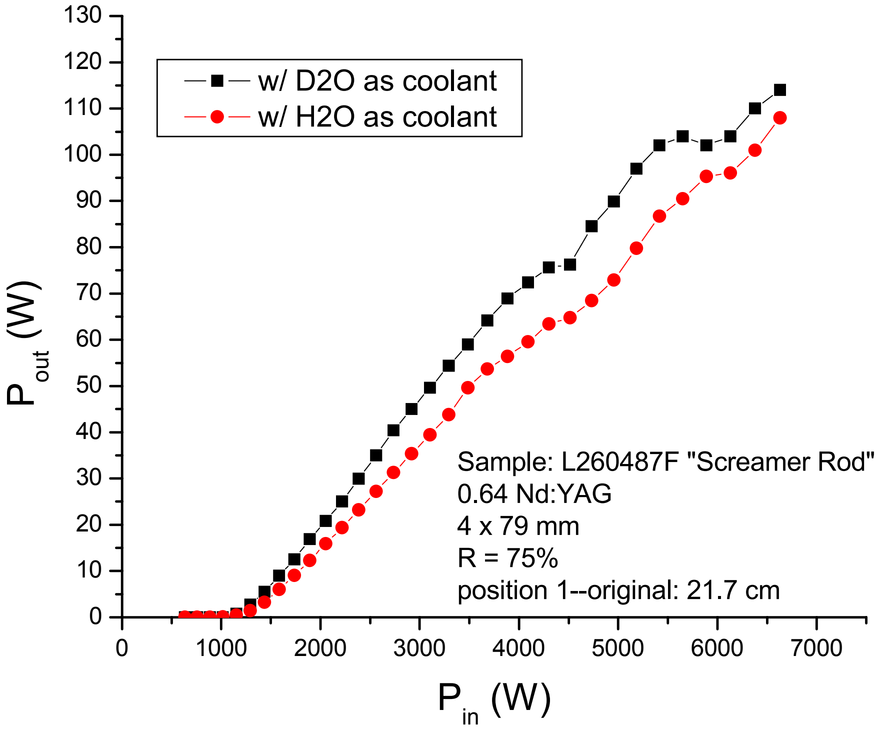

Figure 6.13: Comparison of laser output power using H_2O and D_2O as cooling fluids.

Table 6.1: Laser output power and slope efficiency for several Nd:YAG rods using regular and heavy water as a cooling fluid with R = 75% output coupler.

Sample	D_2O η_{slope} (%)	D_2O $P_{out,max}$ (W)	H_2O η_{slope} (%)	H_2O $P_{out,max}$ (W)
V75392T	2.73	115	2.63	114
53522	3.27	140	3.17	130
L260487F	2.59	114	2.19	108
V75393B	3.17	146	3.00	138
68179	3.23	123	2.74	110
V77649	3.02	134	2.73	128

To determine how much heat can be removed by the cooling fluid, one can measure both the incoming cooling fluid temperature and the exiting cooling fluid temperature as well as the flow rate and use the following equation:

$$P = \frac{\Delta T \times f_V}{0.24} \tag{6.6}$$

where P is the heat removed by the cooling fluid and is measured in kW, ΔT is measured in °C, and f_V is the flow rate of the cooling fluid [17].

The problem with using heavy water to remove heat from the laser cavity is the fact that it is difficult to keep the input water temperature constant throughout high-power runs. As can be seen in figure 6.14, as the laser power measurement run progresses, the input water temperature increases. This limits laser performance and reduces the amount of heat that can be removed from the system. In order to reduce input water temperature, a much larger cooling fluid reservoir must be used, which was not accessible for the measurements presented here.

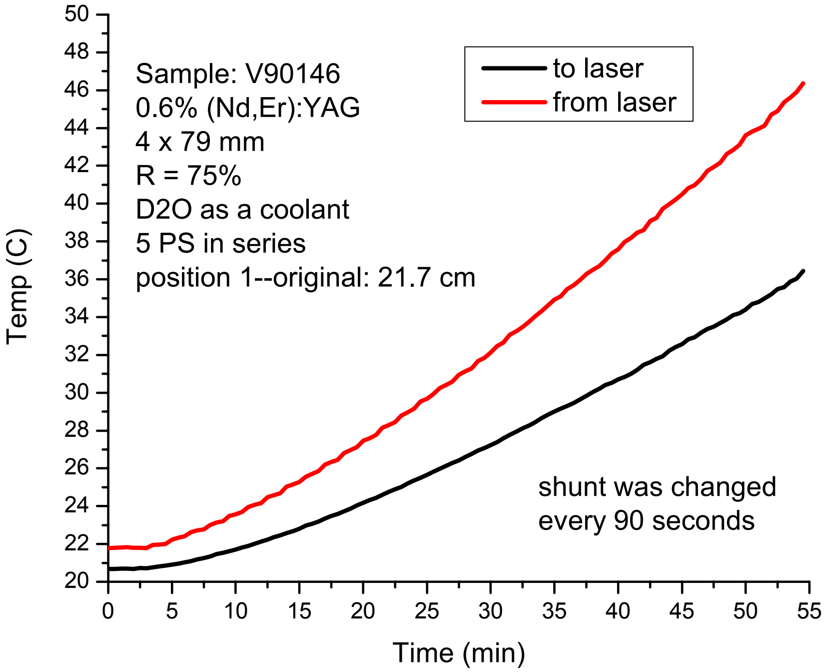

Figure 6.14: Heavy water temperatures both to and from the laser cavity.

Although cooling the crystal can improve the laser output power, too much cooling can create very large temperature gradients which can in turn generate mechanical stresses in the laser rod [2]. These mechanical stresses can degrade the laser beam quality due to thermal lensing and thermally-induced birefringence [8,18]. Thermally-induced birefringence occurs as a result of the crystal's change in refractive index along the different crystallographic directions through the photoelastic effect [3,19-22]. Birefringence causes depolarization of the laser beam which can account for more than 10% laser output power loss under high pumping power conditions [23]. This was observed in the laser input power range above 4,000W in figure 6.13.

Figure 6.15 is a plot of the various cut directions of Nd:YAG rods and their depolarization as a function of absorbed pump power. The plot suggests that instead of the usual (111) orientation of cut laser rods, one should use the (110)-oriented rods as they are less prone to the depolarization effects caused by thermally-induced birefringence and thermal rollover of laser output power.

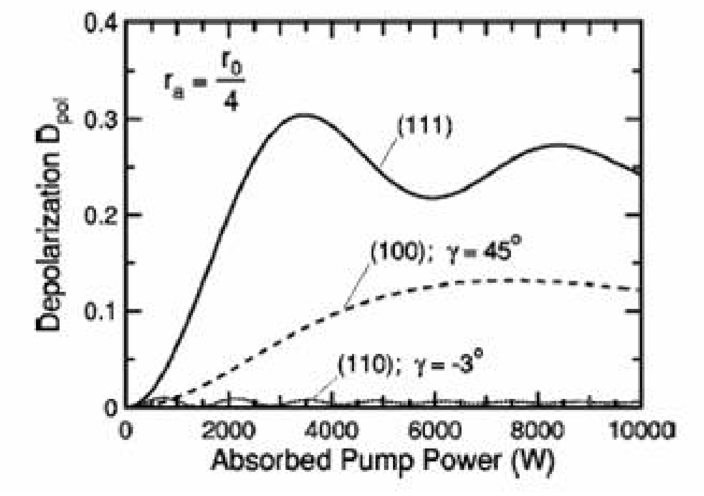

Figure 6.15: Depolarization dependence on absorbed pump power for different cut directions of Nd:YAG. *Source: I. Shoji and T. Taira, Appl. Phys. Lett. 80 (2002) 3050.*

6.5 Core Breakdown Study

The most significant source of stress in the boule is from core faceting. The core-faceting region is located in the central portion of the boule and is the result of three {211} facet-planes intersecting in a [111]-grown YAG boule and is present in almost all garnet-structured crystals [24-32]. Figure 6.16 is a cross-polarization photograph of the core faceting commonly observed in YAG boules. The spoke-like pattern of the core faceting indicates that there are three planes that are contributing to the core strain. The dark portions seen in the boule photograph are regions of little to no strain, and it is from these areas that laser rods should be cored. There can also exist boules that have more than the three {211} planes intersecting to form the core-faceting region of the boule. For example, in slightly off-axis, [111]-grown Nd:YAG, {110} planes can also intersect in addition to the {211} planes causing a non-symmetric core-faceting region [28,30]. Such a core region can be seen in figure 6.17. According to several studies, core-free or minimal core-facet-region boules can be obtained by maintaining a flat crystal/melt interface during crystal growth [33,34]. A cross-polarization photograph of a boule with a very small core region can be seen in figure 6.18. The lattice parameter of a faceted region is slightly larger than that of an unfaceted region with the difference, $\Delta a/a$, being 1.3×10^{-4} and which may be attributed a variety of effects including impurity segregation in the facets, stoichiometry variations in the core region, and dislocation enrichment in the facets [35]. This is evidenced by the fact that the core region contains a higher concentration of electron traps [36].

Coring laser rods from regions that are not affected by the core faceting should yield higher laser output powers and better efficiencies. Also, reducing core size should decrease the amount of strain in the crystal and should increase the useful coring area of the boule [27]. Currently, the cutting loss is more than 50%, and faceting regions can still be found in some commercial laser rods [37]. It is suspected that reducing the diameter of the boule during growth may reduce the size of the core faceting, but that has not yet been substantiated. Strain from core faceting can lead to core breakdown, the severe cracking of the boule [38]. Core breakdown is often associated with the presence of two conditions, core faceting and the presence of crack initiators such as voids [38]. While the presence of voids near the core does not necessarily result in boule fracture, voids can act as stress concentrators [38,39].

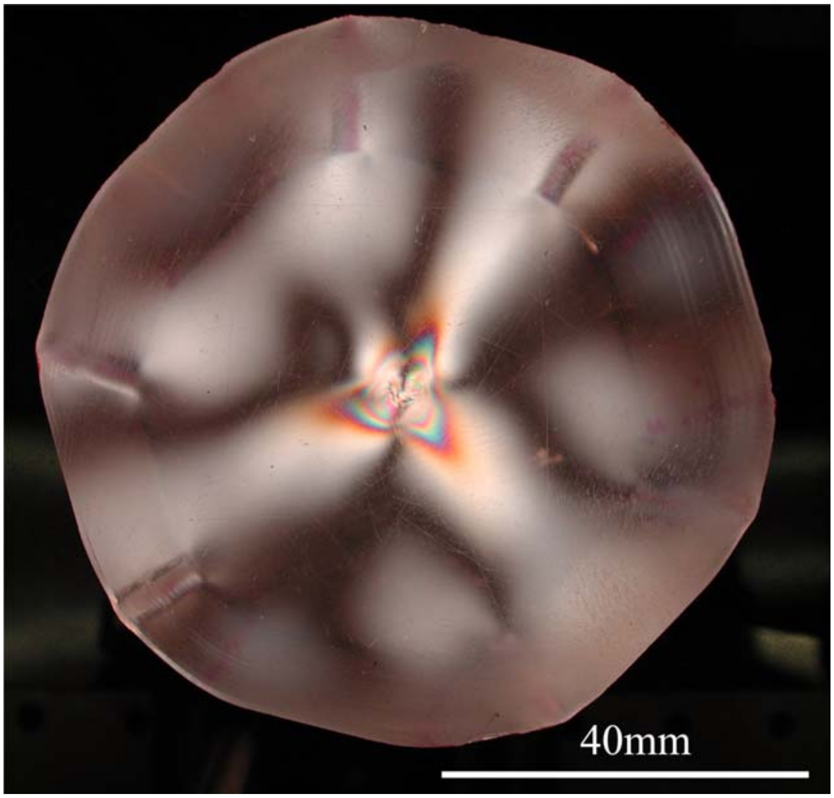

Figure 6.16: Cross-polarization photograph of the core faceting seen in YAG boules.

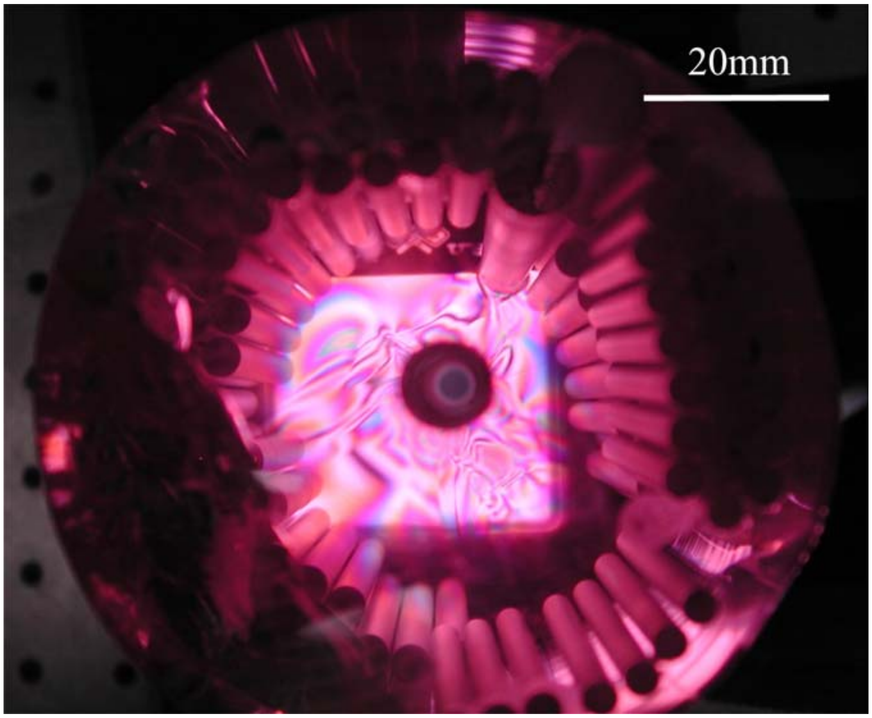

Figure 6.17: Cross-polarization photograph of a multiple plane core-faceting region in a Nd:YAG boule.

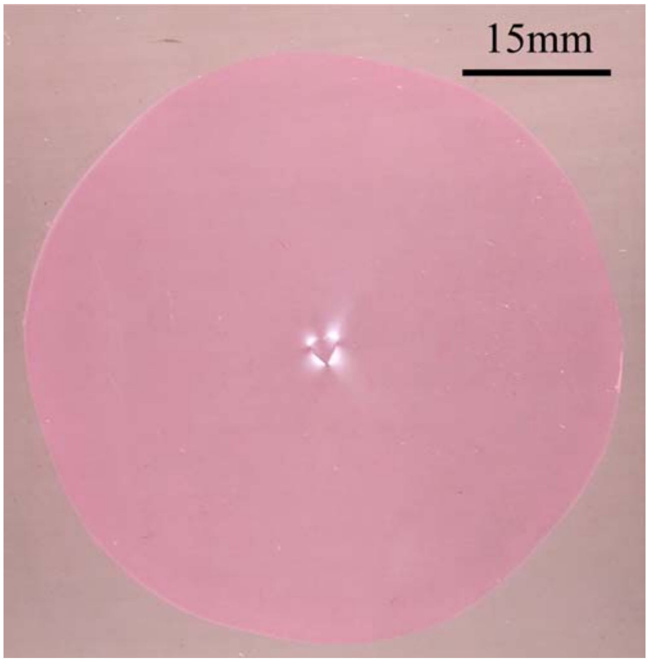

Figure 6.18: Cross-polarization photograph of a Nd:YAG boule slice with a small core.

6.6 Annealing Study of V981 Series Laser Rods

To determine the effects of oxidizing heat treatment on output laser power and laser power threshold, four rods, V98138, V98139, V98140, and V98141, were obtained without AR-coatings on the barrel ends. This series of rods contained Nd^{3+} ion concentrations of roughly 0.6%at. Each rod was measured for laser performance in their as-received state up to an input power maximum of 3,200W. The samples were then annealed in a SentroTech high-temperature box furnace (model ST-1700) equipped with $MoSi_2$ heating elements.

Samples V98138 and V98140 were annealed at 1,500°C for 72 hours in 0.5L/min UHP O_2. Laser performance was then subsequently measured using both the R= 75% and R = 90% output couplers. Then the samples were annealed again for 72 hours in 0.5L/min UHP O_2 but at a temperature of 1,400°C. Laser performance was measured after this second anneal using both output coupler reflectivities. Finally, these two rods were annealed in 0.5L/min UHP N_2 at a temperature of 1,400°C for 72 hours. Laser performance was then measured once again using both output coupler reflectivities. The results of laser output power and change in threshold can be seen in table 6.2.

Samples V98139 and V98141 were measured for laser performance using both R = 75% and R = 90% output couplers in their as-received states. The samples were then annealed at 1,400°C in 0.5L/min UHP O_2 for 72 hours. The laser performance of both rods was measured once again using both output coupler reflectivities. The results for these two rods can be seen in table 6.3.

As is evident for both sets of rods, annealing in either an oxidizing or reducing atmosphere does not improve laser performance or threshold. Results are in fact mixed, especially for changes in laser threshold.

Table 6.2: Effects of annealing on laser performance for V98138 and V98140.

Treatment	V98138 $P_{out,max}$ (W)	V98138 P_{th} change	V98140 $P_{out,max}$ (W)	V98140 P_{th} change
As-received R = 75%	29.3	-	28.0	-
As-received R = 90%	22.8	-	21.8	-
Post 1,500°C O_2 R = 75%	27.0	increase	22.9	decrease
Post 1,500°C O_2 R = 90%	17.5	decrease	16.6	decrease
Post 1,400°C O_2 R = 75%	26.8	decrease	25.0	increase
Post 1,400°C O_2 R = 90%	20.2	increase	20.0	increase
Post 1,400°C N_2 R = 75%	24.5	increase	22.5	decrease
Post 1,400°C N_2 R = 90%	18.9	decrease	14.5	decrease

Table 6.3: Effects of annealing on laser performance for V98139 and V98141.

Treatment	V98139 $P_{out,max}$ (W)	V98139 P_{th} change	V98141 $P_{out,max}$ (W)	V98141 P_{th} change
As-received R = 75%	31.0	-	27.7	-
As-received R = 90%	22.1	-	21.8	-
Post 1,400°C O_2 R = 75%	29.1	decrease	26.0	decrease
Post 1,400°C O_2 R = 90%	25.2	decrease	18.4	decrease

6.7 Optimal Temperature Annealing Study of V108 Series Laser Rods

A second annealing study was conducted to determine if a lower temperature anneal would increase laser performance. Nine rods, marked consecutively as V108733 through V108741, were obtained. Each sample contained roughly 0.6%at. Nd^{3+} ion concentration and possessed no AR-coatings on the barrel ends. Each sample, except for V108733, V108734, and V108741 – which either broke after the 1,200°C anneal (V108733 and V108734) or were used for positron measurements for a different study (V108741), were measured for laser performance and annealed in 0.5L/min UHP O_2 as follows: as-receive laser power measurement, 1,000°C anneal, 1,000°C anneal laser performance measurement, 1,200°C anneal, 1,200°C anneal laser performance, 1,500°C anneal, 1,500°C anneal laser performance. One rod, V108740, was measured for laser performance out to high input powers of roughly 5,000W. The other rods were measured for laser performance out to 3,200W. All rods were measured with the R = 90% output coupler reflectivity. The results of the study can be seen in table 6.4.

To determine whether the laser performance results were affected by heat-induced defects in the barrel ends of the rod, the rods were repolished occasionally and laser performance was remeasured. The effect repolishing had on laser performance can be seen in table 6.5.

As is evident by the results of table 6.4, annealing at 1,500°C resulted in a decrease of laser performance. This may be due to heat-induced defects in the barrel ends. Subsequent repolishing shows mixed results, which was expected as each crystal was repolished by human hand by the crystal manufacturer. Because crystal polishing is done entirely by hand, it is a major factor in laser performance. Some sort of standardization should be introduced to the polishing process, or the polishing process should be automated.

Table 6.4: Optimal annealing temperature study for V108 series rods as measured by laser performance.

Sample	As-received (W)	Post 1,000°C (W)	Post 1,200°C (W)	Post 1,500°C (W)
V108733	18.8	20.6	21.7	-
V108734	19.0	21.4	23.1	-
V108735	17.9	20.7	18.7	19.7
V108736	17.0	19.4	19.0	15.5
V108737	15.5	22.7	19.1	18.8
V108738	17.1	23.4	20.0	16.0
V108739	17.0	23.1	20.5	16.2
V108740	21.3	30.3	28.8	27.7
V108741	16.6	15.9	-	-

Table 6.5: The influence of repolishing on laser performance for the V108 series rods.

Sample	Before 1st Repolishing (W)	After 1st Repolishing (W)	Before 2nd Repolishing (W)	After 2nd Repolishing (W)
V108733	20.6	19.1	-	-
V108734	-	-	-	-
V108735	20.7	19.2	19.7	18.2
V108736	15.5	19.1	-	-
V108737	15.5	19.1	18.8	20.5
V108738	20.0	25.3	16.0	21.7
V108739	20.5	21.2	16.2	14.2
V108740	21.3	20.5	27.7	29.0
V108741	-	-	-	-

6.8 Summary of Annealing Studies of Nd:YAG

From the data presented, it does appear that annealing at temperatures in the range of 1,000°C to 1,200°C is ideal for UHP O_2 at a flow rate of 0.5L/min. Annealing at higher temperatures is not beneficial and can be deleterious. Annealing in an oxidizing atmosphere may be beneficial to laser performance, but it does not appear that oxidation annealing solves the laser performance issues observed in all Nd:YAG laser rods as laser threshold was not uniformly improved. In fact, threshold was reduced for some rods regardless of heat treatment parameters.

6.9 Measurements of the Possible Antisite Defect

According to literature, the antisite defect shows luminescence near the ultraviolet range (~400nm) at room temperature when excited by 370nm light [40,41]. This luminescence may be coupled to the presence of oxygen vacancies, which occur as a result of aluminum deficiency in YAG boules [42,43]. To measure the properties of this luminescence, an undoped YAG disk was obtained. It was pumped by a Spectroline Hg vapor lamp (model 11SC-1). The resulting photoluminescence was measured with an Ocean Optics spectrometer. Under 370nm excitation from a mercury vapor lamp, the undoped YAG disk exhibited photoluminescence as can be seen in figure 6.19. The emission spectrum taken of this photoluminescence can be seen in figure 6.20. The intensity of the photoluminescence observed in undoped YAG can be reduced by high-temperature oxidation anneal as can be seen in figure 6.21. From the photograph, it is seen that the photoluminescence from the annealed YAG disk is not as intense as that from the as-grown YAG disk.

Annealing in an oxidizing environment may have a two-fold effect on YAG. The oxygen atoms may fill oxygen vacancies, and the antisites may return to their proper lattice sites. While antisites are a concern in the growth of Nd:YAG, they are not presently considered responsible for the loss observed in Nd:YAG. However, their presence may indicate the presence of aluminum vacancies.

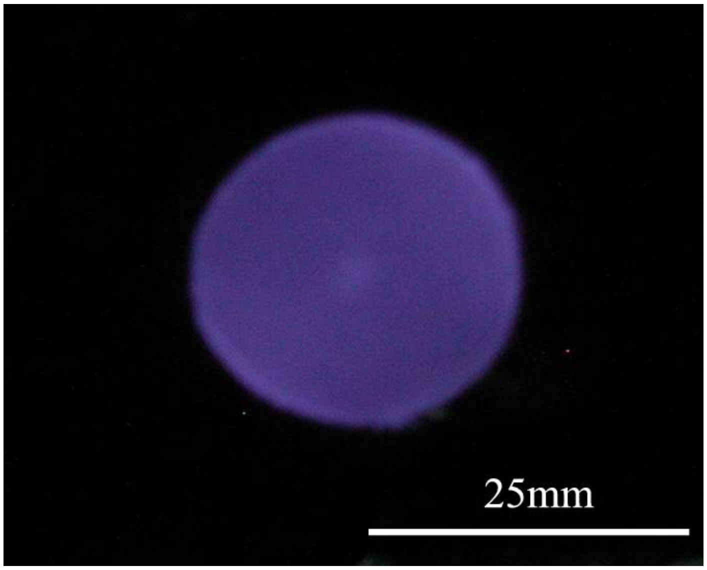

Figure 6.19: Photograph of an undoped YAG disk photoluminescing as a result of 370nm excitation.

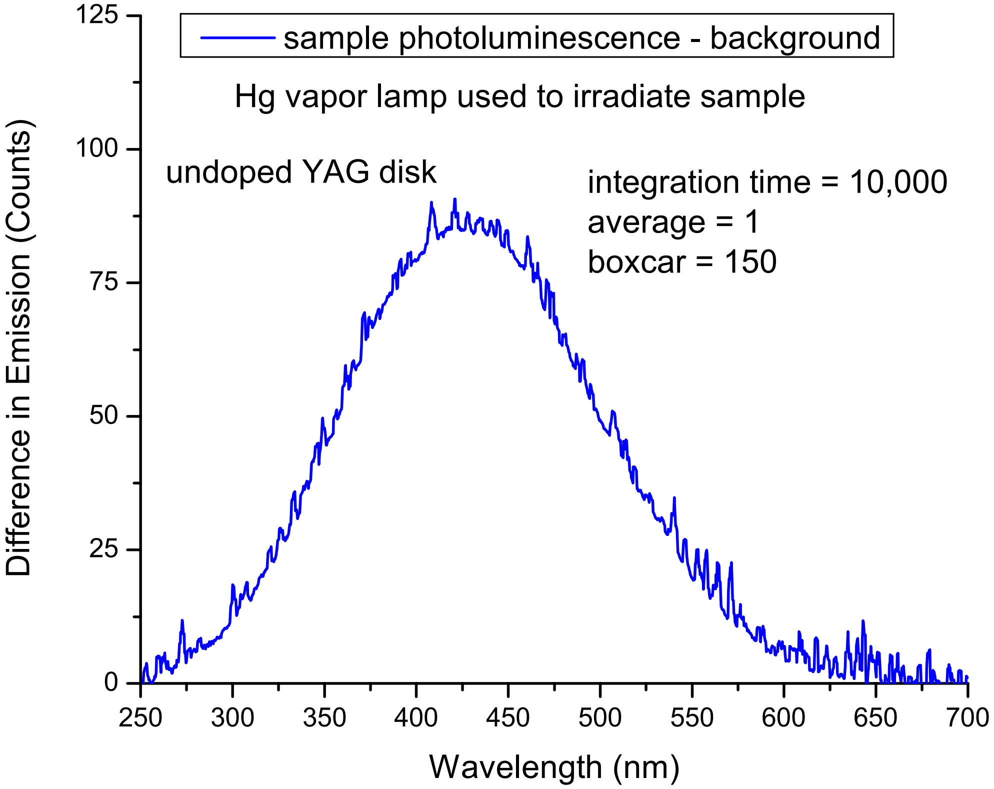

Figure 6.20: Photoluminescence spectrum of the undoped YAG disk seen in figure 6.19.

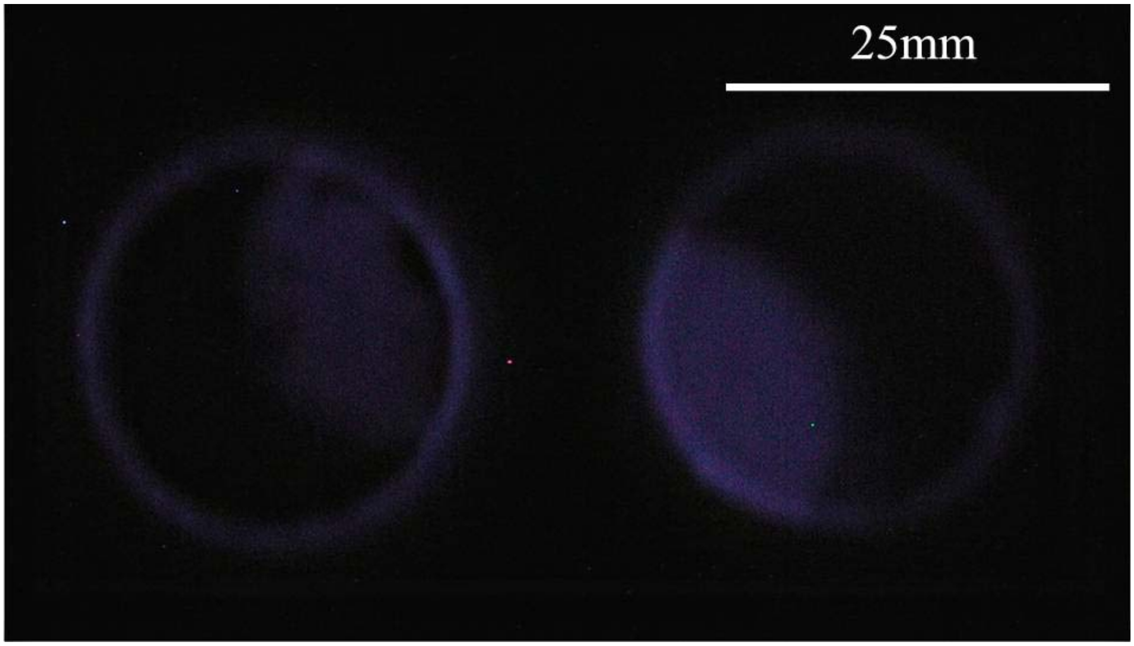

Figure 6.21: Photoluminescence of two identical, undoped YAG disks both partially exposed to 370nm light. The disk on the left has been annealed at 1,500°C in air. The disk on the right has not been annealed.

6.10 Neutron Activation Analysis of Nd:YAG Rods

Using just the literature, it can be concluded that the 256nm absorption peak may not be due to iron and could be the result of iridium incorporation into the crystal from the crucible. To experimentally verify this, several rods and growth powders were obtained and absorption spectra for each rod were taken. All rods contained the 256nm absorption peak. The rods were then sent to the Washington State University Radiation Center for neutron irradiation. A certified standard was also obtained to aid in the determination of the absolute impurity concentrations within the rods and powders. The rods, powders, and the standard were all irradiated for six hours and were then allowed to radiologically decay for three weeks until the 35% Ge detector used to measure the gamma-rays emitted from the rods and powders had deadtimes of less than 2%. Each sample including the standard was measured by the detector for 10,000 seconds, and the results were analyzed using Canberra's Genie 2000 software. Further details of the neutron activation analysis (NAA) process are contained in Appendix D. The plots seen in figure 6.22 and figure 6.23 contain raw data obtained by the NAA measurements. Figure 6.22 is a gamma-ray spectrum of the 1,099keV Fe-59 gamma-ray region, and figure 6.23 is a gamma-ray spectrum of the 468keV Ir-192 gamma-ray region. As is evident from the plots, iridium was found in every rod and no iron was detected in any of the rods. Concentration analysis from NAA measurements regarding these two impurities can be found in table 6.6. The results show that none of the Nd:YAG rods contained any measurable amounts of iron. This was also the case with the yttria powder; however, the alumina powder proved to contain 3.83 ± 0.93ppm %at. iron impurity concentration. Accepting that the data obtained from the very accurate and sensitive method of NAA is valid and correct; it then follows that the 256nm absorption peak observed during spectroscopic measurements cannot be from the Fe-O charge transfer band ascribed by most of the literature as these rods contain no observable iron impurities. The results obtained help support the contention that the charge transfer band found at 256nm may be the result of iridium impurities from the crucible and not iron impurities, as iridium was found in each rod but not in either powder.

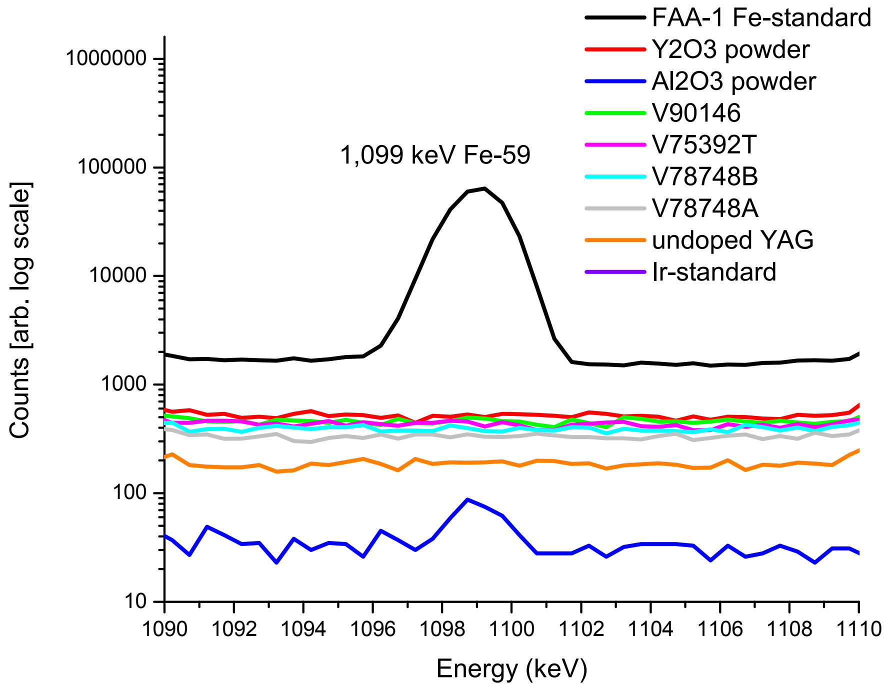

Figure 6.22: Gamma-ray spectrum for the Fe-59 energy region (1,099keV).

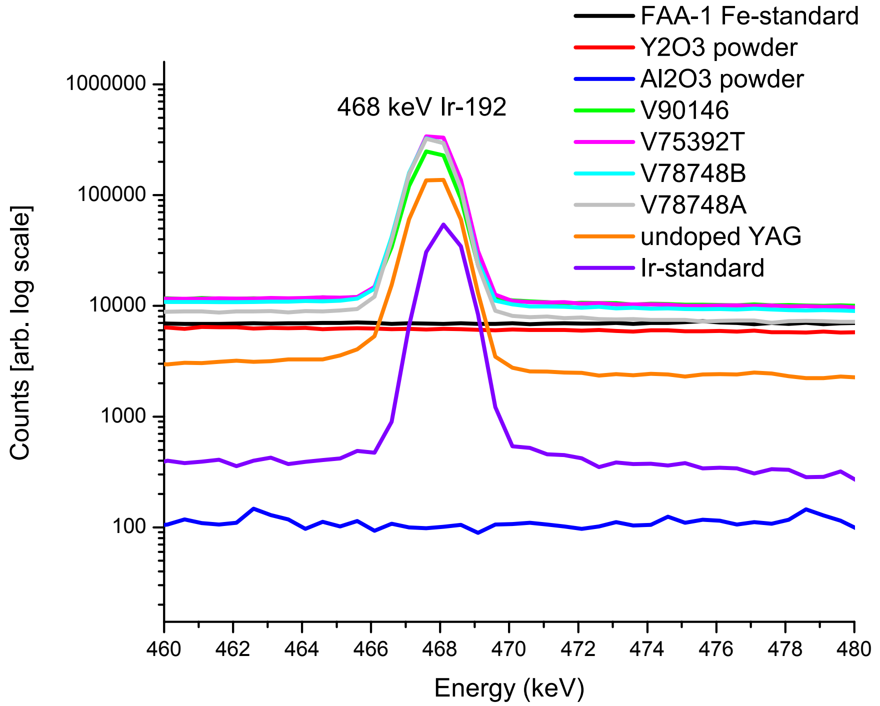

Figure 6.23: Gamma-ray spectrum for the Ir-192 energy region (468keV).

Table 6.6: NAA results of Nd:YAG rods and raw materials (powders). Other impurities found by NAA measurements can be found in Appendix E.

Sample ID	Fe conc. (ppm %at.)	Ir conc. (ppm %at.)
V90146	< 0.0494	2.29 ± 0.12
V75392T	< 0.0494	4.27 ± 0.22
V78748B	< 0.0502	2.85 ± 0.15
V78748A	Not detected	1.63 ± 0.08
V75393B	Not detected	2.19 ± 0.11
Al_2O_3 powder	3.83 ± 0.93	Not detected
Y_2O_3 powder	< 0.0584	Not detected

6.11 Measurements to Correlate Ir Impurity Concentration with Laser Performance

It has been argued that the 256nm absorption peak found in YAG is most likely due to iridium incorporation from the crucible into the growing crystal. It has also been shown through literature that the presence of iridium in the crystal can have a deleterious affect on laser performance. To correlate laser power with iridium concentration, three 1.0% Nd:YAG rods were obtained. Laser power and absorption spectra were taken for the rods. The rods were then sent for NAA. Table 6.7 contains the results of the NAA analysis along with the results of the laser output power measurements and absorption spectra. When this data is plotted, as can be seen in figure 6.24, figure 6.25, and figure 6.26, it is apparent that the 256nm absorption peak intensity, iridium impurity concentration, and measured maximum laser output power correspond well with one another.

Table 6.7: NAA results of three 1.0% Nd:YAG rods with corresponding absorption data at 256nm and laser output power measurements—maximum laser output power using a constant input power and an R = 90% output coupler ($P_{out,max}$) and slope efficiency (η_s).

Sample ID	$P_{out,max}$ (W)	A_{256nm} (arb. units)	Ir conc. (ppm %at.)	η_s (%)
V113295	74.6	2.326	4.94 ± 0.27	2.85 ± 0.04
V113389	69.9	2.373	5.20 ± 0.28	2.53 ± 0.01
V108224	58.9	2.478	6.12 ± 0.38	2.25 ± 0.06

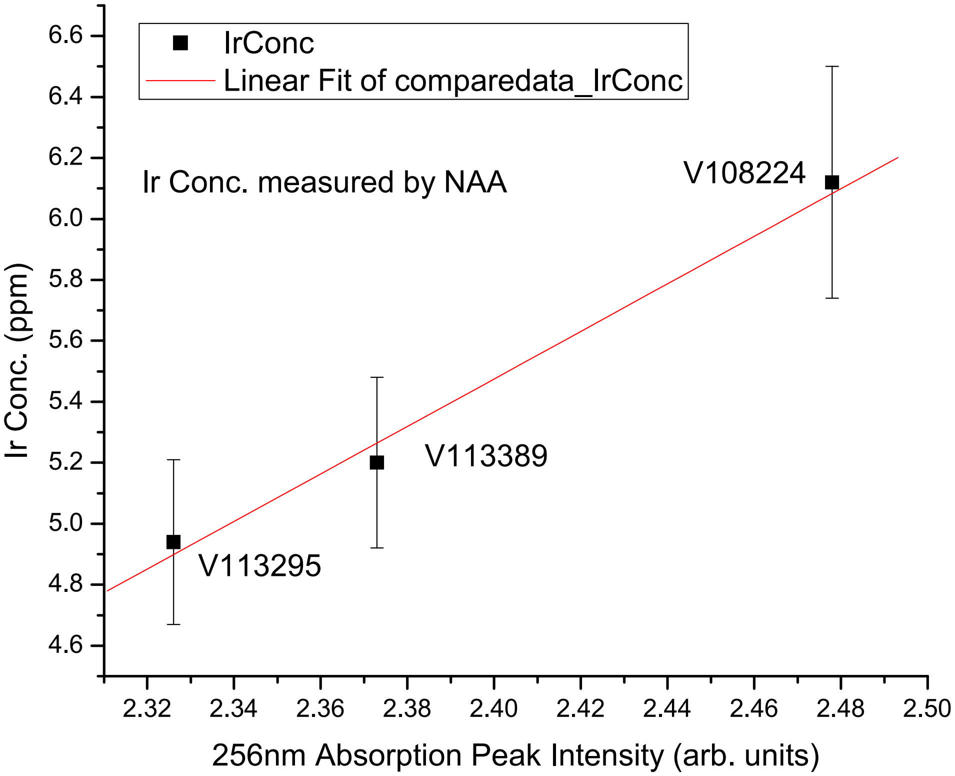

Figure 6.24: Iridium impurity concentration vs. 256nm absorption peak intensity.

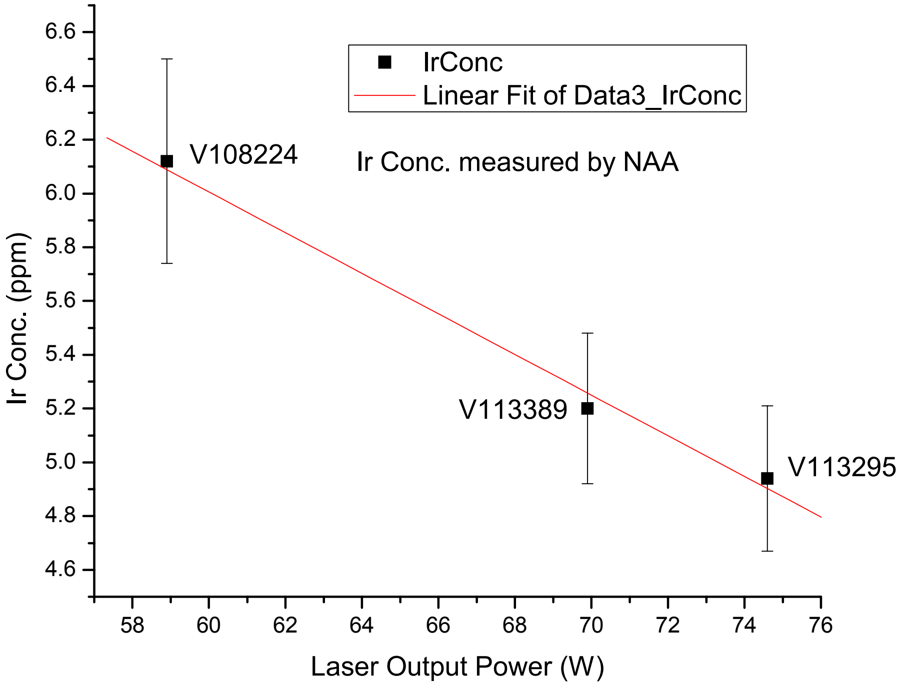

Figure 6.25: Maximum laser output power vs. 256nm absorption peak intensity.

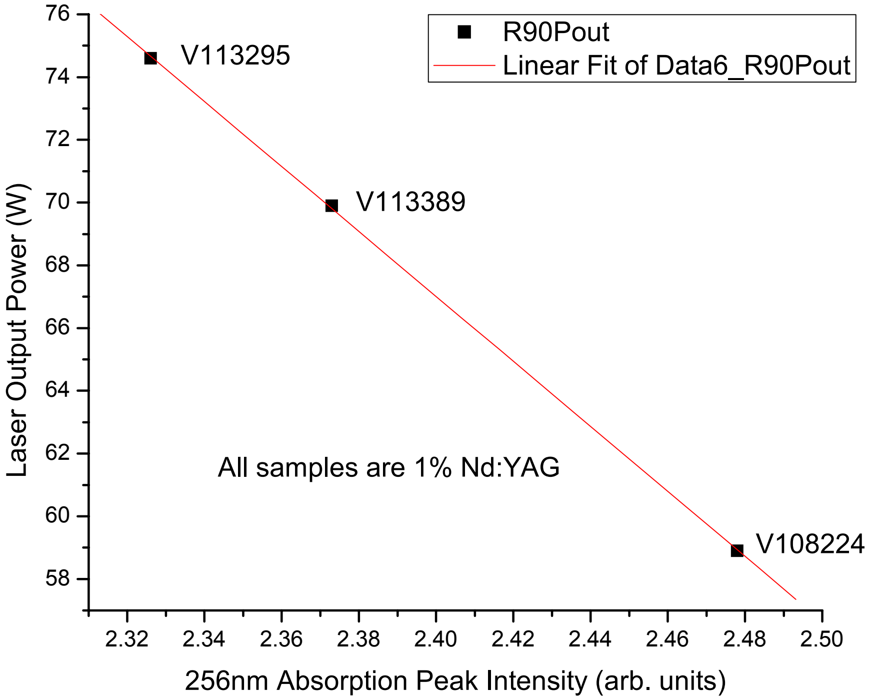

Figure 6.26: Iridium impurity concentration vs. maximum laser output power.

6.12 GDMS Measurements of Nd:YAG Laser Rods

The same rods that were used for NAA and laser power studies in the previous section were sent to Evans Analytical Group for glow discharge mass spectroscopy (GDMS) to determine if GDMS results could be as accurate as NAA results. The results of the GDMS measurements can be seen in table 6.8. As is evident from the table, no iron was detected in the rods above the detection limit of 1.0ppm %at. However, iridium impurities were found in the rods at detectable limits. While NAA and GDMS measurements differ in regard to iridium impurity concentration, these two spectroscopy processes further suggest that the identity of the 256nm absorption peak observed in YAG may be due to iridium impurity ions and not iron impurities.

Table 6.8: Glow discharge mass spectroscopy results for the same rods measured by NAA in table 6.7. Values of ND indicate the impurity concentration was below the detection limit. Two measurements were taken for each rod. The listed values are the average of the two measurement sets.

Sample ID	[Fe] (ppm %at.)	[Ir] (ppm %at.)
V113389	ND	1.0
V108224	ND	1.1
V113295	ND	0.9

A second set of GDMS studies were done using a Nd:YAG laser rod that is considered to be the benchmark for laser power. Two pieces of the rod were sent to Evans Analytical Group for full scans. The results of the GDMS study can be seen in table 6.9, and the full scan results can be seen in Appendix F. As can be seen in table 6.9, iron impurities were not detected but iridium impurities were found.

Table 6.9: GDMS results for benchmark Nd:YAG laser rod. ND indicates that the impurity was not detected.

Sample	Fe Conc. (ppm %at.)	Ir Conc. (ppm %at.)
Screamer Rod Piece 1	ND	1.1
Screamer Rod Piece 2	ND	1.0

6.13 Photoluminescence Studies of Nd:YAG

Additionally, low-temperature photoluminescence (PL) data was taken on several rods to verify the presence of iridium. A portion of the measurements taken at Pacific Northwest National Laboratory's Environmental Molecular Sciences Laboratory (EMSL) can be seen in figure 6.27. Samples were immersed in liquid nitrogen at a temperature of 70K. A Continuum NY61-20 laser, a frequency-quadrupled Nd:YAG laser emitting at 15 Hz, 40mJ beam at 266nm with a pulsewidth of 7ns, was used to pump a portion of the 256nm absorption band observed in the samples. The emission was collected by a Princeton Instruments PI-MAX 1024 RB-18 intensified CCD camera.

While several peaks emerged from pumping the absorption band, the PL peak located near 830nm is of particular interest. As can be seen from figure 6.27, PL counts at 830nm seem to correspond with iridium concentration as determined by NAA. This seems to also correlate with literature [44]. Further, no 830nm PL peak was found in a sample of Nd:YAG that was not grown in an iridium crucible. This sample was grown using a rhenium crucible. Further measurements on this Re-crucible grown Nd:YAG sample are present in a later section.

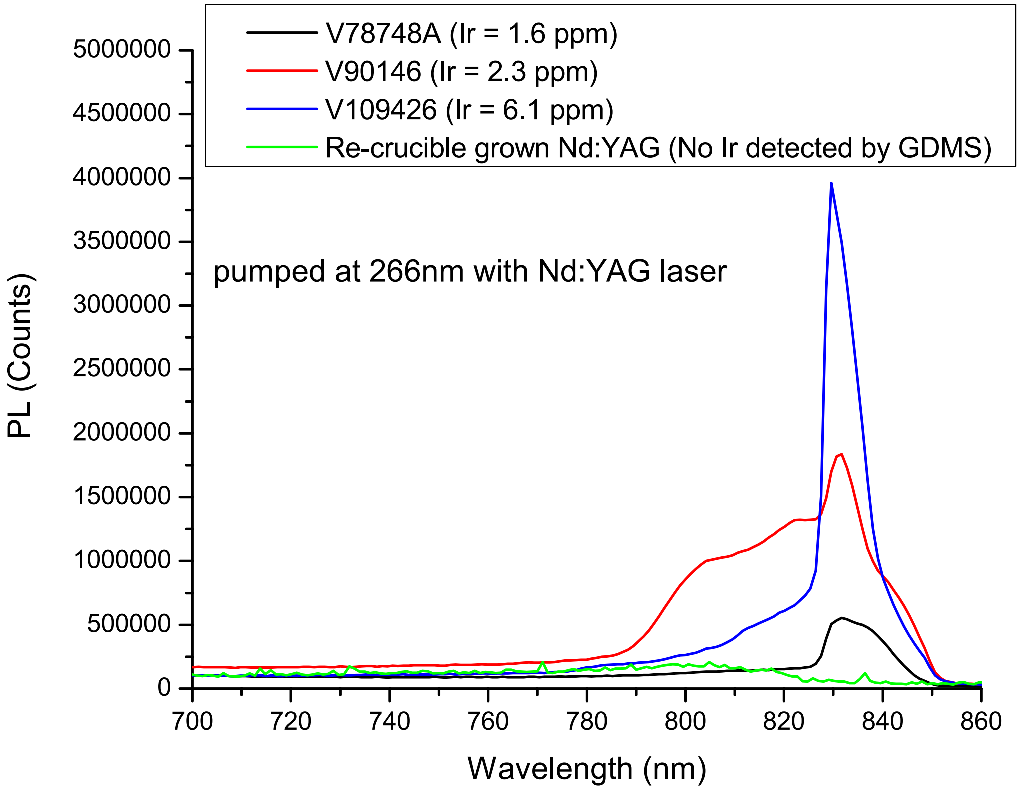

Figure 6.27: Photoluminescence of four Nd:YAG samples near 830nm.

6.14 Suggested Mechanism of Ir Inclusion in Nd:YAG

Iridium can enter as both 4+ and 3+ depending on its lattice entry site. Iridium enters the YAG lattice, as it is used as a crucible material. The iridium crucible experiences oxidation by chemically reacting with oxygen in the growth atmosphere during the high-temperature growth process which causes it to leave the crucible in the form of iridium oxide [33]. The iridium will then move from the high-temperature crucible wall to the relatively lower-temperature melt and/or the growing crystal's surfaces where it can then be incorporated into the crystal [45]. If the iridium resides on the melt surface, it can interfere with the symmetrical growth of the boule by distorting the melt surface in the growth interface [45]. If too much of the iridium covers the surface of the melt, then crystal growth may terminate. High oxygen concentration in the growth atmosphere or considerable water vapor concentration (~50ppm weight) accelerates this growth termination [45]. To avoid iridium ever entering the melt, a different crucible material may be used such as rhenium or molybdenum. Also changing the growth atmosphere may help inhibit iridium transport. One proposed growth atmosphere consists of a 20% CO_2 in N_2 gas mixture [45].

When the iridium enters the YAG lattice, it may do so in its 4+ valence state. This presents a problem for the YAG lattice as a charge compensator must be present to account for charge neutrality. According to theory, the most energetically-favorable charge compensator is an aluminum vacancy, V_{Al}, and one such mechanism for the generation of the aluminum vacancy is [46]:

$$IrO_2 + \frac{4}{3} Al_{Al}^{X} \rightarrow Ir_{Al}^{\bullet} + \frac{1}{3} V_{Al}^{'''} + \frac{2}{3} Al_2O_3$$

The presence of the aluminum vacancy and the iridium impurity may reduce laser output power and increase laser threshold energy requirements [47].

6.15 Measurements of Solarization and Annealing of Nd:YAG

Since iridium is a variable-charge-state impurity ion, solarization and annealing should change its absorption spectrum. The experiment to verify the reaction above was carried out, and the results of that experiment can be seen in figure 6.28. As can be seen from the plot, solarization creates the ~330nm absorption peak while oxidation heat treatment nearly eliminates this ~330nm absorption peak and increases the intensity of the 256nm absorption peak. To determine the affect of solarization on laser performance as well as absorption for a Nd:YAG laser rod, a rod was selected and its absorption spectrum was taken in addition to its laser output power profile. The rod was then solarized using a xenon lamp for five hours, and the rod was once again measured for absorption and laser performance. The results of these measurements can be seen in figure 6.29 and figure 6.30. As can be seen from the plots, solarization, possibly leading to more Ir^{4+} ions in the rod, has a deleterious effect on laser performance. As a result of the solarization, the 256nm absorption-peak intensity was reduced and laser output power was also reduced significantly. Therefore, a mechanism accounting for the valence change of the iridium impurity ions in the crystal observed during solarization and oxidation annealing is proposed:

$$Ir^{\bullet}_{Al_{oct}} + \frac{1}{3}V'''_{Al} + \frac{2}{3}Al_2O_3 \xleftrightarrow{\frac{\Delta}{O_2},hv} Ir^{X}_{Al_{tet}} + \frac{1}{3}V'''_{Al} + \frac{2}{3}Al_2O_3 + h^+$$

where the h^+ can be absorbed into the surrounding anions.

Vacancies also control the rate of matrix- or substitutional-atom diffusion [48]. In YAG, oxygen has the highest self-diffusion coefficient followed by aluminum [43,49]. Yttrium has the lowest self-diffusion coefficient in YAG indicating that any sort of diffusion will be best accomplished by oxygen and aluminum [43,49]. Moreover, in order to get aluminum to be mobile in YAG, oxygen must also be mobile to accommodate for the motion of the aluminum in the YAG matrix [43]. This is easily accomplished as the Al-O complex is the most dissociated and disordered lattice part of YAG [43].

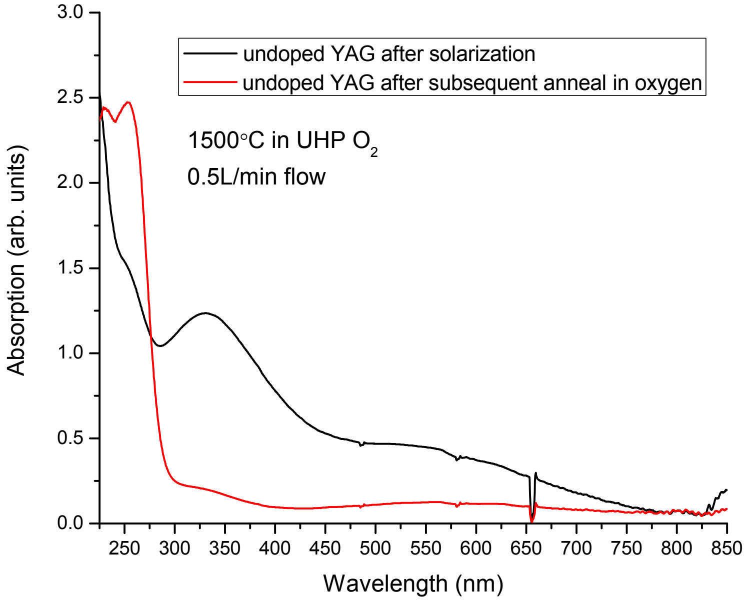

Figure 6.28: Absorption spectra for an undoped YAG rod after solarization and subsequent high-temperature oxidizing heat treatment.

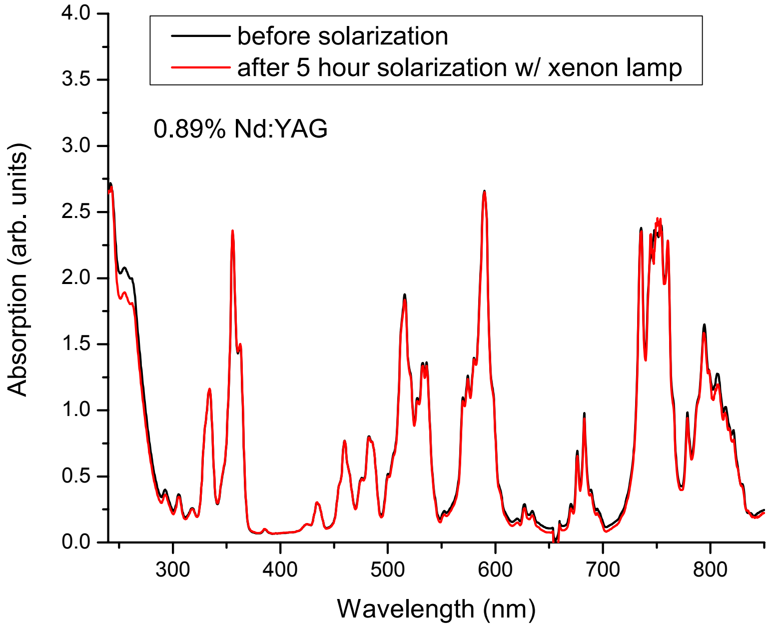

Figure 6.29: Absorption spectra taken before and after 5-hour Xe lamp solarization.

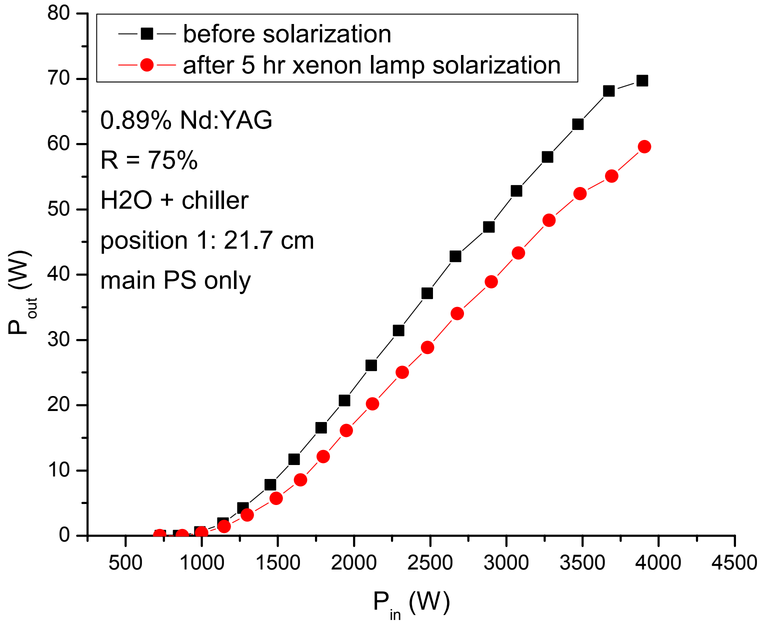

Figure 6.30: Laser output power profile taken before and after 5-hour Xe lamp solarization.

6.16 Aluminum Diffusion and Subsequent Oxidation Anneal Studies

Because of the preferential evaporation of aluminum and oxygen in the melt during crystal growth as well as the Ir^{4+} ion charge-compensating aluminum vacancies, which result in excess yttrium conditions and non-stoichiometry in the grown crystal, it made sense to try to diffuse aluminum and oxygen back into a cored Nd:YAG laser rod to fill aluminum vacancies and help restore stoichiometry and, as a result, improve laser output power and efficiency. A rod was selected and its laser output power profile was taken. The rod was then sputtered with aluminum. The rod was then annealed in argon for 72 hours at a temperature of 600˚C. The rod was then further annealed at 1,000˚C for another 72 hours in argon. Finally, the rod was annealed at 1,500˚C for 72 hours in an oxygen atmosphere to help drive the aluminum into the center of the rod as well as fill any resulting oxygen vacancies. Laser output power was then remeasured. The results can be seen in figure 6.31 and figure 6.32. As is evident from the plots, diffusing aluminum into the rod can increase laser output power and improve laser threshold.

To determine the effect of aluminum diffusion on the as-grown defects in a rod, positron annihilation measurements were performed. Two rods from the same boule were selected for measurements. On rod was sputtered with aluminum and annealed following the same procedure that was described on the previous page, while the other rod was not sputtered but still underwent the same annealing process as the sputtered rod. Both rods were then measured for defect concentrations using positron annihilation spectroscopy. The diffusion lengths for the sputtered and non-sputtered rod were 141±19nm and 40±1.7nm, respectively, as can be seen in figure 6.33. Using the plot found in figure 6.34, this results in an approximate defect concentration reduction of slightly more than one order of magnitude. Since aluminum vacancies hold a negative charge, positrons will trap near them reducing the diffusion length of the positron [50]. If those vacancies are filled, then the positron will travel a greater distance to

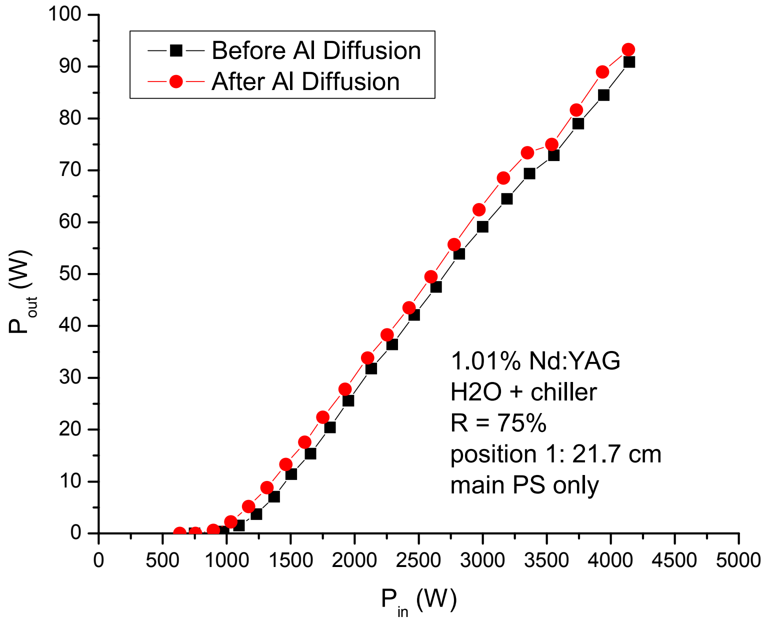

Figure 6.31: Laser output power profile for a Nd:YAG rod before and after aluminum diffusion.

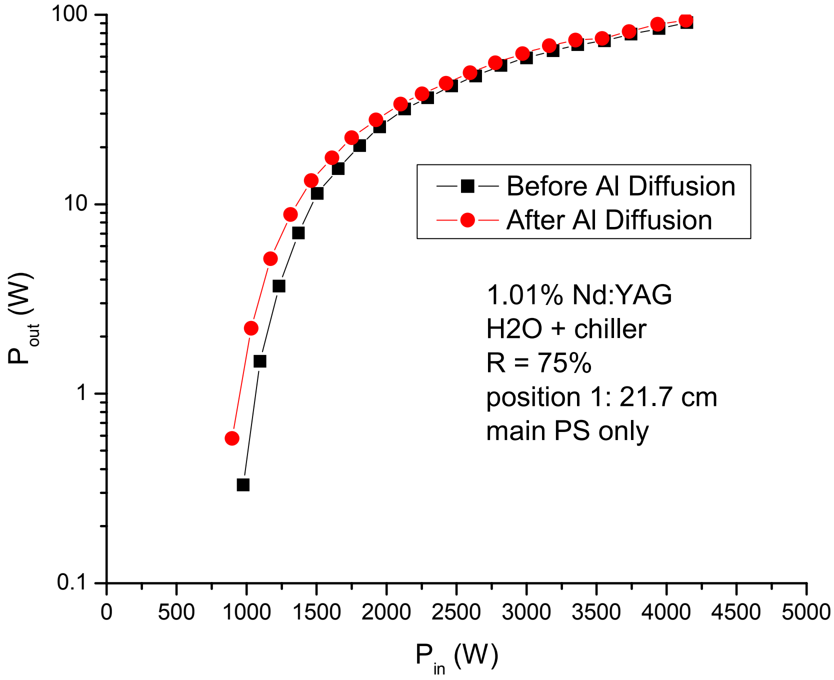

Figure 6.32: Threshold energy for Nd:YAG rod before and after aluminum diffusion.

find a suitable annihilation center. This filling of aluminum vacancies by diffusing aluminum into the rod may account for the change in positron diffusion length observed in this study. Therefore, a proposed mechanism for the elimination of the aluminum vacancies is proposed:

$$Ir_{Al_{tet}}^{X} + h^{+} + \frac{1}{3}V_{Al}^{'''} + \frac{2}{3}Al_2O_3 \xrightarrow{Al,\frac{\Delta}{O_2}} Ir_{Al_{tet}}^{X} + \frac{1}{3}Al_{Al}^{X} + \frac{1}{2}Al_2O_3 + \frac{1}{4}O_2$$

in which the h^{+} comes from the surrounding anions.

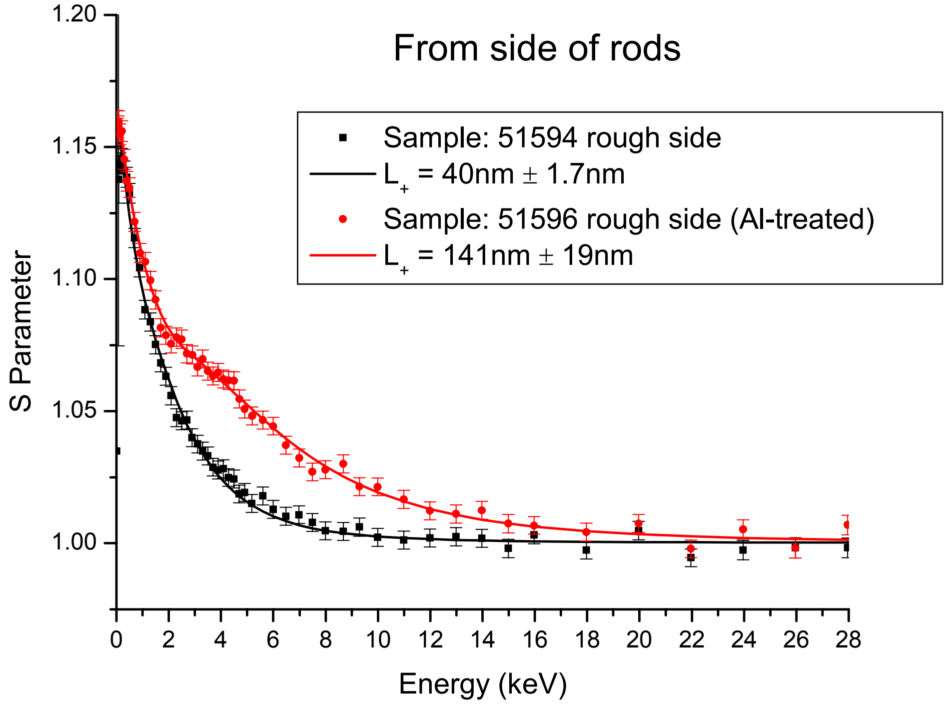

Figure 6.33: Positron annihilation spectroscopy measurements on one aluminum-diffused rod and one rod that was not treated with aluminum. *Source: Data courtesy of Marc Weber.*

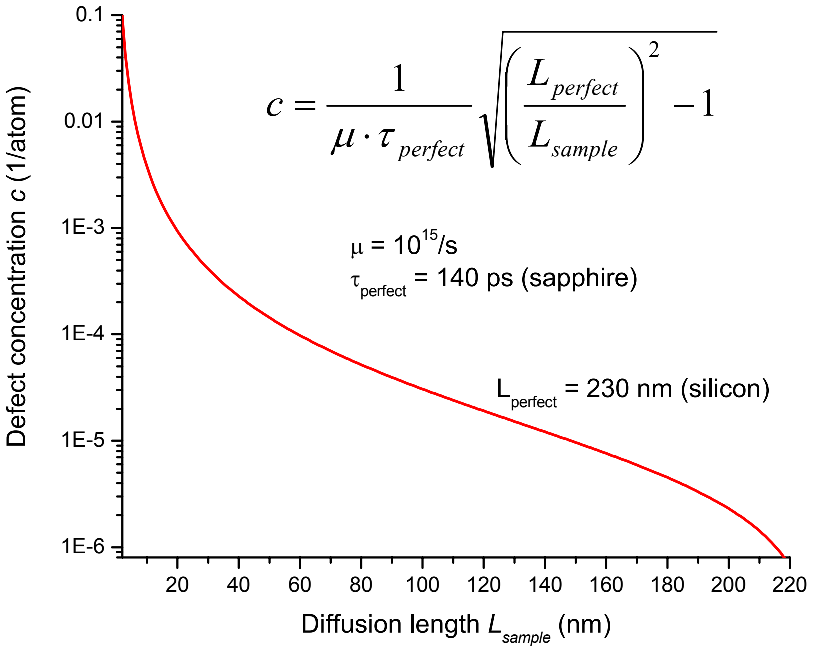

Figure 6.34: Estimated defect concentration versus positron diffusion length for YAG. *Source: Plot courtesy of Marc Weber.*

The aluminum diffusion process and subsequent oxidation heat treatment were done to several other rods. Laser performance and absorption were measured for each sample and given a qualitative analysis, the results of which can be seen in table 6.10. As is evident from the table, laser threshold improved for almost all samples upon aluminum diffusion and heat treatment. Laser output power results were mixed for the R = 90% output coupler reflectivity, but may be the result of heat-induced defects on the barrel ends of the laser rod. Subsequent repolishing of the ends may eliminate these defects and improve laser output power. Also, the 256nm absorption peak increased for almost every rod, which was expected.

Table 6.10: Qualitative results of Al diffusion and oxidation annealing study.

Sample	threshold R = 75%	threshold R = 90%	output power R = 75%	output power R = 90%	absorption 256nm change
51588	-	**improves post Al**	-	**declines post Al**	**increased intensity post Al**
51590	-	**improves post Al**	-	**improves post Al**	**increased intensity post Al**
51595	-	**improves post Al**	-	**declines post Al**	**increased intensity post Al**
51596	-	**improves post Al**	-	**improves post Al**	**increased intensity post Al**
51597	-	**declines post Al**	-	**declines post Al**	**increased intensity post Al**
51598	-	**declines post Al**	-	**declines post Al**	**increased intensity post Al**
V108224	**improves post Al**	**improves post Al**	**improves post Al**	**improves post Al**	**increased intensity post Al**
V113295	**improves post Al**	**improves post Al**	**no change in power**	**declines post Al**	**increased intensity post Al**
V113389	**improves post Al**	**improves post Al**	**improves post Al**	**improves post Al**	**increased intensity post Al**
V109426	**improves post Al**	**improves post Al**	**no change in power**	**improves post Al**	**no change in intensity**

6.17 Using a Different Crucible Material

Since iridium impurity ions have been shown to be deleterious to Nd:YAG laser performance, it is logical to consider eliminating iridium as the crucible material for growing Nd:YAG crystals. Two possible suggestions for alternative crucible materials include molybdenum and rhenium. Molybdenum only has the 6+ oxidation state which would avoid the charge transfer process with oxygen that is observed with variable-charge state impurity ions. Rhenium can exist in the 4+, 6+, or 7+ charge states making it less than ideal for use as a crucible material. However, using one of these materials as the crucible may be promising in that no 256nm absorption peak should be found in the absorption spectra of grown Nd:YAG crystal.

Such a situation was tried with a rhenium crucible, and a grown crystal from the rhenium crucible was compared to a crystal grown from an iridium crucible. The absorption spectrum comparing the two crystals can be seen in figure 6.35. While the resulting crystal was of poor optical quality, its absorption spectrum did not show the 256nm absorption peak that is characteristic of iridium-crucible grown Nd:YAG. This may be further evidence that the 256nm absorption peak is indeed the result of iridium impurity ions within the Nd:YAG crystal.

To verify this, a full scan GDMS study was done on a Re-crucible grown Nd:YAG crystal. The full scan results can be seen in table 6.11. As is evident from the table, no iridium or iron impurities were found. However, rhenium impurities were found as was expected as rhenium was the crucible material. This bolsters the claim that iridium impurities are responsible for the 256nm absorption peak.

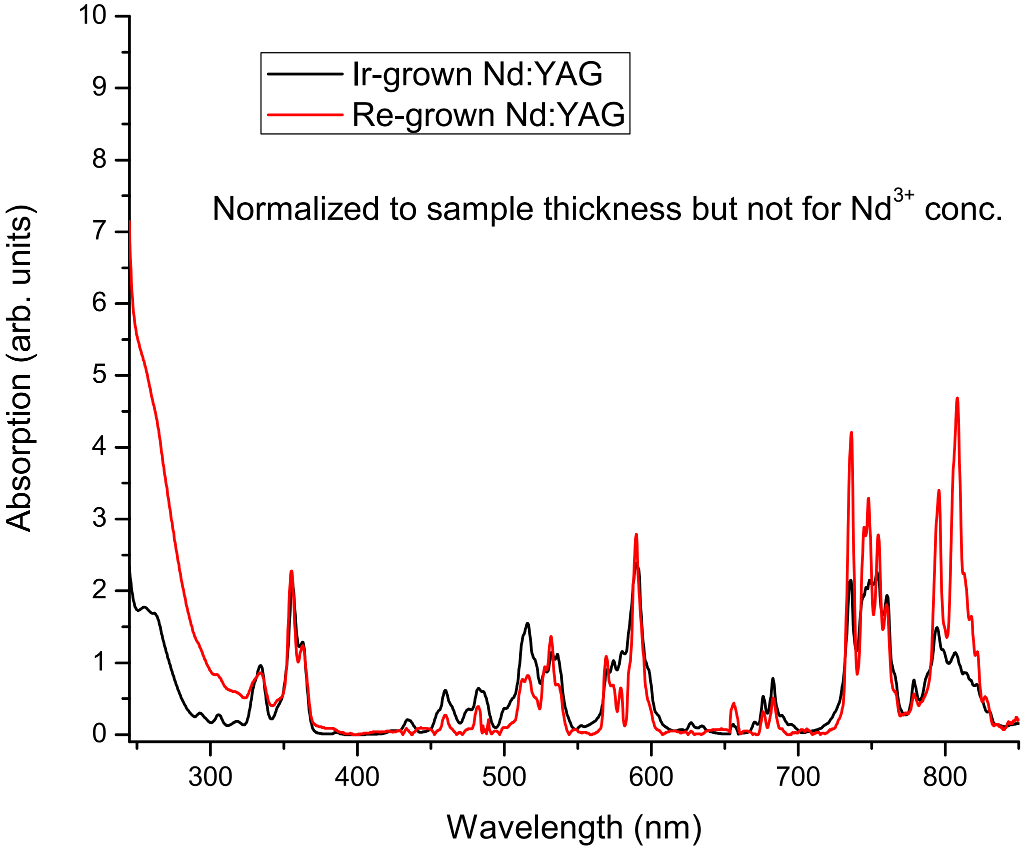

Figure 6.35: Absorption spectra comparison of Nd:YAG crystals grown using a rhenium crucible and an iridium crucible.

Table 6.11: Full scan GDMS results on a Re-crucible grown Nd:YAG sample.

Element	Concentration (ppm %wt.)	Element	Concentration (ppm %wt.)
Li	< 0.05	Ag	< 0.5
Be	< 0.05	Cd	< 0.5
B	< 0.05	In	< 0.5
O	Matrix	Sn	1.5
F	< 5	Sb	< 0.1
Na	1.8	Te	< 0.1
Mg	0.41	I	< 0.5
Al	Matrix	Cs	< 0.5
Si	2.5	Ba	< 0.1
P	< 0.1	La	< 0.1
S	< 0.5	Ce	< 0.1
Cl	< 0.1	Pr	< 0.1
K	< 0.5	Nd	~ 1.4 wt.%
Ca	2.2	Sm	< 0.1
Sc	< 0.05	Eu	< 0.1
Ti	14	Gd	< 0.5
V	0.07	Tb	< 1
Cr	1.9	Dy	1.2
Mn	0.11	Ho	< 0.5
Fe	< 1	Er	360
Co	< 0.05	Tm	< 0.5
Ni	< 0.5	Yb	< 0.5
Cu	< 10	Lu	< 0.5
Zn	< 0.5	Hf	0.94
Ga	< 0.1	Ta	Cathode
Ge	< 1	W	< 20
As	< 0.5	Re	8.1
Se	< 0.5	Os	< 0.05
Br	< 0.5	Ir	< 0.1
Rb	< 0.5	Pt	< 0.5
Sr	< 0.5	Au	Interference
Y	Matrix	Hg	< 0.5
Zr	37	Tl	< 0.1
Nb	< 50	Pb	< 0.1
Mo	< 20	Bi	< 0.1
Ru	<0.5	Th	< 0.01
Rh	<0.5	U	< 0.01
Pd	<0.5	-	-

6.18 Summary for Improving Laser Performance in Nd:YAG

Putting all the aforementioned pieces together, it was discovered that no iron was found in the rods tested by NAA. However, the 256nm absorption peak has been observed in those same rods that NAA and GDMS results showed contain no iron. Iron is, therefore, probably not the defect responsible for the 256nm peak observed in YAG rods. This is backed by literature and by experimentation seen in the previous section showing that no 256nm peak was found in growth methods where iridium crucibles were not used. The absorption intensity of the 256nm peak can be manipulated by ultraviolet solarization as well as oxidation heat treatment. This may suggest that the defect responsible for this absorption band is most likely a multivalent transition metal. NAA results indicate that this metal is most likely iridium, which can exist in the 3+ and 4+ valance states in YAG. Since iridium crucibles are used to grow YAG, this conclusion is logical. Literature has shown that IrO_2 formation results from the interaction of the iridium crucible walls with oxygen molecules found in the crystal-growth atmosphere. Therefore, it is logical that Ir^{4+} ions can enter the YAG lattice.

Ir^{4+} ions require charge compensation within the YAG lattice and theory indicates that tetravalent impurities in YAG are charge-compensated best by aluminum vacancies [51]. These negatively-charged defects can act as annihilation sites for positrons. Aluminum diffusion may eliminate some of the aluminum vacancies which as was verified by positron diffusion length measurements. Elimination of these aluminum vacancies can increase laser output power and improve lasing threshold.

Solarization increases the ~330nm absorption-band intensity, thus that band may correspond with the Ir^{4+} valence state. Because that broad band of absorption centered at ~330nm extends into the visible region—the laser pumping region—it is the least desirable valence state that iridium can have in YAG. Solarizing rods to increase the ~330nm absorption intensity has a detrimental effect on laser output power and laser threshold. Therefore, the 256nm absorption peak that corresponds to the Ir^{3+} valence state is the more desirable valence state for iridium as it is not pumped in the laser cavity due to the Sm-doped flow tubes that filter out the ultraviolet light emitted by the krypton arc-lamp.

There does seem to be a direct correlation between iridium impurity concentration and 256nm absorption peak intensity. There also seems to be a connection between iridium impurity concentration and maximum laser output power. From the data, it can be determined that a 25% reduction of iridium within the laser rod can increase maximum laser output power of the rod by roughly that same percentage.

6.19 Future Work for Improving Laser Performance of Nd:YAG

As is evident from the data presented in the previous sections, it seems reasonable that future Czochralski growths of Nd:YAG boules should utilize a different crucible material than the traditional iridium-metal crucible. Molybdenum and rhenium are potential candidates to investigate.

Also, it has been suggested that increasing oxygen partial pressure during crystal growth may volatilize the iridium oxide impurities within the melt. This could possibly result in expulsion of iridium oxide from the melt by vaporization reducing the inclusion of iridium into the grown crystal. High-oxygen partial pressures should be investigated to determine whether this reduces iridium impurity concentration in grown crystals. To date, only a handful of boules have been grown in this manner, and results have been mixed mainly due to other necessary adjustments to the growth process that are needed to accommodate the increase in oxygen partial pressure during growth.

Switching from single crystalline Nd:YAG to ceramic YAG may also be a possible method for improving laser performance as impurities from the crucible material should not be an issue. The topic of ceramic YAG is covered briefly in Appendix B.

References

[1] S. Goldring, R. Lavi, A. Tal, E. Lebiush, Y. Tzuk, and S. Jackal, IEEE J. Quantum Electron. 40 (2004) 384-389.

[2] W. Koechner, Solid State Laser Engineering. Springer-Verlag, Berlin, 1999.

[3] J.S. Uppal, P.D. Gupta, and D.D. Bhawalker, J. Appl. Phys. 54 (1983) 6615-6619.

[4] M. Bass and A.E. Paladino, J. Appl. Phys. 38 (1967) 2706-2707.

[5] K. Takehisa, M. Yano, and K. Kuwabara, Appl. Opt. 32 (1993) 7391-7393.

[6] U. Brauch and M. Schubert, Opt. Commun. 117 (1995) 116-122.

[7] R. Iffländer, Solid-State Lasers for Materials Processing: Fundamental Relations and Technical Realizations. Springer-Verlag, Berlin, 2001.

[8] M.T. Bronksi, Development of a Process for Characterization of Nd:YAG Crystals. Thesis, Worchester Polytechnic Institute, Worchester, Massachusetts, 2003.

[9] S. Yoshikawa, K. Iwamoto, and K. Washio, Appl. Opt. 10 (1971) 1620-1623.

[10] R.H. Dishington, W.R. Hook, and R.P. Hilberg, Appl. Opt. 13 (1974) 2300-2312.

[11] J.R. Oliver and F.S. Barnes, IEEE J. Quantum Electron. 5 (1969) 232-237.

[12] G. Phillipps and J. Vater, Appl. Opt. 32 (1993) 3210-3216.

[13] W. Koechner, L.C. DeBenedictis, E. Matovich, and G.E. Mevers, IEEE J. Quantum Electron. 8 (1972) 310-316.

[14] R.J. Pressley, editor, CRC Handbook of Lasers with Selected Data on Optical Technology. CRC Press, Cleveland, 1971.

[15] I. Liberman, D.A. Larson, and C.H. Church, IEEE J. Quantum Electron. 5 (1969) 238-241.

[16] I.R. Walker, F.L. Curzon, and S.F. Dindo, J. Appl. Phys. 59 (1986) 358-364.

[17] R. Lavi, S. Jackel, A. Tal, E. Lebiush, Y. Tzuk, and S. Goldring, Opt. Commun. 195 (2001) 427-430.

[18] Q. Lü, U. Wittrock, and S. Dong, Opt. Laser Technol. 27 (1995) 95-101.

[19] M.P. Murdough and C.A. Denman, Appl. Opt. 35 (1996) 5925-5936.

[20] I. Moshe and S. Jackel, Opt. Commun. 214 (2002) 315-325.

[21] J. Sherman, Appl. Opt. 37 (1998) 7789-7796.

[22] W. Koechner, Appl. Opt. 9 (1970) 2548-2553.

[23] K. Du, Y. Liao, and P. Loosen, Opt. Commun. 140 (1997) 53-56.

[24] M.R. Kokta, Mater. Res. Soc. Symp. Proc. 329 (1994) 33-43.

[25] A. Ikesue, K. Kamata, and K. Yoshida, J. Am. Ceram. Soc. 79 (1996) 1921-1926.

[26] J.A. L'huillier, G. Bitz, V. Wesemann, P. von Loewis, R. Wallenstein, A. Borsutzky, L. Ackermann, K. Dupré, D. Rytz, and S. Vernay, Appl. Opt. 41 (2002) 4377-4384.

[27] J.A. Caird, M.D. Shinn, T.A. Kirchoff, L.K. Smith, and R.E. Wilder, Appl. Opt. 25 (1986) 4294-4305.

[28] Y. Peizhi, D. Peizhen, Y. Zhiwen, and T. Yulian, J. Cryst. Growth 218 (2000) 87-92.

[29] D. Jun, D. Peizhen, and X. Jun, J. Cryst. Growth 203 (1999) 163-167.

[30] S. Ishibashi, K. Naganuma, and I. Yokohama, J. Cryst. Growth 183 (1998) 614-621.

[31] B. Cockayne, M. Chesswas, and D.B. Gasson, J. Mater. Sci. 4 (1969) 450-456.

[32] G.J. Zhao, X.H. Zeng, J. Xu, S.M. Zhou, and Y.Z. Zhou, Phys. Status Solidi A 199 (2003) 355-359.

[33] G. Zhao, X. Zeng, J. Xu, and Y. Zhou, J. Cryst. Growth 253 (2003) 290-296.

[34] J.A. Caird, M.D. Shinn, T.A. Kirchoff, L.K. Smith, and R.E. Wilder, Appl. Opt. 25 (1986) 4294-4305.

[35] H. Haneda, Y. Miyazawa, and S. Shirasaki, J. Cryst. Growth 68 (1984) 581-588.

[36] W.T. Stacy, R. Metselaar, P.K. Larsen, A. Bril, and J.A. Pistorius, Appl. Phys. Lett. 24 (1974) 254-256.

[37] J. Lu, H. Yagi, K. Takaichi, T. Uematsu, J.F. Bisson, Y. Feng, A. Shirakawa, K.L. Ueda, T. Yanagitani, and A.A. Kaminskii, Appl. Phys. B 79 (2004) 25-28.

[38] D.E. Eakins, M. Held, M.G. Norton, and D.F. Bahr, J. Cryst. Growth 267 (2004) 502-509.

[39] D.E. Eakins, J.B. LeBret, M.G. Norton, D.F. Bahr, and J.Q. Dumm, Proc. SPIE 4970 (2003) 1-9.

[40] M. Springis, A. Pujats, and J. Valbis, J. Phys.: Condens. Matter 3 (1991) 5457-5461.

[41] Y. Zorenko, A. Voloshinovskii, I. Konstankevych, V. Kolobanov, V. Mikhailin, and D. Spassky, Radiat. Measurements 38 (2004) 677-680.

[42] C.R. Stanek, K.J. McClellan, M.R. Levy, C. Milanese, and R.W. Grimes, submitted to Nucl. Instrum. Methods A (2006).

[43] A.Y. Neiman, E. Tkachenko, and V. Zhukovskii, Dokl. Akad. Nauk SSSR 240 (1978) 876-879.

[44] Y.A. Voitukevich, M.V. Korzhik, V.V. Kuzmin, M.G. Livshits, and M.L. Meilman, Opt. Spectrosc. (USSR) 63 (1987) 480-484.

[45] S.E. Stokowski, M.H. Randles, and R.C. Morris, IEEE J. Quantum Electron. 24 (1988) 934-948.

[46] M.M. Kuklja, J. Phys.: Condens. Matter 12 (2000) 2953-2967.

[47] M.R. Bedilov and U. Égamov, Sov. J. Quantum Electron. 11 (1981) 969-970.

[48] C.R. Barrett, W.D. Nix, A.S. Tetelman, The Principles of Engineering Materials. Prentice-Hall, New Jersey, 1973.

[49] D.J. Cheriak, Phys. Chem. Minerals 26 (1998) 156-163.

[50] C.L. Wang, K.G. Lynn, S. Tebaldi, M.H. Weber, K. Shafer, R. Tjossem, T.T. Williams, and J.D. Dougherty, Proc. SPIE Solid State Lasers XII 4968 (2003) 143-150.

[51] M.A. Gülgün, W.Y. Ching, Y.N. Xu, and M. Rühle, Philo. Mag. B 79 (1999) 921-940.

CHAPTER SEVEN

CONCLUSIONS

Defects in laser crystals can have a deleterious effect on laser performance. Minimizing these defects during the growth process is likely the key to improving the quality of the crystals. This may be achieved by properly compensating for the non-stoichiometry caused by the preferential evaporation of a few of the melt constituents. For YVO_4, excess vanadium oxide can be added to the melt to accommodate for vanadium oxide loss during growth, and, for YAG, excess aluminum oxide can be added to the melt to accommodate for its loss during growth. In addition to improving stoichiometry, it is important to use the purest raw materials available to avoid unintentional transition-metal doping of the resulting crystal. Particularly, iron and water impurities should be minimized in the powders used for the growth of YAG.

Also of vital importance is the proper weighing of the powders used for the melt as these powders can readily absorb water throwing off the carefully-calculated stoichiometry needed for proper growth. Often, the powders are calcinated at 1,000°C to eliminate water from the powders, but the powder is often allowed to cool before its weight is measured. To eliminate subsequent water absorption after calcination, the powders must be weighed while still hot and loaded into a partially-heated growth-furnace crucible before the growth is started. This may help reduce hydroxyl impurities in the crystal and may also help promote stoichiometric growth.

Maintaining a proper growth atmosphere is also very important before, during, and after crystal growth to avoid the incorporation of water vapor into the powders, the melt, or into the cooling crystal, respectively. The growth atmosphere should include some partial pressure of oxygen. While the presence of oxygen can promote partial crucible material integration into the crystal thus limiting the crucible lifetime and crystal purity, oxygen is important for maintaining the stoichiometry of the crystal, which may have a significant effect on laser performance.

Boules should be grown slowly with a fast enough rotation rate to ensure a flat crystal/melt interface shape. This flat interface can help minimize the core-faceting region often observed in YAG boules. Also, for YAG, growing smaller diameter boules, which may consequently reduce yield and increase production prices, may also reduce the size of the core-faceting region as well as the overall residual stress in the boule, thus allowing for more rods of higher-quality to be cored from the boule, as rods should only be cored from stress-free regions in the boule as determined by cross-polarization.

Cooling should also be very slow to help avoid boule fracture. This is especially important for *c*-axis grown YVO_4 which has the tendency to thermally fracture. However, *c*-axis YVO_4, when grown properly, can minimize defects such as grain boundaries producing higher-powered laser crystals than *a*-axis grown laser elements. Of even more importance though in choosing *c*-axis grown YVO_4 is the fact that *c*-axis $Nd:YVO_4$ can accommodate more Nd^{3+} ions than *a*-axis grown $Nd:YVO_4$.

The identification of the source of the 256nm absorption peak is very important to understanding parasitic absorption in Nd:YAG laser crystals. While not completely conclusive, it appears that iridium is responsible for this absorption. This is in departure to several decades of literature on the subject. The proposal that the 256nm absorption peak is the consequence of incorporation of the crucible material is significant as it could lead to changes in the growth process of Nd:YAG boules. This research could pave the way for a better understanding of the role that the crucible material plays in solid-state laser growth and subsequent crystal characterization.

Minimizing the effect of this impurity defect is also of importance. It was shown that oxidation heat treatment and aluminum diffusion in Nd:YAG can improve laser performance in lower-quality crystals indicating that crystal stoichiometry may be improved through the elimination of oxygen vacancies and aluminum vacancies. Oxidation heat treatment must be performed at high temperatures reaching 1,500°C to sufficiently fill oxygen vacancies and diffuse aluminum into the center of the laser rods. Also, high-temperature, oxidizing heat treatment can change the valence state of impurity ions in the lattice such as iridium. Iridium can be incorporated in the YAG lattice in a 4+ valence state, a valence state that requires charge compensation, usually in the form of aluminum vacancies. Converting Ir^{4+} ions into Ir^{3+} ions can eliminate the need for charge compensation and aluminum ions can fill these no-longer-required aluminum vacancies. However, it was also shown that oxidation heat treatment alone is not sufficient for fixing this issue. It must also be accompanied by aluminum diffusion.

Using optical methods for identifying defects in laser crystals is advantageous as they are quick, require minimal equipment, use large sample sizes, and are generally non-destructive. Absorption techniques can be used to verify the presence of impurities and other color centers using their distinctive absorption energies, as was the case for finding iridium and its oxygen vacancy-related complex. For YVO_4, identification of defects using cross-polarization optical microscopy was helpful in determining the best growth axis for the material. While the complete elimination of defects in solid-state laser crystals is thermodynamically impossible, their concentration can be greatly reduced first and foremost by careful crystal growth practices, and to a lesser extent, through common techniques such as post-growth heat treatment and diffusion.

APPENDIX

APPENDIX A

GADOLINIUM ORTHOVANADATE

Nd:$GdVO_4$ was first developed as a laser material by A.I. Zaguniennyi et al. in 1992 [1-3]. Nd:$GdVO_4$ has the same space group as Nd:YVO_4, but Nd:$GdVO_4$ will absorb more energy than Nd:YVO_4 as it has a much higher absorption coefficient and a larger absorption cross-section [1-4]. Its thermal conductivity is greater than that of Nd:YVO_4 and is comparable to that of Nd:YAG which makes it preferable to Nd:YVO_4 for higher laser generation [1,3,4]. Various physical properties of both $GdVO_4$ and YVO_4 can be seen in table A1.1. From the table, it can be seen that $GdVO_4$ has a larger segregation coefficient which has been confirmed elsewhere [3]. Many of the properties of both $GdVO_4$ and YVO_4 are similar, and some of the properties favor

Table A1.1: Property comparison between $GdVO_4$ and YVO_4. *Source: H. Zhang, X. Meng, J. Liu, L. Zhu, C. Wang, Z. Shao, J. Wang, and Y. Liu, J. Cryst. Growth 216 (2000) 370.*

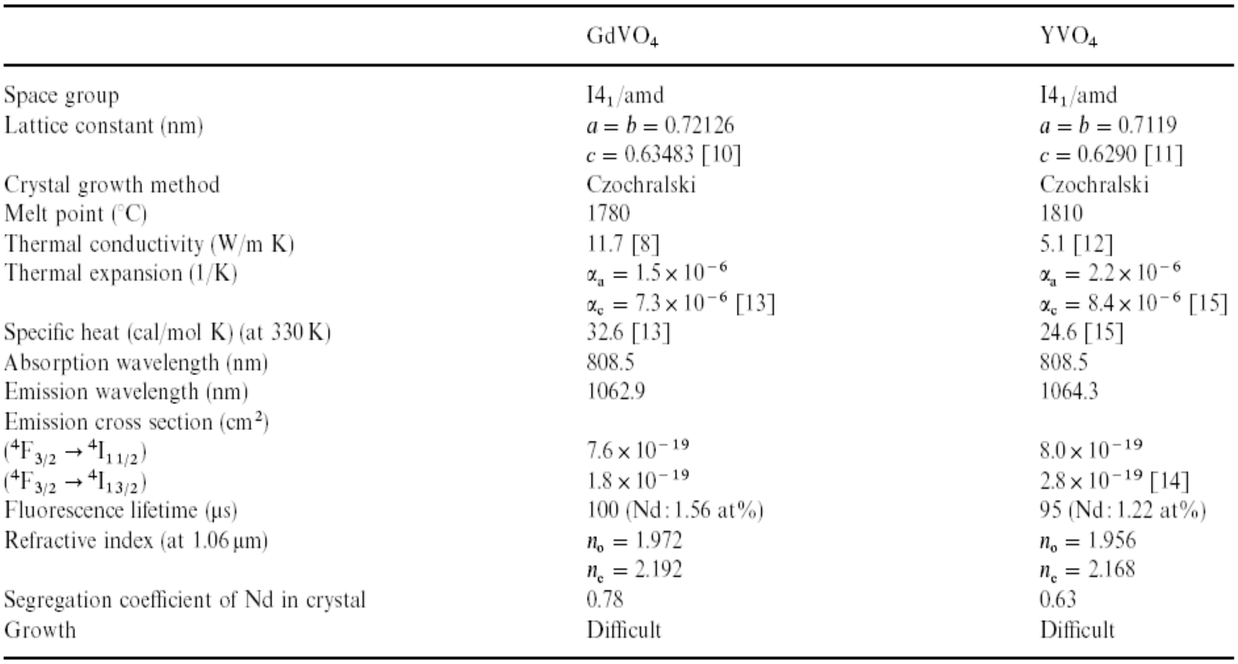

	$GdVO_4$	YVO_4
Space group	$I4_1/amd$	$I4_1/amd$
Lattice constant (nm)	$a = b = 0.72126$ $c = 0.63483$ [10]	$a = b = 0.7119$ $c = 0.6290$ [11]
Crystal growth method	Czochralski	Czochralski
Melt point (°C)	1780	1810
Thermal conductivity (W/m K)	11.7 [8]	5.1 [12]
Thermal expansion (1/K)	$\alpha_a = 1.5 \times 10^{-6}$ $\alpha_c = 7.3 \times 10^{-6}$ [13]	$\alpha_a = 2.2 \times 10^{-6}$ $\alpha_c = 8.4 \times 10^{-6}$ [15]
Specific heat (cal/mol K) (at 330 K)	32.6 [13]	24.6 [15]
Absorption wavelength (nm)	808.5	808.5
Emission wavelength (nm)	1062.9	1064.3
Emission cross section (cm^2)		
($^4F_{3/2} \rightarrow {}^4I_{11/2}$)	7.6×10^{-19}	8.0×10^{-19}
($^4F_{3/2} \rightarrow {}^4I_{13/2}$)	1.8×10^{-19}	2.8×10^{-19} [14]
Fluorescence lifetime (μs)	100 (Nd: 1.56 at%)	95 (Nd: 1.22 at%)
Refractive index (at 1.06 μm)	$n_o = 1.972$ $n_e = 2.192$	$n_o = 1.956$ $n_e = 2.168$
Segregation coefficient of Nd in crystal	0.78	0.63
Growth	Difficult	Difficult

using $GdVO_4$ as a laser host. In fact, some experiments have shown that Nd:$GdVO_4$ is a more efficient laser-diode-pumped solid-state laser crystal than Nd:YVO_4 [1]. However, Nd:$GdVO_4$ has its drawbacks. Cracking is the most common problem associated with Nd:$GdVO_4$, and it suffers from the same inclusion and low-angle grain boundary problems that plague Nd:YVO_4 [3]. In addition, Nd:$GdVO_4$ can also suffer from the same oxygen-deficiency problems as Nd:YVO_4 with oxygen vacancies creating the same crystal coloration in Nd:$GdVO_4$ as they do in Nd:YVO_4 [3]. However, Nd:$GdVO_4$ is easier to grow than Nd:YVO_4 because of its higher segregation coefficient, and it may one day replace Nd:YVO_4 laser elements [3].

References

[1] H. Zhang, X. Meng, J. Liu, L. Zhu, C. Wang, Z. Shao, J. Wang, and Y. Liu, J. Cryst. Growth 216 (2000) 367-371.

[2] J. Kong, D.Y. Tang, S.P. Ng, L.M. Zhao, L.J. Qin, and M.L. Meng, Opt. Laser Technol. 37 (2004) 51-54.

[3] L. Qin, X. Meng, J. Zhang, L. Zhu, H. Zhang, B. Xu, and H. Jiang, J. Cryst. Growth 242 (2002) 183-188.

[4] H. Zhang, X. Meng, L. Zhu, and Z. Yang, Mater. Res. Bull. 34 (1999) 1589-1593.

APPENDIX B

CERAMIC YAG

Ceramic YAG laser materials have become an attractive alternative to single-crystal YAG due to their ease of manufacture, low cost, and scalability [1]. However, it has been difficult to produce high-quality ceramic YAG crystals. In recent years, a technique for producing highly-transparent ceramic YAG has been developed [2]. The main advantage of using ceramic Nd:YAG is that the Nd^{3+}-doping level can be much higher than in single-crystal Nd:YAG, and doping levels as high as 8.2%at. have been reached [2,3]. This level of doping is possible because the small crystal grain sizes in the ceramic YAG allow for stress, induced by the size mismatch of Nd^{3+} ions to the Y^{3+} ions for which they are substituting, to be relieved in short distances at grain boundaries [4]. In addition to being able to achieve higher doping levels, ceramic YAG also allows for precise control over the doping concentration as grain size determines the amount of Nd^{3+} ion concentration that can be obtained [5]. Narrow grain boundaries and very low pore volume facilitate low scattering in ceramic YAG, helping make high power and high efficiency lasers possible [1]. One final advantage of using ceramic YAG is the fact that ceramic YAG is not grown in an iridium crucible, thus eliminating the 256nm and ~330nm absorption peaks common to single-crystal YAG.

Growth rate of ceramic YAG is on the order of single-crystal YAG, roughly about 1μm per hour [3]. This slow growth helps minimize the defect density in the ceramic YAG, just as it does in single-crystal YAG [3]. However, unlike single-crystal YAG, the granularity of the ceramic YAG causes scattering losses and less effective absorption of pump power, resulting in scattering losses of 0.9% per centimeter of crystal length [2]. However, unlike single-crystal YAG, ceramic YAG contains no core faceting [3].

Similar to single-crystal YAG, there exists an optimum Nd^{3+}-doping concentration for ceramic YAG. Figure B1.1 is a plot of fluorescence intensity versus Nd^{3+} ion concentration. From the plot, it can be seen that the maximum fluorescence intensity of Nd:YAG ceramics occurs at a Nd^{3+} ion concentration of somewhere around 2.4at.% [6].

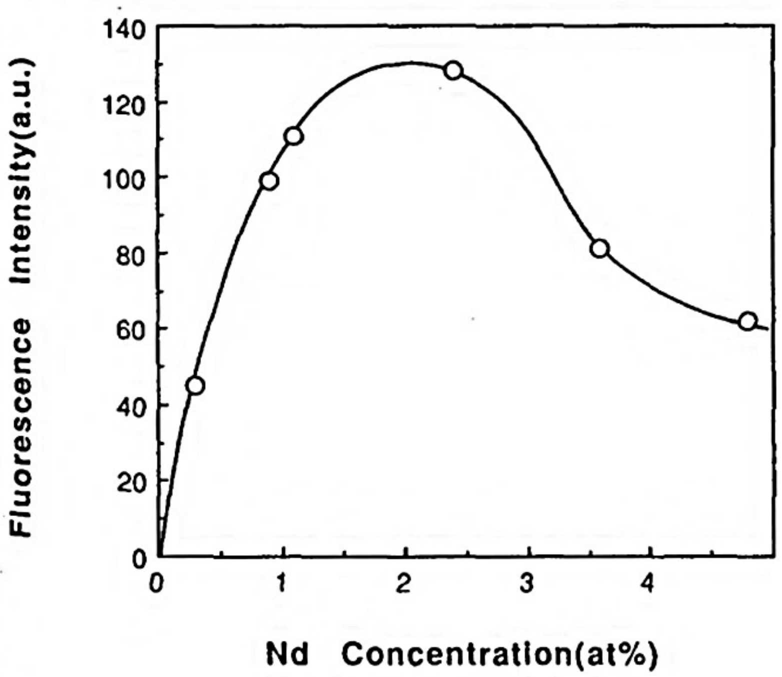

Figure B1.1: Fluorescence intensity versus Nd^{3+} ion concentration for Nd:YAG ceramics.
Source: A. Ikesue, K. Kamata, and K. Yoshida, J. Am. Ceram. Soc. 79 (1996) 1925.

A ceramic Nd:YAG samples was obtained and sent for GDMS analysis by Evans Analytical Group. The results can be seen in table B1.1. As is evident from the table, ceramic YAG contains iron and silicon but not iridium. This may be further argument in favor of using ceramic YAG. However iron is not a desirable impurity and can inhibit laser performance.

Table B1.1: Full scan GDMS result for a ceramic Nd:YAG sample.

Element	Concentration (ppm %wt.)	Element	Concentration (ppm %wt.)
Li	0.99	Ag	< 0.5
Be	0.59	Cd	< 0.5
B	0.06	In	< 0.5
O	Matrix	Sn	< 0.5
F	< 5	Sb	1.6
Na	2	Te	< 0.1
Mg	5.9	I	< 0.5
Al	Matrix	Cs	< 0.5
Si	270	Ba	< 0.1
P	0.27	La	3.2
S	< 0.5	Ce	9.4
Cl	< 0.1	Pr	23
K	< 0.5	Nd	~ .81 wt.%
Ca	34	Sm	2.8
Sc	< 0.05	Eu	0.29
Ti	6.3	Gd	< 0.5
V	12	Tb	< 1
Cr	9.9	Dy	0.99
Mn	1.8	Ho	< 0.5
Fe	23	Er	3
Co	0.45	Tm	< 0.5
Ni	2.3	Yb	< 0.5
Cu	< 10	Lu	< 0.5
Zn	< 0.5	Hf	< 0.5
Ga	< 0.1	Ta	Cathode
Ge	< 1	W	< 20
As	< 0.5	Re	< 0.05
Se	< 0.5	Os	< 0.05
Br	< 0.5	Ir	< 0.1
Rb	< 0.5	Pt	< 0.5
Sr	< 0.5	Au	Interference
Y	Matrix	Hg	< 0.5
Zr	2.7	Tl	< 0.1
Nb	< 50	Pb	< 0.1
Mo	< 20	Bi	0.11
Ru	<0.5	Th	0.03
Rh	<0.5	U	6.8
Pd	<0.5	-	-

References

[1] G. Qin, J. Lu, J.F. Bisson, Y. Feng, K. Ueda, H. Yagi, and T. Yanagitani, Solid State Commun. 132 (2004) 103-106.

[2] J.A. L'huillier, G. Bitz, V. Wesemann, P. von Loewis, R. Wallenstein, A. Borsutzky, L. Ackermann, K. Dupré, D. Rytz, and S. Vernay, Appl. Opt. 41 (2002) 4377-4384.

[3] J. Lu, H. Yagi, K. Takaichi, T. Uematsu, J.-F. Bisson, Y. Feng, A. Sirakawa, K.-L. Ueda, T. Yanagitani, and A.A. Kaminskii, Appl. Phys. B 79 (2004) 25-28.

[4] J. Wisdom, M. Digonnet, and R.L. Byer, Photonics Spectra. "Ceramic Lasers: Ready for Action," Feb. 2004.

[5] J. Lu, M. Prabhu, J. Song, C. Li, J. Xu, K. Ueda, A.A. Kaminskii, H. Yagi, and T. Yanagitani, Appl. Phys. B 71 (2000) 469-473.

[6] A. Ikesue, K. Kamata, and K. Yoshida, J. Am. Ceram. Soc. 79 (1996) 1921-1926.

APPENDIX C

OCEAN OPTICS UV/VIS SPECTROMETER

The spectrometer used to measure all absorption and fluorescence spectra contained in this dissertation was the 8-channel Ocean Optics PC2000 Fiber Optic Spectrometer using solarization-resistant, silica-clad, silica-core, aluminum-coated optical fibers with a 600μm core diameter having a numerical aperture of 0.22 and having the capability of high-quality transmission of wavelengths in the 190-800nm range. The detector in the spectrometer is a Sony ILX511 CCD camera capable of approximately 5nm resolution, and the software used to operate the spectrometer was the OOIBase32 program.

The light source used in the measurements was the DT1000 deuterium light source with a spectral output that can be seen in figure C1.1. The power spike near 650nm is due to the fluorescence of chromium impurities located in the glass envelope surrounding the lamp.

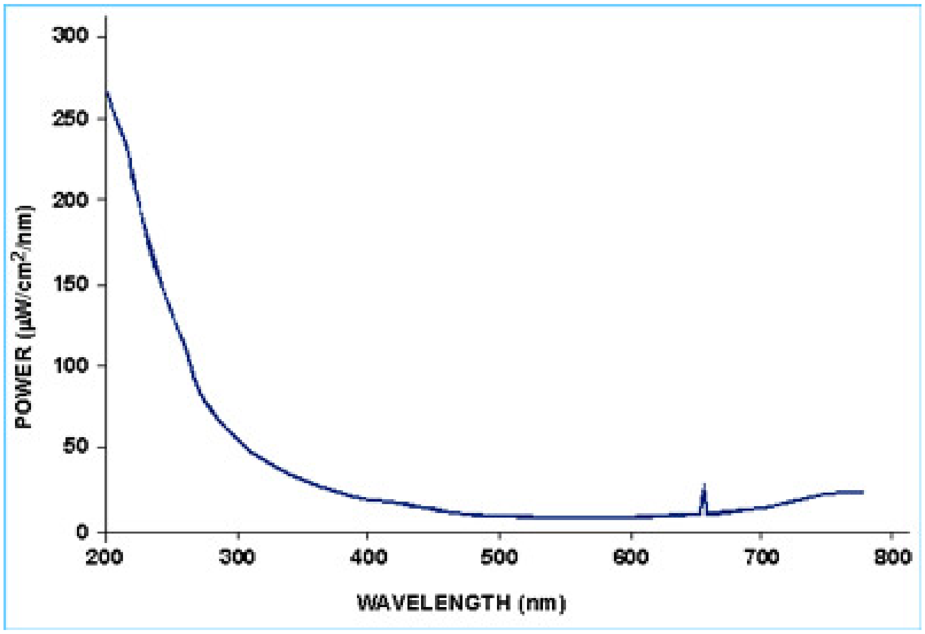

Figure C1.1: The deuterium light source emission spectrum for the DT1000 lamp. *Source: Ocean Optics catalog, 2006, p. 124.*

The three major modes of operation utilized in this spectrometer are the fluorescence measurement, the absorption measurement, and the transmission measurement. The fluorescence measurement is the simplest of the measurements as the software simply records what the detector senses. Absorption and transmission measurements require the subtraction of a background spectrum. Absorption spectra are taken following the equation:

$$A_\lambda = -\log\left(\frac{S_\lambda - D_\lambda}{R_\lambda - D_\lambda}\right) \tag{C1.1}$$

where A_λ is the absorbance at a specific wavelength, λ, S_λ is the sample intensity at the specific wavelength, λ, R_λ is the reference intensity at that same wavelength, λ, and D_λ is the dark intensity also at that same wavelength, λ. Transmission measurements are calculated similarly with the equation:

$$\%T_\lambda = \frac{S_\lambda - D_\lambda}{R_\lambda - D_\lambda} \times 100\% \tag{C1.2}$$

where S_λ, R_λ, and D_λ are the same values as in equation C1.1, and $\%T_\lambda$ is the percentage of transmission relative to that of air for the given wavelength, λ.

Fluorescence measurements are made by simply placing the detector fiber in the path of the fluorescing sample and saving the sample spectrum. Absorption and transmission measurements can be a bit trickier and are made by first allowing the deuterium light source to warm up for about 20 minutes. Then the emission and detection fibers are collimated so that the peak of the emission spectrum of the deuterium light lies at roughly the 3,500 counts line. If the peak maximum cannot reach that count value, the integration time of the spectrometer can be adjusted so it does reach it. The integration time function adjusts the amount of time in milliseconds that the detector will collect signal counts to produce a reading. When the fiber and integration time have both been adjusted, a reference peak is read without any sample in the path of the light beam. Then a dark spectrum is recorded by completely blocking light from the detector fiber. Then the covered detector fiber is uncovered and the detector is allowed to reach its previous reference spectrum values. This is done by letting the spectrometer run through a couple of cycles of its data collection. Finally, the correct function is selected for the mode of measurement to be taken, either absorption or transmission (there are several other modes that were not often used in the measurements needed for this research), and the sample is placed between the fibers to make the measurement. The processed spectrum is then saved by the user and can then retrieved in the form of a text document on the computer used to operate the spectrometer.

APPENDIX D

NEUTRON ACTIVATION ANALYSIS

Neutron activation analysis is one of the most sensitive methods for conducting chemical analysis measurements [1]. It is also one of the older methods of chemical analysis, first used in 1936 by Hevesy and Levi who used neutrons as the bombarding projectiles to activate dysprosium and europium [1].

Neutron activation is accomplished by the absorption of a neutron by a target nucleus producing a highly-energetic state of the resulting nucleus with the extra neutron [2]. The excess energy gained by this absorption of the additional neutron is immediately lost, usually with the emission of a gamma-ray, a proton, or an alpha particle [2]. Analysis of the emissions usually focuses on the gamma-ray emissions due to their high penetration, the large number of elements that produce gamma-emitting nuclides, and the existence of high-resolution, gamma-ray spectrometers which allow the gamma-ray energies to be measured [1].

Neutron activation analysis also has the benefit of possessing many adjustable parameters to aid in chemical analysis. Some of the adjustable parameters include irradiation time, decay time, counting time, irradiation flux, irradiation energy, sample-size requirements, gamma-ray counting geometry, and irradiation geometry [1]. Parameters involving the irradiation and decay aspect of the process allow for the targeting of specific atoms within the sample to be measured. Parameters involving the counting aspect of the process target the sensitivity of the analysis in addition to aiding in the targeting of specific atoms thought to be present in the sample.

The relationship between activation rate, the number of target nuclei, and the neutron flux is often expressed in terms of the absorption cross-section and is defined by:

$$A_r = \sigma \varphi N \tag{D1.1}$$

where A_r is the activation rate in s^{-1}, σ is the cross-section in m^2, φ is the neutron flux in $m^{-2}s^{-1}$, and N is the number of target nuclei in atoms [2]. Therefore, the activity, A_T, of the given radionuclide at time, t, is:

$$A_T = \varphi \sigma N_A \left(1 - e^{-\lambda t}\right) \tag{D1.2}$$

where φ is the neutron flux in neutrons $m^{-2}s^{-1}$, σ is the cross-section in m^2, N_A is Avogadro's number, and λ is the decay constant which is defined as $0.693/T$, where T is the half-life of the radionuclide [3].

The absorption cross-section as seen in equation D1.1 is defined as the probability that an incident particle will react with a target nucleus per unit area [1]. For iridium, that value is approximately $1{,}000 \times 10^{-24}$cm^2 [4]. In comparison, the absorption cross-section for iron is roughly 2×10^{-24}cm^2 [5,6]. Because the absorption cross-section for iridium is so high in comparison to iron, neutron activation analysis is a great tool for finding iridium even in very minute quantities within samples [4].

Using a known, certified standard, one can use neutron activation analysis to determine the concentration of a specific element within a sample. This is accomplished with congruent irradiation and counting conditions and by utilizing a simple mathematical relation:

$$[x_{sample}] = [x_{s\tan dard}]\left(\frac{C_{sample}}{C_{s\tan dard}}\right) \tag{D1.3}$$

where $[x_{sample}]$ is the element concentration within the sample, $[x_{standard}]$ is the element concentration in a known sample, C_{sample} is the count rate of the target gamma-ray of the sample, and $C_{standard}$ is the count rate of the target gamma-ray of the known sample [1,2]. The target gamma-ray of interest for iridium concerning the measurements presenting in section 4.6.13 was 468keV, and for iron, the target gamma-ray for the measurements was 1,099keV [4-6].

To measure these gamma-rays, a 35% Ge detector with 0.14% resolution (calibrated with a ^{60}Co source at 1,332keV) was used, and the results were analyzed with Canberra's Genie 2000 software.

References:

[1] Z.B. Alfassi, editor, Activation Analysis Vol. I. CRC Press, Boca Raton, 1990.

[2] J.D. Winefordner, editor, Chemical Analysis. Wiley-Interscience, New York, 1991.

[3] M. Rakovič, Activation Analysis. Iliffe Books LTD, Prague, 1970.

[4] L.S. Jowanovitz, F.B. McNatt, R.E. McCarley, and D.S. Martin, Analy. Chem. 32 (1960) 1270.

[5] P.J. Elving and I.M. Kolthoff, editors, Chemical Analysis. Wiley-Interscience, London, 1972.

[6] G. Erdtmann, editor, Neutron Activation Tables. Verlag Chemie, Weinhelm, 1978.

APPENDIX E

COMPLETE NEUTRON ACTIVATION ANALYSIS RESULTS

The tables in this appendix contain full NAA results for several YAG and Nd:YAG samples that were presented in chapter 6. Only the elements found in the YAG samples that possessed standards for comparison are presented in these tables. Other elements may be contained in these samples, but no standard was available to determine absolute concentration. Therefore, they are not included in these tables.

Table E1.1: NAA results for sample V90146, an Er co-doped, low O_2 growth.

ELEMENT NAME	***CONCENT (ppm %at.)***	***ERROR (1-sigma)***
Ba-131	<1.7459E-02	
Ce-141	<2.0426E+00	
Co-60	<8.5573E-05	
Co-60	<1.2984E-02	
Cr-51	7.2943E+01	2.3736E+00
Cs-134	4.4404E+00	3.0676E-01
Cs-134	1.5634E-02	6.0028E-03
Eu-152	1.9794E-01	1.0921E-02
Eu-152	4.8885E-02	4.0018E-03
Eu-152	3.9951E-02	3.3496E-03
Fe-59	<4.9391E-02	
Fe-59	<6.8502E+00	
Hf-181	7.3146E-01	3.1051E-02
Lu-177	8.2360E-01	1.5478E-01
Lu-177	*NOT IN STD	
Nd-147	1.8005E+03	3.8681E+02
Ni-58(Co-58)	5.5352E+00	2.1580E+00
Rb-86	<2.6584E-03	
Sb-124	<2.3144E-02	
Sc-46	1.8562E-03	2.0085E-04
Sc-46	2.6753E-03	2.4273E-04
Se-75	<2.8934E-04	
Sr-85	1.7883E+02	1.4429E+01
Ta-182	<7.8236E-05	
Ta-182	<1.5756E-02	
Tb-160	<8.1373E-03	
Tb-160	2.5773E-02	3.7536E-03
Th-(Pa-233)	<3.4369E-02	
U-(La-140)	<9.6693E-04	
U-(La-140)	1.3593E+01	1.8016E+00
U-(La-140)	<1.7458E-03	
Yb-169	<1.1664E-01	
Yb-169	7.1014E-01	6.9511E-02
Zn-65	<3.2711E-01	
Zr-95	<2.8313E+00	
Zr-95	<1.5613E-02	

Table E1.2: NAA results for sample V75392T, a standard growth.

ELEMENT NAME	*CONCENT (ppm %at.)*	*ERROR (1-sigma)*
Ba-131	<1.7904E-02	
Ce-141	<2.0491E+00	
Co-60	<1.0662E-02	
Co-60	<1.3205E-02	
Cr-51	6.9628E+01	2.2660E+00
Cs-134	6.2740E+00	4.3286E-01
Cs-134	<6.6496E-05	
Eu-152	1.8794E-01	1.0390E-02
Eu-152	3.0708E-02	2.8704E-03
Eu-152	3.4156E-02	2.9792E-03
Fe-59	<4.9373E+00	
Fe-59	<7.4476E-02	
Hf-181	1.0439E+00	4.4084E-02
Lu-177	1.1794E+00	2.2255E-01
Lu-177	*NOT IN STD	
Nd-147	1.7269E+03	3.7099E+02
Ni-58(Co-58)	<1.0234E-02	
Rb-86	6.7133E-01	1.5088E-01
Sb-124	<3.2482E-04	
Sc-46	1.0441E-03	1.5503E-04
Sc-46	1.6812E-03	1.7486E-04
Se-75	4.6130E-01	1.4649E-01
Sr-85	1.7581E+02	1.4196E+01
Ta-182	<7.8618E-05	
Ta-182	<1.8135E-04	
Tb-160	1.7681E-02	2.5463E-03
Tb-160	2.9800E-02	4.3869E-03
Th-(Pa-233)	<3.5192E-02	
U-(La-140)	<9.8967E-04	
U-(La-140)	1.9682E+01	2.6072E+00
U-(La-140)	<1.7869E-03	
Yb-169	<1.1784E-01	
Yb-169	6.7809E-01	6.6455E-02
Zn-65	1.1999E+00	7.8709E-02
Zr-95	<1.0659E-02	
Zr-95	<1.5716E-02	

Table E1.3: NAA results for sample V78748B, an O_2-rich growth.

ELEMENT NAME	CONCENT (ppm %at.)	ERROR (1-sigma)
Ba-131	<1.8521E-02	
Ce-141	<1.9672E+00	
Co-60	<8.5750E-05	
Co-60	<9.5441E-05	
Cr-51	7.5230E+01	2.4479E+00
Cs-134	5.8728E+00	4.0521E-01
Cs-134	<6.6475E-05	
Eu-152	2.0389E-01	1.1221E-02
Eu-152	4.2038E-02	3.5105E-03
Eu-152	3.6315E-02	3.1506E-03
Fe-59	<5.0224E-02	
Fe-59	<7.5092E-02	
Hf-181	9.9222E-01	4.1916E-02
Lu-177	1.0707E+00	2.0112E-01
Lu-177	*NOT IN STD	
Nd-147	1.9137E+03	4.1111E+02
Ni-58(Co-58)	<1.9673E+00	
Rb-86	3.9929E-01	1.5707E-01
Sb-124	<3.2674E-04	
Sc-46	1.2382E-03	1.5919E-04
Sc-46	1.7799E-03	1.8030E-04
Se-75	<2.9146E-04	
Sr-85	1.7156E+02	1.3809E+01
Ta-182	<7.8829E-05	
Ta-182	<1.8184E-04	
Tb-160	1.8651E-02	2.6272E-03
Tb-160	2.4121E-02	3.0817E-03
Th-(Pa-233)	<3.4478E-02	
U-(La-140)	1.1040E+00	5.9530E-01
U-(La-140)	1.9126E+01	2.5337E+00
U-(La-140)	<1.8430E-03	
Yb-169	1.1863E-01	4.4112E-02
Yb-169	7.1168E-01	6.9591E-02
Zn-65	<2.3229E-03	
Zr-95	<1.0717E-02	
Zr-95	3.4574E+00	1.6179E+00

Table E1.4: NAA results for sample V78748A, an O_2-rich growth.

ELEMENT NAME	***CONCENT (ppm %at.)***	***ERROR (1-sigma)***
Ba-131	<2.0120E-02	
Ce-141	<1.2561E-03	
Co-60	<8.6012E-05	
Co-60	<9.5733E-05	
Cr-51	6.4816E+01	2.1096E+00
Cs-134	5.8750E+00	4.0527E-01
Cs-134	<6.6730E-05	
Eu-152	1.6631E-01	9.1727E-03
Eu-152	4.1331E-02	3.3773E-03
Eu-152	3.3325E-02	3.0090E-03
Fe-59	6.3379E+00	2.8592E+00
Fe-59	<7.6886E-02	
Hf-181	1.0113E+00	4.2693E-02
Lu-177	1.0963E+00	2.0590E-01
Lu-177	*NOT IN STD	
Nd-147	1.7415E+03	3.7412E+02
Ni-58(Co-58)	<1.0448E-02	
Rb-86	4.3816E-01	1.5289E-01
Sb-124	<3.3273E-04	
Sc-46	1.1591E-03	1.4901E-04
Sc-46	2.1329E-03	1.9852E-04
Se-75	<2.9451E-04	
Sr-85	<2.9281E-02	
Ta-182	<7.2755E-03	
Ta-182	<1.8380E-04	
Tb-160	1.5813E-02	2.2756E-03
Tb-160	3.0489E-02	4.3020E-03
Th-(Pa-233)	<3.4289E-02	
U-(La-140)	<1.1013E-03	
U-(La-140)	2.0520E+01	2.7181E+00
U-(La-140)	<1.9885E-03	
Yb-169	1.3891E-01	4.1552E-02
Yb-169	6.4812E-01	6.3385E-02
Zn-65	3.3385E-01	4.5193E-02
Zr-95	<1.0899E-02	
Zr-95	<1.6070E-02	

Table E1.5: NAA results for sample V94408, a standard growth, undoped YAG sample.

ELEMENT NAME	CONCENT (ppm %at.)	ERROR (1-sigma)
Barium	<0.0505	
Cerium	<0.00265	
Cobalt	<0.0178	
Cesium	<0.0140	
Europium	0.0570 ±	0.0047
Iron	<7.91	
Hafnium	0.0790 ±	0.0052
Lutetium	0.721 ±	0.127
Neodymium	<0.00989	
Rubidium	0.997 ±	0.264
Antimony	<6.6E-4	
Scandium	0.00236 ±	0.00026
Selenium	<0.343	
Strontium	<0.0394	
Tantalum	<1.62E-4	
Thorium	<0.0387	
Uranium	<0.00358	
Ytterbium	0.0658 ±	0.0118
Zinc	<0.00309	
Zirconium	<0.0355	
Calcium	<2.33	
Gallium	<3.03E-4	
Lanthanum	<0.0240	
Lutetium	0.682 ±	0.120
Molybdenum	<3.85E-4	
Sodium	<1.19	
Samarium	<9.37E-4	

Table E1.6: NAA results for Y_2O_3 powder used as a raw material for the growth of YAG.

ELEMENT NAME	CONCENT (ppm)	ERROR (1-sigma)
Ba-131	<2.2497E-02	
Ce-141	2.8667E+00	7.3805E-01
Co-60	<9.8215E-05	
Co-60	<1.0931E-04	
Cr-51	<5.4591E-04	
Cs-134	<1.3314E-04	
Cs-134	<1.4455E-02	
Eu-152	7.1037E-02	5.3861E-03
Eu-152	1.0127E-01	9.5062E-03
Eu-152	8.2215E-02	5.5989E-03
Fe-59	<5.8402E-02	
Fe-59	<8.7320E-02	
Hf-181	<5.2437E-05	
Lu-177	<3.4644E-02	
Lu-177	*NOT IN STD	
Nd-147	<3.1391E-03	
Ni-58(Co-58)	<1.1890E-02	
Rb-86	9.6096E-01	2.0579E-01
Sb-124	<3.7843E-04	
Sc-46	1.2306E-03	4.3738E-04
Sc-46	2.2870E-03	2.3048E-04
Se-75	<3.3564E-04	
Sr-85	2.5782E+02	1.8046E+01
Ta-182	<9.0802E-05	
Ta-182	<2.0945E-04	
Tb-160	7.2280E-02	1.0005E-02
Tb-160	5.6084E-02	6.9411E-03
Th-(Pa-233)	1.3405E-01	1.1882E-02
U-(La-140)	<1.2336E-03	
U-(La-140)	<1.0497E-03	
U-(La-140)	<2.2274E-03	
Yb-169	1.9813E-01	4.5104E-02
Yb-169	1.2559E-01	2.2211E-02
Zn-65	<3.9207E-01	
Zr-95	<3.1104E+00	
Zr-95	<1.8283E-02	

Table E1.7: NAA results for Al_2O_3 powder used as a raw material for the growth of YAG.

ELEMENT NAME	***CONCENT (ppm)***	***ERROR (1-sigma)***
Ba-131	<1.2423E+00	
Ce-141	<1.4127E-03	
Co-60	3.7650E-03	1.4806E-03
Co-60	3.7597E-03	1.4305E-03
Cr-51	6.0781E-01	2.7508E-02
Cs-134	<6.2596E-03	
Cs-134	2.9767E-03	1.2750E-03
Eu-152	<6.2881E-06	
Eu-152	<5.4985E-05	
Eu-152	<1.0019E-03	
Fe-59	3.8262E+00	9.2687E-01
Fe-59	3.4324E+00	8.8635E-01
Hf-181	4.0247E-02	2.6722E-03
Lu-177	<2.9784E-05	
Lu-177	*NOT IN STD	
Nd-147	<1.5976E-01	
Ni-58(Co-58)	4.6031E-01	1.9976E-01
Rb-86	<1.1103E-01	
Sb-124	<5.0193E-03	
Sc-46	<4.9314E-06	
Sc-46	7.9246E-04	8.0118E-05
Se-75	<3.2772E-04	
Sr-85	<3.2693E-02	
Ta-182	<8.8682E-05	
Ta-182	<2.0456E-04	
Tb-160	<4.8537E-05	
Tb-160	1.5280E-03	2.6492E-04
Th-(Pa-233)	<4.3493E-05	
U-(La-140)	<1.2667E-03	
U-(La-140)	<1.0779E-03	
U-(La-140)	<2.2872E-03	
Yb-169	<8.5170E-05	
Yb-169	<4.3503E-05	
Zn-65	1.3316E-01	1.8778E-02
Zr-95	8.5311E-01	3.4937E-01
Zr-95	2.5752E+00	8.5238E-01

APPENDIX F

FULL SCAN GDMS RESULTS FOR VARIOUS RODS

The tables in this appendix contain full GDMS scan results for several YAG and Nd:YAG samples that were presented in chapter 6. The GDMS scans were done by Evans Analytical Group.

Table F1.1: GDMS results for V113389 run number 1.

Element	Concentration (ppm %wt.)	Element	Concentration (ppm %wt.)
Li	< 0.05	Ag	< 0.5
Be	< 0.05	Cd	< 0.5
B	< 0.05	In	< 0.5
O	Matrix	Sn	< 0.5
F	< 5	Sb	< 0.5
Na	< 0.1	Te	< 0.1
Mg	0.54	I	< 0.5
Al	Matrix	Cs	< 0.5
Si	2.3	Ba	< 0.1
P	< 0.1	La	< 0.1
S	< 0.5	Ce	< 0.1
Cl	< 0.1	Pr	< 0.1
K	< 0.5	Nd	~ .65 wt.%
Ca	< 0.5	Sm	< 0.1
Sc	< 0.05	Eu	< 0.1
Ti	< 0.1	Gd	< 0.5
V	< 0.05	Tb	< 1
Cr	< 0.5	Dy	< 0.5
Mn	< 0.05	Ho	< 0.5
Fe	< 1	Er	< 0.5
Co	< 0.05	Tm	< 0.5
Ni	< 0.5	Yb	< 0.5
Cu	< 10	Lu	< 0.5
Zn	< 0.5	Hf	< 0.5
Ga	< 0.1	Ta	Cathode
Ge	< 1	W	< 20
As	< 0.5	Re	< 0.05
Se	< 0.5	Os	< 0.05
Br	< 0.5	Ir	0.29
Rb	< 0.5	Pt	1
Sr	< 0.5	Au	Interference
Y	Matrix	Hg	< 0.5
Zr	< 0.5	Tl	< 0.1
Nb	< 50	Pb	< 0.1
Mo	< 20	Bi	< 0.1
Ru	<0.5	Th	< 0.01
Rh	<0.5	U	0.04
Pd	<0.5	-	-

Table F1.2: GDMS results for V113389 run number 2.

Element	Concentration (ppm %wt.)	Element	Concentration (ppm %wt.)
Li	< 0.05	Ag	< 0.5
Be	< 0.05	Cd	< 0.5
B	< 0.05	In	< 0.5
O	Matrix	Sn	< 0.5
F	< 5	Sb	< 0.5
Na	0.5	Te	< 0.1
Mg	< 0.1	I	< 0.5
Al	Matrix	Cs	< 0.5
Si	2	Ba	< 0.1
P	< 0.1	La	< 0.1
S	< 0.5	Ce	< 0.1
Cl	0.5	Pr	< 0.1
K	< 0.5	Nd	~ .6 wt.%
Ca	< 0.5	Sm	< 0.1
Sc	< 0.05	Eu	< 0.1
Ti	< 0.1	Gd	< 0.5
V	< 0.05	Tb	< 1
Cr	< 0.5	Dy	< 0.5
Mn	< 0.05	Ho	< 0.5
Fe	< 1	Er	< 0.5
Co	< 0.05	Tm	< 0.5
Ni	< 0.5	Yb	< 0.5
Cu	< 10	Lu	< 0.5
Zn	< 0.5	Hf	< 0.5
Ga	< 0.1	Ta	Cathode
Ge	< 1	W	< 20
As	< 0.5	Re	< 0.05
Se	< 0.5	Os	< 0.05
Br	< 0.5	Ir	0.35
Rb	< 0.5	Pt	< 0.5
Sr	< 0.5	Au	Interference
Y	Matrix	Hg	< 0.5
Zr	< 0.5	Tl	< 0.1
Nb	< 50	Pb	< 0.1
Mo	< 20	Bi	< 0.1
Ru	<0.5	Th	< 0.01
Rh	<0.5	U	0.05
Pd	<0.5	-	-

Table F1.3: GDMS results for V108224 run number 1.

Element	Concentration (ppm %wt.)	Element	Concentration (ppm %wt.)
Li	< 0.05	Ag	< 0.5
Be	< 0.05	Cd	< 0.5
B	< 0.05	In	< 0.5
O	Matrix	Sn	< 0.5
F	< 5	Sb	< 0.5
Na	< 0.1	Te	< 0.1
Mg	0.27	I	< 0.5
Al	Matrix	Cs	< 0.5
Si	2.7	Ba	< 0.1
P	< 0.1	La	< 0.1
S	< 0.5	Ce	< 0.1
Cl	< 0.1	Pr	< 0.1
K	< 0.5	Nd	~ .65 wt.%
Ca	< 0.5	Sm	< 0.1
Sc	< 0.05	Eu	< 0.1
Ti	0.25	Gd	< 0.5
V	< 0.05	Tb	< 1
Cr	< 0.5	Dy	< 0.5
Mn	< 0.05	Ho	< 0.5
Fe	< 1	Er	< 0.5
Co	< 0.05	Tm	< 0.5
Ni	< 0.5	Yb	< 0.5
Cu	< 10	Lu	< 0.5
Zn	< 0.5	Hf	< 0.5
Ga	< 0.1	Ta	Cathode
Ge	< 1	W	< 20
As	< 0.5	Re	< 0.05
Se	< 0.5	Os	< 0.05
Br	< 0.5	Ir	0.37
Rb	< 0.5	Pt	3.2
Sr	< 0.5	Au	Interference
Y	Matrix	Hg	< 0.5
Zr	< 0.5	Tl	< 0.1
Nb	< 50	Pb	< 0.1
Mo	< 20	Bi	< 0.1
Ru	<0.5	Th	< 0.01
Rh	<0.5	U	0.05
Pd	<0.5	-	-

Table F1.4: GDMS results for V108224 run number 2.

Element	Concentration (ppm %wt.)	Element	Concentration (ppm %wt.)
Li	< 0.05	Ag	< 0.5
Be	< 0.05	Cd	< 0.5
B	< 0.05	In	< 0.5
O	Matrix	Sn	< 0.5
F	< 5	Sb	< 0.5
Na	< 0.1	Te	< 0.1
Mg	0.19	I	< 0.5
Al	Matrix	Cs	< 0.5
Si	2.5	Ba	< 0.1
P	< 0.1	La	< 0.1
S	< 0.5	Ce	< 0.1
Cl	< 0.1	Pr	< 0.1
K	< 0.5	Nd	~ .6 wt.%
Ca	< 0.5	Sm	< 0.1
Sc	< 0.05	Eu	< 0.1
Ti	0.23	Gd	< 0.5
V	< 0.05	Tb	< 1
Cr	< 0.5	Dy	< 0.5
Mn	< 0.05	Ho	< 0.5
Fe	< 1	Er	< 0.5
Co	< 0.05	Tm	< 0.5
Ni	< 0.5	Yb	< 0.5
Cu	< 10	Lu	< 0.5
Zn	< 0.5	Hf	< 0.5
Ga	< 0.1	Ta	Cathode
Ge	< 1	W	< 20
As	< 0.5	Re	< 0.05
Se	< 0.5	Os	< 0.05
Br	< 0.5	Ir	0.35
Rb	< 0.5	Pt	2.7
Sr	< 0.5	Au	Interference
Y	Matrix	Hg	< 0.5
Zr	< 0.5	Tl	< 0.1
Nb	< 50	Pb	< 0.1
Mo	< 20	Bi	< 0.1
Ru	<0.5	Th	< 0.01
Rh	<0.5	U	0.04
Pd	<0.5	-	-

Table F1.5: GDMS results for V113295 run number 1.

Element	Concentration (ppm %wt.)	Element	Concentration (ppm %wt.)
Li	< 0.05	Ag	< 0.5
Be	< 0.05	Cd	< 0.5
B	< 0.05	In	< 0.5
O	Matrix	Sn	< 0.5
F	< 5	Sb	< 0.5
Na	0.3	Te	< 0.1
Mg	0.15	I	< 0.5
Al	Matrix	Cs	< 0.5
Si	4.5	Ba	< 0.1
P	< 0.1	La	< 0.1
S	< 0.5	Ce	< 0.1
Cl	0.16	Pr	< 0.1
K	< 0.5	Nd	~ .58 wt.%
Ca	1.4	Sm	< 0.1
Sc	< 0.05	Eu	< 0.1
Ti	0.23	Gd	< 0.5
V	< 0.05	Tb	< 1
Cr	< 0.5	Dy	< 0.5
Mn	< 0.05	Ho	< 0.5
Fe	< 1	Er	< 0.5
Co	< 0.05	Tm	< 0.5
Ni	< 0.5	Yb	< 0.5
Cu	< 10	Lu	< 0.5
Zn	< 0.5	Hf	< 0.5
Ga	< 0.1	Ta	Cathode
Ge	< 1	W	< 20
As	< 0.5	Re	< 0.05
Se	< 0.5	Os	< 0.05
Br	< 0.5	Ir	0.23
Rb	< 0.5	Pt	3.9
Sr	< 0.5	Au	Interference
Y	Matrix	Hg	< 0.5
Zr	0.59	Tl	< 0.1
Nb	< 50	Pb	< 0.1
Mo	< 20	Bi	< 0.1
Ru	<0.5	Th	< 0.01
Rh	<0.5	U	< 0.01
Pd	<0.5	-	-

Table F1.6: GDMS results for V113295 run number 2.

Element	Concentration (ppm %wt.)	Element	Concentration (ppm %wt.)
Li	< 0.05	Ag	< 0.5
Be	< 0.05	Cd	< 0.5
B	< 0.05	In	< 0.5
O	Matrix	Sn	< 0.5
F	< 5	Sb	< 0.5
Na	0.32	Te	< 0.1
Mg	< 0.1	I	< 0.5
Al	Matrix	Cs	< 0.5
Si	4	Ba	< 0.1
P	< 0.1	La	< 0.1
S	< 0.5	Ce	< 0.1
Cl	< 0.1	Pr	< 0.1
K	< 0.5	Nd	~ .63 wt.%
Ca	< 0.5	Sm	< 0.1
Sc	< 0.05	Eu	< 0.1
Ti	0.35	Gd	< 0.5
V	< 0.05	Tb	< 1
Cr	0.54	Dy	< 0.5
Mn	< 0.05	Ho	< 0.5
Fe	< 1	Er	< 0.5
Co	0.38	Tm	< 0.5
Ni	< 0.5	Yb	< 0.5
Cu	< 10	Lu	< 0.5
Zn	< 0.5	Hf	< 0.5
Ga	< 0.1	Ta	Cathode
Ge	< 1	W	< 20
As	< 0.5	Re	< 0.05
Se	< 0.5	Os	< 0.05
Br	< 0.5	Ir	0.32
Rb	< 0.5	Pt	2.6
Sr	< 0.5	Au	Interference
Y	Matrix	Hg	< 0.5
Zr	< 0.5	Tl	< 0.1
Nb	< 50	Pb	< 0.1
Mo	< 20	Bi	< 0.1
Ru	<0.5	Th	< 0.01
Rh	<0.5	U	< 0.01
Pd	<0.5	-	-

Table F1.7: GDMS results for the "Screamer Rod," a benchmark Nd:YAG laser rod run 1.

Element	Concentration (ppm %wt.)	Element	Concentration (ppm %wt.)
Li	< 0.05	Ag	< 0.5
Be	< 0.05	Cd	< 0.5
B	< 0.05	In	< 0.5
O	Matrix	Sn	< 0.5
F	< 5	Sb	1.5
Na	0.14	Te	< 0.1
Mg	0.16	I	< 0.5
Al	Matrix	Cs	< 0.5
Si	0.68	Ba	< 0.1
P	< 0.1	La	< 0.1
S	< 0.5	Ce	< 0.1
Cl	< 0.1	Pr	< 0.1
K	< 0.5	Nd	~ .41 wt.%
Ca	< 0.5	Sm	< 0.1
Sc	< 0.05	Eu	< 0.1
Ti	< 0.1	Gd	< 0.5
V	< 0.05	Tb	< 1
Cr	1.5	Dy	< 0.5
Mn	< 0.05	Ho	< 0.5
Fe	< 1	Er	< 0.5
Co	< 0.05	Tm	< 0.5
Ni	< 0.5	Yb	< 0.5
Cu	< 10	Lu	< 0.5
Zn	< 0.5	Hf	< 0.5
Ga	< 0.1	Ta	Cathode
Ge	< 1	W	< 20
As	< 0.5	Re	< 0.05
Se	< 0.5	Os	< 0.05
Br	< 0.5	Ir	0.37
Rb	< 0.5	Pt	< 0.5
Sr	< 0.5	Au	Interference
Y	Matrix	Hg	< 0.5
Zr	< 0.5	Tl	< 0.1
Nb	< 50	Pb	< 0.1
Mo	< 20	Bi	< 0.1
Ru	<0.5	Th	< 0.01
Rh	<0.5	U	< 0.01
Pd	<0.5	-	-

Table F1.8: GDMS results for the “Screamer Rod,” a benchmark Nd:YAG laser rod run 2.

Element	Concentration (ppm %wt.)	Element	Concentration (ppm %wt.)
Li	< 0.05	Ag	< 0.5
Be	< 0.05	Cd	< 0.5
B	< 0.05	In	< 0.5
O	Matrix	Sn	< 0.5
F	< 5	Sb	1.6
Na	0.68	Te	< 0.1
Mg	0.19	I	< 0.5
Al	Matrix	Cs	< 0.5
Si	4.3	Ba	< 0.1
P	< 0.1	La	< 0.1
S	< 0.5	Ce	< 0.1
Cl	< 0.1	Pr	< 0.1
K	< 0.5	Nd	~ .4 wt.%
Ca	< 0.5	Sm	< 0.1
Sc	< 0.05	Eu	< 0.1
Ti	0.25	Gd	< 0.5
V	< 0.05	Tb	< 1
Cr	1.4	Dy	< 0.5
Mn	< 0.05	Ho	< 0.5
Fe	< 1	Er	7
Co	< 0.05	Tm	< 0.5
Ni	< 0.5	Yb	< 0.5
Cu	< 10	Lu	< 0.5
Zn	< 0.5	Hf	< 0.5
Ga	< 0.1	Ta	Cathode
Ge	< 1	W	< 20
As	< 0.5	Re	< 0.05
Se	< 0.5	Os	< 0.05
Br	< 0.5	Ir	0.33
Rb	< 0.5	Pt	< 0.5
Sr	< 0.5	Au	Interference
Y	Matrix	Hg	< 0.5
Zr	0.72	Tl	< 0.1
Nb	< 50	Pb	< 0.1
Mo	< 20	Bi	< 0.1
Ru	<0.5	Th	< 0.01
Rh	<0.5	U	< 0.01
Pd	<0.5	-	-

APPENDIX G

SAMPLE HISTORIES FOR WORK ON Nd:YVO$_4$

Table G1.1: Measurement histories for Nd:YVO$_4$ samples used for chapter 4.

Sample	Date & Process	Date & Process	Date & Process	Date & Process	Date & Process
0129-5552 #1	12/10/03 - Laser Power Run	2/10/04 - Laser Power Run	3/31/04 - Laser Power Run	4/1/04 - Laser Power Run	4/26/04 - Laser Power Run
0129-5552 #2	12/10/03 - Laser Power Run	2/10/04 - Laser Power Run	3/31/04 - Laser Power Run	4/1/04 - Laser Power Run	4/26/04 - Laser Power Run
979074-VLOC YV115 #7	12/16/03 - Laser Power Run	12/22/03 - Laser Power Run			
979074-VLOC YV116 #8	12/11/03 - Laser Power Run	12/16/03 - Laser Power Run	12/22/03 - Laser Power Run	3/31/04 - Laser Power Run	4/1/04 - Laser Power Run
979074-VLOC YV117 #9	12/16/03 - Laser Power Run	12/22/03 - Laser Power Run	3/31/04 - Laser Power Run	4/1/04 - Laser Power Run	4/27/04 - Laser Power Run
979074-VLOC YV126 #32	12/16/03 - Laser Power Run	12/22/03 - Laser Power Run	3/31/04 - Laser Power Run	4/1/04 - Laser Power Run	4/27/04 - Laser Power Run
979074-VLOC YV127 #33	12/16/03 - Laser Power Run	12/22/03 - Laser Power Run	3/31/04 - Laser Power Run	4/1/04 - Laser Power Run	4/28/04 - Laser Power Run
979074-VLOC YV128 #35	12/16/03 - Laser Power Run	12/22/03 - Laser Power Run	3/31/04 - Laser Power Run	4/1/04 - Laser Power Run	4/28/04 - Laser Power Run
Baseline #4	9/5/03 - Laser Power Run	12/9/03 - Laser Power Run			
Baseline #5	9/4/03 - Laser Power Run	12/9/03 - Laser Power Run			
Baseline #6	9/19/03 - Laser Power Run	12/9/03 - Laser Power Run			
F200V01 #10	3/31/04 - Laser Power Run	4/1/04 - Laser Power Run	6/22/04 - Laser Power Run		
F200V36 #4	9/18/03 - Laser Power Run	9/19/03 - Laser Power Run			
WSU 4/23/03 #6	9/19/03 - Laser Power Run	2/12/04 - Laser Power Run	3/31/04 - Laser Power Run	4/1/04 - Laser Power Run	4/26/04 - Laser Power Run
WSU 4/23/03 #7	9/25/03 - Laser Power Run	2/12/04 - Laser Power Run	4/26/04 - Laser Power Run	4/26/04 - Laser Power Run	4/28/04 - Laser Power Run

Sample	Date & Process	Date & Process	Date & Process	Date & Process	Date & Process
0129-5552 #1	4/26/04 - Laser Power Run	4/28/04 - Laser Power Run			
0129-5552 #2	4/26/04 - Laser Power Run	4/28/04 - Laser Power Run			
979074-VLOC YV115 #7					
979074-VLOC YV116 #8	4/27/04 - Laser Power Run	4/27/04 - Laser Power Run	4/28/04 - Laser Power Run		
979074-VLOC YV117 #9	4/27/04 - Laser Power Run	4/28/04 - Laser Power Run			
979074-VLOC YV126 #32	4/27/04 - Laser Power Run	4/29/04 - Laser Power Run			
979074-VLOC YV127 #33	4/28/04 - Laser Power Run	4/29/04 - Laser Power Run	5/14/04 - Laser Power Run	5/14/04 - Laser Power Run	7/13/05 - OIM
979074-VLOC YV128 #35	4/28/04 - Laser Power Run	4/29/04 - Laser Power Run			
Baseline #4					
Baseline #5					
Baseline #6					
F200V01 #10					
F200V36 #4					
WSU 4/23/03 #6	4/26/04 - Laser Power Run	4/28/04 - Laser Power Run	6/22/04 - Laser Power Run		
WSU 4/23/03 #7					

APPENDIX H

SAMPLE HISTORIES FOR WORK ON Nd:YAG

Table H1.1: Measurement histories for Nd:YAG samples used for chapter 6.

Sample	Date & Process	Date & Process	Date & Process	Date & Process	Date & Process	Date & Process
51588	3/15/05 - Absorption Spectrum	10/2/06 - Laser Power Run	10/2/06 - Absorption Spectrum	10/5/06 - Al Sputtering	10/5/06 - Diffusion Anneal	10/16/06 - New AR-Coating
51589	10/17/06 - Absorption Spectrum	10/17/06 - Laser Power Run				
51590	10/2/06 - Laser Power Run	10/2/06 - Absorption Spectrum	10/5/06 - Al Sputtering	10/5/06 - Diffusion Anneal	10/16/06 - New AR-Coating	11/7/06 - Laser Power Run
51594	3/15/05 - Absorption Spectrum	6/7/06 - Laser Power Run	6/9/06 - Anneal	6/12/06 - Absorption Spectrum	6/13/06 - Anneal	6/15/06 - New AR-Coating
51595	6/5/06 - Absorption Spectrum	6/5/06 - Laser Power Run	6/8/06 - Al Sputter	6/9/06 - Diffusion Anneal	6/12/06 - Absorption Spectrum	6/13/06 - Anneal
51596	6/5/06 - Absorption Spectrum	6/5/06 - Laser Power Run	6/8/06 - Al Sputter	6/9/06 - Diffusion Anneal	6/12/06 - Absorption Spectrum	6/13/06 - Anneal
51597	3/15/05 - Absorption Spectrum	10/2/06 - Laser Power Run	10/2/06 - Absorption Spectrum	10/5/06 - Al Sputtering	10/5/06 - Diffusion Anneal	10/16/06 - New AR-Coating
51598	10/2/06 - Laser Power Run	10/2/06 - Absorption Spectrum	10/5/06 - Al Sputtering	10/5/06 - Diffusion Anneal	10/16/06 - New AR-Coating	11/8/06 - Laser Power Run
53522	6/29/04 - Laser Power Run	7/12/04 - Lamp Test	7/13/04 - Laser Power Run	7/20/04 - Laser Power Run	7/20/04 - Laser Power Run	7/22/04 - Laser Power Run
68179	11/20/03 - Laser Power Run	11/20/03 - Laser Power Run	11/20/03 - Laser Power Run	11/20/03 - Laser Power Run	11/20/03 - Laser Power Run	11/20/03 - Laser Power Run
94408	4/22/05 - Absorption Spectrum	4/22/05 - Solarization	4/22/05 - Absorption Spectrum	4/28/05 - In Situ PL	4/28/05 - Anneal	5/23/05- Transmission Spectrum
Kentek 2	2/9/06 - In Situ PL	4/20/06 - Laser Coolant Test	12/11/06 - Laser Power Run	12/12/06 - Solarization	12/12/06 - Laser Power Run	12/12/06 - Absorption Spectrum
L260487F	3/30/04 - Laser Power Run	3/31/04 - Laser Power Run	3/31/04 - Laser Power Run	3/31/04 - Laser Power Run	4/29/04 - Absorption Spectrum	6/29/04 - Laser Power Run
Screamer Rod	7/6/05 - Absorption Spectrum	7/6/05 - Transmission Spectrum				
V108733	1/26/06 - Absorption Spectrum	1/26/06 - Laser Power Run	1/27/06 - Absorption Spectrum	2/21/06 - Anneal	2/27/06 - Absorption Spectrum	2/28/06 - Laser Power Run
V108734	1/26/06 - Absorption Spectrum	1/26/06 - Laser Power Run	1/27/06 - Absorption Spectrum	2/21/06 - Anneal	2/27/06 - Absorption Spectrum	2/28/06 - Laser Power Run
V108735	1/26/06 - Absorption Spectrum	1/26/06 - Laser Power Run	1/27/06 - Absorption Spectrum	2/21/06 - Anneal	2/27/06 - Absorption Spectrum	3/2/06 - Laser Power Run
V108736	1/26/06 - Absorption Spectrum	1/26/06 - Laser Power Run	1/27/06 - Absorption Spectrum	2/21/06 - Anneal	2/27/06 - Absorption Spectrum	3/6/06 - Laser Power Run
V108737	1/26/06 - Absorption Spectrum	1/26/06 - Laser Power Run	1/27/06 - Absorption Spectrum	2/21/06 - Laser Power Run	2/21/06 - Anneal	2/27/06 - Absorption Spectrum
V108738	1/26/06 - Absorption Spectrum	1/26/06 - Laser Power Run	1/27/06 - Absorption Spectrum	2/21/06 - Anneal	2/27/06 - Absorption Spectrum	3/17/06 - Laser Power Run
V108739	1/26/06 - Absorption Spectrum	1/26/06 - Laser Power Run	1/27/06 - Absorption Spectrum	2/21/06 - Anneal	2/27/06 - Absorption Spectrum	3/17/06 - Laser Power Run
V108740	1/26/06 - Absorption Spectrum	1/27/06 - Laser Power Run	1/27/06 - Absorption Spectrum	2/21/06 - Laser Power Run	2/21/06 - Anneal	2/27/06 - Absorption Spectrum
V108741	1/31/06 - Absorption Spectrum	1/31/06 - Laser Power Run	3/17/06 - Anneal	5/26/06 - Laser Power Run	5/26/06 - Absorption Spectrum	5/30/06 - Anneal
V109426	11/17/06 - Absorption Spectrum	11/20/06 - Laser Power Run	11/20/06 - Laser Power Run	11/22/06 - Al Sputtering	12/4/06 - Diffusion Anneal	12/14/06 - New AR-Coatings
V113295	11/17/06 - Absorption Spectrum	11/20/06 - Laser Power Run	11/20/06 - Laser Power Run	11/22/06 - Al Sputtering	12/4/06 - Diffusion Anneal	12/14/06 - New AR-Coatings
V113389	11/17/06 - Absorption Spectrum	11/20/06 - Laser Power Run	11/20/06 - Laser Power Run	11/22/06 - Al Sputtering	12/4/06 - Diffusion Anneal	12/14/06 - New AR-Coatings
V75392T	4/4/04 - Laser Power Run	4/4/04 - Laser Power Run	4/4/04 - Laser Power Run	4/4/04 - Laser Power Run	4/4/04 - Laser Power Run	4/4/04 - Laser Power Run
V75393B	6/25/04 - Laser Power Run	6/25/04 - Laser Power Run	6/25/04 - Laser Power Run	6/25/04 - Laser Power Run	6/25/04 - Laser Power Run	6/25/04 - Laser Power Run
V77649	5/14/04 - Laser Power Run	5/14/04 - Laser Power Run	5/14/04 - Laser Power Run	5/14/04 - Laser Power Run	5/14/04 - Laser Power Run	5/14/04 - Laser Power Run
V77650T	4/20/04 - Absorption Spectrum	4/21/04 - Laser Power Run	4/21/04 - Laser Power Run	4/21/04 - Laser Power Run	4/21/04 - Laser Power Run	4/22/04 - Laser Power Run
V78748A	10/13/04 - Laser Power Run	10/20/04 - Laser Test	10/22/04 - Laser Power Run	11/10/04 - Absorption Spectrum	11/12/04 - Absorption Spectrum	12/6/04 - Absorption Spectrum
V78748B	9/23/04 - Laser Power Run	10/8/04 - Laser Power Run	10/11/04 - Laser Test	10/22/04 - Laser Power Run	11/10/04 - Absorption Spectrum	11/12/04 - Absorption Spectrum
V90146	3/3/05 - Laser Power Run	3/15/05 - Absorption Spectrum	3/15/05 - Transmission Spectrum	6/2/05 - Absorption Spectrum	6/2/05 - Transmission Spectrum	6/2/05 - Solarization
V90147	3/7/05 - Laser Power Run	3/15/05 - Absorption Spectrum	3/15/05 - Transmission Spectrum	3/28/05 - In Situ PL	3/28/05 - Laser Power Run	3/31/05 - Anneal
V90301	2/9/05 - Laser Power Run	2/15/05 - Absorption Spectrum	3/15/05 - Transmission Spectrum	3/31/05 - Anneal	8/13/05 - Absorption Spectrum	1/31/06 - Laser Power Run
V98138	7/6/05 - Absorption Spectrum	8/26/05 - Anneal	8/26/05 - Absorption Spectrum	9/2/05 - Laser Power Run	9/14/05 - Anneal	9/19/05 - Repolish
V98139	7/6/05 - Absorption Spectrum	8/26/05 - Anneal	8/26/05 - Absorption Spectrum	9/12/05 - Laser Power Run	9/14/05 - Anneal	9/19/05 - Repolish
V98140	7/6/05 - Absorption Spectrum	8/26/05 - Anneal	8/26/05 - Absorption Spectrum	9/7/05 - Laser Power Run	9/14/05 - Anneal	9/19/05 - Repolish
V98141	7/6/05 - Absorption Spectrum	8/26/05 - Anneal	8/26/05 - Absorption Spectrum	9/9/05 - Laser Power Run	9/14/05 - Anneal	9/19/05 - Repolish
Re-grown Nd:YAG	5/29/07 - Absorption Spectrum	5/31/07 - Solarization	5/31/07 - Absorption Spectrum	5/8/08 - PL		

Sample	Date & Process	Date & Process	Date & Process	Date & Process	Date & Process	Date & Process
51588	11/7/06 - Laser Power Run	11/8/06 - Absorption Spectrum				
51589						
51590	11/8/06 - Absorption Spectrum					
51594	7/17/06 - Absorption Spectrum	7/17/06 - Laser Power Run	12/14/06 - PAS	5/8/08 - PL		
51595	6/15/06 - New AR-Coatings	7/17/06 - Absorption Spectrum	7/17/06 - Laser Power Run	7/18/06 - Anneal	8/24/06 - New AR-Coatings	8/24/06 - Absorption Spectrum
51596	6/15/06 - New AR-Coatings	7/17/06 - Absorption Spectrum	7/17/06 - Laser Power Run	8/7/06 - Laser Power Run	8/8/06 - Laser Power Run	12/14/06 - PAS
51597	11/8/06 - Laser Power Run	11/8/06 - Absorption Spectrum				
51598	11/8/06 - Absorption Spectrum					
53522	8/30/04 - Laser Power Run	8/31/04 - Laser Power Run	9/1/04 - Laser Power Run	11/5/04 - Laser Power Run	11/10/04 - Absorption Spectrum	11/12/04 - Laser Power Run
68179	11/20/03 - Laser Power Run	4/15/04 - Laser Power Run	4/15/04 - Laser Power Run	4/19/04 - Laser Power Run	4/19/04 - Laser Power Run	4/20/04 - Laser Power Run
94408	5/23/05 - Solarization	5/23/05 - Transmission Spectrum	8/5/05 - Absorption Spectrum	10/17/05 - PL	2/2/06 - In Situ PL	11/30/06 - Cut Rod
Kentek 2	5/28/08 - Low Temp PL					
L260487F	7/13/04 - Laser Power Run	7/17/04 - Laser Power Run	7/20/04 - Laser Power Run	8/12/04 - Absorption Spectrum	8/30/04 - Laser Power Run	3/15/05 - Transmission Spectrum
Screamer Rod						
V108733	3/17/06 - Laser Power Run	4/13/06 - Repolish	5/1/06 - Absorption Spectrum	5/2/06 - Laser Power Run	5/2/06 - Absorption Spectrum	5/8/06 - Absorption Spectrum
V108734	2/28/06 - Laser Power Run	3/17/06 - Laser Power Run	4/13/06 - Anneal	4/13/06 - Absorption Spectrum	4/17/06 - Laser Power Run	4/19/06 - Absorption Spectrum
V108735	3/3/06 - Laser Power Run	3/3/06 - Laser Power run	3/17/06 - Laser Power Run	4/13/06 - Repolish	5/1/06 - Absorption Spectrum	5/2/06 - Laser Power Run
V108736	3/6/06 - Laser Power Run	3/17/06 - Laser Power Run	4/13/06 - Anneal	4/13/06 - Absorption Spectrum	4/17/06 - Laser Power Run	4/19/06 - Absorption Spectrum
V108737	3/17/06 - Laser Power Run	4/13/06 - Anneal	4/13/06 - Absorption Spectrum	4/17/06 - Laser Power Run	4/19/06 - Absorption Spectrum	4/20/06 - Laser Coolant Test
V108738	4/13/06 - Anneal	4/13/06 - Absorption Spectrum	4/18/06 - Laser Power Run	4/19/06 - Absorption Spectrum	5/17/06 - Absorption Spectrum	5/17/06 - Laser Power Run
V108739	3/29/06 - Absorption Spectrum	4/13/06 - Anneal	4/13/06 - Absorption Spectrum	4/18/06 - Laser Power Run	4/19/06 - Absorption Spectrum	5/17/06 - Absorption Spectrum
V108740	3/20/06 - Laser Power Run	4/13/06 - Anneal	4/13/06 - Absorption Spectrum	4/18/06 - Laser Power Run	4/19/06 - Absorption Spectrum	5/15/06 - Anneal
V108741	6/5/06 - Absorption Spectrum					
V109426	1/11/07 - Absorption Spectrum	1/11/07 - Laser Power Run	1/11/07 - Laser Power Run	4/22/08 - Laser Power Run	5/8/08 - PL	5/28/08 - Low Temp PL
V113295	1/11/07 - Absorption Spectrum	1/12/07 - Laser Power Run	1/12/07 - Laser Power Run	10/19/07 - Cut Rod	10/19/07 - NAA	1/17/08 - Cut Rod
V113389	1/11/07 - Absorption Spectrum	1/12/07 - Laser Power Run	1/12/07 - Laser Power Run	10/19/07 - Cut Rod	10/19/07 - NAA	1/17/08 - Cut Rod
V75392T	4/6/04 - Laser Power Run	4/6/04 - Laser Power Run	4/29/04 - Absorption Spectrum	6/28/04 - Laser Power Run	7/14/04 - Laser Power Run	8/12/04 - Absorption Spectrum
V75393B	6/25/04 - Laser Power Run	6/28/04 - Laser Power Run	6/28/04 - Laser Power Run	8/12/04 - Absorption Spectrum	8/30/04 - Laser Test	8/30/04 - Laser Power Run
V77649	5/14/04 - Laser Power Test	6/22/04 - Laser Power Run	6/22/04 - Laser Power Run	6/23/04 - Laser Power Run	6/23/04 - Laser Power Run	6/23/04 - Laser Power Run
V77650T	4/22/04 - Laser Power Run	4/22/04 - Laser Power Run	4/22/04 - Laser Power Run	4/22/04 - Laser Power Run	4/22/04 - Laser Power Run	4/22/04 - Laser Power Run
V78748A	12/22/04 - In Situ PL	1/4/05 - Transmission Spectrum	6/2/05 - Absorption Spectrum	6/2/05 - Transmission Spectrum	6/2/05 - Solarization	6/2/05 - Absorption Spectrum
V78748B	12/6/04 - Absorption Spectrum	12/27/04 - In Situ PL	1/4/05 - Transmission Spectrum	4/6/05 - Laser Power Run	4/3/06 - Absorption Spectrum	11/9/06 - Absorption Spectrum
V90146	6/2/05 - Absorption Spectrum	6/2/05 - Transmission Spectrum	6/6/05 - Anneal	6/10/05 - Transmission Spectrum	7/28/05 - Absorption Spectrum	2/1/07 - Cut Rod
V90147	4/19/05 - Laser Power Run	7/28/05 - Absorption Spectrum	11/6/06 - Absorption Spectrum			
V90301	2/1/06 - Laser Coolant Test	2/9/06 - In Situ PL	5/5/06 - Al Sputtering	5/8/06 - Diffusion Anneal	5/10/06 - Anneal	5/12/06 - New AR-Coatings
V98138	10/19/05 - Laser Power Run	10/25/05 - Absorption Spectrum	11/14/05 - Laser Power Run	11/15/05 - Laser Power Run	11/21/05 - Removed AR-Coatings	12/9/05 - Laser Power Run
V98139	10/20/05 - Laser Power Run	10/25/05 - Absorption Spectrum	11/29/05 - Laser Power Run	12/1/05 - Laser Power Run	12/2/05 - Laser Power Run	12/5/05 - Removed AR-Coatings
V98140	10/24/05 - Laser Power Run	10/25/05 - Absorption Spectrum	11/16/05 - Laser Power Run	11/17/05 - Laser Power Run	11/21/05 - Removed AR-Coatings	12/12/05 - Laser Power Run
V98141	10/25/05 - Laser Power Run	10/25/05 - Absorption Spectrum	11/22/05 - Laser Power Run	11/29/05 - Laser Power Run	12/5/05 - Removed AR-Coatings	12/21/05 - Laser Power Run
Re-grown Nd:YAG						

Sample	Date & Process	Date & Process	Date & Process	Date & Process	Date & Process	Date & Process
51588						
51589						
51590						
51594						
51595	8/24/06 - Laser Power Run	10/17/06 - Absorption Spectrum				
51596						
51597						
51598						
53522	11/23/04 - Laser Power Run	12/2/04 - Laser Power Run	12/2/04 - Laser Power Run	12/6/04 - Absorption Spectrum	12/8/04 - Laser Power Run	12/9/04 - Laser Power Run
68179	4/20/04 - Laser Power Run	4/20/04 - Laser Power Run	7/8/04 - Laser Power Run	7/13/04 - Laser Power Run	7/13/04 - Lamp Test	7/16/04 - Laser Power Run
94408	11/30/06 - NAA	5/28/08 - Low Temp PL				
Kentek 2						
L260487F	6/2/05 - Solarization	6/2/05 - Transmission Spectrum	4/3/06 - Absorption Spectrum			
Screamer Rod						
V108733	5/9/06 - Laser Power Run	5/9/06 - Absorption Spectrum	5/15/06 - Anneal			
V108734	5/15/06 - Anneal					
V108735	5/2/06 - Absorption Spectrum	5/8/06 - Absorption Spectrum	5/9/06 - Laser Power Run	5/9/06 - Absorption Spectrum	5/15/06 - Anneal	5/26/06 - Laser Power Run
V108736	5/15/06 - Anneal	5/26/06 - Laser Power Run	5/26/06 - Absorption Spectrum	6/21/06 - Absorption Spectrum	6/22/06 - Laser Power Run	6/23/06 - Absorption Spectrum
V108737	5/15/06 - Anneal	5/26/06 - Laser Power Run	5/26/06 - Absorption Spectrum	6/21/06 - Absorption Spectrum	6/22/06 - Laser Power Run	6/23/06 - Absorption Spectrum
V108738	5/26/06 - Anneal	5/30/06 - Absorption Spectrum	5/30/06 - Laser Power Run	5/30/06 - Absorption Spectrum	6/21/06 - Absorption Spectrum	6/22/06 - Laser Power Run
V108739	5/17/06 - Laser Power Run	5/26/06 - Anneal	5/30/06 - Absorption Spectrum	5/30/06 - Laser Power Run	5/30/06 - Absorption Spectrum	6/21/06 - Absorption Spectrum
V108740	5/26/06 - Laser Power Run	5/26/06 - Absorption Spectrum	6/21/06 - Absorption Spectrum	6/22/06 - Laser Power Run	6/23/06 - Absorption Spectrum	
V108741						
V109426						
V113295	1/30/08 - GDMS					
V113389	1/30/08 - GDMS					
V75392T	8/30/04 - Laser Power Run	3/22/05 - Laser Power Run	3/22/05 - In Situ PL	3/31/05 - Anneal	4/3/06 - Absorption Spectrum	11/6/06 - Absorption Spectrum
V75393B	9/1/04 - Laser Power Run	10/22/04 - Laser Power Run	10/25/04 - Laser Power Run	10/28/04 - Laser Power Run	10/29/04 - Laser Power Run	11/1/04 - Laser Power Run
V77649	6/23/04 - Laser Power Run	6/23/04 - Laser Power Run	6/24/04 - Laser Power Run	6/24/04 - Laser Power Run	6/24/04 - Laser Power Run	6/24/04 - Laser Power Run
V77650T	4/22/04 - Laser Power Run	4/22/04 - Laser Power Run	4/23/04 - Laser Power Run	4/23/04 - Laser Power Run	6/28/04 - Laser Power Run	7/13/04 - Laser Power Run
V78748A	6/2/05 - Transmission Spectrum	6/6/05 - Polarized Transmission	6/28/05 - In Situ PL	4/3/06 - Absorption Spectrum	11/9/06 - Absorption Spectrum	12/8/06 - Solarization
V78748B	2/1/07 - Cut Rod	2/8/07 - NAA	5/28/08 - Low Temp PL			
V90146	2/8/07 - NAA	5/28/08 - Low Temp PL				
V90147						
V90301	5/31/06 - Absorption Spectrum	6/1/06 - Laser Power Run	5/23/08 - Absorption Spectrum	5/28/08 - Low Temp PL		
V98138	12/12/05 - Laser Power Run	12/16/05 - Anneal	12/20/05 - Absorption Spectrum	12/20/05 - Laser Power Run	12/20/05 - Laser Power Run	12/21/05 - Anneal
V98139	12/21/05 - Laser Power Run	12/21/05 - Laser Power Run	12/21/05- Anneal	12/27/05 - Laser Power Run	12/28/05 - Absorption Spectrum	1/11/06 - Anneal
V98140	12/14/05 - Laser Power Run	12/16/05 - Anneal	12/20/05 - Absorption Spectrum	12/20/05 - Laser Power Run	12/20/05 - Laser Power Run	12/21/05 - Anneal
V98141	12/21/05 - Laser Power Run	12/21/05 - Laser Power Run	12/21/05- Anneal	12/27/05 - Laser Power Run	12/28/05 - Absorption Spectrum	12/29/05 - Laser Power Run
Re-grown Nd:YAG						

Sample	Date & Process	Date & Process	Date & Process	Date & Process	Date & Process	Date & Process
51588						
51589						
51590						
51594						
51595						
51596						
51597						
51598						
53522	12/10/04 - In Situ PL	3/15/05 - Transmission Spectrum	3/17/05 - Solarization	3/17/05 - Absorption Spectrum	3/25/05 - In Situ PL	3/25/05 - Laser Power Run
68179	3/15/05 - Transmission Spectrum	12/11/06 - Laser Power Run	12/12/06 - Solarization	12/12/06 - Laser Power Run	12/12/06 - Absorption Spectrum	5/8/08 - PL
94408						
Kentek 2						
L260487F						
Screamer Rod						
V108733						
V108734						
V108735	5/26/06 - Absorption Spectrum	6/21/06 - Absorption Spectrum	6/22/06 - Laser Power Run	6/23/06 - Absorption Spectrum		
V108736						
V108737						
V108738	6/23/06 - Absorption Spectrum					
V108739	6/22/06 - Laser Power Run	6/23/06 - Absorption Spectrum				
V108740						
V108741						
V109426						
V113295						
V113389						
V75392T	11/9/06 - Absorption Spectrum	2/1/07 - Cut Rod	2/8/07 - NAA	5/28/08 - Low Temp PL		
V75393B	11/2/04 - Laser Power Run	4/26/07 - Cut Rod	4/26/07 - NAA	5/28/08 - Low Temp PL		
V77649	6/29/04 - Laser Power Run	8/12/04 - Absorption Spectrum	8/30/04 - Laser Power Run	3/15/05 - Transmission Spectrum	6/2/05 - Solarization	6/2/05 - Absorption Spectrum
V77650T	8/12/04 - Absorption Spectrum	8/30/04 - Laser Power Run	11/9/04 - Absorption Spectrum	11/10/04 - Absorption Spectrum	3/15/05 - Transmission Spectrum	4/3/06 - Absorption Spectrum
V78748A	12/8/06 - Absorption Spectrum	12/8/06 - Solarization	12/8/06 - Absorption Spectrum	2/1/07 - Cut Rod	2/8/07 - NAA	5/28/08 - Low Temp PL
V78748B						
V90146						
V90147						
V90301						
V98138	12/28/05 - Laser Power Run	12/28/05 - Laser Power Run	12/28/05 - Absorption Spectrum	1/11/06 - Anneal	1/17/06 - Absorption Spectrum	1/17/06 - Laser Power Run
V98139						
V98140	12/28/05 - Laser Power Run	12/28/05 - Laser Power Run	12/28/05 - Absorption Spectrum	1/11/06 - Anneal	1/17/06 - Absorption Spectrum	1/17/06 - Laser Power Run
V98141	12/29/05 - Laser Power Run	1/11/06 - Anneal				
Re-grown Nd:YAG						

Sample	Date & Process	Date & Process	Date & Process	Date & Process	Date & Process	Date & Process
51588						
51589						
51590						
51594						
51595						
51596						
51597						
51598						
53522	3/31/05 - Anneal	4/5/05 - Laser Power Run	4/11/05 - Laser Power Run	8/4/05 - Removed AR-coatings	8/4/05 - Absorption Spectrum	8/4/05 - Transmission Spectrum
68179	5/28/08 - Low Temp PL					
94408						
Kentek 2						
L260487F						
Screamer Rod						
V108733						
V108734						
V108735						
V108736						
V108737						
V108738						
V108739						
V108740						
V108741						
V109426						
V113295						
V113389						
V75392T						
V75393B						
V77649	6/2/05 - Transmission Spectrum					
V77650T						
V78748A						
V78748B						
V90146						
V90147						
V90301						
V98138	1/17/06 - Laser Power Run					
V98139						
V98140	1/17/06 - Laser Power Run	1/18/06 - Laser Power Run	2/22/06 - Laser Power Run	2/23/06 - Laser Power Run		
V98141						
Re-grown Nd:YAG						